Lehrstuhl für Elektrische Antriebssysteme und Leistungselektronik
der Technischen Universität München

Optimization of Velocity and Displacement Measurement with Optical Encoder and Laser Self-Mixing Interferometry

Hui Sun

Vollständiger Abdruck der von der Fakultät für Elektrotechnik und Informationstechnik der Technischen Universität München zur Erlangung des akademischen Grades eines

Doktor-Ingenieurs

genehmigten Dissertation.

Vorsitzender: Prof. Dr.-Ing. Christian Jirauschek
Prüfer der Dissertation:
1. Prof. Dr.-Ing. Dr. h.c. Ralph Kennel
2. Prof. Dr.-Ing. habil. Dr. h.c. Alexander W. Koch

Die Dissertation wurde am 29.07.2019 bei der Technischen Universität München eingereicht und durch die Fakultät für Elektrotechnik und Informationstechnik am 20.01.2020 angenommen.

Acknowledgment

My sincere and profound gratitude goes first and foremost to my supervisor, Prof. Dr.-Ing. Ralph Kennel, for his valuable guidance, great patience, and constant support during the entire period of my research study. I appreciate that Prof. Kennel gave me the opportunity to do my Ph.D. research at the Institute for Electrical Drive Systems and Power Electronics at Technische Universität München (TUM). The open atmosphere and international group of the institute sustained by Prof. Kennel benefited me a lot.

I want to express my special appreciation and thanks to ChenYang Technologies GmbH & Co.KG for the funding source that made my Ph.D. work possible. My greatly thanks and respects are reserved for Dr.-Ing. habil. Jigou Liu, the chief executive officer of the company, who has guided at crucial moments in my work while also allowed me to work independently at the majority of the time. The profound and invaluable knowledge that I gained from him will benefit me in my future life and career. It is my great pleasure to work with colleagues in the company. The team has been a source of friendships as well as good advice and collaboration. Many thanks to Dr. Cheng Liu, for the cooperation and the helps he gave me at the beginning of my research. Master students that I have supervised have also helped me a lot.

My sincere thanks go to my colleagues at EAL, for the opening and fruitful discussions during our meetings. I appreciate the collaboration experience with Dr. Xinbo Cai. His creative ideas and abundant practical experience benefited me greatly. I give my special thanks to our group, for cooperation in the study and happy time in life.

My sincere appreciation goes out to my beloved family, my parents, my husband, my son, and my brother. Their unconditional love, care, and support have always been my strength. Especially my husband, Quan Zhang, he has been by my side, encouraging me throughout my Ph.D. study. Without his support, I could hardly finish my work.

in Munich, January 2019
Hui Sun

Abstract

This dissertation aims to optimize the measurement of velocity with the optical encoder, and velocity and displacement with the laser self-mixing interferometry (SMI). The main contributions are as follows: An efficient and tuning-easy fixed gain filter is provided to obtain the position, velocity, and acceleration in electrical drives by analyzing the shaft position signal from the optical encoder. With employing the SMI, in an attempt to increase the accuracy of velocity measurement, algorithms including the interpolation of fast Fourier transform (FFT), maximum likelihood estimation (MLE), and extended Kalman filter (EKF) are thoroughly investigated and fully detailed. The algorithm for displacement retrieving is improved by proposing a simple and effective method for estimating the feedback factor C of the interference signal. In addition, the EKF is used for retrieving displacement under weak feedback regime. It simplifies the process for discarding the tedious transition detection and the feedback factor C estimation in the general phase unwrapping method (PUM).

Kurzzusammenfassung

Das Ziel der vorliegenden Dissertation besteht in der Optimierung der Geschwindigkeitsmessung mit dem optischen Encoder, und der Geschwindigkeit- und Verschiebungsmessung mit der Laser-Self-Mixing-Technologie. Die wichtigsten Erkenntnisse dieser Arbeit sind wie folgt aufgeführt: Es wird ein effizienter und einfach einzustellender Filter mit fester Verstärkung vorgeschlagen, um die Winkelposition, Geschwindigkeit und Beschleunigung des elektrischen Antriebs durch die Analyse des Positionssignals von der Antriebswelle durch einen optischen Encoder zu erhalten. Bei der Verwendung der Self-Mixing-Interferometrie (SMI) werden die Algorithmen zur Erhöhung der Genauigkeit in der Geschwindigkeitsmessung gründlich untersucht und ausführlich dargelegt, einschließlich der Interpolation der schnellen Fourier-Transformation (engl. fast Fourier transform, FFT), der Maximum-Likelihood-Schätzung (engl. maximum likelihood estimator, MLE) und der Extended-Kalman-Filterung (EKF). Währenddessen wird der Algorithmus zur Verschiebungsbestimmung verbessert, indem eine einfache und zugleich effiziente Methode zur Schätzung des Rückkopplungspegelfaktors C des interferometrischen Signals vorgeschlagen wird. Zusätzlich wird der EKF für die Bestimmung der Verschiebung unter einem schwachen Rückkopplungssignal verwendet. Es vereinfacht den Prozess durch die Verwerfung der Übergangsdetektion sowie die Schätzung des Rückkopplungsfaktors C durch die allgemeine Phasen-Unwrapping-Methode (PUM).

Contents

Chapter 1

Introduction

This work focuses on the measurement of velocity and displacement using optical technology, including the optical encoder and the laser SMI. In this chapter, the background, research focus, motivations, and objectives of this dissertation are introduced. The contributions indexed to each of the following chapters are summarized as well.

1.1 Motivations and objectives

Velocity and position are critical parameters in the electrical drive, for the purpose of current control on the motor side, and for providing feedback information for superior regulation of the load on the machine side. Different types of transducers are customarily used to provide angular displacement and angular velocity information in the digital or analog form [1]. According to the measurement principle, they can be classified into four categories: magnetic, capacitive, conductive, and optical. In practice, the optical incremental encoder is the most popular position sensor in the industrial field due to its simple detection circuit, high resolution, high accuracy, and relative easy adaptability to digital control systems. Since the optical encoder only provides position information, it is necessary to numerically obtain a high-quality velocity signal from the measured angular displacement [2].

Numerous solutions have been explored and published to estimate the velocity and acceleration based on the angular displacement obtained by the optical incremental encoder. Generally, these solutions are roughly divided into three types: the finite-difference method (FDM), inverse-time method (ITM), and Kalman filter (KF). The FDM is more suitable in the high-speed range, and the ITM is better suited in the low-speed range. Therefore, these two methods can be used in combination, namely, in the high-velocity region using the FDM, and in the low-velocity region using the ITM. However, it is prob-

lematic to determine the critical point of these two methods. Moreover, discontinuous points in the velocity estimation may severely disturb the controller. Another drawback of this combination method is that its update period is variable. Thus, conventional methods are difficult to guarantee an accurate estimation of the entire velocity range. Due to the quantization errors, the acceleration estimates based on these two methods are much worse. Then, extensive research was conducted on the KF to estimate the position and speed of electric motors in academics and industry [3–5]. The KF usually requires a relatively accurate model of the control plant [6, 7] and its parameters (for example, the inertia and friction factor). The implementation steps involve complex matrix calculations and bring a lot of computational burden to the digital controller. The tuning process that needs knowledge of process noise and measurement noise requires a lot of professional knowledge and is quite tedious. Motivated by these considerations, a simple method to solve the above problems will be proposed and discussed.

High-resolution encoders are usually required to precisely control speed and/or position, especially when control at very low speeds is required. The positioning accuracy and speed stability of the machine axes greatly determine the quality of the workpiece and product. This necessitates a position encoder with a large number of measurement steps and high signal quality. In addition, at low speed, the position error of the encoder within one signal period affects speed stability. Encoder with higher resolution and accuracy can decisively improve the speed stability of the motor and significantly reduce the disturbance in the motor current. However, the increase in the resolution of the optical encoder is related to the increase in cost. Diffraction-based optical encoders utilize the diffraction and interference characteristics of high-precision grating disks, enabling designers to improve system performance while reducing cost and size.

In 2008, P. Drabarek and R. M. Kennel reported some developments in the field of laser interferometric encoder based on Laser Doppler technology, which are designed to provide a very high resolution [8]. The interferometric sensors do not rely on the teeth or poles of the object, but obtain the measurement parameters by interfering with their center wavelengths. Therefore, they have inherent high resolution and accuracy. The technical results obtained through some preliminary studies and experiments are quite encouraging. This showed that the interferometric encoders have good potential, and further investigation and research should be carried out to improve the performance-to-cost ratio by using the homodyne type interferometer, instead of the heterodyne interferometer.

The laser Doppler anemometers (LDAs), laser Doppler velocimeters (LDVs), and laser Doppler vibrometers are optical metrology systems that use the laser Doppler effect to encode information generated by the displacement and velocity of the measured surface [9]. They can easily obtain fairly high resolution and accuracy. The major drawbacks of them are high cost and large size due to the complex optical system of the sensing head. With the continuous pursuit of precise control, smaller feature sizes, and lower prices, there has been a growing interest in another interference technology, namely laser SMI, which is based on dynamic characteristics of the optical feedback effect. Based on this technology, Philips, Microsoft, and Covidien have been granted U.S. patents pertaining

to optical input devices and movement sensors [10–27]. In 2008, Pruijmboom et al. reported a commercial product based on this technology, the Philips Twin-Eye Laser sensor for quasi-three-dimensional displacement measurement [28, 29]. This miniature laser Doppler interferometer can work on all light scattering surfaces, and can be compared with expensive laser interferometers, but at a cost that is compatible with the requirements for consumer products.

Generally, a laser SMI consists of a laser diode, a focusing lens, and related electronics without any additional or complicated optical components. The field within the laser cavity is superimposed with the weak field back-reflected or back-scattered by a remote target, thereby causing modulation of the amplitude and frequency of the laser field. The modulated power emitted by the laser is a function of the phase of the back-reflected field. The fringe shift caused by the feedback light is related to the amount of displacement [30], which is the same as the LDV. In comparison with the traditional LDV, the first significant feature of this SMI is that this technique allows the laser to perform as both a light source and a detector. It has the advantages of lower cost, fewer components, and a self-aligning system for various applications, such as solid and liquid velocity measurement [31–34], displacement construction [35–37], absolute distance measurement [38, 39], and vibration detection [40–42]. Another important feature of SMI is that the signal can be asymmetric, which makes it possible to discriminate the direction of the moving target. Moreover, it is self-aligned because the signal can be detected by the monitoring photo-diode integrated into the laser diode, so no complicated adjustment process is required. In spite of its simple configuration, it also has good resolution and accuracy.

Sensing applications based on the self-mixing effect in low-cost commercial semiconductor lasers has begun to appear in scientific researches since 1986 [31,32]. The feasibility of velocity, distance, and displacement measurements has been demonstrated in enormous quantities of literature [31–33]. The advantages of self-mixing sensing are listed as follows:

- Only one or two lenses are required, without any other additional optical components, thus realizing a very simple and compact system.
- The integrated photo-diode included in most laser diodes can be used as a detector. Therefore, no external photo-detector is required. The change in the terminal voltage of the laser diode can also be used to obtain the SMI signal.
- Due to the simple configuration, the system is self-aligned and spares the trouble of aligning the optical path.
- The system is very sensitive because it realizes a coherent detection of the return field and can easily attain the quantum detection regime [43].
- The inclination of the power fringe can be exploited to discern the direction of motion.
- The basic resolution using the fringe counting method is half the wavelength. Using other signal processing techniques, the resolution can be several nanometers.

- The effective information is carried by the laser beam.
- It can operate on rough surfaces.
- High bandwidth.

Although numerous studies using SMI to measure velocity and displacement have been reported, there are still some problems remained before the SMI based sensors can be reliably used to provide high accuracy:

- When a rough target scatters the light emitted from the coherent laser, the generated SMI signal will be affected by the multiplicative noise caused by the speckle effect. The speckle effect leads to random amplitude modulation of the signal, which results in the loss of the ideal sinusoidal waveform of the signal and broadens the spectrum in the frequency domain. In addition, wide-band additive noise often appears in practical situations. The presence of these two types of noise makes it more difficult to acquire the accurate Doppler frequency. Therefore, a suitable and effective frequency estimation algorithm has to be developed [44].
- In the case of velocity measurement, it is difficult to discriminate the direction of velocity using the differential method due to the speckle effect or the weak feedback level.
- The retrieve process of conventional PUM for measuring displacement is tedious, and it has a poor performance when the signal is affected by noise.

1.2 Contributions

This dissertation aims to improve the velocity and displacement estimation results of the optical encoder and the laser SMI sensor. The original contributions presented in this dissertation are listed as follow:

1. The methods of measuring position and velocity of electric motors using an optical incremental encoder were revisited, and an efficient and tuning-easy fixed gain filter was proposed.
2. A system for measuring velocity and displacement using laser self-mixing interference technology has been developed.
3. The methods of accurately estimating the Doppler frequency of SMI signal were analyzed.

4. A new algorithm based on the EKF for estimating velocity and displacement using the SMI was proposed. Based on the model of SMI signal, the multiplicative noise caused by the speckle effect and the direction of the velocity are taken into account.

5. In order to retrieve the displacement, a simple and effective method was proposed to estimate the feedback factor C of the SMI sensor. Discarding the complicated and demanding calculation process of the general C estimation method, a final equation is obtained.

6. An algorithm based on the theory of EKF for retrieving displacement using SMI sensor under weak feedback regime was presented. The main novelty of the algorithm is the ability to discriminate the direction of displacement inherently and no extra effort is required. It does not need the process of transition detection and feedback factor C estimation in the general PUM.

1.3 Outline

Following this introduction, the basic principles of optical encoder and SMI are presented in Chapter 2. The resonator model and rate equation model of SMI and its applications are introduced in detail.

In Chapter 3, an efficient and tuning-easy fixed gain filter is proposed to estimate position, velocity, and acceleration from the position of shaft encoder.

In Chapter 4, a system using the SMI technology to measure velocity is introduced. The error analysis and different algorithms for precise measurement of velocity are discussed.

In Chapter 5, the SMI is used to measure displacement. Algorithms improving its measurement performance are thoroughly investigated.

Finally, this dissertation finishes with some concluding remarks and thoughts on future work in Chapter 6.

Chapter 2

Background and theory

This chapter reviews the theoretical background of the optical encoder and laser SMI. In commercial electrical drives, the most common sensor used for the position and speed measurement is the optical incremental encoder, because of its simple detection circuit, high resolution, high accuracy, and relatively easy adaptation in digital control systems. The general methods used to estimate velocity from the position obtained by the encoder are introduced in this chapter.

Laser interferometry is a well-established technique, widely used in industry. In the past decades, extensive research on optical feedback has proven that it is a promising solution for a wide range of applications, such as chaotic signal transmission, coherent echo detection, measurement of physical quantities, etc. This chapter describes why the optical feedback in a system consisting of a semiconductor laser and a remote reflector or diffuser can be regarded as an interferometric system. It also provides detailed analysis of the signal characteristic, which is a function of target distance, target motion, optical feedback strength, and semiconductor laser parameters.

2.1 Optical encoder

2.1.1 Introduction

Servo drives are widely used in automation technology, robotics, and handling systems, as well as drive technology for production machines and machine tools. The requirements regarding dynamics, speed stability, and rigidity necessitate ever-increasing gain factors in the control loops. Position resolution and error are important factors for the quality of drive control. The selection of a certain encoder technology strongly depends on the resolution and accuracy requirements of the corresponding application. The properties

of encoders have a decisive influence on important motor qualities (such as positioning accuracy, speed stability, bandwidth), which determine drive command-signal response and disturbance rejection capability, power loss, size, noise emission, and safety [45].

The optical encoder has become the most popular encoder among all encoding methods due to its long-life, simple structure, versatility, high accuracy, and high resolution. An optical encoder is an electromechanical device used to convert the mechanical position of a shaft or axle into an analog or digital electrical signal. The most common configuration of optical encoders is based on a dual grating system. It has two gratings in tandem: one is the scale, and the other is placed in the scanning head. This pair of gratings forms a fringe pattern at a certain distance from the second grating. Optical encoders can mainly be divided into two types: incremental and absolute. The structures of these two types are quite similar. However, they differ in physical properties and movement interpretation. Incremental rotary encoder utilizes transparent discs that contain evenly spaced opaque sections. As the encoder rotates, it generates a train of equally spaced pulses. By counting the pulses or by timing the pulse width using a clock signal, the angular displacement can be determined. The absolute encoder contains components that can also be found in the incremental encoder, but the absolute encoder uses a disc with concentric circle patterns instead of a disc with evenly spaced lines. When the disc of the absolute encoder rotates, it generates multiple pulse trains simultaneously, the number of which is equal to the tracks on the disc. Therefore, the output of the absolute encoder provides a unique code for each shaft position. In other words, each position of the absolute encoder is distinctive. Another feature of the absolute encoder is that it does not lose position information whenever the power is switched off. In the following section, only the optical incremental encoder is studied because it is the most widely used encoder. After this, the optical encoder always denotes the optical incremental encoder in this dissertation.

Generally, an optical encoder consists of five essential components: a light source, a moveable disc, a fixed mask, a photo-detector, and electronics. The moving disc has been etched with concentric tracks. These tracks have a periodic opening called a window. Corresponding tracks and windows are also grooved on the mask. As the light source shines onto the mask through the moving disc, different unique light patterns illuminate the detector. Each optical rotary encoder track contains one or two detectors. Each detector outputs its own signal, and the outputs are slightly shifted from each other, creating slightly offset outputs. Therefore, the output of the optical encoder can be a single line of pulses (an “A” channel) or two lines of pulses (an “A” and “B” channel) that are quadrature.

The optical encoder generates a specified amount of pulses in one rotation. It does not indicate an absolute position, but only provides incremental changes in position, namely the angular displacement. The number of lines of an optical disc is equivalent to the number of pulses per revolution (PPR), which is usually defined as the resolution. Encoder pulse refers to the smallest segment of a given physical quantity that the encoder can measure or display. In other words, it is the granularity with which the encoder can monitor the equipment. On the code disc of an optical encoder, the denser the pattern is

scribed, the higher the resolution. For each incremental change in position, the encoder produces a sinusoidal electrical signal. These signals are counted by a calibrated starting point in an up-down counter or processed by other complicated algorithms. Except for determining the position of the shaft, the dual-channel encoder can also provide information about the direction of rotation by identifying the leading channel. For example, in the case of clockwise rotation, channel A leads channel B, and in the case of counter-clockwise rotation, channel B leads channel A.

The position accuracy is limited by the quantized position measurement of the encoder. The quantization errors can be reduced using more expensive encoders with more increments, at the expense of increased cost price. Counting pulses of optical encoder only provide information about angular displacement. In order to obtain velocity and acceleration of the motion, an additional state observer is required to perform the estimation algorithm with good accuracy and dynamics. In the last several decades, a myriad of solutions has been explored and published. These solutions can be broadly categorized into three types: FDM, ITM, and KF. They will be introduced in the following sections.

2.1.2 Finite-difference method

The FDM is also called the M method, which is the most widely used method for estimating velocity from encoder pulses. The basic concept of the FDM is to count the number of pulses in a fixed time interval and estimate the velocity by dividing the number of pulses by the duration. The shaft speed N in revolutions per minute (RPM) is given by

$$N = \frac{60 m_e}{T_s P}, \tag{2.1}$$

where P is the PPR of the encoder, and m_e refers to the number of encoder output pulses during a fixed sampling period T_s.

This method can provide the simplest and most efficient velocity estimation when precisely sampling the position. Due to the limitation of resolution and the existence of measurement noise, the number of pulses in a fixed time interval may vary abruptly, hence, severe noise will be generated in the velocity estimation, especially in the low-velocity range. To solve this problem, digital filters are often used to smooth the velocity. However, an inevitable delay caused by the filter will greatly reduce the bandwidth of the control loop. Since the time interval T_s and the PPR P are fixed in (2.1), it is obvious that the shaft speed N is proportional to the number of the pulses m_e. In the high-speed region, the number of pulses m_e is large, so the quantization error is relatively small. As the speed decreases, the encoder pulse-width becomes wider. If the speed is small enough, the number of pulses m_e will be a decimal, and the error would be significantly large. Thus, the FDM is more suitable for use in the high-speed range.

2.1.3 Inverse-time method

The ITM, also called T method, is usually used to provide higher accuracy in the low-velocity range. This method calculates velocity by dividing the angle by the time interval between two consecutive position pulses. The shaft speed N in RPM is given by

$$N = \frac{60 f_t}{P m_s}, \tag{2.2}$$

where P is the PPR of the encoder, f_t is the frequency of the clock pulses, and m_s is the number of frequency clock pulses between two encoder pulses. The estimator is updated each time when an encoder pulse event is received. However, due to the limited resolution of time measurement, accuracy cannot be ensured at high-speed.

These square-wave input signal counting methods for position and velocity measurement are very sensitive to quantization errors. This is a digital residual error, which is mainly caused by sampling the analog square wave signal and obtaining an approximate digital value.

2.1.4 Kalman filter

The latest advancements in velocity estimation techniques concentrate more on state-estimation approaches. The KF is one of the most famous and commonly used methods in the significant toolbox of mathematical tools, which can be used for stochastic estimation from noisy sensor measurements. For a long time, it has been regarded as the optimal solution for many tracking and data prediction tasks. The KF is named after Rudolph E. Kalman, who published a famous paper in 1960, describing a recursive solution of the discrete-data linear filtering problem [46]. The KF is essentially a set of mathematical equations that can implement a predictor-corrector type of estimator that is optimal in the sense of minimizing the estimated error covariance when certain assumptions are satisfied [47].

To use the KF to estimate the internal state of a process, given only a sequence of noisy observations, the process must be modeled in accordance with the framework of the KF. The dynamic model is commonly described as

$$\boldsymbol{x}_{k+1} = \mathbf{F}\boldsymbol{x}_k + \mathbf{G}\boldsymbol{u}_k + \boldsymbol{\Gamma}\boldsymbol{w}_k, \tag{2.3}$$

where
$\boldsymbol{x}$ is the state variable;
$\boldsymbol{u}$ is the system input;
$\boldsymbol{w}$ is the process noise;
$\mathbf{F}$ is the state transition matrix;

$\mathbf{G}$ is the control-input matrix;
$\mathbf{\Gamma}$ is the process noise transition matrix.

The measurement model is given by

$$\boldsymbol{y}_{k+1} = \mathbf{H}\boldsymbol{x}_k + \mathbf{D}\boldsymbol{v}_k, \tag{2.4}$$

where
$\boldsymbol{y}$ is the measurement output;
$\boldsymbol{v}$ is the measurement noise;
$\mathbf{H}$ is the observation matrix which maps the state variable into observed variable;
$\mathbf{D}$ is the observation noise transition matrix.

Because the process noise $\boldsymbol{w}_k$ and measurement noise $\boldsymbol{v}_k$ are white Gaussian random sequences with zero mean, the following equations hold:

$$\varepsilon\{\boldsymbol{w}_k\} = 0,\ \varepsilon\{\boldsymbol{v}_k\} = 0, \tag{2.5}$$

where $\varepsilon\{\}$ denotes the expected value. Both of these two sequences are uncorrelated random variables, then it can be expressed as

$$\varepsilon\left\{\boldsymbol{w}_i\boldsymbol{w}_j^T\right\} = 0,\ \varepsilon\left\{\boldsymbol{v}_i\boldsymbol{v}_j^T\right\} = 0, (i \neq j) \tag{2.6}$$

Thus, the covariances are defined as

$$\varepsilon\left\{\boldsymbol{w}_k\boldsymbol{w}_k^T\right\} = \sigma_w^2,\ \varepsilon\left\{\boldsymbol{v}_k\boldsymbol{v}_k^T\right\} = \sigma_v^2. \tag{2.7}$$

The KF is usually used to process position signals to estimate position, velocity, and acceleration. When the target motion and the measurement model are linear, and the process error and the measurement error are Gaussian, the KF gives the minimum mean-square error estimate. For an angular motion system, the position θ, angular velocity ω, and acceleration a are selected as the state variables, which is $\boldsymbol{x} = \begin{bmatrix} \theta & \omega & a \end{bmatrix}^T$. The system matrix described in (2.3) is

$$\mathbf{F} = \begin{bmatrix} 1 & T_s & T_s^2/2 \\ 0 & 1 & T_s \\ 0 & 0 & 1 \end{bmatrix}, \tag{2.8}$$

where T_s is the sample interval.

Since the input vector of the system is zero, the input matrix is $\mathbf{G} = 0$. When using a Wiener-sequence acceleration model assuming that the acceleration increment is an independent (white noise) process, the acceleration increment in a time period is the integral of the jerk over the period. Therefore, the noise transmission matrix can be directly expressed as

$$\mathbf{\Gamma} = \begin{bmatrix} \frac{T_s^2}{2} & T_s & 1 \end{bmatrix}^T. \tag{2.9}$$

If we know the initial state $\boldsymbol{x}_0$, the matrix $\mathbf{P}$ is initialized to zero. Otherwise, appropriate values on the diagonal should be used to initialize the matrix $\mathbf{P}$. According to (2.8), the state transition matrix $\mathbf{F}$ only depends on the time interval T_s.

Since the position is usually measured in the optical encoder, the observation matrix $\mathbf{H}$ is expressed as

$$\mathbf{H} = \begin{bmatrix} 1 & 0 & 0 \end{bmatrix}. \tag{2.10}$$

The observation noise transition matrix is $\mathbf{D} = 1$. Using these coefficient matrices, the KF algorithm can be used to estimat the state. The whole process of the KF involves two sub-processes, namely prediction and correction, as demonstrated in Algorithm 1. In the prediction step, the current state variables are estimated along with their uncertainties. Once the next measurement that is corrupted by some amount of error is observed, these estimates are updated using a weighted average. The KF is recursive and can run in real-time, using only the current input measurement and the previously calculated state and its uncertainty matrix. No additional past information is required.

Prediction:
Predicted state estimate, $\hat{\boldsymbol{x}}_k^- = \mathbf{F}\hat{\boldsymbol{x}}_{k-1} + \mathbf{G}\boldsymbol{u}_{k-1}$;
Predicted state covariance, $\mathbf{P}_k^- = \mathbf{F}\mathbf{P}_{k-1}\mathbf{F}^T + \boldsymbol{\Gamma}\sigma_w^2\boldsymbol{\Gamma}^T$;
Correction:
Optimal Kalman gain, $\mathbf{K}_k = \mathbf{P}_k^-\mathbf{H}^T\left(\mathbf{H}\mathbf{P}_k^-\mathbf{H}^T + \mathbf{D}\sigma_v^2\mathbf{D}^T\right)^{-1}$;
Corrected state estimate, $\hat{\boldsymbol{x}}_k = \hat{\boldsymbol{x}}_k^- + \mathbf{K}_k\left(\boldsymbol{y}_k - \mathbf{H}\hat{\boldsymbol{x}}_k^-\right)$;
Corrected estimate covariance, $\mathbf{P}_k = \left(\mathbf{I} - \mathbf{K}_k\mathbf{H}\right)\mathbf{P}_k^-$;
$k = k + 1$;

Algorithm 1: The Kalman filter.

2.2 Theoretical model of laser self-mixing interferometry

Laser interferometry is a well-established technique widely used in industrial and laboratory environments. Applications have been flourishing in the fields of mechanical metrology, machine-tools control, profilometry, velocimetry, and vibrometry, etc. The optical feedback is mostly an unavoidable consequence with the application of lasers. It appears everywhere in optical systems, such as optical communication systems, optical data storage, optical measurements, etc. The effects of optical feedback in semiconductor lasers have been studied from the beginning of their development [48, 49]. This effect is usually used for the control of oscillation frequency, selection of mode, suppression of side modes, and interferometry in semiconductor lasers.

The mixing of the field in the laser cavity and the weak field back-reflected/back-scattered by the remote target modulates both the amplitude and frequency of the laser field. For static operation, it is sufficient to model the laser and the target as a compound cavity resonator, which is fully detailed in Section 2.2.1. For dynamical operation, the resonant operation of the laser can be evaluated at different points in time, which is known as a quasi-stationary or steady-state analysis. Another more accurate analysis of the optical feedback interferometer, which is performed by using the standard Lang and Kobayashi rate equations that consider the amplitude of the electric field and the dynamical interplay between the electrical charge carriers and photons in the semiconductor laser cavity, will be introduced in Section 2.2.2.

2.2.1 Theory of resonator model

The semiconductor laser described here is a Fabry-Perot type with a mono-layer of the active region. Theoretically, other narrow-stripe edge-emitting lasers, such as multi-quantum well (MQW) lasers and distributed feedback (DFB) lasers, can be treated in the same way as Fabry-Perot lasers. Therefore, from the viewpoint of chaotic dynamics, the macroscopic features of these lasers show the same behaviors, although their detailed characteristics strongly depend on the laser structure and the particular values of the device parameters [50].

To analyze this behavior, a simple model is sketched in Figure 2.1, which consists of a three-mirror Fabry-Perot-type laser with a reflection/scattering surface. For ease of analysis, the laser is assumed to operate in single mode, although this is not always true in actual situations. Lasers sometimes oscillate in multi-mode under certain parameter conditions of optical feedback [50].

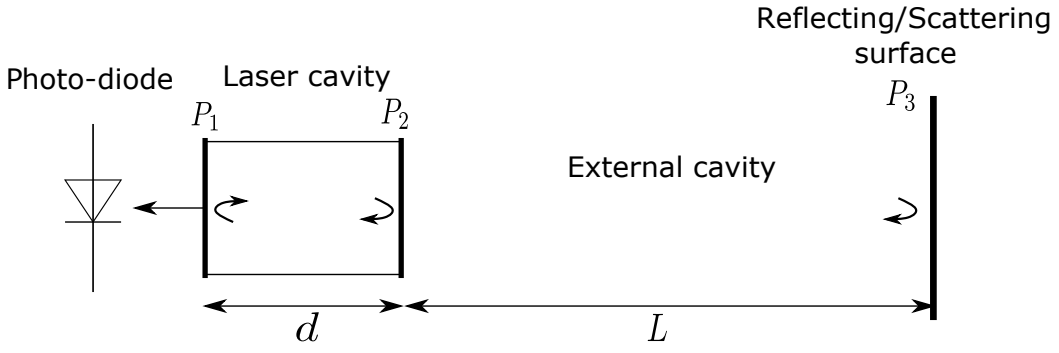

Figure 2.1: Basic configuration of optical feedback in a Fabry-Perot semiconductor laser.

The surfaces P_1 and P_2 are facets of the laser cavity with a uniform active medium that the refractive index is μ_1. The reflection coefficients of P_1 and P_2 are r_1 and r_2. Surface P_3

represents the external surface with reflection coefficient r_3. d and L denote the length of the laser cavity and the length of the external cavity with uniform medium, respectively.

Combining the external cavity, the surface P_2, and the surface P_3 into a single term, an reflection coefficient r_{eff} is introduced [51],

$$r_{\text{eff}} = r_2 + \left(1 - |r_2|^2\right) r_3 \exp(-i2\pi\nu\tau_{ext}), \tag{2.11}$$

where $1 - |r_2|^2$ accounts for the light transmission through the laser facet P_2. ν and $\tau_{ext} = 2L/c$ denote the optical frequency and the round trip delay in the external cavity, respectively. c is the speed of light in the vacuum. Equation (2.11) only counts for a single round trip in the external cavity. Generally, the external reflection r_3 is much less than the reflection coefficient r_2 in the case of weak optical feedback ($|r_3| \ll |r_2|$). Therefore, the multiple round trips in the external cavity are ignored [52]. For strong optical feedback with multiple reflections in the external cavity, we can refer to [53–56]. To simplify the expression of the rest chapters, only the single round trip mode is considered. The reflection coefficient r_{eff} in (2.11) can be represented as

$$r_{\text{eff}} = |r_{\text{eff}}| \exp(-i\phi_r), \tag{2.12}$$

where $|r_{\text{eff}}|$ and ϕ_r denote the amplitude and phase of r_{eff}, respectively.

For the weak feedback condition with $|r_3| \ll |r_2|$. The reflection coefficients r_2 and r_3 are considered as real and positive. In this case, we can write

$$|r_{\text{eff}}| \approx \Re(r_{\text{eff}}) = r_2[1 + \kappa_{ext} \cos(\phi_{ext})], \tag{2.13}$$

$$\phi_r = \frac{\Im(r_{\text{eff}})}{r_2} = \kappa_{ext} \sin(\phi_{ext}), \tag{2.14}$$

where $\kappa_{ext} = r_3/r_2\,(1 - |r_2|^2)$ is the coupling coefficient, and $\phi_{ext} = 2\pi\nu\tau_{ext}$ denotes the phase of external cavity. The required threshold gain denoted as $g = g_c$ for the compound cavity laser must satisfy the amplitude condition

$$r_1|r_{\text{eff}}| \exp\left[(g_c - a_s)d\right] = 1, \tag{2.15}$$

where the losses a_s represent any optical loss in the laser cavity that does not yield a generation of carriers in the active layer, such as scattering losses.

The round trip phase within the semiconductor laser cavity must be equal to an integer multiple of 2π, which generates the phase condition

$$2\beta d + \phi_r = 2\pi m, \qquad m = \text{integer}. \tag{2.16}$$

where β is the phase constant of the optical wave. The phase constant β depends on the optical frequency ν, so (2.16) yields the possible emission frequency of the laser resonator.

The optical feedback causes changes in laser emitting properties, such as threshold gain, optical frequency, line-width, etc. The threshold gain g_{th} in the absence of optical feedback can be written as

$$g_{th} = a_s + \frac{1}{d} \ln\left(\frac{1}{r_1 r_2}\right). \tag{2.17}$$

The threshold g_c in the presence of optical feedback can be found by substituting $|r_{\text{eff}}|$ for r_2 in (2.17),

$$g_c = a_s + \frac{1}{d} \ln\left(\frac{1}{r_1 r_2 \left[1 + \kappa_{ext} \cos(\phi_{ext})\right]}\right). \tag{2.18}$$

Thus, the excess gain Δg due to the optical feedback is

$$\Delta g = g_c - g_{th} = \frac{-\ln\left[1 + \kappa_{ext} \cos(\phi_{ext})\right]}{d}. \tag{2.19}$$

Since natural logarithm can be expanded into a power series as

$$\ln(1+x) = x - \frac{x^2}{2} + \frac{x^3}{3} - \frac{x^4}{4} \cdots + (-1)^{n-1} \frac{x^n}{n}, \tag{2.20}$$

equation (2.19) is rewritten as

$$\Delta g \approx -\frac{\kappa_{ext}}{d} \cos(\phi_{ext}) \qquad (\kappa_{ext} \ll 1). \tag{2.21}$$

The equation (2.21) indicates that the excess gain depends on the phase of external cavity $\phi_{ext} = 2\pi\nu\tau_{ext}$ with a periodic variation. The maximum gain can be obtained when $\phi_{ext} = m2\pi$, where m is an integer.

By using the effective refractive index $\mu_1 = c\beta/(2\pi\nu)$, the phase condition in (2.16) is rewritten as

$$\frac{4\pi\mu_1\nu d}{c} + \phi_r = 2m\pi \qquad (m = \text{integer}). \tag{2.22}$$

Due to the optical feedback, the emission frequency ν may change as well as the threshold gain, thus, the refractive index has a change of [57]

$$\Delta(\mu_1\nu) = \Delta\mu_1\nu_{th} + (\nu - \nu_{th})\mu_1. \tag{2.23}$$

Hence, the change of phase condition with optical feedback can be presented as

$$\Delta\phi = \frac{4\pi d\left[\Delta\mu_1\nu_{th} + (\nu - \nu_{th})\mu_1\right]}{c} + \phi_r. \tag{2.24}$$

In absence of optical feedback, the output frequency of laser is $\nu = \nu_{th}$. In consequence of optical feedback, the emission frequency ν changes. The effective refractive index μ_1 can be expressed as [51]

$$\mu_1 = \mu_0 + \frac{\partial \mu_1}{\partial \nu}(\nu - \nu_{th}) + \frac{\partial \mu_1}{\partial n}(n - n_{th}), \tag{2.25}$$

where μ_0 denotes the refractive index with frequency ν_{th} and threshold carrier density n_{th} without optical feedback.

Inserting (2.25) into (2.24), where $\Delta\mu_1 = \mu_1 - \mu_0$, one obtains

$$\Delta\phi = \frac{4\pi d}{c}\left[\nu_{th}\frac{\partial \mu_1}{\partial n}(n - n_{th}) + \overline{\mu}_1(\nu - \nu_{th})\right] + \phi_r, \tag{2.26}$$

where the effective group refractive index $\overline{\mu}_1$ can be rewritten as [51]

$$\overline{\mu}_1 = \nu\frac{\partial \mu_1}{\partial \nu} + \mu_1. \tag{2.27}$$

To present the wave propagation in a laser active medium, a complex refractive index is introduced [51],

$$\mu_1 = \mu_1' - i\mu_1''. \tag{2.28}$$

with $i = \sqrt{-1}$. In fact, μ_1' is more strongly affected by the stimulated emission than μ_1'', which is expressed by a parameter $\alpha = \delta\mu_1'/\delta\mu_1''$, relating a change in μ_1'' to a change in μ_1'. The parameter α called linewidth enhancement factor of usual semiconductor lasers has positive values from 3 to 7 [50, 58, 59].This nonzero value gives rise to complex dynamics of semiconductor lasers. The typical feature of semiconductor lasers is a broad linewidth of laser oscillations due to a nonzero α.

The gain g is related to μ_1'' by

$$\mu_1'' = -\frac{g\lambda}{4\pi} = -\frac{gc}{4\pi\nu_{th}}. \tag{2.29}$$

The variation of the refractive index with varying carrier density is related to gain variations through the parameter α,

$$\frac{\partial \mu_1}{\partial n} = \alpha\frac{\partial \mu_1''}{\partial n} = -\alpha\frac{\partial g}{\partial n}\frac{c}{4\pi\nu_{th}}. \tag{2.30}$$

Thus [51],

$$\frac{\partial \mu_1}{\partial n}(n - n_{th}) = -\frac{\alpha c}{4\pi\nu_{th}}(g - g_{th}). \tag{2.31}$$

Because g must satisfy the amplitude condition of $g = g_c$, the excess phase is

$$\Delta\phi = -\alpha d(g_c - g_{th}) + \frac{4\pi\overline{\mu}_1 d}{c}(\nu - \nu_{th}) + \phi_r. \tag{2.32}$$

Inserting (2.14) and (2.21) into (2.32), $\Delta\phi$ can be expressed as

$$\Delta\phi = \frac{4\pi\overline{\mu}_1 d}{c}(\nu - \nu_{th}) + \kappa_{ext}\left[\sin(\phi_{ext}) + \alpha\cos(\phi_{ext})\right]. \tag{2.33}$$

The equation (2.33) can be rewritten with time delay in the laser cavity $\tau_d = \frac{2\overline{\mu}_1 d}{c}$ as

$$\Delta\phi = 2\pi\tau_d(\nu - \nu_{th}) + \kappa_{ext}\left[\sin(\phi_{ext}) + \alpha\cos(\phi_{ext})\right]. \tag{2.34}$$

Since

$$\sin(\phi_{ext}) + \alpha\cos(\phi_{ext}) = \sqrt{1+\alpha^2}\sin(\phi_{ext} + \arctan\alpha), \tag{2.35}$$

equation (2.34) can be rewritten as

$$\Delta\phi = 2\pi\tau_d(\nu - \nu_{th}) + \kappa_{ext}\sqrt{1+a^2}\sin(2\pi\nu\tau_{ext} + \arctan\alpha). \tag{2.36}$$

The phase condition of the compound cavity satisfies for $\Delta\phi = 0$ [51],

$$\Delta\phi = 2\pi\tau_d(\nu - \nu_{th}) + \kappa_{ext}\sqrt{1+a^2}\sin(2\pi\nu\tau_{ext} + \arctan\alpha) = 0. \tag{2.37}$$

Here an important parameter C called feedback factor that represents the external feedback strength can be introduced [60],

$$C = \frac{\tau_{ext}}{\tau_d}\kappa_{ext}\sqrt{1+\alpha^2}, \tag{2.38}$$

where the value of C denotes different feedback regimes. Then (2.37) can be rewritten as

$$\Delta\phi = 2\pi\tau_{ext}(\nu - \nu_{th}) + C\sin(2\pi\nu\tau_{ext} + \arctan\alpha) = 0. \tag{2.39}$$

If $C << 1$, *very weak optical feedback regime*. Both the instantaneous frequency and the emitted power are represented by cosine function. The linewidth of the laser oscillation becomes broad or narrow depending on the feedback fraction [57].

If $0.1 < C < 1$, *weak feedback regime*. The interference signal gets distorted with a non-symmetrical shape.

If $1 < C < 4.6$, *moderate feedback regime*. The function of power exhibits hysteresis, and the interference signal becomes like a sawtooth.

If $C > 4.6$, *strong feedback regime*. The function of power may become five-valued. In some cases, the semiconductor laser enters the mode-hopping regime, and interferometric measurements cannot be performed due to the instability of the signal [61].

The simulation of the excess phase versus the change of optical frequency is implemented in MATLAB. The simulation results are shown in Figure 2.2. Values of C are presented in Figure 2.2 and other parameters used for simulation are given below:

1) The central wavelength of the semiconductor laser without optical feedback is 785 nm.

2) The internal cavity length d of the semiconductor laser is 1.5 μm, and the group refractive index $\overline{\mu}_1$ of the medium in the laser cavity is 3.53.

3) The initial external cavity length L is 30 mm.

4) The linewidth enhancement factor α is 3.

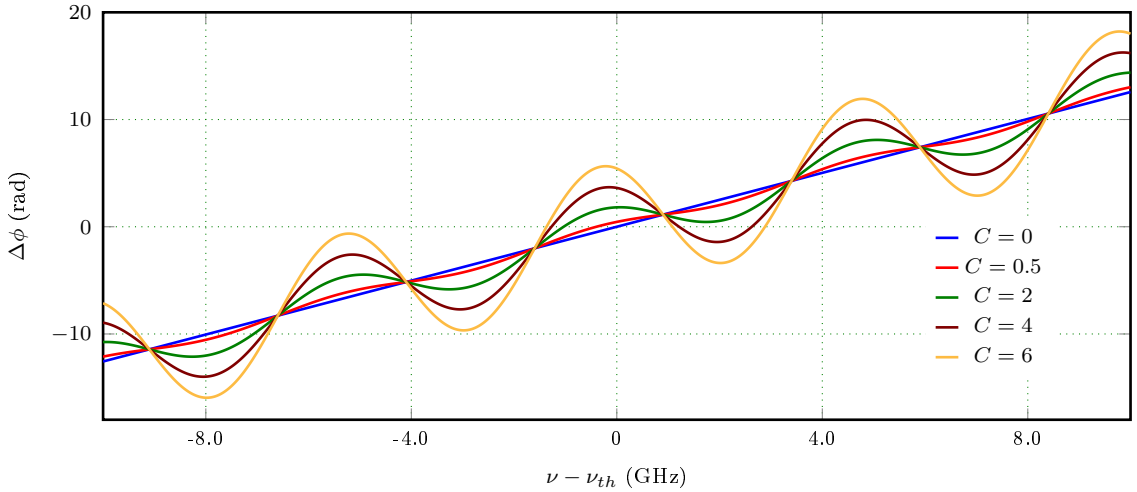

Figure 2.2: Simulation results of excess phase $\Delta\phi$ versus the change in the emission frequency $(\nu - \nu_{th})$.

Without the optical feedback $(C = 0)$, the excess phase $\Delta\phi$ has a linear relationship with the frequency change $\nu - \nu_{th}$ as plotted in Figure 2.2, and the excess phase $\Delta\phi$ will be 0 when $\nu = \nu_{th}$. For the weak feedback regime$(0 < C < 1)$, the excess phase versus frequency change is monotonic and yields only one solution for $\Delta\phi = 0$, and for $C > 1$, it may have several solutions when $\Delta\phi = 0$. Therefore, for $C < 1$, equation (2.39) can be solved by using a first-order approximation. According to Newton iterative formula, it is assumed that r is the root of $f(x) = 0$, and x_0 is selected as the initial value of r, thus $x_1 = x_0 - \frac{f(x_0)}{f'(x_0)}$ is the first-order approximate solution of $f(x)$.

For (2.39), the first-order approximate solution is

$$x_1 = x_0 - \frac{x_0 - \nu_{th} + \frac{C}{2\pi\tau_{ext}} \sin(2\pi x_0 \tau_{ext} + \arctan\alpha)}{1 + C\cos(2\pi x_0 \tau_{ext} + \arctan\alpha)}. \tag{2.40}$$

Table 2.1: Parameters of the semiconductor laser for simulation [54]

Symbols	**Parameters**	**Values**
d	Internal cavity length	1.5 μm
L	External cavity length	30 mm
T_s	Spontaneous recombination time	5 ns
γ	Longitudinal confinement factor	0.012
λ	Central wavelength without feedback	785 nm
g	Gain cross-section	2×10^{-20}
η_{ex}	External quantum efficiency	0.22
I	Operating current	10 mA
I_{th}	Threshold current	6 mA
V	Active volume of the laser cavity	37.5 μm^3

If the initial value is the frequency without feedback, that is $x_0 = \nu_{th}$,

$$\nu = \nu_0 - \frac{C\sin(2\pi\nu_0\tau_{ext} + \arctan\alpha)}{2\pi\tau_{ext}[1 + C\cos(2\pi\nu_0\tau_{ext} + \arctan\alpha)]}. \tag{2.41}$$

So far, the external cavity is considered to be a fixed position, and the length from the laser facet is L. If the external face moves with a displacement of l, the external delay time is $\tau_{ext} = 2(L + l)/c$. The device parameters related to the semiconductor laser are listed in Table 2.1. Firstly, the relationship between the frequency change and the displacement according to (2.41) is simulated. The results are shown in Figure 2.3.

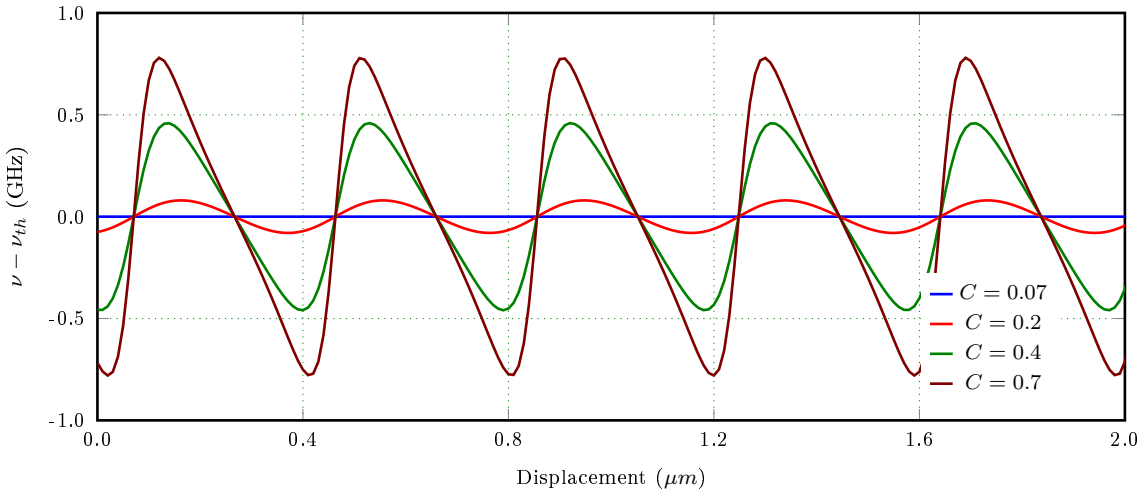

Figure 2.3: Change of frequency versus displacement.

For small variations in threshold gain with optical feedback, namely $|g_c - g_{th}|/g_{th} \ll 1$, both the threshold current I_{th} and the threshold gain g_{th} can be expanded in the first order of the threshold carrier density n_{th} [51, 62]:

$$\Delta I_{th} = qV(1/T_s)\Delta n_{th}, \tag{2.42}$$

$$\Delta g = a\gamma\Delta n_{th}, \tag{2.43}$$

where
a is a constant that depends on the threshold gain-carrier density characteristics;
q is the elementary charge;
V is the active volume of the laser cavity;
T_s is the spontaneous recombination time;
γ is the mode confinement factor [51].

Combine eqs. (2.21), (2.42) and (2.43) to obtain the change of threshold current [51],

$$\Delta I_{th} = -\frac{qV\kappa_{ext}\cos(2\pi\nu\tau_{ext})}{T_s a\gamma d}. \tag{2.44}$$

The stimulated optical power P_{in} inside the laser cavity linearly increases with the injection current I according to [63]

$$P_{in} = \frac{\eta_{in}h\nu(I - I_{th})}{q}, \tag{2.45}$$

where η_{in} denotes the internal quantum efficiency, h is the Planck constant, and I is the operating current of the semiconductor laser. The external power P_{ext} is

$$P_{ext} = \frac{\eta_{ext}h\nu(I - I_{th})}{q}, \tag{2.46}$$

where the external differential quantum efficiency η_{ext} is [63]

$$\eta_{ext} = \frac{1}{2\alpha_s d/\ln\left(\frac{1}{r_1 r_2}\right) + 1}\eta_i, \tag{2.47}$$

where α_s represents photons lost in the laser cavity, and $(1/2d)\ln(1/r_1 r_2)$ corresponds to the number of photons that have a chance to leave the cavity [51].

The typical differential external quantum efficiency listed in the specification of commercial semiconductor laser is given in the form of W/A, which can be obtained by

$$\eta = \eta_{ext}\frac{h\nu}{q}. \tag{2.48}$$

For weak feedback, the threshold current is $\Delta I_{th} + I_{th}$, and the external power is

$$P_{ext} = \frac{\eta_{ext}h\nu}{q}\left[I - (\Delta I_{th} + I_{th})\right], \tag{2.49}$$

where ν is the output frequency. The simulation of output optical power is shown in Figure 2.4. The output power has an asymmetric shape and is periodic with a period of

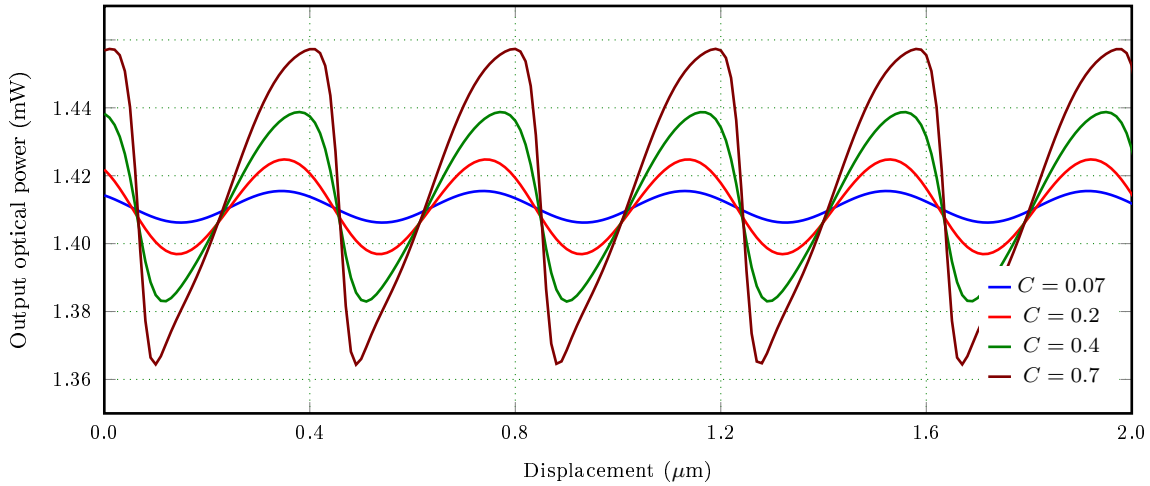

Figure 2.4: Output power versus displacement.

$\lambda/2$. With the increase of the feedback factor C, the amplitude becomes larger and the inclination becomes stronger. The total incremental power ΔP_{ext} emitted from the laser can be expressed as

$$\Delta P_{ext} = P_{ext} - P_0 = \frac{\eta_{ext} h}{q} \left\{ \nu \left[I - (\Delta I_{th} + I_{th}) \right] - \nu_0 (I - I_{th}) \right\}. \tag{2.50}$$

The spectral linewidth of laser oscillation decreases with the increase of photon rate. Therefore, as the laser output power increases, the linewidth becomes narrower. Hence, semiconductor lasers show stable operation for higher output power, and they often become unstable oscillations at lower output power. It should be noted that unstable behavior is not only observed under low output power but also observed at high output power by introducing external perturbations [57].

Even though the above derivation is carried out for Fabry-Perot-type lasers, it is qualitatively applicable to DFB lasers. As long as ν is very close to the emission frequency ν_{th} of the solitary laser, the round trip phase change of DFB lasers may also be set up as in (2.37). However, the appropriate round trip delay and the external reflection coefficient must be determined for DFB lasers.

2.2.2 Theory of rate equation model

In the previous section, the semiconductor laser with optical feedback was introduced under the weak feedback regime based on the resonator model. In this section, another model will be detailed to discuss the laser output of all feedback regimes.

A milestone paper that proposed a rate equation model for semiconductor lasers under optical feedback has been published by Lang and Kobayashi in 1980 [64]. The scattered/reflected light injects back into the laser cavity and superimposes on the existing

internal field. The dynamical change of the carrier density of the semiconductor laser caused by the optical feedback will lead to a modification of the refractive index, which in turn changes the resonant frequency of the laser [63]. The static characteristics of semiconductor lasers with optical feedback can be theoretically investigated through relationship among the reflectivity of the internal cavity and external reflector, the gain in a medium, and other static laser parameters [50].

This model shuns details and dynamics of interaction between the optical field and substance. According to the rate equation of Lang and Kobayashi, the field equation can be written as [57, 63],

$$\frac{\mathrm{d}E(t)}{\mathrm{d}t} = \frac{1}{2}\left\{G_n\left[N(t)-N_0\right]-\frac{1}{\tau_p}\right\}E(t)+\frac{\kappa_{ext}}{\tau_{in}}E(t-\tau_{ext})\cos\left[\omega_0\tau_{ext}+\phi(t)-\phi(t-\tau_{ext})\right], \tag{2.51a}$$

$$\frac{\mathrm{d}\phi(t)}{\mathrm{d}t} = \frac{1}{2}\alpha G_n\left[N(t)-N_{th}\right]-\frac{\kappa_{ext}}{\tau_{in}}\frac{E(t-\tau_{ext})}{E(t)}\sin\left[\omega_0\tau_{ext}+\phi(t)-\phi(t-\tau_{ext})\right], \tag{2.51b}$$

$$\frac{\mathrm{d}N(t)}{\mathrm{d}t} = \frac{J\eta}{ed}-\frac{N(t)}{\tau_e}-G_n\left[N(t)-N_0\right]E^2(t), \tag{2.51c}$$

where,
$E(t)$ is the slowly changing envelope of the electric field and it is normalized to make $E^2(t)$ corresponding to the photon density S $[m^{-3}]$;
G_n is the modal gain coefficient (typical value: $G_n = 8\times10^{-13}\ m^3s^{-1}$);
$\phi(t)$ is the electric field phase;
$N(t)$ is the spatially averaged carrier density;
N_0 is the carrier density without optical feedback (typical value: $1.4\times10^{24}\ m^{-3}$);
N_{th} is the carrier density at the laser threshold (typical value: $N_{th} = 2.3\times10^{24}\ m^{-3}$);
τ_{ext} is the time delay in the external cavity;
τ_p is the photon lifetime within the cavity, a typical value for a Fabry-Perot semiconductor laser is $1.6ps$, and the following equation holds: $1/\tau_p = G_n(N_{th}-N_0)$;
τ_e is the carrier lifetime (typical value: $\tau_e = 2$ nm);
τ_{in} is the time delay in the internal cavity (typical value $\tau_{in} = 8\ ps$);
κ_{ext} is the feedback coefficient of external optical feedback. It can be calculated by considering the multiple reflection effects of light in the external cavity;
ω_0 is the angular oscillation frequency of the unperturbed semiconductor laser;
J is the injection current density;
d is the active layer thickness;
q is the electron charge;
η is the internal quantum efficiency;
α is the linewidth enhancement factor.

The dynamics of semiconductor lasers with optical feedback can be studied by numerically solving the above equations. Stationary solutions are found by setting the time derivation of (2.51a) and (2.51c) to zero. Since the instantaneous frequency is given by

$\omega(t) = \omega_0 + d\phi(t)/dt$, where $d\phi(t)/dt$ is the deviation of instantaneous frequency, we can take $\phi(t) = [\omega_F(\tau_{ext}) - \omega_0]t$, where $\omega_F(\tau_{ext})$ is the instantaneous angular oscillation frequency of the semiconductor laser with optical feedback. By substituting (2.51a), the carrier density can be expressed as

$$N_F(\tau_{ext}) = N_{th} - \frac{2\kappa_{ext}}{\tau_{in}G_n}\cos[\omega_F(\tau_{ext})\tau_{ext}]. \tag{2.52}$$

The angular oscillation frequency with optical feedback can be written as

$$\omega_F(\tau_{ext}) = \omega_0 - \frac{\kappa_{ext}}{\tau_{in}}\Big\{\alpha\cos\left[\omega_F(\tau_{ext})\tau_{ext}\right] + \sin\left[\omega_F(\tau_{ext})\tau_{ext}\right]\Big\}. \tag{2.53}$$

Here an important parameter C called feedback factor can be introduced [60],

$$C = \frac{\tau_{ext}}{\tau_{in}}\kappa_{ext}\sqrt{1+\alpha^2}. \tag{2.54}$$

Equation (2.53) can be rewritten as

$$\omega_F(\tau_{ext})\tau_{ext} = \omega_0\tau_{ext} - C\sin[\omega_F(\tau_{ext})\tau_{ext} + \arctan\alpha]. \tag{2.55}$$

The feedback factor C dictates the degree of nonlinear coupling between the phase stimulus and response, while the linewidth enhancement factor α governs the asymmetry of the phase transfer function induced by 2.55.

To determine the output power of the semiconductor laser, equation (2.52) is substituted into the carrier density equation (2.51c), obtaining

$$P \propto E_F^2(\tau_{ext}) = \frac{J\eta/ed - N_F(\tau_{ext})/\tau_e}{G_n[N_F(\tau_{ext}) - N_0]} = \frac{\tau_p}{\tau_e}\frac{\tau_e J\eta/ed - N_{th} + \frac{2\kappa_{ext}}{\tau_{in}G_n}\cos[\omega_F(\tau_{ext})\tau_{ext}]}{1 - \frac{2\kappa_{ext}\tau_p}{\tau_{in}}\cos[\omega_F(\tau_{ext})\tau_{ext}]}. \tag{2.56}$$

Equation (2.56) can be linearized under the assumption $\kappa_{ext} \ll \tau_{in}/2\tau_p$,

$$P \approx \frac{\tau_p}{\tau_e}\Big\{\tau_e J\eta/ed - N_{th} + \frac{2\kappa_{ext}}{\tau_{in}G_n}\cos[\omega_F(\tau_{ext})\tau_{ext}]\Big\}\Big\{1 + \frac{2\kappa_{ext}\tau_p}{\tau_{in}}\cos[\omega_F(\tau_{ext})\tau_{ext}]\Big\} \tag{2.57}$$

$$\approx \frac{\tau_p}{\tau_e}\Big\{\tau_e J\eta/ed - N_{th}\Big\}\Big\{1 + \frac{2\kappa_{ext}\tau_p}{\tau_{in}}\cos[\omega_F(\tau_{ext})\tau_{ext}]\Big\}. \tag{2.58}$$

The output power of the semiconductor laser without optical feedback is

$$P_0 \propto E_0^2 \approx \frac{\tau_p}{\tau_e}(\tau_e J\eta/ed - N_{th}). \tag{2.59}$$

Therefore, the output power of the semiconductor laser can be expressed as follow,

$$P(\phi) = P_0[1 + mF(\phi)], \tag{2.60}$$

where m is a modulation index,

$$m = \frac{2\kappa_{ext}\tau_p}{\tau_{in}} = C\frac{2\tau_p c}{L\sqrt{1+\alpha^2}}. \tag{2.61}$$

The modulation function $F(\phi)$ is

$$F(\phi) = \cos[\omega_F(\phi)\tau_{ext}] = cos\left[\omega_F(\phi)\frac{\phi\lambda}{2\pi c}\right], \tag{2.62}$$

where
$\omega_F(\phi)$ is the instantaneous angular oscillation frequency of laser with feedback;
λ is the wavelength of laser without feedback;
$F(\phi)$ is a periodic function of the interference phase ϕ using the relation $\tau_{ext} = \frac{\phi\lambda}{2\pi c}$ [51].

Figure 2.5 depicts the dependence of the change of angular frequency $\Delta\omega$ and the output power $P(\phi)$ on the displacement L for different values of C. For C=0.1, $\Delta\omega$ and $P(\phi)$ are represented by a cosine-like function. As the feedback factor C increases, the fringes in the signal will be tilted and sharpened, resulting in an abrupt vertical feature when $C > 1$. For C=1, $\Delta\omega$ and $P(\phi)$ will be distorted. When C=3, for some specific values, the function has three solutions, and a hysteresis will occur. Thus, a stability analysis is performed. For C=7, for some specific values, the function exists five solutions.

2.3 Applications of laser self-mixing interferometry

The first report of velocity measurement with the self-mixing technique in a gas laser was published by Rudd in 1968 [65], whereas in the first report [66] in 1978, both the amplitude modulation and frequency modulation of SMI were demonstrated. With the rapid development of laser technology, numerous preliminary applications for velocity measurement using semiconductor lasers instead of gas lasers have been reported [32, 44]. The applications of SMI were introduced in [43,57,63], and an overview of instrumentation and measurement developed according to the concept of SMI was presented in [67, 68].

With a continual pursuit of more precise control, smaller feature size, and lower cost, there is a growing interest of laser self-mixing sensors. Compared with the traditional LDV, the SMI has a very simple configuration. It consists of a laser diode, a focusing lens, a test target, and related electronics for extracting the self-mixing signals without any additional or complicated optical components. Figure 2.6 outlines a standard laser self-mixing interferometer. The light beam emitted from the laser diode is focused by the

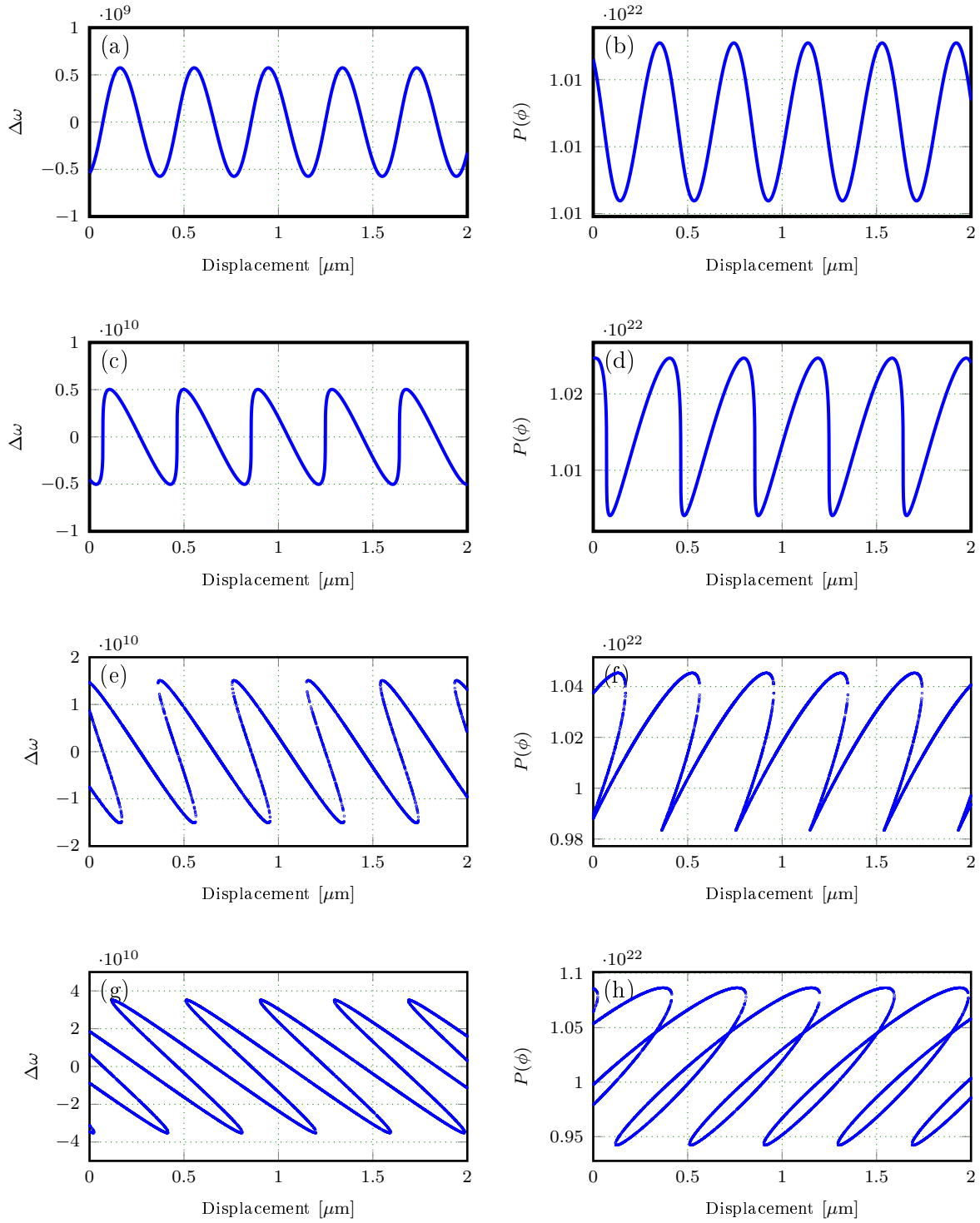

Figure 2.5: Dependence of the change of angular frequency $\Delta\omega$ and the output power $P(\phi)$ on the displacement L for different values of C. (a) and (b) C=0.1; (c) and (d) C=1; (e) and (f) C=3; (g) and (h) C=7.

lens and then strikes on the target. The light scattered by the target surface injects back into the laser cavity, superimposed on the existing internal field, and modulates both the amplitude and frequency of the laser field. The self-mixing signal is simply obtained by

observing the laser output power with the integrated photo-diode [61] or by recording the terminal voltage [69].

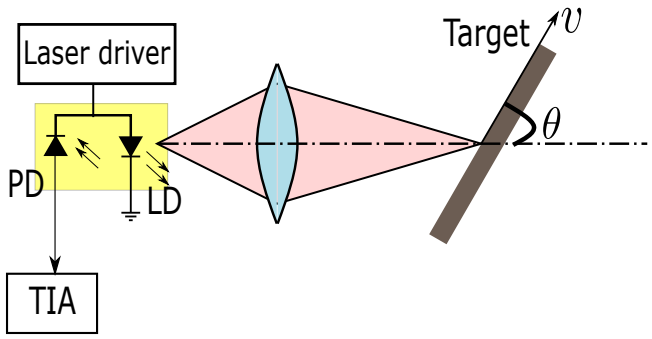

Figure 2.6: The schematic of a standard laser self-mixing interferometer. LD is the laser diode, and PD is the photo-diode. v is the velocity of the moving target.

The first significant feature of such SMI is that this technique allows the laser to perform as both a light source and a detector, and possibly offers the advantages of lower-cost, fewer-component, and self-aligned system for a variety of applications as follows:

- related to the optical path length, such as displacement reconstruction [35–37], solid and liquid velocity measurement [31–34], absolute distance measurement [38, 39], and vibration detection [40–42];
- sensing of weak optical echoes, return loss and isolation factor measurements [70];
- measuring the physical parameters of special features that interact with the medium, such as laser linewidth [71], alpha factor [72, 73], and coherence length [74];
- sensing of thickness, refractive index [75], roughness [76, 77], and mechanical resonance [78–80].

Following, the applications of the SMI are introduced in detail.

2.3.1 Velocity measurement

Velocity measurement based on the self-mixing effect has been well performed before the non-ambiguous interferometric measurement was demonstrated [81, 82]. In the past few decades, numerous researches have been conducted on self-mixing sensors to measure the velocity of solids and fluids. Generally, the photo-diode integrated into the laser diode is used to observe the variation of laser output power. In the case of velocity measurement,

the output power of the laser with optical feedback is modulated by a frequency f_D, which is related to the linear speed v by the following equation,

$$f_D = \frac{2v\cos(\theta)}{\lambda}, \tag{2.63}$$

where λ is the wavelength of the laser diode, θ is the angle between the moving direction of the target and the incident direction of the laser beam.

In (2.63), the speed v is linearly proportional to the frequency f_D, which indicates that a sensor monitoring Doppler frequency f_D can be used to measure the speed. A variety of methods have been used to accurately estimate the Doppler frequency. The most widely used processing method is the classical spectral analysis based on the FFT, which can provide reasonable high resolution for a sufficiently long data length.

In the absence of the speckle effect, an ideal SMI signal is a harmonic function with constant amplitude. However, in practice, when a rough target back-scatters light from a coherent laser, the SMI signal is corrupted by the multiplicative noise caused by the speckle effect. As shown in Figure 2.7, an example of SMI signal from velocity measurement is exhibited. It can be clearly seen that the amplitude is strongly altered by the speckle effect, and there may be difficulties in reconstructing the target motion.

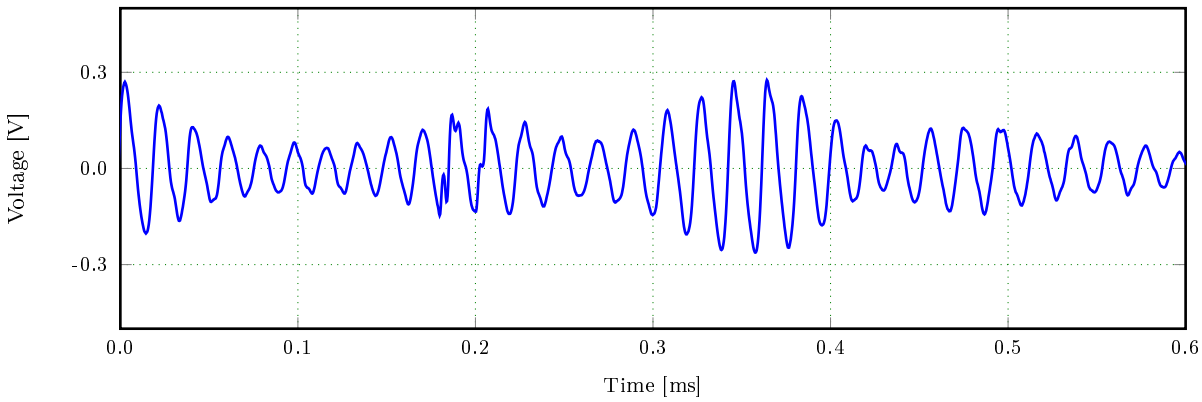

Figure 2.7: Example of an experimental self-mixing signal obtained from velocity measurement of a solid target.

In addition to measuring the velocity of solid, the self-mixing velocimetry has been also performed on scattering fluids. Of particular interest are medical applications for measuring blood flow in vitro and vivo. It is achieved through an optical fiber, which guides the light into biological vessels [31, 83]. Another approach based on speckle-correlation has been applied to in vitro and in vivo blood flow measurement, and different self-mixing signal auto-correlation functions have been obtained for different blood flow regimes [84].

Directional discrimination is necessary for SMI sensors, because the spectrum analysis of SMI signal only provides the absolute value of the velocity but does not provide information about the direction of velocity. One feature of SMI differing from other

interferometry methods is that the inclination of the power fringe can be exploited to discern the motion direction. It provides a significant advantage over other interference techniques, allowing to discriminate the direction of the velocity vector. This feature is indeed attractive because it can be applied to reduce the complexity of the optical solution used to determine the velocity direction.

1) Sawtooth-like waveform

   The asymmetry in the shape of SMI signal when $C > 0.5$ allows clear discrimination of the target direction of motion in the time domain. The inclination of the sawtooth-like waveform reverses when the target changes its moving direction [85]. This distortion has been extensively used to discriminate the direction of movement. Usually, by differentiation of the SMI signal [30, 86, 87], the moving direction can be achieved. In [88], another method using the duty cycle of the fringe was utilized to discern the movement direction.

   However, in practice, many factors may affect the signal and make it difficult to discriminate direction.

   - The rough surface will cause the speckle effect, which strongly modulates and reduces the amplitude of the SMI signal.
   - For weak coupling factor, the waveform is almost symmetrical, keeping from waveform recognition[1].

2) Triangular driving current modulation of the laser diode

   Another method is to discern the direction by modulating the current of the laser diode. When the injection current is modulated, the optical frequency is also modulated. In 1994, Tsukuda et al. [89] successfully realized the direction discrimination in the velocity range of 4-30 mm/s through the triangularly modulating current. However, the measurable velocity range is so narrow that the application of the SMI is limited. In 2002, Philips used triangle modulation of the laser current to determine the direction of movement in optical motion sensors [90]. The working principle is that the frequency of the SMI signal is different in the rising part and the falling part of the triangular modulation.

3) Frequency-domain method

   A novel technique for direction discrimination of SMI was proposed by A. Magnani et al. in 2013 [91,92]. This method employs the non-linearity of signal to directly recover the speed sign in the frequency domain. The target speed is measured by the signal frequency, whereas the speed sign is evaluated by the signal phase.

2.3.2 Displacement measurement

According to the previous analysis, eqs. (2.55), (2.60) and (2.62) give the relationship between the emitted frequency, the optical power, and the distance. The optical power

and the emitted frequency are constant when the distance is not changing. Once the movement occurs in the direction of the light beam, the distance in the external cavity will change, resulting in the variation of the emitted frequency and optical power. By detecting and processing variation of the optical power, the displacement can be achieved. The sensor head of the basic displacement measurement system is the same as that of the velocity sensor. The laser diode is driven by a constant current, and the light beam is focused on the target through a conjugating lens. A precaution is generally required for reflective and retro-reflective targets that an optical attenuator may be inserted into the optical path to avoid excessive optical feedback, depending on the target type [61]. A basic SMI sensor has a resolution of $\lambda/2$ by easily counting the number of fringes in the signal according to (2.62)

$$\phi = 2\pi\nu\tau = \frac{4\pi L}{\lambda}, \tag{2.64}$$

where ϕ is the interference phase, λ represents the laser wavelength under free-running condition, and L is the length of the external cavity.

When $C > 0.5$, the asymmetry of the shape of function (2.60) can precisely determinate the direction of the moving target. This property of the SMI makes the non-ambiguous measurement of the displacement possible by using a single interferometric channel. It makes the SMI different from conventional interferometry, which usually requires two quadrature signals or frequency modulation. Therefore, the simplest solution to realize the SMI sensor for displacement measurement is to operate the laser diode under the moderate feedback regime (C>1). Then the signal is sawtooth-like and the direction is easy to discern. In [93], the displacement was reconstructed without ambiguity by counting the occurrence of negative and positive pulses generated from the analog derivative of the self-mixing signal. This compact system has a sufficiently wide operation range to ensure 1.2 m displacement measurement of distance up to 2.5 m [93]. Figure 2.8 shows an example of a sawtooth-like SMI signal obtained from displacement measurement. Obviously, the inclination of the signal is different in different moving directions.

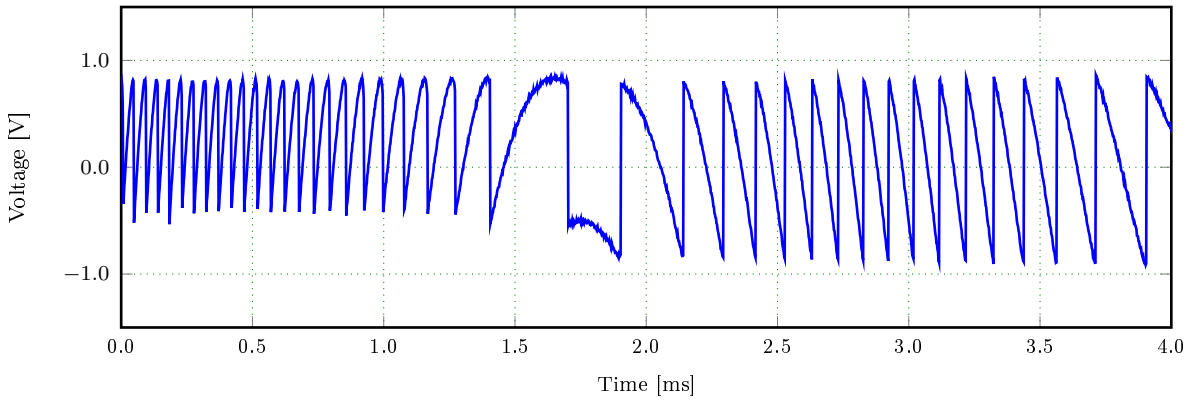

Figure 2.8: Example of an experimental self-mixing signal obtained from displacement measurement of a solid target.

Different methods have been proposed to improve the resolution of the displacement reconstruction. An SMI with the electro-optic modulator was demonstrated in [94]. The

lithium niobate crystal produces a phase shift to modulate at a frequency of 580 kHz that generates an optical path difference between the sensor and the target. The resolution of the reconstructed displacement is $\lambda_0/2N$ and the separated phase is $2\pi/N$. The overall accuracy is better than 65 nm for a 1 kHz sinusoidal motion of the target 10 cm away from the sensor. However, this method increases the complexity and cost of the sensor.

When the feedback factor C is $1 < C < 4.6$, in other words, the self-mixing signal is sawtooth-like, the resolution better than $\lambda/2$ can be achieved by linearizing the interference fringe into a sawtooth signal [95]. By this approach, even in the case of hysteresis, a resolution of $\lambda/12$ has been obtained for displacements up to several micrometers. The residual error is mainly caused by the non-linearity of the actual self-mixing waveform.

Another method to improve the resolution is to perform off-line signal processing to invert the function $F(\phi)$ to accurately reconstruct the target displacement. It requires knowing the derivative sign of the actual displacement. To perform the above reconstruction, the value of the feedback factor C must be determined. It can indeed be achieved experimentally by evaluating the asymmetry of the interferometric waveform $F(\phi)$ [96]. Experimental results in [96] reported a displacement reconstruction error around 50 nm, with an increase in accuracy of factor ≈ 10 concerning the fringe-counting method.

Other researchers [35,36] have applied an auto-adaptive signal processing method called PUM to estimate both harmonic and aleatory displacements under moderate feedback. This method can realize a joint, online, and adaptive estimation of the target displacement, as well as the two self-mixing fundamental parameters C and α. The displacement measurement up to 10 μm has been achieved with an accuracy of ± 80 nm.

2.3.3 Vibration measurement

Vibration measurement involves the detection of zero-mean displacements, and the vibration frequency ranges from zero to tens of MHz. Vibration measurement using the optical non-contact sensing technique is commonlly referred to as laser vibrometry. The most widely used method is the LDV technique. Commercial LDV has been successfully used in a variety of scientific and industrial applications. The self-mixing scheme has proven to be efficient for this application [42, 97, 98]. The sensor developed by M. C. Amann et al. [98] was able to operate on almost any kind of rough surface, covering a bandwidth between 0.1 Hz and 70 kHz, and the maximum measurable vibration amplitude is 180 μm. An example of self-mixing interference signal from vibration measurement is shown in Figure 2.9.

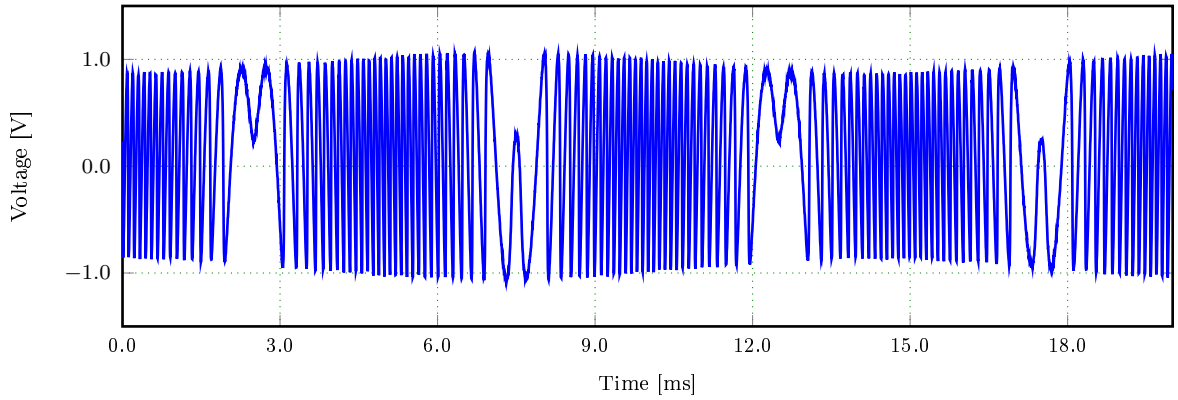

Figure 2.9: Example of the self-mixing signal from vibration measurement of a diffusive target.

2.3.4 Distance measurement

Many laser range finder techniques have been developed to measure the absolute distance of a stationary target. They are broadly classified into three types: geometrical (or triangulation), time-of-flight, and interferometric [99]. Among them, the interference technique is the most accurate but the most expensive one. The SMI can measure the absolute distance by modulating the emission wavelength of a semiconductor laser, which is realized by modulating the injection current with a triangular waveform. The detected photo-current is triangularly modulated because of the power variation of the semiconductor laser, and a self-mixing interference signal is superimposed on it. A prototype, which is capable of measuring distance in the range of 0.2 m to 3 m with an accuracy of 0.3 mm, was developed by M. Norgia et al. [40]. A typical self-mixing signal for absolute distance measurement is shown in Figure 2.10. By counting the number of interferometric

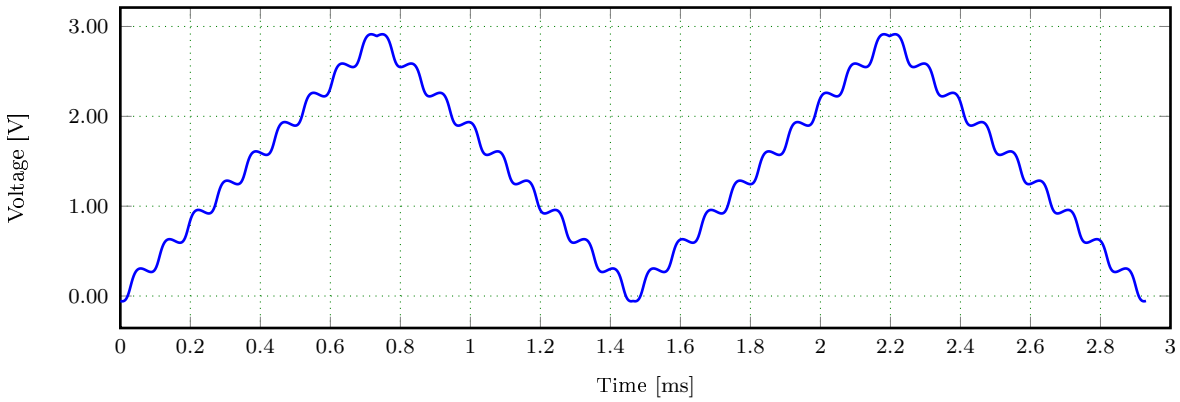

Figure 2.10: Example of the self-mixing signal from absolute distance measurement.

fringes, the target distance D is retrieved by

$$D = \frac{N\lambda^2}{2\Delta\lambda}, \tag{2.65}$$

where N is the number of fringes during the increasing and decreasing triangular semi-period, λ is the wavelength of the laser diode, $\Delta\lambda$ is the known peak to peak wavelength variation.

2.3.5 Other measurements and developments

In addition to the main general applications of the SMI mentioned above, other applications have also been developed. A partial summary is reported here.

1) Physical parameter measurement

- thickness measurement of the transparent glass slab [75];
- simultaneous measurement of the linear displacement and two rotation angles (yaw and pitch) [100];
- measuring both mechanical and thermal deformations in single-mode optical fibers attached to a solid bar [101];
- measurement of laser-related parameters characteristic of semiconductor lasers [71, 102].

2) Biomedical applications

- measurement of the shape of the cardiovascular pulse shape from the radial artery [103];
- measurement of the red blood cell velocity distributions in individual capillaries [104];
- measurement of muscle amplitude of vibration [105].

3) Characterization of sensor performance

- applied to the characterization of micro-electro-mechanical-systems (MEMS) silicon devices such as accelerometers or gyroscopes, to support or complement electrical techniques [79, 106, 107];
- measurement of optical isolators placed into a semiconductor laser package [70];
- absolute calibration of measurement microphones as a laser pistonphone [108].

2.4 Summary

This chapter has presented the theory of optical encoder and SMI for a general overview of these techniques. The conventional methods for estimating the velocity from the angular displacement provided by the optical encoder have been introduced. Besides, the

physical phenomenon and applications of the SMI has been outlined. The two models (the equivalent cavity model and the Lang-Kobayashi equation) describing the optical feedback in semiconductor laser have been discussed, and the effects of different feedback levels on the SMI have been presented. Furthermore, a general review of the common applications of SMI has been introduced. This complete review has shown the advantages and basics of SMI sensors, and it has also shown the limitations of current researches on the effects of the feedback level and speckle noise in the signal. In the following chapters, other solutions for general management of these problems are provided.

Chapter 3

Velocity measurement with optical encoder

In this chapter, algorithms for velocity measurement using optical encoder in electrical drives are introduced. An efficient and tuning-easy fixed gain filter is proposed to estimate position, velocity, and acceleration based on the position of the shaft encoder. Unlike the traditional KF that requires online tuning of the feedback gain matrix, this solution employs an optimal fixed feedback gain matrix obtained through a straight-forward calculation process. This greatly reduces the computational burden. In addition, the proposed fixed gain filter has only one parameter that needed to be tuned, which is theoretically calculated and refined to a small range. This greatly simplifies the tuning work required.

The content of this chapter is arranged as follows: in Section 3.2, the mathematical model of the proposed fixed gain filter will be introduced and developed in detail. Simulation and experimental results and the hardware implementation are presented in Section 3.3. Finally, conclusions are drawn in Section 3.4.

3.1 Statement of the problem

High-performance motion control with fast speed and enhanced accuracy has been increasingly used in robotics, precision machining, and many automation processes. The performances of these systems are decisively influenced by the accuracy/dynamic of signals of position and/or velocity [109–111]. In the feed-forward control, sometimes the acceleration signal is also desired, which can be used to ease the adjustment range of the controller, thereby suppressing the disturbance influences and improving system control dynamics and robustness, etc. A common solution is to mount different sensors (e.g., magnetic devices, resolvers, and optical encoders) on the motor shaft to directly

obtain quantified position signals. According to different measuring principles, they can be classified into four categories: magnetic, capacitive, conductive, and optical. Magnetic encoders rely on three main components: a disk, sensors, and a conditioning circuit. The disk is magnetized and has some magnetic poles on its circumference. The sensors detect the change in the magnetic field as the disk rotates and convert this information into a sine wave. Magnetic encoders have a simple structure and have excellent robustness under harsh environmental conditions. Capacitive encoders have three main parts: rotor, stationary transmitter, and stationary receiver. The capacitor rotor is a printed circuit board (PCB) with an etched sinusoidal pattern that predictably modulates the high-frequency signal of the transmitter as it rotates. Conductive encoders are now rarely seen except as a user input in digital multimeters. Optical encoders generally consist of four parts: light sources, photo-detectors, a movable disk, and a fixed mask. Its disk is made of glass or plastic with transparent and opaque segments. The light coming from the light source can only pass through the transparent area of the disk and is blocked by the opaque part. Consequently, a pulse sequence is generated and read out at the output, which serves to be processed for estimating or calculating position or velocity. In commercial electrical drives, the optical incremental encoder is the most common sensor to obtain position signals because of its simple detection circuit, high resolution, high accuracy, and relative easy adaptation to digital control systems. Since the encoder cannot directly obtain the instantaneous velocity and acceleration, an additional state observer performing the estimation algorithm is required to achieve the velocity and the acceleration with good accuracy and dynamics [112, 113].

The latest advancements in velocity estimation technique concentrate more on the state-estimation approaches. In particular, the KF plays a pivotal role in electrical engineering due to its excellent observation characteristics. A novel algorithm based on polynomial approximations was proposed in [114], which has the capability to reduce the total position error to a range as small as $\pm 0.2^{\circ}$. However, the more massive amount of memory required to store the look-up table (LUT) is a compromise in embedded applications running on low-cost micro-controller unit (MCU), in which hardware resources are very limited. In [115], an edge-time Kalman filter (ETKF) including prediction of edge time and periodic sampling time was proposed to ensure a more accurate state estimation under the condition of lower encoder resolution and uncertainty of motor parameters. However, the coefficients need to be tuned according to the changes in the plant parameters (e.g., the load side inertia and friction factor). Otherwise, the performance of the ETKF will be quite limited. Similar drawbacks can also be found in [6, 7].

Although the state-of-the-art KF-based estimators have been proven to have excellent performance, the performance of the KF estimation method largely depends on the value or setting of the process noise covariance matrix $\mathbf{Q}$ and the measurement noise covariance matrix $\mathbf{R}$, which determine the dynamic characteristics of this kind of estimator. Therefore, these parameters should be tuned appropriately to obtain a combination of the filter tuning parameters suitable for the KF. However, the issue of tuning the dependent parameters of the KF and the corresponding time consuming are still a challenge in industry [116, 117]. How to find the optimal parameter setting of the KF is still an open

question. Moreover, since the computational time of the feedback gain matrix is relatively long and will be updated every sampling time, the process of the algorithm is also a high burden. This means that a faster MCU is required to implement the KF algorithm in real-time.

Based on the above analysis, in this chapter, an efficient and tuning-easy fixed gain filter is proposed to solve the problems mentioned above. The concept of the fixed gain filter has been discussed in radar tracking systems [118–120], but to the best of our knowledge, it is for the first time synthesized in the estimate of position, velocity, and acceleration with the position signal from a shaft encoder.

The major contributions include:

(i) the feedback gain of the fixed gain filter is a constant that can reduce the processing time;

(ii) fixed gain filter employs not only the characteristic of fixed gain, but also the characteristic of constant covariance that leads to a single regulation coefficient, thereby reducing the number of tuning parameters;

(iii) the stability of the fixed gain filter is analyzed while taking digital implementation into account, which allows us to narrow the range of the only and single regulation coefficient.

As a result, this efficient and tuning-easy method is excellent to be utilized in electrical drives.

3.2 Fixed gain filter

As mentioned above, the KF can provide more accurate state estimation at a lower encoder resolution. Nevertheless, the primary drawback of the KF is the calculation and tuning process. Therefore, the FGF is proposed to inherit the advantages of the KF and make the calculation and tuning processing more applicable. Since the classical KF has been reviewed in Section 2.1.4, this section only introduces the FGF in detail. The stability of FGF is also analyzed to determine the optimal range of the filter parameters.

3.2.1 Mathematical model

As analyzed in Section 2.1.4, to achieve steady-state condition of the KF, the error process $\boldsymbol{w}_k$ and $\boldsymbol{v}_k$ must have stationary statistics, and the data rate must be constant. When

the error process cannot meet these criteria, the proposed filter provides a suboptimal estimate. Because the input matrix is $\mathbf{G} = 0$, the proposed optimal steady-state filter could be expressed as

$$\begin{aligned} \hat{\boldsymbol{x}}_k^- &= \mathbf{F}\hat{\boldsymbol{x}}_{k-1}, \\ \hat{\boldsymbol{x}}_k &= \hat{\boldsymbol{x}}_k^- + \mathbf{K}\left(\boldsymbol{y}_k - \mathbf{H}\hat{\boldsymbol{x}}_k^-\right), \end{aligned} \tag{3.1}$$

where $\hat{\boldsymbol{x}}_k^-$ is the predicted state estimate, the gain $\mathbf{K}$ is a constant, and $\hat{\boldsymbol{x}}_k$ is the updated state estimate. Therefore, the error covariances $\mathbf{P}_k^-$ and $\mathbf{P}_{k-1}$ converge to a steady state value according to $\mathbf{K}_k = \mathbf{P}_k^-\mathbf{H}^T\left(\mathbf{H}\mathbf{P}_k^-\mathbf{H}^T + \mathbf{D}\sigma_v^2\mathbf{D}^T\right)^{-1}$ and $\mathbf{P}_k^- = \mathbf{F}\mathbf{P}_{k-1}\mathbf{F}^T + \mathbf{\Gamma}\sigma_w^2\mathbf{\Gamma}^T$. Theoretically, the condition that $\mathbf{P}^-$ and $\mathbf{P}$ are constant is necessary, but not sufficient for $\mathbf{K}$ is constant. In other words, when $\mathbf{P}^-$ and $\mathbf{P}$ are constants, $\mathbf{K}$ is also a constant. On the contrary, when $\mathbf{K}$ is a constant, $\mathbf{P}^-$ and $\mathbf{P}$ are not always constants. In this chapter, this feature is fully utilized to obtain the relationship of the three terms in $\mathbf{K}$. Thus, the following equations can be obtained

$$\begin{aligned} \mathbf{P}_k^- &= \mathbf{P}_{k-1}^-, \\ \mathbf{P}_k &= \mathbf{P}_{k-1}. \end{aligned} \tag{3.2}$$

The prediction function and correction function are expressed as

$$\mathbf{P}_k^- = \mathbf{F}\left(\mathbf{I} - \mathbf{K}\mathbf{H}\right)\mathbf{P}_k^-\mathbf{F}^T + \mathbf{\Gamma}\sigma_w^2\mathbf{\Gamma}^T, \tag{3.3}$$

$$\mathbf{K}\mathbf{D}\sigma_v^2\mathbf{D}^T = \left(\mathbf{I} - \mathbf{K}\mathbf{H}\right)\mathbf{P}_k^-\mathbf{H}^T. \tag{3.4}$$

For the fixed gain filter, the fixed gain can be written as

$$\mathbf{K} = \begin{bmatrix} \alpha & \frac{\beta}{T_s} & \frac{2\gamma}{T_s^2} \end{bmatrix}^T. \tag{3.5}$$

To better simplify the solution process, the target maneuvering index (that is, the ratio of the motion to the observation uncertainty) is defined as: $\lambda = \frac{T_s^2\sigma_w}{\sigma_v}$. Therefore, solving (3.3) and (3.4) yields the following relations

$$\lambda = \frac{2\,\gamma}{\sqrt{1-\alpha}}, \tag{3.6}$$

$$\gamma = \frac{\beta^2}{4\,\alpha}, \tag{3.7}$$

$$\beta = \begin{pmatrix} 4 - 4\sqrt{1-\alpha} - 2\,\alpha \\ 4\sqrt{1-\alpha} - 2\,\alpha + 4 \end{pmatrix}. \tag{3.8}$$

Since $\lambda > 0$, thus, $0 \leq \alpha < 1$. By defining $s = \sqrt{1-\alpha}$, α, β, and γ can be characterized by using the free parameter s,

$$\begin{aligned} \alpha &= 1 - s^2, \\ \beta &= \begin{bmatrix} \beta_0 \\ \beta_1 \end{bmatrix} = \begin{bmatrix} 2(s-1)^2 \\ 2(s+1)^2 \end{bmatrix}, \\ \gamma &= \begin{bmatrix} \gamma_0 \\ \gamma_1 \end{bmatrix} = \begin{bmatrix} \frac{(1-s)^3}{s+1} \\ \frac{(s+1)^3}{1-s} \end{bmatrix}. \end{aligned} \tag{3.9}$$

The curves of α, β, and γ are shown with s as the horizontal axis in Fig. 3.1. As can be seen from the Fig. 3.1, α, β_0, and γ_0 have the same monotonicity. Therefore, β_0, and γ_0 are the real solutions. β_1 and γ_1 can also be excluded by the stability analysis, because the conjugate pair of the complex roots lies outside of the unit circle. Once the process noise and the measurement noise are evaluated, the optimal steady-state gain parameters α, β, and γ are specified in advance and applied to the system directly.

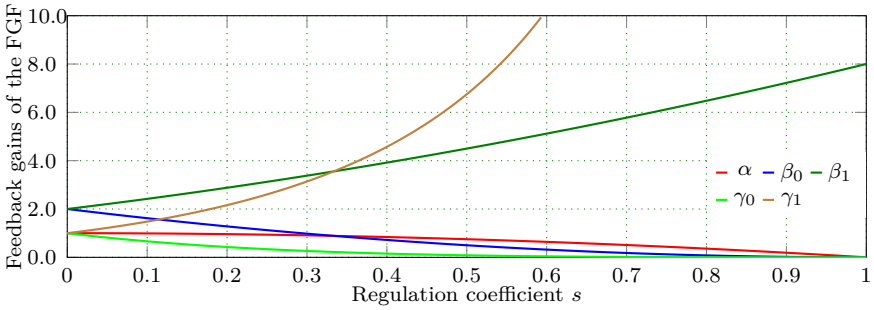

Figure 3.1: Graph of α, β_0, β_1, γ_0, and γ_1 taken s as input.

The value of s is expressed as

$$s = \frac{\sigma}{6} - \frac{\lambda}{6} + \frac{\lambda\,(\lambda - 18)}{6\sigma} + 1, \tag{3.10}$$

where

$$\sigma = \sqrt[3]{27\lambda^2 - 108\lambda - \lambda^3 + 3\sqrt{3}\lambda\sqrt{432 - \lambda^2}}. \tag{3.11}$$

The detailed algorithm process of the fixed gain filter is listed in Algorithm 2. It is clear to see that the calculation process is very simple. The algorithm only requires three equations with multiplication and additions, which greatly simplify the calculation process compared to the traditional KF in Algorithm 1. Therefore, it is very efficient in terms of computation and application with a digital signal processor (DSP) controller.

Function *Initialization*
  if k=0 **then**
    $\hat{\theta}_0 = 0$; $\hat{\omega}_0 = 0$; $k = 1$;
  end if
Function *Calculation*
  if k>1 **then**
    $\Delta\theta_k = \theta_k - \hat{\theta}_k^-$;
    $\hat{a}_k = \hat{a}_{k-1} + \frac{2\gamma}{T_s^2}\Delta\theta_k$;
    $\hat{\omega}_k = \hat{\omega}_{k-1} + \hat{a}_{k-1}T_s + \frac{\beta}{T_s}\Delta\theta_k$;
    $\hat{\theta}_k = \hat{\theta}_{k-1} + \hat{\omega}_{k-1}T_s + \hat{a}_{k-1}\frac{T_s^2}{2} + \alpha\Delta\theta_k$;
    $\hat{\theta}_k = \hat{\theta}_k \bmod 2\pi$;
  end if
  $k = k + 1$;

Algorithm 2: Algorithm of fixed gain filter-based estimation.

3.2.2 Evaluation of parameter tuning process

To tune the KF to achieve its best performance, a parameter-tuning process is needed. The main aim of parameter tuning is to find the best parameter settings to minimize the total number of iterations (TNI). Assuming that the number of independent parameters of the KF is m, the TNI of the KF is $\mathrm{O}(n^m)$, where n is the average number of iterations needed for one parameter to make the found performance close enough to the optimal performance. Therefore, the parameter-tuning process of KF is usually very time-consuming. They may not be achievable in practice.

Since the proposed method has only one tuning parameter, the TNI is $\mathrm{O}(n)$. Furthermore, the average number of iterations needed for one parameter in the proposed method is less than the average number of iterations in the KF. According to the discrete system control theorem, the asymptotic stability requirement of a discrete system is that all eigenvalues (roots of the characteristic equation) must be strictly within the unit circle. Thus, the range of s can be refined to $3 - 2\sqrt{2} < s < 1$, and the range of each term in $\mathbf{Q}$ and $\mathbf{R}$ in the KF is the entire set of real numbers.

3.3 Simulation and experimental results

3.3.1 Programming complexity evaluation

To compare the complexity of the KF and fixed gain filter (FGF) in programming realization, these two algorithms are run in C language on the 168 MHz advanced reduced instruction set computing machine (ARM) processor STM32F417IGTx. All variables are represented by normalized values to better evaluate the performance and make it easier to compare in different system setups. When using floating-point numbers, because of the large dynamic range, both algorithms are easy to implement. In the case of using fixed-point numbers, the KF and fixed gain filter have different complexity although the same scale factors of the variables (θ, ω, a) can be selected for both algorithms. Since the covariance matrix $\mathbf{P}$ of the KF is unknown and has a wide dynamic range, the scale factors of each element of the matrix $\mathbf{P}$ should be selected carefully. Because $\mathbf{P}$ is symmetric, the 3×3 matrix has only six unique terms. Therefore, $\mathbf{P}$ is composed of six different elements. Besides, all results having operations based on the matrix $\mathbf{P}$ must be scaled to the respective format according to the scale factor of the operator. Therefore, it is tough to design a proper program to satisfy the accuracy requirements of the KF using fixed point (FXP) numbers (KF-FXP). It is much easier to implement the fixed gain filter using fixed-point numbers (FGF-FXP), because the parameters (α, β, γ) only involve one factor s and can be calculated offline. Thus, it saves a lot of effort to choose a proper scale factor for the fixed-point numbers. The factor is selected according to its range. In the implementation, the scale factors of α, $\frac{\beta}{T_s}$, and $\frac{2\gamma}{T_s^2}$ are selected as 2^{29}, 2^{19}, and 2^6, respectively. This is another reason for choosing normalized values instead of physical values.

Firstly, the KF and fixed gain filter are evaluated by comparing their programming complexity. Based on the preceding analysis, the level of implementation complexity is divided into three stages from the most positive to the most negative degree, namely, positive (1), neutral (0), and negative (-1), as shown in Table 3.1. It can be noted that the KF using fixed-point numbers is the most complicated programming.

The second assessment is the computational time. Table 3.1 shows the execution time of the KF and fixed gain filter in different cases. Among them, the KF using floating point (FLP) number (KF-FLP) with a floating point unit emulator (FPUE) takes the longest time (9.7 μs) to execute, while the fixed gain filter using floating point number (FGF-FLP) with a floating point unit (FPU) takes the shortest time (only 0.7 μs) to execute. Compared to the KF-FXP, the execution time of FGF-FXP is reduced by 83.3%. Compared to the KF-FLP with an FPU (KF-FLP-FPU), the execution time of FGF-FLP with an FPU (FGF-FLP-FPU) is reduced by 63.2%. In comparison with the KF-FLP with an FPUE (KF-FLP-FPUE), the execution time of FGF-FLP with an FPUE (FGF-FLP-FPUE) is reduced by 45.2%. In short, the execution time of fixed gain filter is much shorter than the KF under any circumstances.

Table 3.1: Programming complexity and execution time of the KF and FGF

Methods	**Complexity**	**CPU ticks**	**Execution time**
KF-FXP	-1	1105	6.6μs
FGF-FXP	0	187	1.1μs
KF-FLP-FPU	1	320	1.9μs
FGF-FLP-FPU	1	121	0.7μs
KF-FLP-FPUE	1	1631	9.7μs
FGF-FLP-FPUE	1	894	5.3μs

Table 3.2: System parameters and configuration of the KF and FGF

Symbols	Parameter	Value
θ_{base}	base value of position	2π rad
ω_{base}	base value of velocity	100π rad s^{-1}
a_{base}	base value of acceleration	$10\,00\pi$ rad s^{-2}
T_s	sampling time	$100\,\mu$s
n	encoder bits	12
$\mathbf{D}\sigma_v^2\mathbf{D}^T$	covariance of measurement noise	1
$\mathbf{\Gamma}\sigma_w^2\mathbf{\Gamma}^T$	covariance of process noise	diag[5e$-$5, 2.5e6, 4e10]
s	FGF tuning parameter	0.8339
α	FGF parameter	0.3047
β	FGF parameter	0.0552
γ	FGF parameter	0.0025

Considering the programming complexity and the execution time, it is recommended to use the FGF-FLP when the micro-controller has an FPU, and the FGF-FXP is recommended when the micro-controller does not have an FPU. This conclusion can also be applied to other processors.

3.3.2 Performance evaluation with simulation

In this section, numerical simulations are performed in the matrix laboratory (MATLAB) with the proposed algorithm and other mentioned methods to demonstrate its performance. To assess the performances of the FDM, KF, and FGF, these methods are performed under both ideal conditions and quantized input conditions. The parameters used for simulation are listed in the Table 3.2. All the positions, velocities, and accelerations acquired through simulation and experiment are normalized using the base value.

The tracking performances of step, ramp, and parabolic velocities under ideal conditions are shown in Figure 3.2(a), Figure 3.4(a), and Figure 3.6(a), respectively. The position

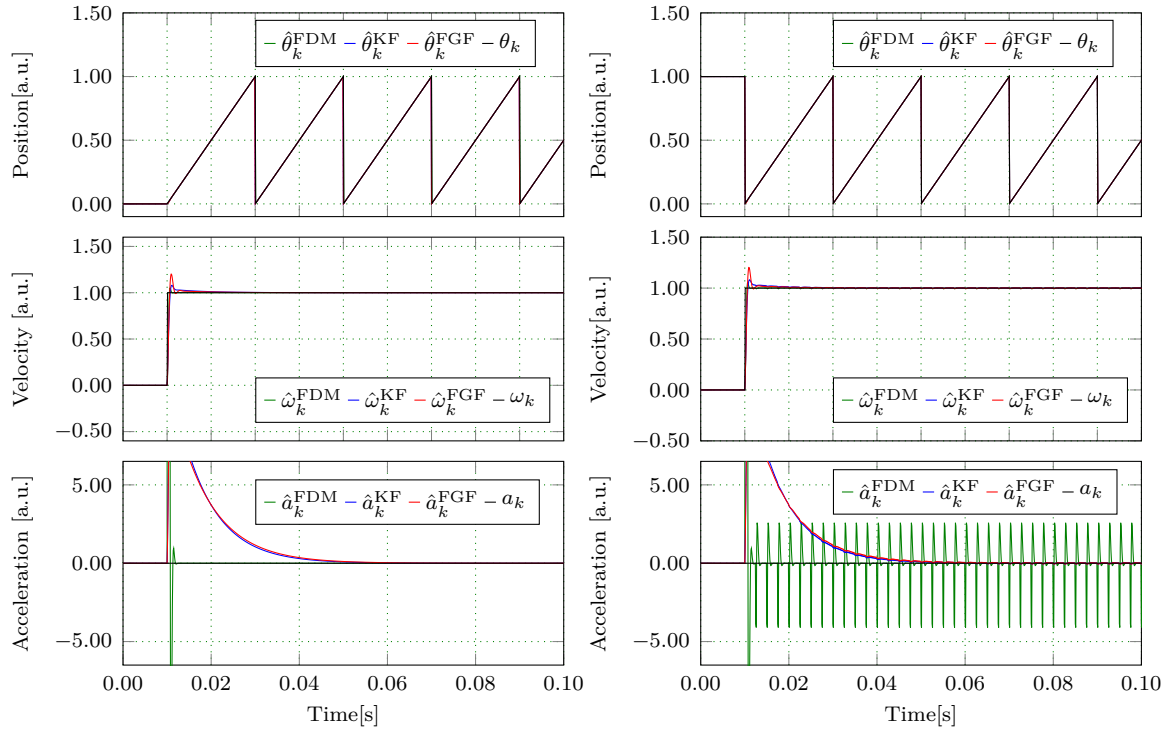

(a) Ideal condition (b) Noisy condition

Figure 3.2: The step response of the FDM, KF, and FGF. The velocity is a step signal. θ_k is the real position. $\hat{\theta}_k^{\mathrm{FDM}}$, $\hat{\theta}_k^{\mathrm{KF}}$, and $\hat{\theta}_k^{\mathrm{FGF}}$ are the estimated positions with the FDM, KF, and FGF, respectively. ω_k is the real angular velocity. $\hat{\omega}_k^{\mathrm{FDM}}$, $\hat{\omega}_k^{\mathrm{KF}}$, and $\hat{\omega}_k^{\mathrm{FGF}}$ are the estimated angular velocities with the FDM, KF and FGF, respectively. a_k is the real acceleration. $\hat{a}_k^{\mathrm{FDM}}$, $\hat{a}_k^{\mathrm{KF}}$, and $\hat{a}_k^{\mathrm{FGF}}$ are the estimated accelerations with the FDM, KF, and FGF, respectively.

input of the estimator is the real position signal, which is generated by integrating velocity over time. Since the input position signal has no quantization error under the ideal condition, the position $\hat{\theta}_k^{\mathrm{FDM}}$ and velocity $\hat{\omega}_k^{\mathrm{FDM}}$ estimated using the FDM are very close to the ideal position θ_k and ideal velocity ω_k. However, in practice, the position signals in electrical drive always have quantized errors that affect the estimated results. Therefore, comparisons of the conventional FDM, KF, and FGF tracking positions with quantized errors are also shown in Figure 3.2(b), Figure 3.4(b), and Figure 3.6(b). Note that the FDM uses a second-order low-pass filter (LPF) (the cut-off frequency is set to 500 Hz) to smooth the quantization error.

Errors of the estimated position, velocity, and acceleration in Figure 3.2 where the velocity is a step signal are shown in Figure 3.3. Under the ideal condition, the errors of these three methods are very small after about 0.06 s. In the case of noisy conditions, the error of the estimated position $\delta_\theta^{\mathrm{FDM}}$ using the FDM is 0.025%, while the position errors of $\delta_\theta^{\mathrm{KF}}$ and $\delta_\theta^{\mathrm{FGF}}$ are 0.020%. The error of the estimated velocity $\delta_\omega^{\mathrm{FDM}}$ using the FDM at the base value ω_{base} is 0.71%, while the velocity errors of $\delta_\omega^{\mathrm{KF}}$ and $\delta_\omega^{\mathrm{FGF}}$ are 0.50%. The error of the estimated acceleration δ_a^{FDM} using the FDM is larger than 30%, as the errors

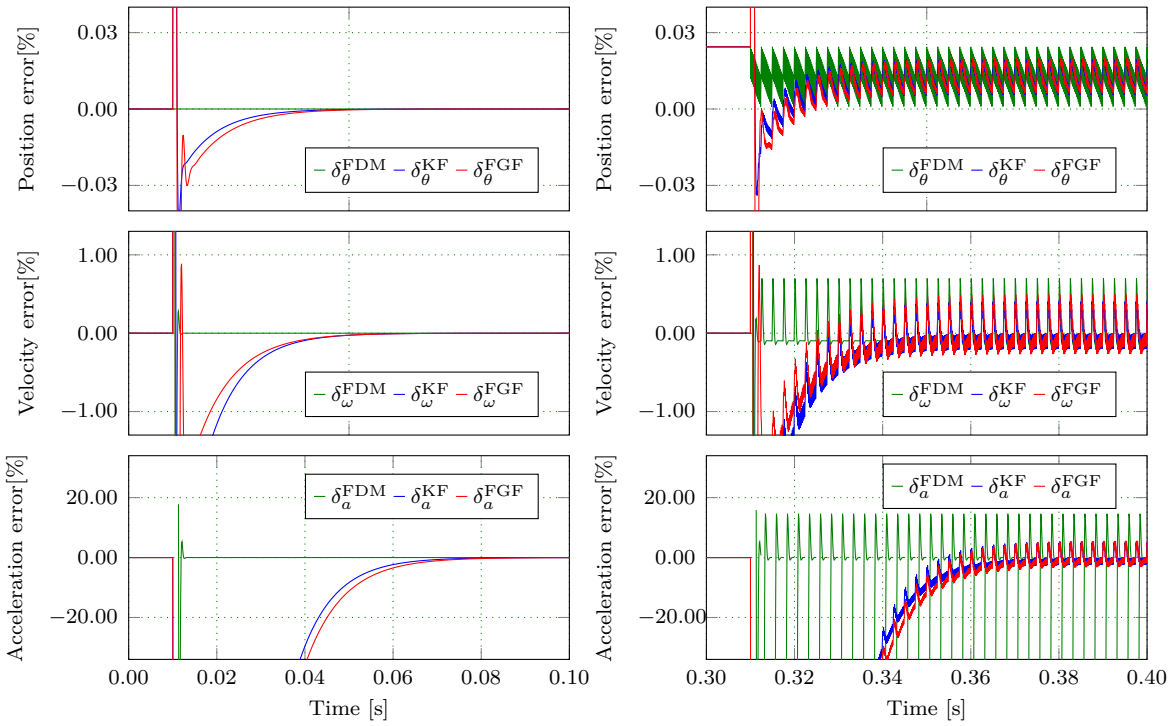

(a) Ideal condition (b) Noisy condition

Figure 3.3: Errors for tracking a step velocity under ideal and noisy conditions. $\delta_\theta^{\mathrm{FDM}}$, $\delta_\theta^{\mathrm{KF}}$, and $\delta_\theta^{\mathrm{FGF}}$ are the estimated errors of positions with the FDM, KF, and FGF. $\delta_\omega^{\mathrm{FDM}}$, $\delta_\omega^{\mathrm{KF}}$, and $\delta_\omega^{\mathrm{FGF}}$ are the estimated errors of angular velocities with the FDM, KF, and FGF. δ_a^{FDM}, δ_a^{KF}, and δ_a^{FGF} are the estimated errors of accelerations with the FDM, KF, and FGF.

of δ_a^{KF} and δ_a^{FGF} are 6.70%.

The performance indices of the estimated step velocity using the three methods exhibited in Figure 3.2 are summarized in Table 3.3. The root mean square error (RMSE) generated from the position difference is calculated as the performance metric and defined as

$$\mathrm{RMSE} = \sqrt{\frac{\sum_{k=1}^{n} \left(\hat{\theta}_k - \theta_k\right)^2}{n}}, \tag{3.12}$$

where n is the number of experimental sampling points, $\hat{\theta}_k$ is the estimated position, and θ_k is the true position at the kth sampling instant.

The comparison in Table 3.3 indicates that compared with the KF, the proposed fixed gain filter method can provide similar performance (e.g., rising time, peak time, settling time, and $\mathrm{RMSE}_\omega^{\max}$) except for a slightly higher overshoot under both ideal conditions and noisy conditions. Meanwhile, the FDM has better performance (smaller rising time, peak time, settling time, overshoot, and $\mathrm{RMSE}_\omega^{\max}$) than the KF and FGF for step velocity estimation. However, it can be seen from Figure 3.2(b) that the FDM is unable to track

Table 3.3: Performance indices of step velocity obtained with FDM, KF, and FGF.

	Ideal conditions			Conditions with noise		
	FDM	KF	FGF	FDM	KF	FGF
Rising time (ms)	0.3	0.6	0.5	0.4	0.6	0.6
Peak Time (ms)	0.7	1.1	1.0	0.7	1.1	0.9
Settling time[1](ms)	0.6	1.6	1.6	0.6	1.6	1.6
Overshoot (%)	5.1	8.0	18.2	5.2	8.2	20.2
$\text{RMSE}_{\omega}^{\max 2}$	0.0384	0.0418	0.0435	0.0383	0.0417	0.0434

[1] Error band of the settling time is taken as 5%.
[2] $\text{RMSE}_{\omega}^{\max}$ means the maximum RMSE value of velocity and acceleration between 0 and 0.04 s.

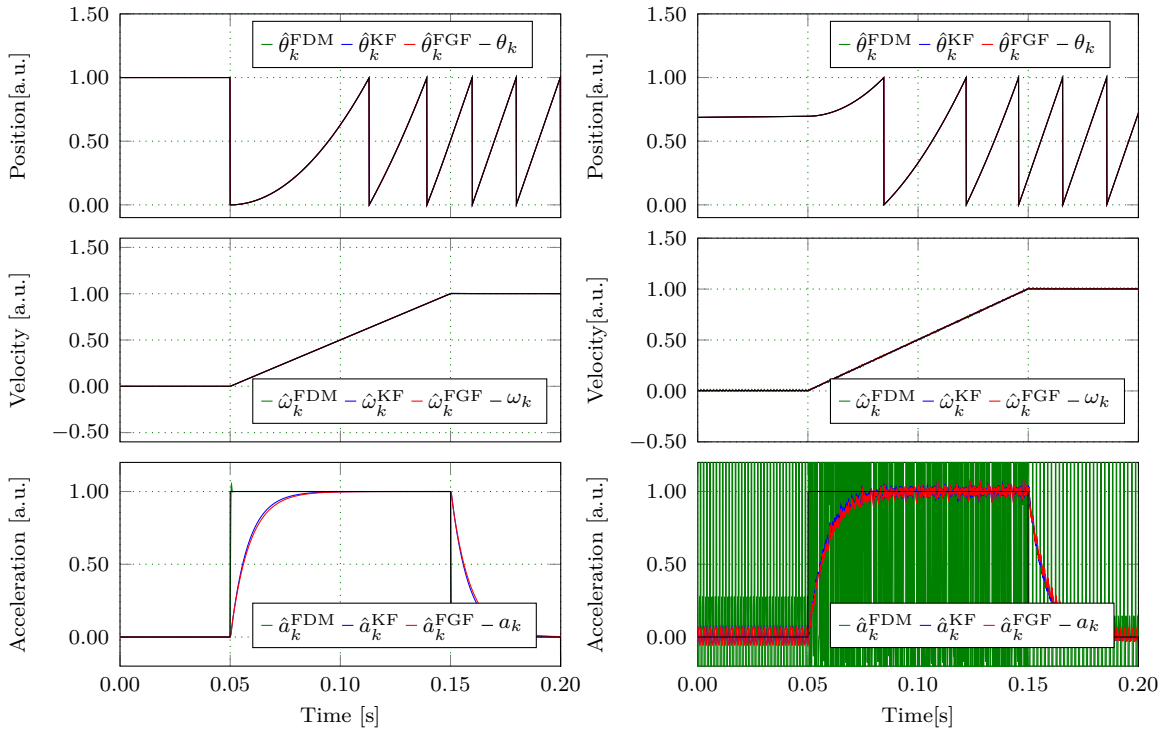

(a) Ideal condition (b) Noisy condition

Figure 3.4: Performance for tracking a ramp velocity. θ_k is the real position. $\hat{\theta}_k^{\text{FDM}}$, $\hat{\theta}_k^{\text{KF}}$, and $\hat{\theta}_k^{\text{FGF}}$ are the estimated positions with the FDM, KF, and FGF, respectively. ω_k is the real angular velocity. $\hat{\omega}_k^{\text{FDM}}$, $\hat{\omega}_k^{\text{KF}}$, and $\hat{\omega}_k^{\text{FGF}}$ are the estimated angular velocities with the FDM, KF, and FGF, respectively. a_k is the real acceleration. $\hat{a}_k^{\text{FDM}}$, $\hat{a}_k^{\text{KF}}$, and $\hat{a}_k^{\text{FGF}}$ are the estimated accelerations with the FDM, KF, and FGF, respectively.

the acceleration under the noisy condition, whereas the FGF tracks the acceleration $\hat{a}_k^{\text{FGF}}$ with a similar result as the $\hat{a}_k^{\text{KF}}$ of the KF. It should be noted that the ideal acceleration is set to zero in Figure 3.2 due to its infinite value.

Figure 3.5 presents estimate errors of tracking the ramp velocity in Figure 3.4. The

errors of the estimated position, velocity, and acceleration are very small in ideal circumstances. Under noisy conditions, the estimated position error $\delta_\theta^{\text{FDM}}$ with the FDM is 0.025% in the whole process. The position errors $\delta_\theta^{\text{KF}}$ and $\delta_\theta^{\text{FGF}}$ are 0.025% at zero speed, and the errors reduce to 0.02% after the speed becomes non-zero. The velocity errors $\delta_\omega^{\text{FDM}}$ are around 1.3%, while the errors $\delta_\omega^{\text{KF}}$ and $\delta_\omega^{\text{FGF}}$ are within 0.7%. And the errors of acceleration clearly illustrate that the FDM method is unable to estimate the acceleration while the KF and the FGF can measure the acceleration.

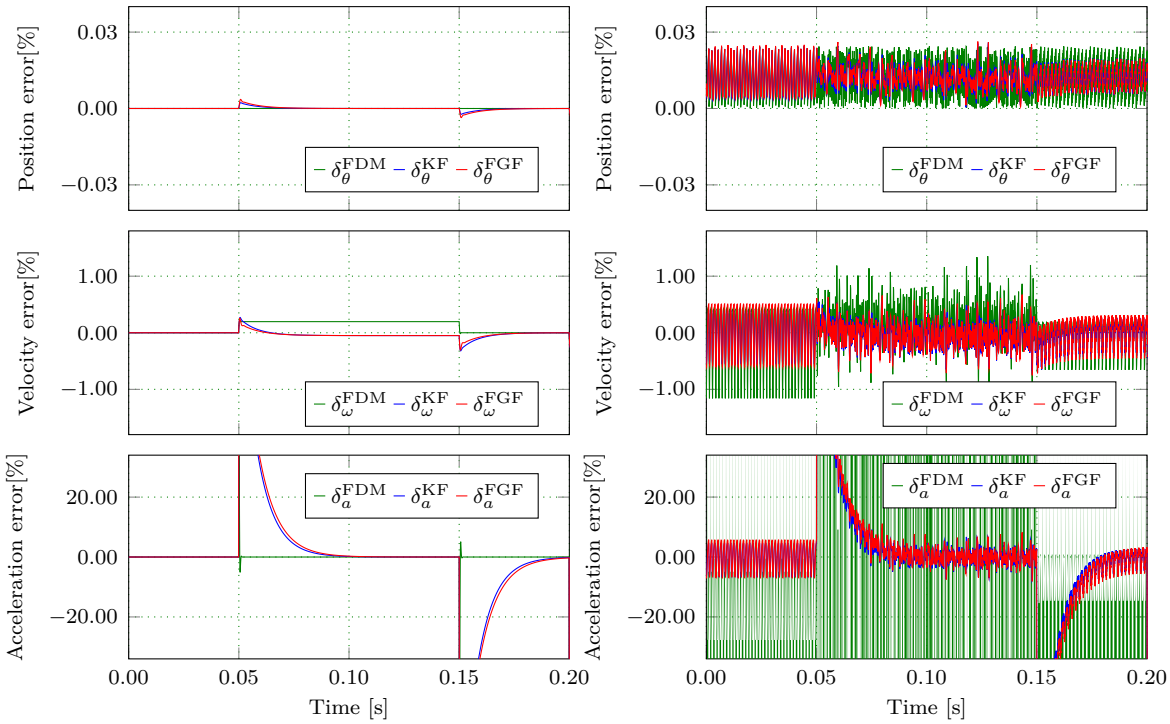

(a) Ideal condition (b) Noisy condition

Figure 3.5: Errors for tracking a ramp velocity under both ideal and noisy conditions. $\delta_\theta^{\text{FDM}}$, $\delta_\theta^{\text{KF}}$, and $\delta_\theta^{\text{FGF}}$ are the estimated errors of positions with FDM, KF, and FGF. $\delta_\omega^{\text{FDM}}$, $\delta_\omega^{\text{KF}}$, and $\delta_\omega^{\text{FGF}}$ are the estimated errors of angular velocities with the FDM, KF, and FGF. δ_a^{FDM}, δ_a^{KF}, and δ_a^{FGF} are the estimated errors of accelerations with the FDM, KF, and FGF.

The performance indices of the estimated step acceleration shown in Figure 3.4 are listed in Table 3.4. Under ideal conditions, the rising time, peak time, settling time of the KF is slightly faster than the FGF, while the $\text{RMSE}_\omega^{\max}$ is larger than that of the FGF. Under the noisy conditions, the FDM is unable to estimate the acceleration. In addition to that, the $\text{RMSE}_\omega^{\max}$ of the FDM method is larger than the other two methods that have quite close results. The similar results can also be obtained for tracking parabolic velocities in Figure 3.6, where the FDM is unable to estimate the acceleration under noisy conditions. Figure 3.7 shows the errors for tracking the parabolic velocity in Figure 3.6. Under noisy conditions, the position error using the FDM is within 0.025%. The position errors using the KF and FGF are within 0.025% when the velocity is zero and the errors $\delta_\theta^{\text{KF}}$ and $\delta_\theta^{\text{FGF}}$ decrease as the velocity is non-zero. The velocity error $\delta_\omega^{\text{FDM}}$ is around 1.3%,

Table 3.4: Performance indices of step acceleration obtained with FDM, KF, and FGF.

	Ideal conditions			Conditions with noise		
	FDM	KF	FGF	FDM	KF	FGF
Rising time (ms)	0.3	8.4	9.8	N/A	8.5	8.5
Peak Time (ms)	0.6	79	81	N/A	34.5	34.5
Settling time[1](ms)	0.7	23.9	25.7	N/A	22.5	22.9
Overshoot (%)	5.1	N/A	N/A	N/A	7.1	8.3
$\text{RMSE}_{\omega}^{\max 2}(\times 10^{-4})$	13.9	6.30	5.19	40.9	26.3	29.1
$\text{RMSE}_{a}^{\max 2}$	0.038	0.20	0.21	2.78	0.20	0.21

[1] Error band of the settling time is taken as 5%.
[2] $\text{RMSE}_{\omega}^{\max}$ and $\text{RMSE}_{a}^{\max}$ mean the maximum RMSE value of velocity and acceleration between 0 and 0.2s.

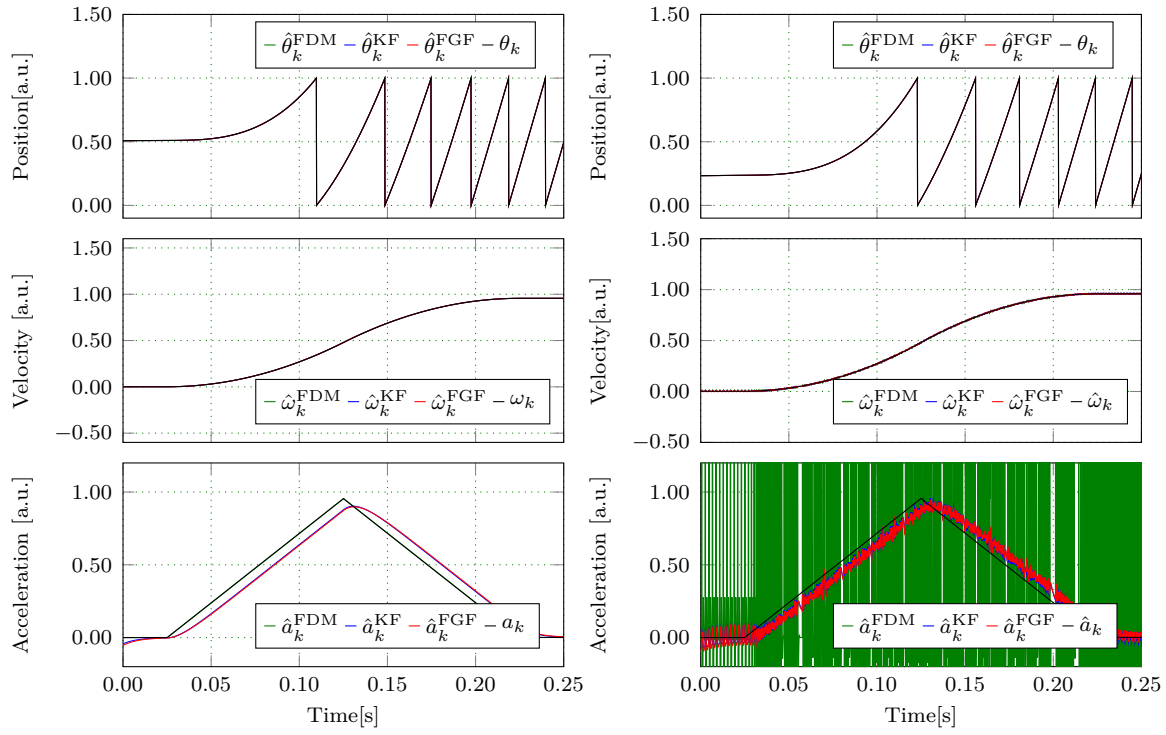

(a) Ideal condition (b) Noisy condition

Figure 3.6: Performance for tracking a parabolic velocity. θ_k is the real position. $\hat{\theta}_k^{\text{FDM}}$, $\hat{\theta}_k^{\text{KF}}$, and $\hat{\theta}_k^{\text{FGF}}$ are the estimated positions with the FDM, KF, and FGF, respectively. ω_k is the real angular velocity. $\hat{\omega}_k^{\text{FDM}}$, $\hat{\omega}_k^{\text{KF}}$, and $\hat{\omega}_k^{\text{FGF}}$ are the estimated angular velocities with the FDM, KF, and FGF, respectively. a_k is the real acceleration. $\hat{a}_k^{\text{FDM}}$, $\hat{a}_k^{\text{KF}}$, and $\hat{a}_k^{\text{FGF}}$ are the estimated accelerations with the FDM, KF, and FGF, respectively.

while the errors $\delta_{\omega}^{\text{KF}}$ and $\delta_{\omega}^{\text{FGF}}$ are within 0.9%.

In conclusion, when the input position signal has quantization errors, the errors of the estimated position and velocity using the FDM are greater than errors of the KF and

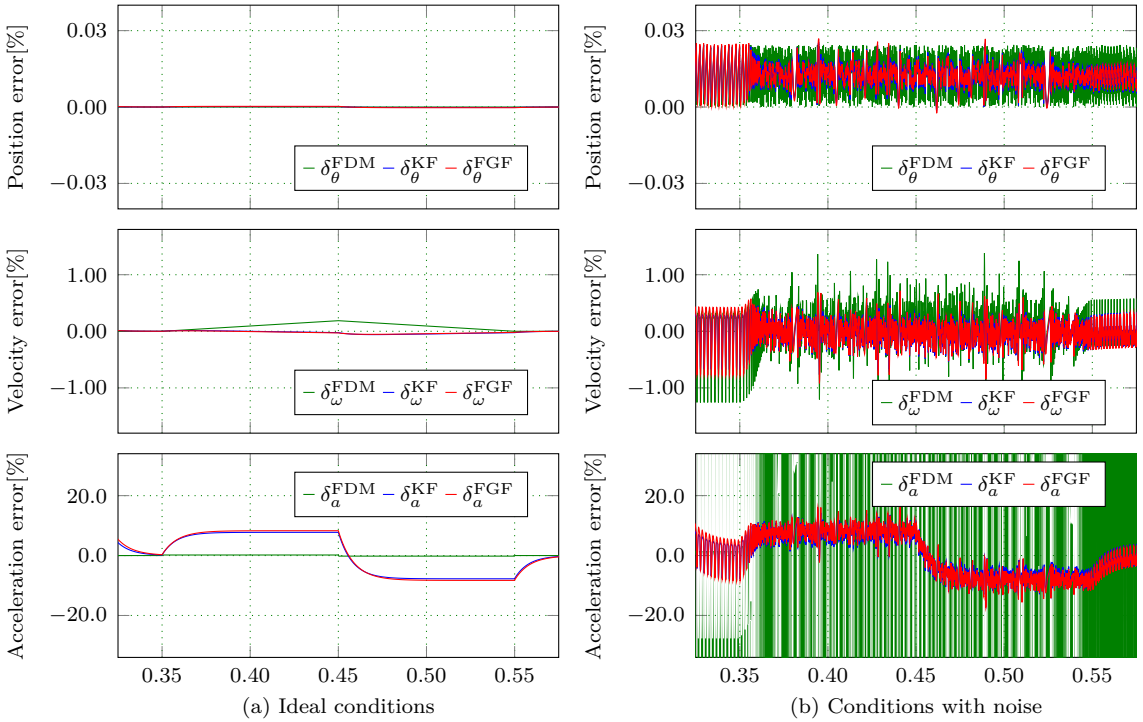

(a) Ideal conditions (b) Conditions with noise

Figure 3.7: Errors for tracking a parabolic velocity under both ideal condition and noisy condition. $\delta_\theta^{\mathrm{FDM}}$, $\delta_\theta^{\mathrm{KF}}$, and $\delta_\theta^{\mathrm{FGF}}$ are the estimated errors of positions with FDM, KF, and FGF methods. $\delta_\omega^{\mathrm{FDM}}$, $\delta_\omega^{\mathrm{KF}}$, and $\delta_\omega^{\mathrm{FGF}}$ are the estimated errors of angular velocities with the FDM, KF, and FGF methods. δ_a^{FDM}, δ_a^{KF}, and δ_a^{FGF} are the estimated errors of accelerations with the FDM, KF, and FGF methods.

the FGF, and the FDM is not able to estimate the acceleration. The KF and the FGF acquire very similar estimated position, velocity, and acceleration under both ideal and noisy conditions. It should be noted that the parameters of the KF need to be tuned with a lot of effort, and the selected parameters are the parameters that make the KF have the optimal performance in the entire tuning process.

3.3.3 Performance evaluation with experiment

To verify the effectiveness of the proposed FGF in practice, an experimental setup has been implemented. The speed control drive system for induction motors is used to fully evaluate the proposed FGF and the other conventional methods. The optical incremental encoder used in the experiment is the KUBLER T5.2400.1222.1024 that usually provides a resolution of 1024. Since the quadrature signal generated by the encoder is combined with the XOR gate, its output will be connected to the counter. When recording the position, the encoder can provide a resolution of 4096. Since the drive system is controlled using vector control, the feedback speed has a significant impact on the control performance. The parameters of the each filter used in the experiment are selected in the same way as in the simulation.

The step velocity in Figure 3.2 cannot be obtained in practice. In the experiment, only the ramp and parabolic velocities are tracked. The experimental results of using the FDM, KF, and FGF to track ramp velocities are shown in Figure 3.8. The three methods successfully track the positions $\hat{\theta}_k^{\mathrm{FDM}}$, $\hat{\theta}_k^{\mathrm{KF}}$, $\hat{\theta}_k^{\mathrm{FGF}}$ and velocities $\hat{\omega}_k^{\mathrm{FDM}}$, $\hat{\omega}_k^{\mathrm{KF}}$, $\hat{\omega}_k^{\mathrm{FGF}}$. The accelerations $\hat{a}_k^{\mathrm{KF}}$, $\hat{a}_k^{\mathrm{FGF}}$ and torque current i_q have the same tendency, indicating that the KF and FGF can correctly track the acceleration, while the FDM fails to track it. It can be seen that the acceleration tracking performance of the KF and FGF are almost the same.

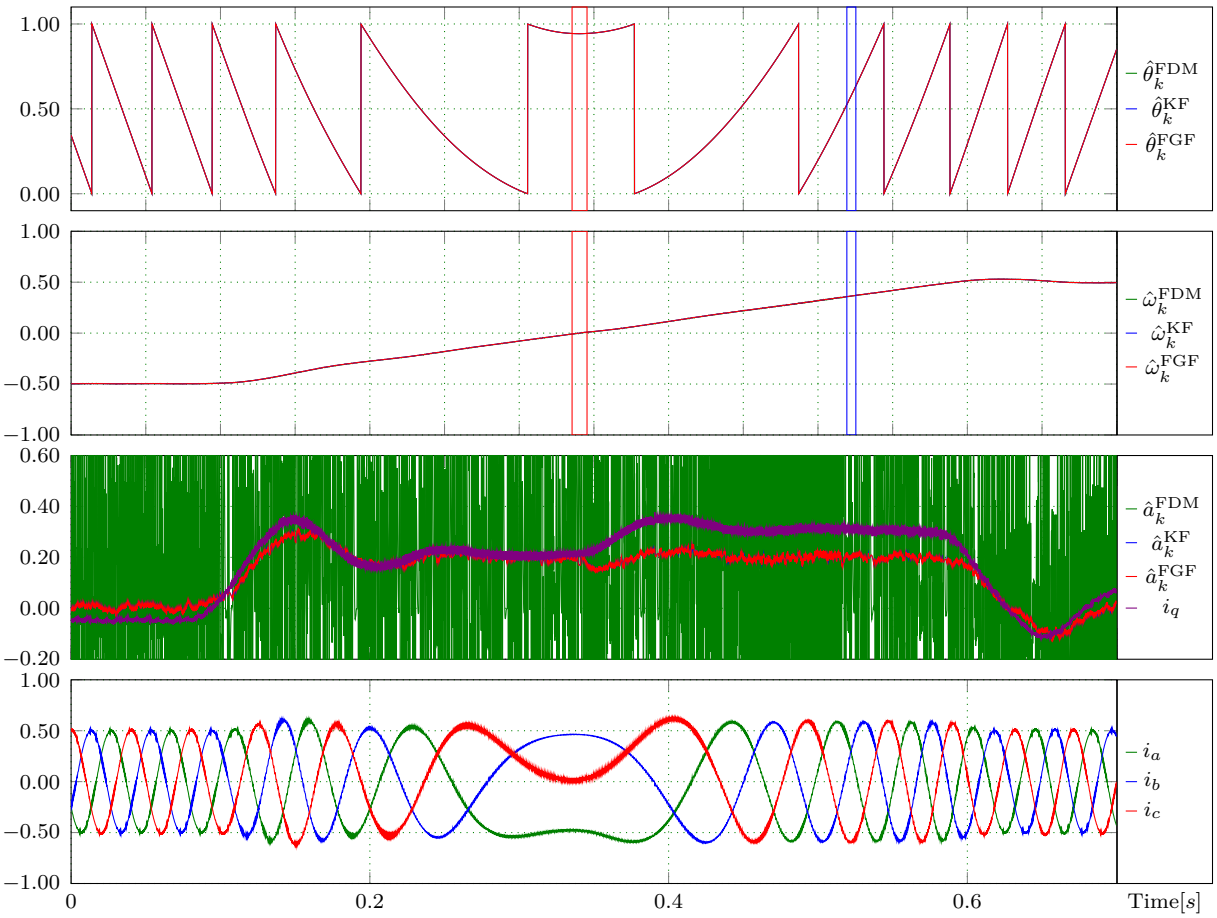

Figure 3.8: Experimental comparison for tracking position, velocity, and acceleration with ramp velocity. i_q is the torque current. i_a, i_b, and i_c are the three-phase current.

To compare the estimation results of these three methods, the zoomed-in positions and velocities from the red frames and blue frames in Figure 3.8 are shown in Figure 3.9 and Figure 3.10. The velocity in Figure 3.9 is around 0 pu, and it can be seen that the position $\hat{\theta}_k^{\mathrm{FDM}}$ acquired with the FDM is a step signal resulting from the quantization error with a resolution ratio of $1/(2^{14})$, which is also the maximum error of the estimated position with the FDM. The KF and FGF successfully smooth out this quantization error. The difference between estimated positions $\hat{\theta}_k^{\mathrm{KF}}$ and $\hat{\theta}_k^{\mathrm{FGF}}$ is inconspicuous. The velocity $\hat{\omega}_k^{\mathrm{FDM}}$ has a much more serious ripple and time delay than the velocities ω_k^{KF} and ω_k^{FGF}. The serious ripple and time delay results in a decreased bandwidth in closed loop systems,

which will significantly influence the performance. Besides, it can be noticed that the velocity ω_k^{FGF} has very similar ripple as the velocity ω_k^{KF}, which confirms the analysis mentioned above that the FGF has very similar performance for estimating position, velocity, and acceleration as the KF. In Figure 3.13, the velocity is around 0.365 pu. Since the drawing range of axis y is larger than that in Figure 3.12, it is not apparent to see the difference between the estimated positions. But it can still notice that the ripple of velocity $\hat{\omega}_k^{\mathrm{FDM}}$ is larger than ω_k^{KF} and ω_k^{FGF}. The estimated velocity $\hat{\omega}_k^{\mathrm{FDM}}$ is smaller than ω_k^{KF} and ω_k^{FGF}, because the FDM acquires a smaller velocity when the electrical drive is speeding up, as shown in Figure 3.5.

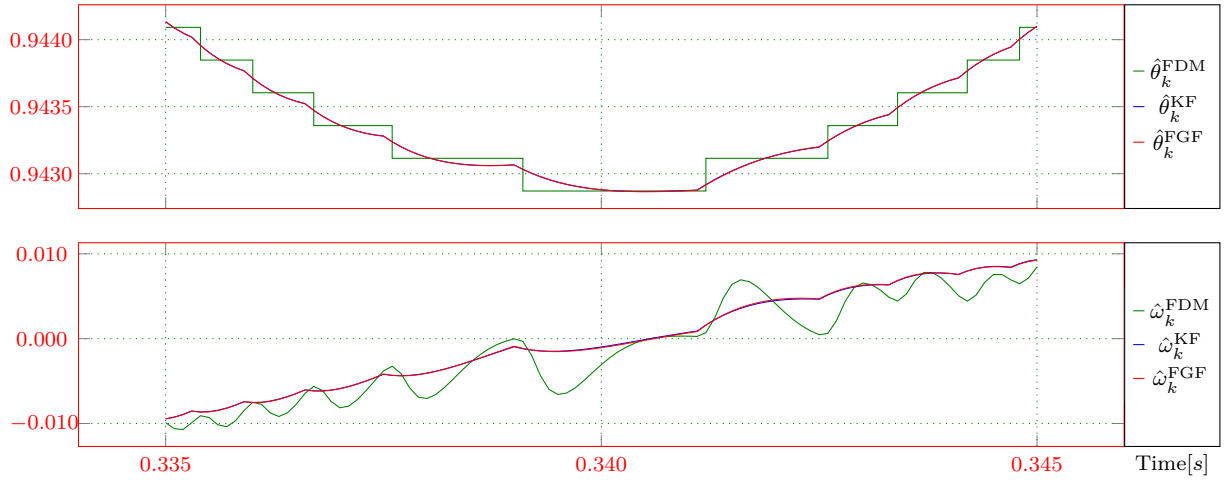

Figure 3.9: Zoomed in experimental comparison for tracking position and velocity from the red frame in Figure 3.8.

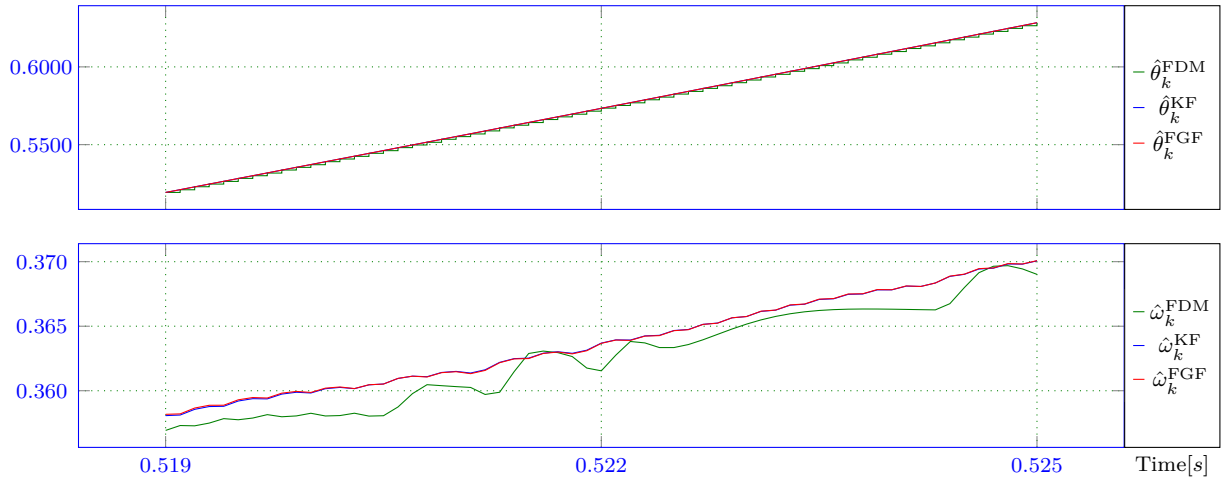

Figure 3.10: Zoomed in experimental comparison for tracking position and velocity from the blue frame in Figure 3.8.

Figure 3.11 shows the experimental comparison for tracking position, velocity, and acceleration with parabolic velocity using the FDM, KF, and FGF. All these three methods successfully estimate the position, velocity. Similar results as in Figure 3.8 are obtained.

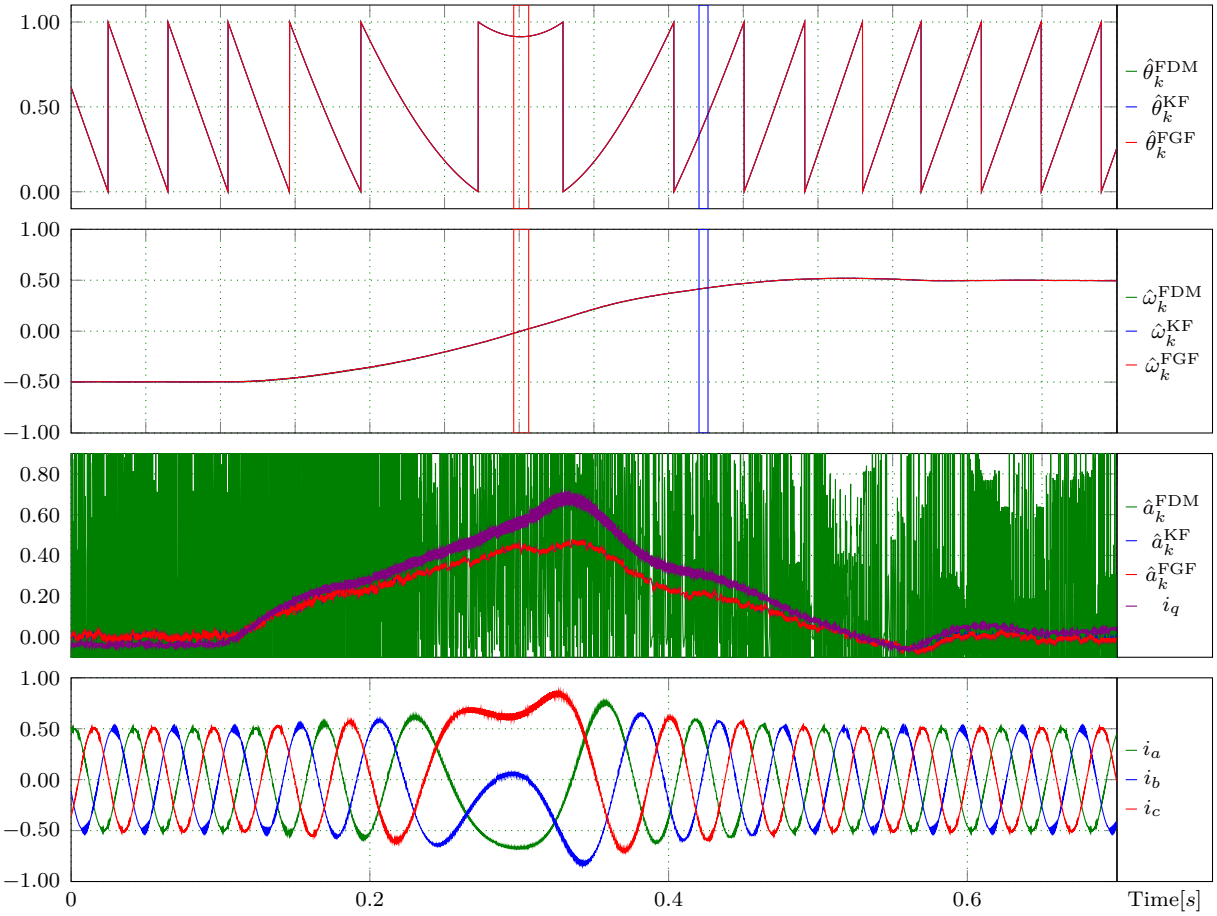

Figure 3.11: Experimental comparison for tracking position, velocity, and acceleration with parabolic velocity.

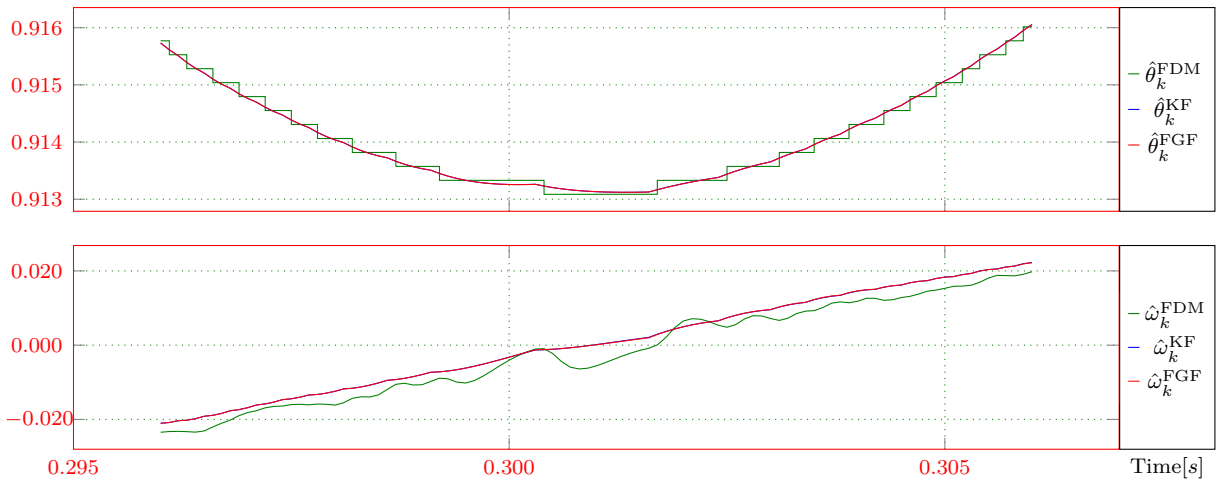

Figure 3.12: Zoomed in experimental comparison for tracking position and velocity from the red frame in Figure 3.11.

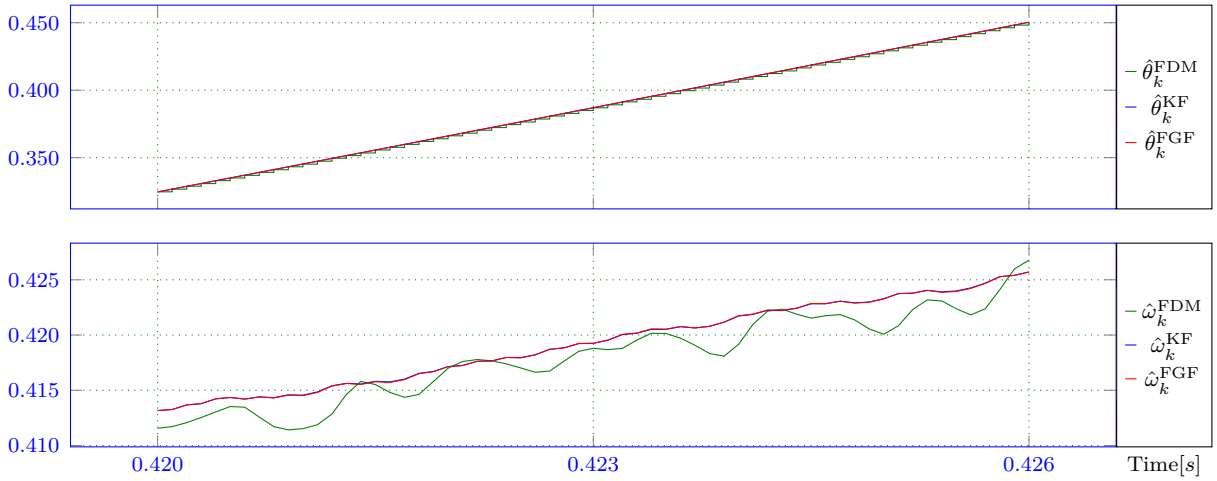

Figure 3.13: Zoomed in experimental comparison for tracking position and velocity from the blue frame in Figure 3.11.

In conclusion, the experimental results are basically consistent with the simulation results when the position signal has quantization errors. It confirms that the simulation model provides a high fidelity in comparison with the real physical hardware. The performance evaluation proves that the results of FGF for tracking positions, velocities, and accelerations are quite similar to the KF since the FGF is a special form of the KF. The FGF and KF have excellent performance to significantly improve the accuracy of position estimation in the entire velocity range, and can reduce the ripple of estimated velocity. Moreover, they can successfully estimate the acceleration in the experiment, while the FDM fails. All results verify that the proposed FGF can be utilized as an substitute for the KF to precisely estimate the position, velocity, and acceleration in electric drives. In the meantime, the FGF significantly saves calculation time comparing to the KF. It outperforms the KF, in terms of faster tracking speed, easier tuning, and lower implementation complexity. The characteristics of fixed gain and narrow tunable range can considerably simplify the application of the fixed gain filter strategy in industry. Both simulation and experimental results confirm that this proposed method outperforms the traditional methods in easier tuning and lower implementation complexity.

3.4 Summary

In this chapter, an efficient and tuning-easy FGF has been proposed to estimate the position, velocity, and acceleration of the electric drives. As the research has proved, there is no doubt that the optimal FGF is very simple to implement and it reduces the execution time compared to the KF, since it takes into account the motion nature of the tracked object. The proposed FGF is similar to the KF in terms of performance and effectiveness in estimating position, velocity, and acceleration in electric drives, because it is a special form of the KF and it is easier to obtain the optimal gain. In this study,

the FGF used for angular motion estimation is evaluated by the encoder in the electric drive. In fact, it can also be used for all position feedback applications in industries such as sensor-less control, grid synchronous, and motion control, etc. With the development of alternating current (AC) drives, the change and evolution of renewable energy systems and new and more demanding standards will promote the application of the FGF.

Chapter 4

Velocity measurement with self-mixing interferometry

This chapter introduces the SMI applied to measure velocity. In Section 4.1, the background is introduced. After that, the experimental setup is presented in Section 4.2. The parameters having effects on the measurement accuracy of velocity are analyzed in Section 4.3. In Section 4.4, the spectrum interpolations of the SMI signal are summarized and detailed. In Section 4.5, the MLE method to improve the estimate results is performed in the frequency domain. Finally, the EKF method based on the model of the SMI signal is proposed to estimate the velocity in Section 4.6.

4.1 Introduction

M. J. Rudd reported the first demonstration to use optical feedback principle to detect the Doppler shift in gas laser with a remote moving target in 1968 [65]. With the rapid development of laser technology, numerous preliminary applications for velocity measurement with semiconductor lasers instead of gas lasers have been reported [32, 44, 121]. Velocity measurement was performed well before the non-ambiguous interferometric displacement measurement was demonstrated. The schematic model of the self-mixing interferometry used in our experiment to measure velocity is shown in Figure 4.1. The sensor layout of the self-mixing velocimeter is shown on the left side of the figure. The commercial LDV is used to provide reference velocity. The light beam emitted from the laser diode is focused by the lens and then strikes on the target. The light back-scattered by the target surface injects into the laser cavity, superimposes on the existing internal field, and modulates both the amplitude and frequency of the laser field. The static characteristics of semiconductor lasers with optical feedback can be theoretically investigated through the relationships between the reflectivity of the internal cavity and external reflector, the

gain in a medium, and other static laser parameters [57], as presented in Section 2.2.2. The self-mixing signal can be simply obtained by observing the laser output power with the built-in photo-diode [61] or by recording the terminal voltage [69]. Throughout this study, the SMI signal is obtained from the photocurrent detected by the photo-diode integrated into the laser diode. The signal is modulated by a frequency f_D, which is related to the linear speed v by (2.63).

According to (2.63), the speed is linearly proportional to the frequency of the self-mixing signal. As long as the angle θ between the laser beam and the moving surface is nonzero, the velocity can be deduced from the Doppler frequency f_D. Therefore, a sensor monitoring the Doppler frequency can be used to calculate the velocity. The velocity of normal incidence can be estimated by analyzing the frequency of the occurrence of 'speckle grains' detected by the amplitude of the self-mixing signal. The reciprocal of the autocorrelation time of speckle signals has a linear relationship with the surface velocity [122, 123]. The possible limitation of this technique is the dependence of sensor calibration on the type of surface being measured [63].

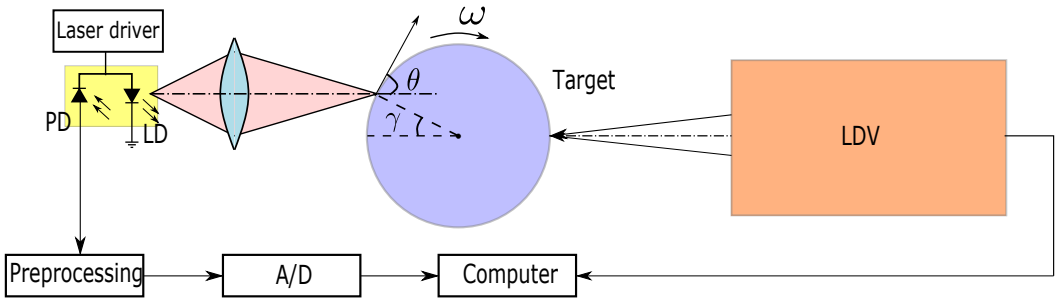

Figure 4.1: The schematic of velocity measurement with an SMI sensor. The commercial LDV provides a reference velocity of the system in our experiment.

A variety of methods has been used to accurately estimate the Doppler frequency, which is proportional to the measured velocity. The most widely used method is the classical spectral analysis based on the FFT. The FFT method can provide reasonably high resolution for sufficiently long data length. However, it has a severe drawback, that is, the FFT based spectrum is equal to the correct spectrum only if the analyzed signal is periodic and an integer multiple of the period is recorded [124, 125]. Otherwise, the spectrum leakage that strongly depends on the selected time-domain window will occur, and the energy of the original spectral line will leak into other spectral lines [126–128]. To deal with the leakage issue, a special method was developed to calculate the frequency, amplitude, and phase with the spectral disturbed leakage. This method is often called the interpolated fast Fourier transform (IFFT) [129].

When a rough target back-scatters light from a coherent laser diode, the SMI signal is corrupted by a multiplicative noise caused by the speckle effect. The speckle effect causes

random amplitude modulation of the signal, resulting in the loss of the ideal waveform of the signal and the spectral broadening in the frequency domain. Moreover, wide-band additive noise often appears in practical situations (i.e., photo-detection shot noise). The existence of these two types of noise makes it more difficult to accurately estimate the Doppler frequency. Therefore, a suitable and efficient frequency estimation algorithm has to be developed [44].

In [130], the Doppler frequency was estimated with Gaussian fitting by minimizing the sum of the squares of the difference between the fitting function and the acquired data, but the minimization procedure is very complicated and time-consuming. To handle the limited record length, parametric techniques which require no restrictive data length assumptions are adopted. A second-order Auto-regressive (AR) method based on the Yule-Walker equation has been proposed to measure the Doppler frequency in [131]. This method has a very low algorithmic complexity, so it is suitable for real-time velocity measurement. Recently, a power spectral density (PSD) estimation method based on the multiple signal classification (MUSIC) has been applied to frequency estimation in distance and velocity measurement [32].

4.2 Experimental system

There are several requirements that affect the design of the laser driver. Foremost is the ability to drive and protect the laser diode. Due to the sensitivity of laser diodes, they are easily damaged in various ways, such as static discharge, electrical spikes, and transients. Therefore, a soft-start mechanism should be established to avoid damage caused by electrical spikes. Besides, laser diodes may be damaged while the operation current exceeds the maximum injection current. Thus, the laser driver should be designed to have the ability to drive the range from threshold current to the maximum operating current, and to ensure that the laser diode will not operate beyond its current limit. To ensure a good interference signal, the driver should be designed to provide a stable and low-noise current.

In the experiment, an AlGaAs laser diode is used as the light source of the SMI. The designed laser driver consists of a stable current controller and a triangular modulation. The stable current controller is designed to protect the laser diode as much as possible:

- slow start of the current;
- protection against the voltage and current spikes;
- protection against the excessive direct current through the laser;
- protection against excessive reverse voltage across the junction;

- current stability within 2 μA.

The sensor head applied to measure velocity consists of a commercial 785 nm laser diode, a lens, and a preprocessing circuit. The typical threshold current and operation current of the laser are 20 mA and 28 mA. Figure 4.2 shows the measuring system and Figure 4.3 shows the labeled photograph of the sensor head. Since the surface of the motor shaft is not ideal, it can be used as a scattering surface. The laser beam is focused on a fixed point on the motor shaft, and the distance between the sensor head and shaft is about 4.9 mm. To acquire a good velocity reference, the servo drive runs at a constant rotational speed controlled by the feedback control of a 21-bit optical encoder. It is found that to acquire a proper signal, several parameters should be optimized, such as the distance between the sensor head and the motor shaft, the noise of the amplifier, and the focal position.

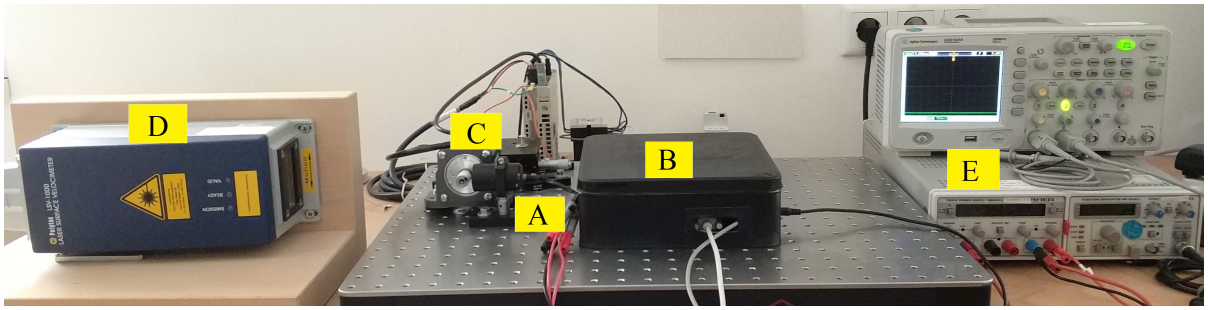

Figure 4.2: Labeled photograph of the measuring system. A: Sensor head, B: Signal processing system, C: Motor, D: LDV, E: Power supply.

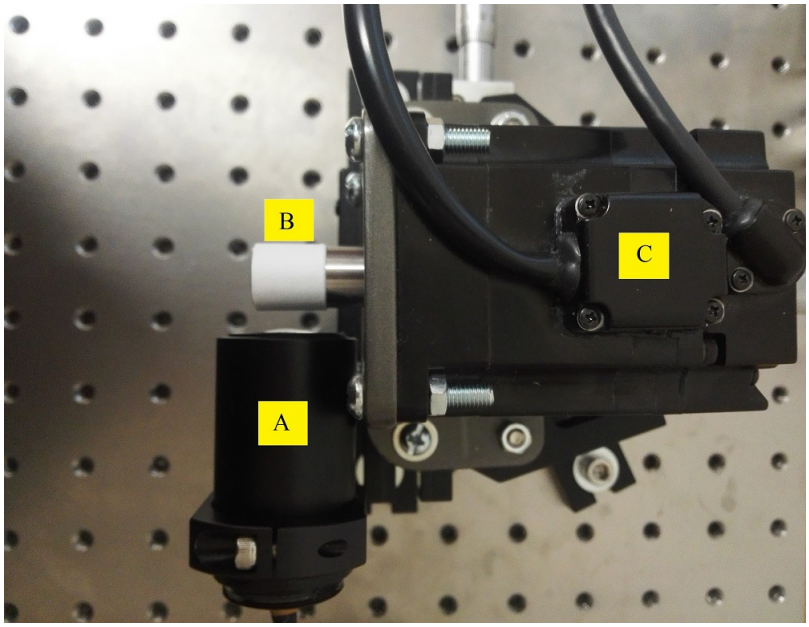

Figure 4.3: Labeled photograph of the sensor head. A: Sensor head, B: Motor shaft, C: Motor.

The self-mixing signal is acquired by tracking the small variations in optical power with the built-in photo-diode. After converting the current signal into voltage with a trans-impedance amplifier (TIA), the direct current (DC) component of the signal is removed by a high-pass filter (HPF), and the weak signal is amplified by a low noise amplifying circuit. The amplifier is designed to have the ability to sense the small variations caused by the self-mixing effect. It requires high-gain, low-noise amplification. Then, the amplified analog signal is digitized for further processing to extract the Doppler frequency. In the experiment, the maximum rotational speed of servo drives is set to 6000 rpm. The minimum rotational speed is 3 rpm since it is the minimum speed being set when the servo drive is controlled by the software provided by the motor manufacturer. Therefore, the measurement of rotational speed is over the range of 3-6000 rpm. The measuring range is not limited by the response frequency of the photo-diode, but by the signal processing circuit, namely, the bandwidth of the amplifier. A potential approach to overcome this problem is to increase the angle θ between the moving direction of the motor shaft and the incident direction of the laser beam, which results in a decrease in the $\cos(\theta)$ term in (2.63), leading to a lower Doppler frequency.

The output power of a laser diode without optical feedback is linearly proportional to the injection current. The previous analysis in (2.50) showed that the output power of a semiconductor laser depends on the injection current, the external cavity length, and the feedback level. To achieve good performance of the SMI, it is essential to assess the optimal operation condition related to the injection current.

The PSDs of self-mixing signals recorded under different injection currents are shown in Figure 4.4. The maximum peak corresponds to the Doppler frequency of the signal. It can be seen that the peak values increases as the injection current increases. Figure 4.5 shows the measured amplitudes and signal to noise ratios (SNRs) of the signal varying with the injection current in the range of 16 mA to 36 mA in steps of 1 mA. A linear increase of amplitude is observed in the range of the injection current. It is consistent with the theoretical calculations and can be found in [63]. The SNR of the signal increases with the growth of the injection current.

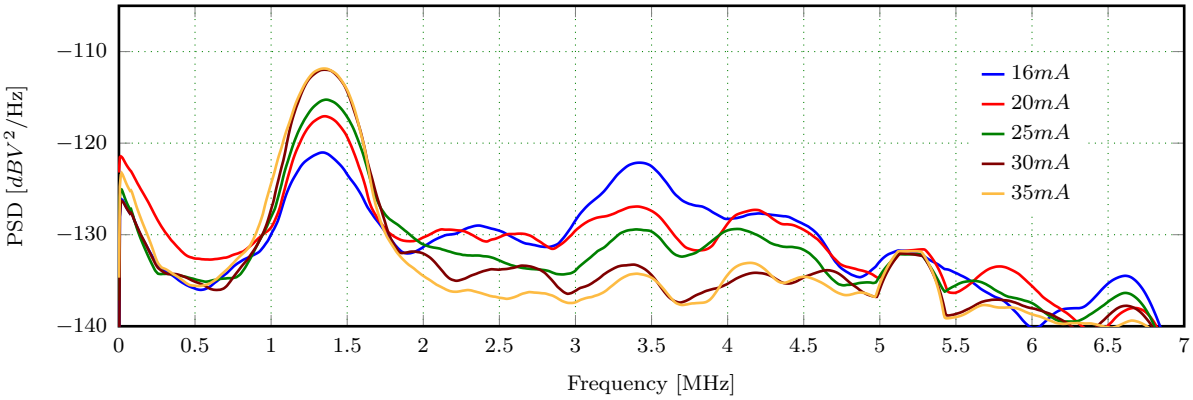

Figure 4.4: PSDs of self-mixing signal for different injection currents (16mA, 20mA, 25mA, 30mA, and 35mA).

Achieving shot-noise-limited operation using an op-amp TIA at very low power level

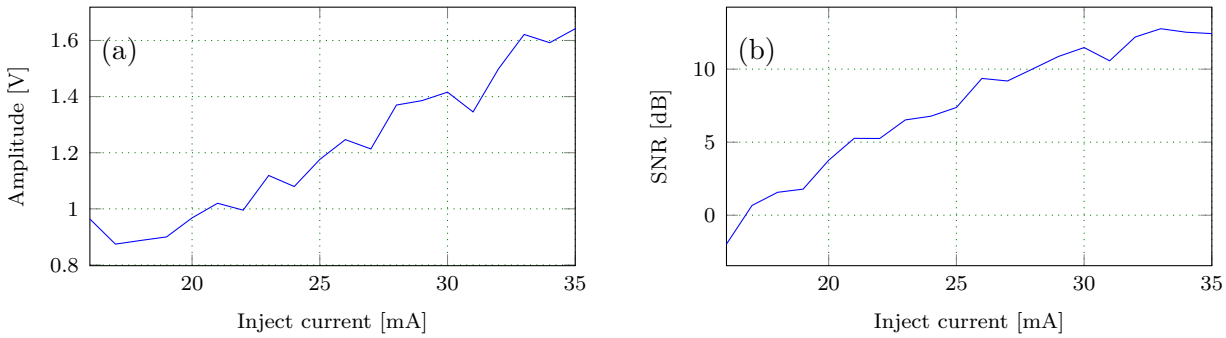

Figure 4.5: (a) Relationship between amplitudes of signal and laser injection currents. (b) Relationship between SNRs and laser injection currents.

requires a large feedback resistance, which severely limits the available bandwidth. Moreover, in general, a proper self-mixing operation can be obtained when the semiconductor laser is operated in a single longitudinal mode, or at least exhibits side-mode suppression greater than 10 dB. Commonly, this condition is not satisfied if the laser is operating just above the threshold [63]. Therefore, to maintain a large SNR and the suitable amplitude of the self-mixing signal, according to the results in Figure 4.5, the optimum operation can be achieved by increasing the injection current of the laser diode.

4.2.1 Velocity measurement

Figure 4.6 shows several typical self-mixing signals in the time domain. Note that the time duration of Figure 4.6(a) is different from Figure 4.6(b)-(d). These signals are distorted by the multiplicative noise caused by the speckle effect since the rough surface of the motor shaft back-scatters the coherent light of the laser diode [132–134]. It results in random amplitudes, leads to some loss of ideal signal waveform, broadens the spectrum, and ultimately affects the measurement results. The presence of the speckle effect introduces an undesirable modulation frequency, which is related to the superimposition of the longitudinal speckle size of the virtual speckles projected on the target side [43, 135] onto the self-mixing signal. The longitudinal vitual speckle dimension is $SS_l = \lambda(2l/D_L)^2$ (where λ is the wavelength of the laser, l is the target-laser distance and D_L is the lens diameter.) [43]. By optimizing the parameters l and D_L, the modulation frequency due to the speckle effect can be reduced, but never eliminated. The servo drive will cause some noise, as shown in the figure, and the noise can be reduced by proper isolation.

Figure 4.7(a) shows the relationship between the Doppler frequency and the rotational speed. The Doppler frequency has a linear relationship with the rotational speed according to (2.63). However, the mechanical errors, the nonzero linewidth of the laser, and the spectral broadening of the signal will affect the estimated frequency. Among them, the nonzero linewidth of the laser was proved to have a negligible effect on the Doppler frequency [136]. The relative error [137], which is defined as the absolute error divided by the span in this case, is exhibited in Figure 4.7(b). It is found that the relative error within the usable speed range is less than 2.5%. The accurate measurement of rotational

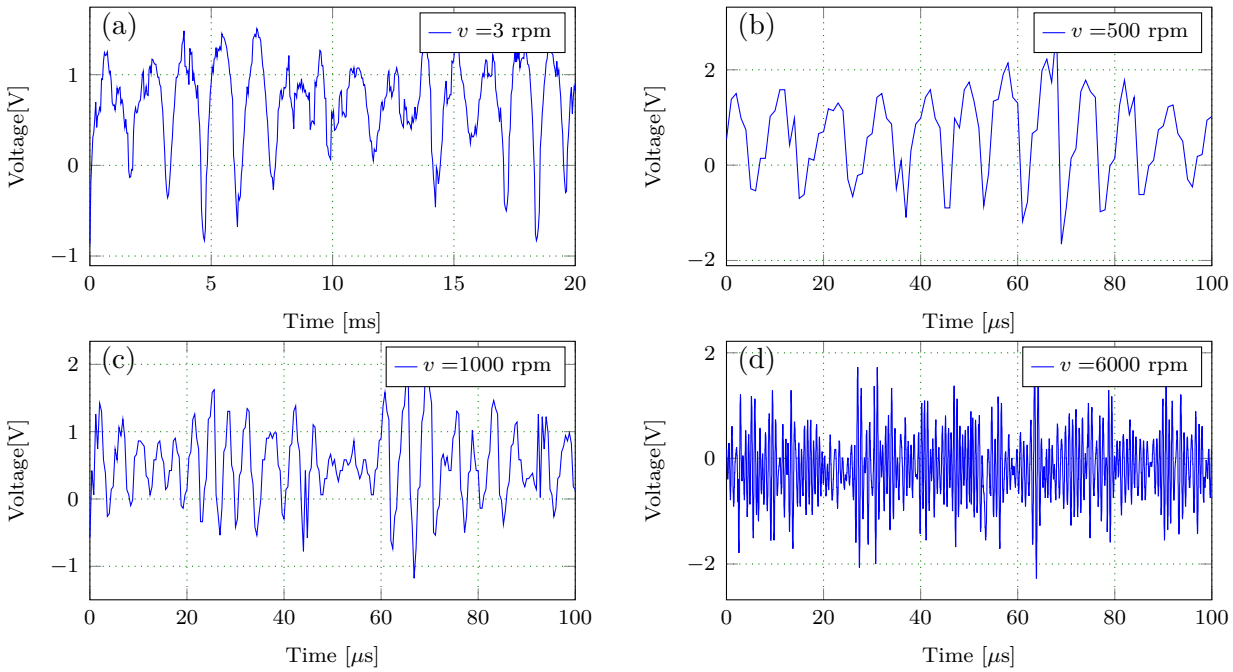

Figure 4.6: Time domain self-mixing signals in different rotational speeds. The rotational speed of (a) is 3 rpm, (b) is 500 rpm, (c) is 1000 rpm, and (d) is 6000 rpm.

speed is hampered by wide distribution range of the PSD.

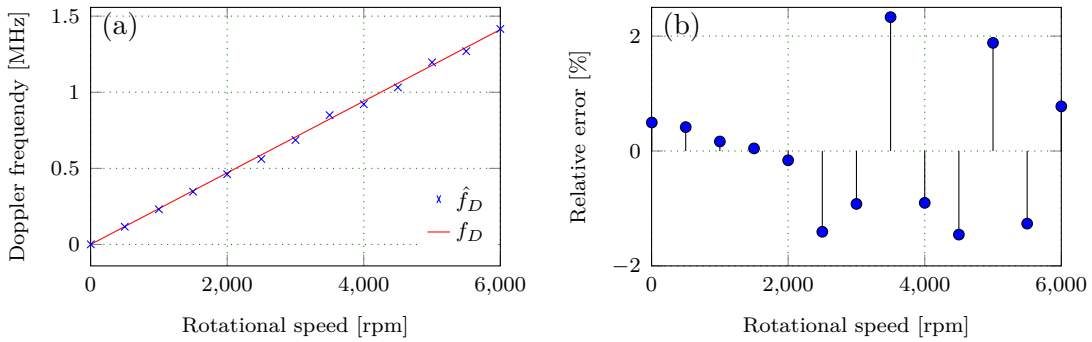

Figure 4.7: The measurement results. (a) Doppler frequency of self-mixing signal versus rotational speed. The red line is obtained by the best fitting of the experimental data. (b) Relative error versus rotational speed.

In this section, SMI is employed to measure the rotational speed of servo drives. The Doppler frequencies are acquired by the FFT method. The experimental results demonstrate that the SMI is applicable to measure the rotational speed of motors up to 6000 rpm or even higher with the relative error within 2.5% in the entire speed range. The presence of two types of noise, additive noise, and multiplicative noise [44] will broaden the spectrum making the accurate estimation of the Doppler frequency more difficult. In the next section, the parameters having an impact on the measurement results will be discussed.

4.3 Error analysis

The main purpose of this section is to improve the velocity measurement accuracy by optimizing the parameters having effect on the speed. Efforts to improve accuracy have been made in other articles. L. Scalise and N. Paone reported the impact of imprecise measurement of incident angle on the results by measuring the angle from 30° to 90°, but it only focused on the impact of imprecise measurement of angle without any analysis of other parameters [138]. W. Huang et al. obtained the dependence of accuracy on the incident angle through experiments, and achieved a laser velocimeter with tracking accuracy better than 1.3% in the range of 10-470 mm/s [139].

In this section, based on studies of the previous papers, the major errors of velocity measurement with SMI are analyzed, and with the optimizing system, a self-mixing sensor is applied to measure velocity accurately. With a simple FFT-based spectrum processing, it can obtain an equally good accuracy as presented by W. Huang [139], where a difference frequency analog phase-locked loop (PLL) was used to improve tracking precision in a wide velocity range before A/D conversion. Besides, the dynamic characteristics of the designed SMI sensor are tested by comparing with a commercial LDV.

The estimated error of Doppler frequency is mainly caused by the spectral broadening. For instance, the spectrum broadening caused by a range of velocities distributing over the light spot region, the vibration and change of surface profile adding uncertainty, and the speckle effect modulating the signal. A comprehensive analysis of factors influencing the morphology of spectrum acquired from the SMI signal was reported by A. Mowla et al. [136]. The effect of optical system parameters was evaluated by three spectral characteristics: central Doppler frequency, broadening, and SNR. A conclusion was drawn that parameters, which have a major effect on the spectrum, are the incident angle, velocity, beam numerical aperture (NA), and fractional change of velocity across the beam spot when the spot is close to the disk center. System vibration, target surface profile, instability of target velocity, laser non-zero linewidth, and fractional change of velocity across the beam spot when the spot is distant from the disk center are all parameters having a minor effect on the spectrum. Therefore, according to the analysis of Russell Kliese and A. D. Rakić [132], the spectral broadening can be quantified by measuring the full-width half-maximum (FWHM) with the equation,

$$\mathrm{FWHM} = \frac{v \sin\theta \sqrt{2 \ln 2}}{\pi w_t}, \tag{4.1}$$

$$w_t = a w_0, \tag{4.2}$$

where w_t is the beam radius on the target, w_0 is the waist radius of the laser, and a is the magnification of the optical system. This simple analytic formula of the FWHM shows that the spectral broadening depends on the velocity component normal to the optical axis ($v \sin\theta$) and the beam radius on the target w_t. It is explicitly independent of the wavelength. The laser linewidth, which is extremely narrow relative to its operating

frequency, has a minor effect on the Doppler frequency. The research [136] proved that the maximum FWHM occurs when the angle between the beam axis and the target is close to zero. When this angle increases, the FWHM decreases. Therefore, when this angle changes sharply, a significant variation in FWHM will be observed.

Next, we will prove the influence of the angle on the measurement results by introducing the relative error, which is simply calculated as the difference between the measured velocity and the virtual velocity and then divided by the virtual velocity. In our experiment, as depicted in Figure 4.1, the magnification of the optical system a and the waist radius of the laser w_0 are constant. Therefore, the error caused by the spectrum broadening primarily depends on the velocity and the incident angle. Since it is difficult to estimate the waist radius of the laser beam inferred from the far-field beam [132], the relative error can be calculated equivalently by (2.63). Assuming that the laser wavelength and the rotational speed are constant, the Doppler frequency depends on the radius of the disk and the incident angle of the laser. It is given by

$$\mathrm{Err}_m = \frac{f_D' - f_D}{f_D} = \left(1 + \frac{\Delta r}{r}\right) \frac{\cos(\theta + \Delta\theta)}{\cos(\theta)} - 1, \tag{4.3}$$

where f_D' is the estimated Doppler frequency, f_D is the theoretical Doppler frequency, r is the radius of the rotary disk, Δr is the variation of the disk radius, and $\Delta\theta$ is the variation of the incident angle.

Figure 4.8 shows the simulation results of the relative error varying with the incident angle. The relative error is obtained by finding the maximum error with Δr and $\Delta\theta$. The relative error increases with the growth of the incident angle from 5° to 80°. Between 0° and 70°, it increases slowly, and then sharply rises after 70°. It illustrates that the incident angle exerts a tremendous influence on the relative error. When the variation of angle changes from 0.2° to 0.4°, the relative error is nearly doubled. Likewise, the variation of the radius also has a great influence on the relative error.

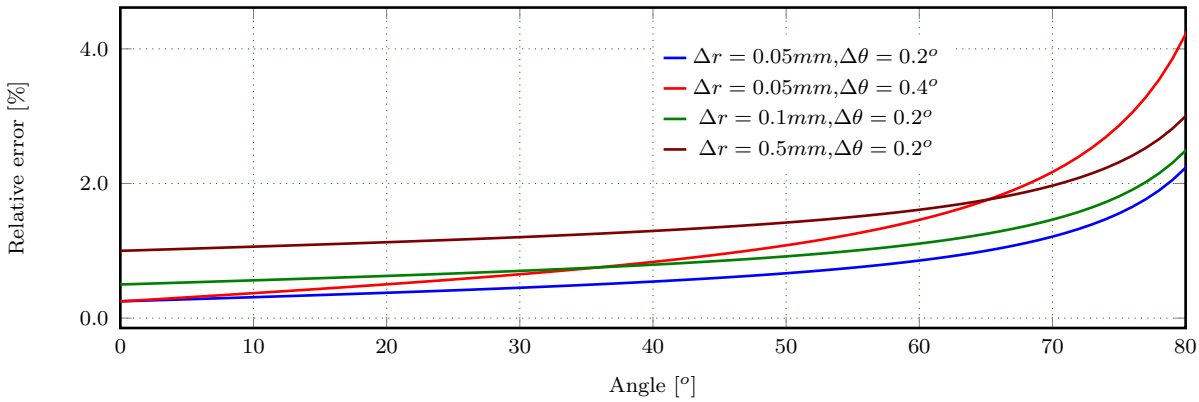

Figure 4.8: Simulated relative errors versus incident angle.

Figure 4.9 shows the dependence of the relative error on the variation of radius and the variation of the angle when the incident angle is 45°.

To verify the analysis in simulation, some experimental data are acquired at different

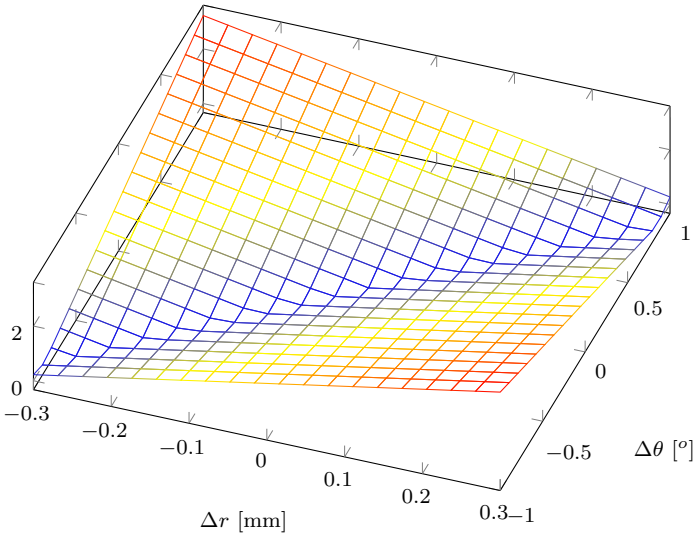

Figure 4.9: Simulated relative errors versus the variation of the incident angle and the variation of the disk radius.

incident angles θ, as shown in Figure 4.10, while the motor rotates at a constant speed of 100 rpm (209 mm/s). The noise spikes in Figure 4.10(a) and (b) are caused by the servo drive, and it can be reduced by proper isolation. The speckle phenomenon is observed as a random amplitude modulation that strongly affects the SMI fringes. Due to this amplitude modulation, the signal loses its sinusoidal feature or even vanishes in some segments. It is worth noting that the signal amplitude increases with the incident angle, and the signal in Figure 4.10(d) has the largest amplitude, because much more light is scattered back into the laser cavity when the incident angle increases, and the signal becomes more like a sawtooth-like wave.

The signals in Figure 4.10 are processed to get the Doppler frequency and velocity. The corresponding PSDs of signals are shown in Figure 4.11. Due to the spectrum broadening, the spectrum displays a Gaussian distribution, where the frequency at the center of the peak corresponds to the Doppler frequency, which is representative of velocity at the center of the beam spot. This velocity and the angular velocity of the disk are easily calculated. For a given signal, the variance of averaged PSD can be reduced by increasing the number of blocks. However, the block length determines the maximum time lag of the PSD resolution. For online measurement, a smaller block length should be implemented. The FFT is applied to each block and respective PSDs are averaged to find the Doppler frequency. In Figure 4.11(c) and Figure 4.11(d), it could be clearly noticed that the PSDs have harmonic components. Besides, Figure 4.11(d) has two maximum peaks near the Doppler frequency, making it much more difficult to determine the correct Doppler frequency.

Figure 4.12 shows the Doppler frequency of different incident angles at a velocity of 209 mm/s. Each Doppler frequency is the average of 150 successively Doppler frequencies, which are determined in the incident angle range of 27°-82°. The Doppler frequencies drop from 480 kHz to 90 kHz with the increase of incident angle. When the incident angle rises

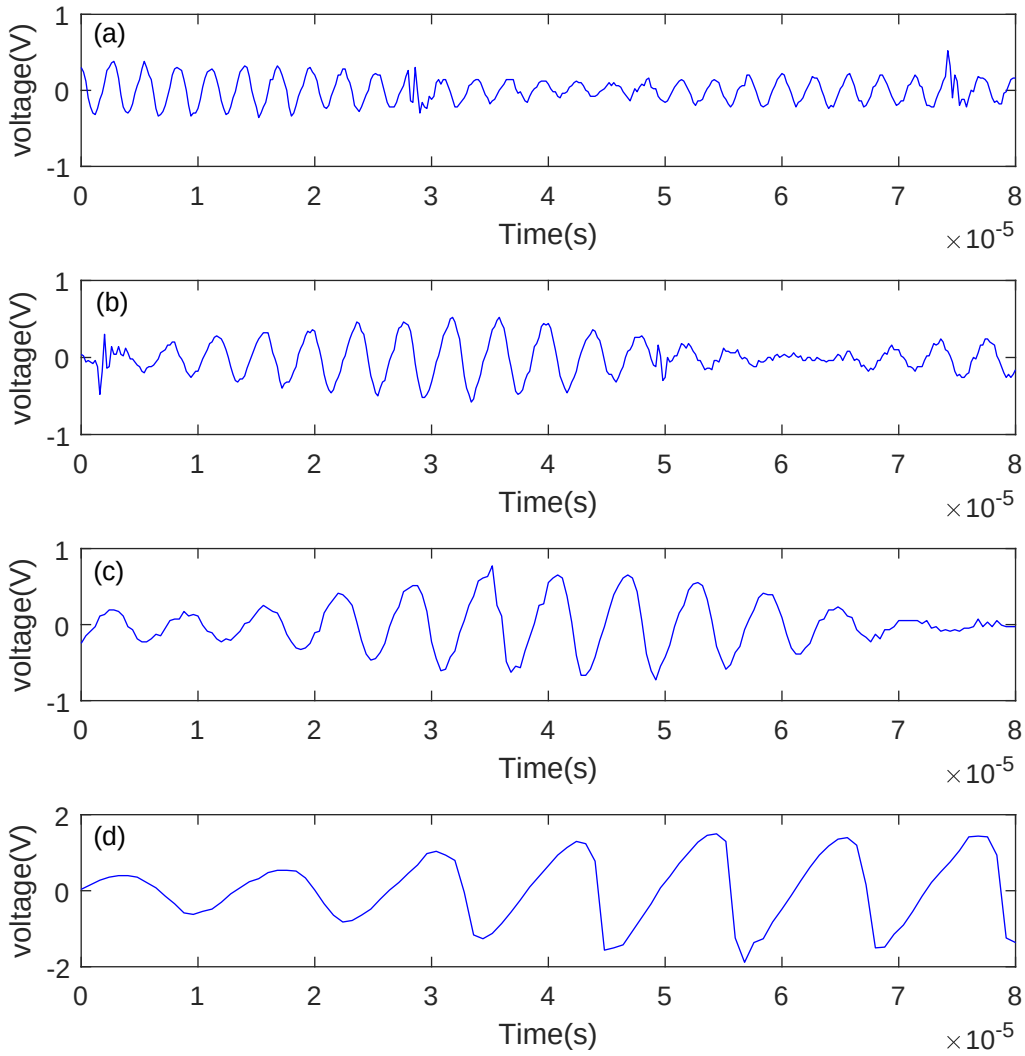

Figure 4.10: Examples of time domain self-mixing signal segment with different incident angles, v=209mm/s. (a) θ=27°, (b) θ=44°, (c) θ=63°, (d) θ=81°.

to 82°, the optical feedback becomes much stronger. Although the back-scattered light increases, the light carrying the velocity information reduces, making it hard to extract the accurate Doppler frequency.

Figure 4.13 exhibits the dependence of signal amplitude and relative error on the incident angle. All the relative errors in this experiment are acquired by finding the maximum of 150 successive relative errors of velocity. In Figure 4.13(a), the amplitude rises with the incident angle. In Figure 4.13(b), the trend of the relative error indicates a good match with the simulation in Figure 4.8. The relative error becomes larger with the increase of the angle, and it increases slowly as the incident angle is smaller than 70°. In the range of 27° to 60°, the relative error is less than 1%. Therefore, by decreasing the incident angle, the relative error can be reduced. However, the incident angle could not be too

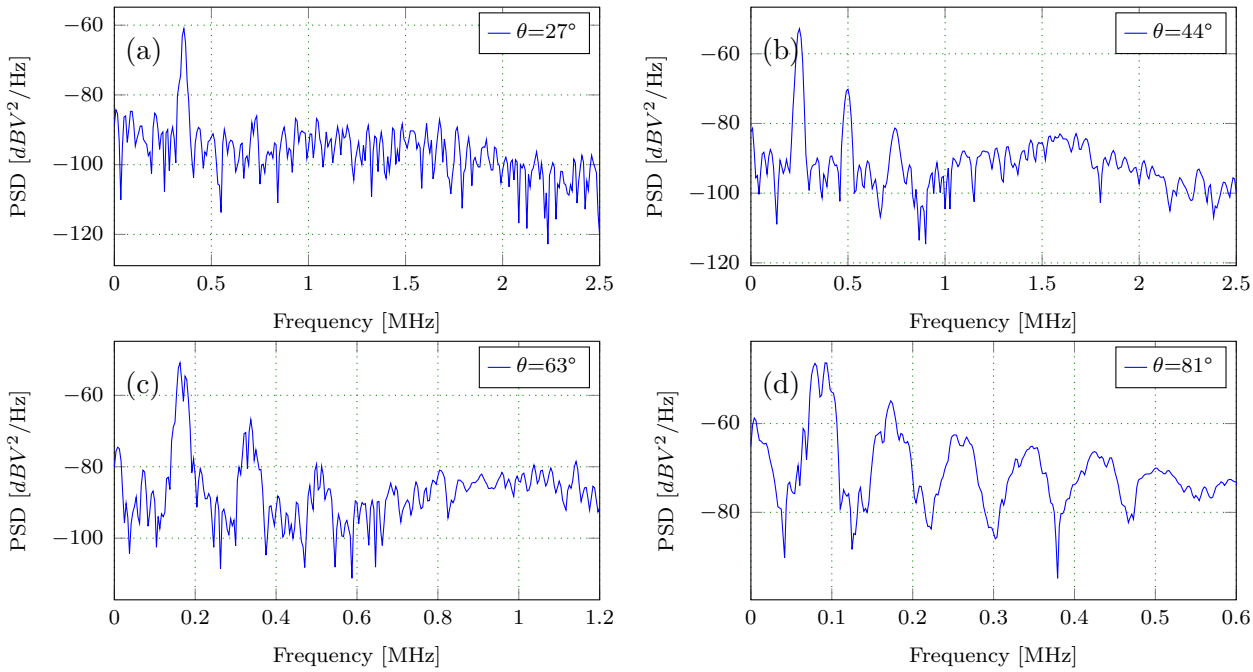

Figure 4.11: Corresponding PSDs of signals in Figure 4.10, v=209mm/s. (a) θ=27°, (b) θ=44°, (c) θ=63°, (d) θ=81°.

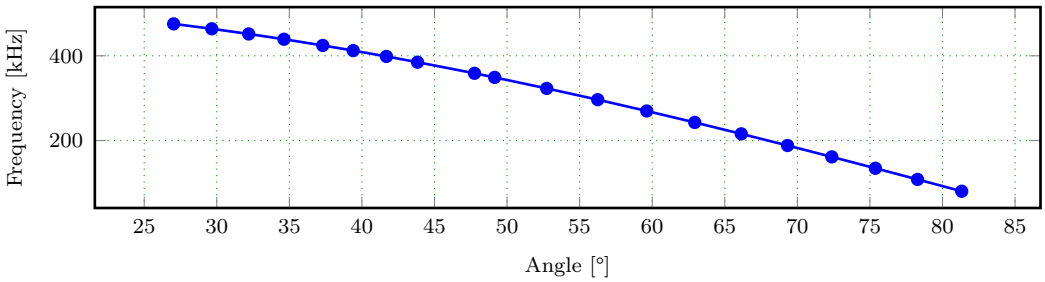

Figure 4.12: The Doppler frequency of different incident angle.

small, as the signal amplitude should also be considered. Too small amplitude makes the signal susceptible to noise interference. Moreover, small signal requires a large feedback resistance, which seriously limits the available bandwidth.

To guarantee the signal amplitude and small relative error, the incident angle is finally set to 46° to measure velocity from 10.43 mm/s to 1043 mm/s. The measured velocity using the self-mixing sensor is compared with a commercial LDV (LSV1000, Polytec). The measuring results are exhibited in Figure 4.14.

Figure 4.14 reveals the average relative errors, the maximum relative errors, and the minimum relative errors of the self-mixing sensor and the LDV. The average relative error of LDV is better than that of the self-mixing sensor, because the eccentricity of the rotary disk modulates the velocity with a small sinusoidal variation. The LDV records the whole change process of the velocity, and the average of the velocity reduces or even eliminates the variation, whereas the self-mixing sensor used here cannot acquire the entire change of the velocity, because the sampling system cannot do non-gap sampling at present.

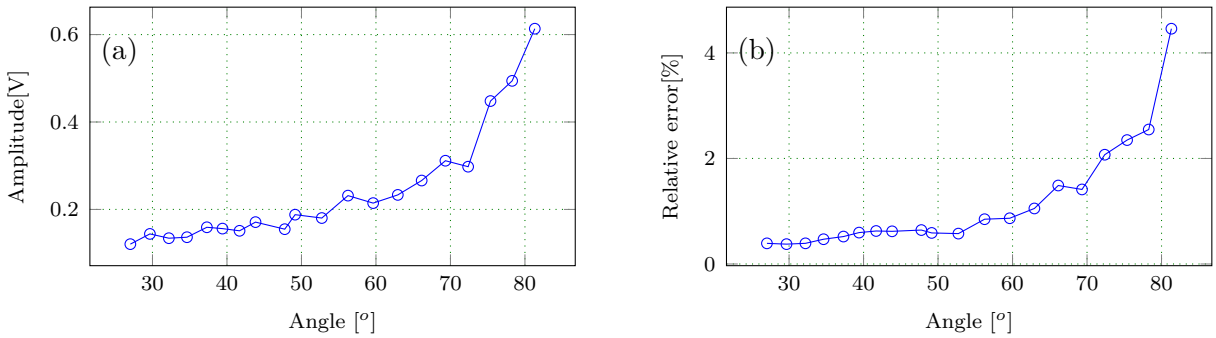

Figure 4.13: The dependence of the amplitude of the SMI signal and the relative error on the incident angle.

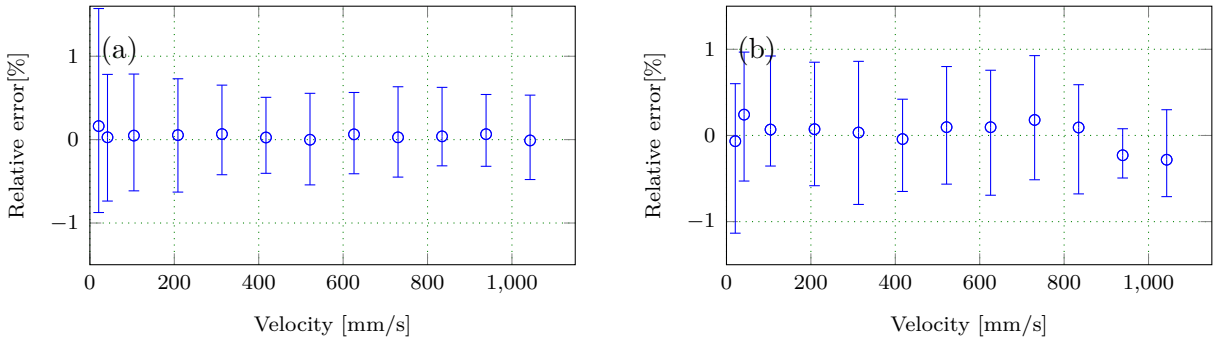

Figure 4.14: The average relative errors, the maximum relative errors, and the minimum relative errors, θ=46°. (a) The relative errors of the LDV, (b) the relative errors of the self-mixing sensor.

Nevertheless, the maximum relative error and the minimum relative error of the self-mixing sensor are comparable to that of the LDV. It proves that the measurement error of the self-mixing sensor can be reduced under the appropriate incident angle.

In this section, the error analysis of SMI for velocity measurement is presented, and a simple error model is proposed. The simulation presents that the incident angle exerts a tremendous influence on the relative error, which will increase with the increase of the incident angle. Comparison between the simulation and experiment under different incident angles proves that the relative error can be reduced by decreasing the incident angle.

4.4 Interpolation of spectrum

Because an integer multiple of periods is not always recorded, the leakage of the spectrum occurs. Thus, it generates a large unacceptable variance of estimated frequency. Besides, sufficient data are usually not available in practice, and the use of side-lobe reducing windows is employed at the expense of estimation variance. F. J. Harris [127] has made an overview of the properties of different windows for FFT. The general impression of the

spectrum can be improved by appropriately choosing the time window, but it does not provide a good solution to measure the frequency of the individual components accurately. To solve these problems, the IFFT is usually used.

As early as 1970, Rife and Vincent presented approximate solutions for the rectangular, the Hanning, and the Rife-Vincent formulas [129], which were later also developed by Jain, et al. [126] (rectangular window), Grandke [128] (Hanning window), Andria et al. [140], and Ofelli et al. [141] (Rife-Vincent windows). Renders et al. [142] solved the problem for the rectangular window analytically without making any approximation. The article [125] studied five IFFT methods concerning their systematic errors and their noise sensitivity.

Suppose the sampled multifrequency signal is written as

$$x(k) = \sum_{m=1}^{M} A_m \sin(2\pi f_m kT + \phi_m), k = 0, 1, 2, \cdots, N-1. \tag{4.4}$$

It is assumed that the sampling frequency exceeds the Nyquist rate, so the aliasing of spectra does not occur. The discrete Fourier transform (DFT) is given as [124]

$$X(h) = \sum_{k=0}^{N-1} x(k) \exp\left(-j\frac{2\pi}{N}hk\right), k = 0, 1, 2, \cdots, N-1. \tag{4.5}$$

It can be written to find the expression of the DFT of these windows in terms of the current frequency $f_h = h\Delta f$ [126, 140],

$$X(h) = \sum_{m=1}^{M} \frac{A_m}{2} \sum_{k=0}^{N-1} \left[X_N^{k(h-\lambda_m)} + X_N^{k(h+\lambda_m)}\right]. \tag{4.6}$$

4.4.1 Interpolation with rectangular window

The rectangle window is unity over the observation interval. The window for a finite Fourier transform is defined as

$$\omega(n) = 1, n = -\frac{N}{2}, \cdots, -1, 0, 1, \cdots, \frac{N}{2}. \tag{4.7}$$

The Dirichlet kernel, which represents the transform of the rectangular window, is defined as [127, 128, 140]

$$X_D(h) = \sum_{k=0}^{N-1} X_N^{kh} = \frac{\sin(\pi h)}{\sin(\pi h/N)} \exp\left(-j\pi\frac{N-1}{N}h\right). \tag{4.8}$$

Equation (4.6) can be rewritten as

$$X(h) = \sum_{m=1}^{M} \frac{A_m}{2} \left[X_D(h - \lambda_m) + X_D(h + \lambda_m) \right]. \tag{4.9}$$

Therefore, the DFT of (4.4) can be written to be

$$\begin{aligned} X(h) = &- 0.5 \sum_{m=1}^{M} A_m \Bigg\{ \exp\left(j[a(\lambda_m - h) + \phi_m]\right) \frac{\sin[\pi(\lambda_m - h)]}{\sin[\pi(\lambda_m - h)/N]} \\ &- \exp\left(-j[a(\lambda_m + h) + \phi_m]\right) \frac{\sin[\pi(\lambda_m + h)]}{\sin[\pi(\lambda_m + h)/N]} \Bigg\}, \end{aligned} \tag{4.10}$$

where $\lambda_m = f_m/\Delta f = h + \delta_m$, h are distinct integers, δ_m is suitable fractions between zero and one, including zero, and $a = \pi(N-1)/N$.

Suppose the fundamental frequency is described by

$$x_1(t) = A_1 \sin(2\pi f_1 t + \phi_1). \tag{4.11}$$

By setting $M = 1$ in (4.10), the DFT of (4.11) is

$$\begin{aligned} X(h) = &- 0.5A_1 \Bigg\{ \exp\left(j[a(\lambda_1 - h) + \phi_1]\right) \frac{\sin[\pi(\lambda_1 - h)]}{\sin[\pi(\lambda_1 - h)/N]} \\ &- \exp\left(-j[a(\lambda_1 + h) + \phi_1]\right) \frac{\sin[\pi(\lambda_1 + h)]}{\sin[\pi(\lambda_1 + h)/N]} \Bigg\}. \end{aligned} \tag{4.12}$$

To proceed further, an approximation is made that the second term in (4.12) is ignored. This approximation contributes to a frequency error of no more than 0.04% when $\lambda \geq 20$ and $N \geq 1024$ [126]. Then the largest two spectrum lines are [128]

$$X(l_1) = -0.5A_1 \exp\left[j(a\delta + \phi_1)\right] \frac{\sin(\pi\delta)}{\sin(\pi\delta/N)}, \tag{4.13a}$$

$$X(l_1 + 1) = -0.5A_1 \exp\left[j(a(\delta - 1) + \phi_1)\right] \frac{\sin[\pi(1-\delta)]}{\sin[\pi(1-\delta)/N]}, \tag{4.13b}$$

where $\delta_1 = \lambda_1 - l_1$ and $0 \leq \delta_1 < 1$, l_1 is the position of the largest spectrum. Since the number of samples N is usually large, the sin function appears in the Dirichlet kernels can be replaced by their respective arguments.

$$|X(l_1)| = 0.5A_1 \frac{|\sin(\pi\delta_1)|}{\pi\delta_1/N}, \tag{4.14a}$$

$$|X(l_1 + 1)| = 0.5A_1 \frac{|\sin[\pi(1-\delta_1)]|}{\pi(1-\delta_1)/N} \approx 0.5A_1 \frac{|\sin(\pi\delta_1)|}{\pi(1-\delta_1)/N}. \tag{4.14b}$$

Then we can get

$$\frac{|X(l_1)|}{|X(l_1+1)|} = \frac{1-\delta_1}{\delta_1}. \tag{4.15}$$

$$\delta_1 = \frac{|X(l_1+1)|}{|X(l_1)|+|X(l_1+1)|}. \tag{4.16}$$

From (4.13), the phase ϕ_1 is

$$\phi_1 = Phase[X(l_1)] - a\delta_1 + \pi/2, \tag{4.17a}$$
$$\phi_1 = Phase[X(l_1+1)] - a(\delta_1 - 1) + \pi/2. \tag{4.17b}$$

Either of the above equations can be used to compute ϕ_1. The one corresponding to the largest spectral line is recommended.

From (4.14), the amplitude A_1 is

$$A_1 = \frac{2\pi\delta_1|X(l_1)|}{N|\sin(\pi\delta_1)|}, \tag{4.18a}$$
$$A_1 = \frac{2\pi(1-\delta_1)|X(l_1+1)|}{N|\sin[\pi(1-\delta_1)]|}. \tag{4.18b}$$

Either of the above two equations can be used to compute A_1. We recommend using the second one only when $|X(l_1+1)|$ is larger than $|X(l_1)|$.

4.4.2 Interpolation with Hanning window

The Hanning window is described as

$$\omega(n) = \frac{1}{2}\left[1 - \cos(\frac{2\pi n}{N-1})\right] = \sin^2(\frac{\pi n}{N-1}), n = 1, 2, 3, \cdots, N. \tag{4.19}$$

The spectrum modulus of the Hanning is [143]

$$|X(x)| = \frac{\sin(\pi x)}{2\pi x(1-x^2)}. \tag{4.20}$$

If the Hanning window is utilized, the spectrum of $\omega(kT) \cdot x(kT)$ is

$$X(h) = \sum_{m=1}^{M} A_m X_N[(h\Delta f - f_m)T]. \tag{4.21}$$

With [127, 128]

$$X(h) = 0.5\{X_D(h) - 0.5[X_D(h+1) + X_D(h-1)]\}. \tag{4.22}$$

The sum of the three Dirichlet kernels can effectively eliminate the sidelobes of a single function. The rate of fall off of the remaining sidelobes is -18 dB per octave as compared to -6 dB per octave for a single Dirichlet kernel [127]. Substitute (4.8), (4.22) into (4.21) , we obtain

$$\begin{aligned} X(h) =& 0.5 \sum_{m=1}^{M} A_m \Bigg\{ \frac{\sin(\pi(h\Delta f - f_m)T)}{\sin(\pi(h\Delta f - f_m)/N)} \exp\left(-j\pi \frac{N-1}{N}(h\Delta f - f_m)T\right) \\ & - 0.5 \frac{\sin[\pi((h\Delta f - f_m)T + 1)]}{\sin[\pi((h\Delta f - f_m)T + 1)/N]} \exp\left(-j\pi \frac{N-1}{N}[(h\Delta f - f_m)T + 1]\right) \\ & - 0.5 \frac{\sin[\pi((h\Delta f - f_m)T - 1)]}{\sin[\pi((h\Delta f - f_m)T - 1)/N]} \exp\left(-j\pi \frac{N-1}{N}[(h\Delta f - f_m)T - 1]\right) \Bigg\}. \end{aligned} \tag{4.23}$$

Because $f_m = (h+\delta_m)\Delta f$, where is h are distinct integers, the DFT of the fundamental signal in (4.23) is written as

$$\begin{aligned} X(h) =& 0.5A_1 \Bigg[\frac{\sin(-\pi\delta_1)}{\sin(-\pi\delta_1/N)} \exp\left(j\pi \frac{N-1}{N}\delta_1\right) \\ & - 0.5 \frac{\sin[\pi(-\delta_1 + 1)]}{\sin[\pi(-\delta_1 + 1)/N]} \exp\left(j\pi \frac{N-1}{N}\delta_1 - j\pi \frac{N-1}{N}\right) \\ & - 0.5 \frac{\sin[\pi(-\delta_1 - 1)]}{\sin[\pi(-\delta_1 - 1)/N]} \exp\left(j\pi \frac{N-1}{N}\delta_1 + j\pi \frac{N-1}{N}\right) \Bigg]. \end{aligned} \tag{4.24}$$

Since the number of samples N is usually large, the sin function appears in the Dirichlet kernels can be replaced by their respective arguments. Similarly, $\exp(j\pi\frac{N-1}{N}) \approx -1 + \pi j/N$. Then

$$\begin{aligned} X(h) =& 0.5A_1 \Bigg[\frac{\sin(\pi\delta_1)}{\pi\delta_1/N} \exp\left(j\pi \frac{N-1}{N}\delta_1\right) \\ & - 0.5 \frac{\sin(\pi\delta_1)}{\pi(-\delta_1 + 1)/N} \exp\left(j\pi \frac{N-1}{N}\delta_1\right) \\ & + 0.5 \frac{\sin(-\pi\delta_1)}{\pi(\delta_1 + 1)/N} \exp\left(j\pi \frac{N-1}{N}\delta_1\right) \Bigg]. \end{aligned} \tag{4.25}$$

Finally,

$$X(l_1) = 0.5A_1 \frac{\sin(\pi\delta_1)}{\pi\delta_1(1-\delta_1^2)/N} \exp\left(j\pi\frac{N-1}{N}\delta_1\right), \tag{4.26a}$$

$$X(l_1+1) = 0.5A_1 \frac{\sin(\pi\delta_1)}{\pi\delta_1(1-\delta_1)(\delta_1-2)/N} \exp\left(j\pi\frac{N-1}{N}\delta_1\right). \tag{4.26b}$$

The modulus of the maximum spectral line and second spectral line in (4.26) are expressed as

$$|X(l_1)| = 0.5A_1 \frac{|\sin(\pi\delta_1)|}{\pi\delta_1(1-\delta_1^2)/N}, \tag{4.27a}$$

$$|X(l_1+1)| = 0.5A_1 \frac{|\sin(\pi\delta_1)|}{\pi\delta_1(1-\delta_1)(2-\delta_1)/N}. \tag{4.27b}$$

Finally, we have

$$\frac{|X(l_1)|}{|X(l_1+1)|} = \frac{2-\delta_1}{1+\delta_1}. \tag{4.28}$$

$$\delta_1 = \frac{2|X(l_1+1)| - |X(l_1)|}{|X(l_1)| + |X(l_1+1)|}. \tag{4.29}$$

From (4.26), the phase is

$$\phi_1 = Phase[X(l_1)] - a\delta_1 + \pi/2, \tag{4.30a}$$

$$\phi_1 = Phase[X(l_1+1)] - a(\delta_1 - 1) + \pi/2. \tag{4.30b}$$

From (4.27), the amplitude A_1 is

$$A_1 = \frac{2\pi\delta_1(1-\delta_1^2)|X(l_1)|}{N|\sin(\pi\delta_1)|}, \tag{4.31a}$$

$$A_1 = \frac{2\pi\delta_1(1-\delta_1)(2-\delta_1)|X(l_1+1)|}{N|\sin(\pi\delta_1)|}. \tag{4.31b}$$

Either of the above equations are able to be used to compute the phase ϕ_1 and amplitude A_1. Only when $|X_N(l_1+1)|$ is larger than $|X_N(l_1)|$ the second one is recommended.

4.4.3 Parabola fit

The inherent frequency resolution of the digital PSD is f_s/N, thus the resolution of the estimated Doppler frequency can be improved by increasing the record length, but this

will lead to an increase in the amount of calculation and a decrease in the resolution of time-frequency. A typical method to improve the resolution is by interpolating the peak position of the broaden PSD.

The basic assumption of these classical spectral estimation is that the signal is interfered by additive noise, which is supposed to be a white Gaussian noise. However, when the target has a rough surface, the SMI signal is more disturbed by the speckle effect, which is multiplicative noise resulting in random amplitude modulation than the additive noise. Many other applications such as lasers, optics, or Doppler radar must also deal with multiplicative noise [131]. To precisely estimate the Doppler frequency in SMI, the interpolation curve should account for the shape of spectral broadening.

For a single speckle, the fundamental signal of the SMI signal is modeled the same as the signal in LDV, which has the form of

$$s(t_i) = a \exp[-\eta(t_i - t_a)^2] \cos(2\pi f_D t_i + \phi_0) + h(t_i), \tag{4.32}$$

where a is the maximum signal amplitude at the arrive time t_a, η is related to the inverse of the residence time squared, f_D is the Doppler frequency, ϕ_0 is the phase associated with the signal, and $h(t_i)$ is the noise. The DFT of the signal given in (4.32) is [144]

$$\begin{aligned} X(s(t_i))(f_k) =& \frac{A f_s}{2} \sqrt{\frac{\pi}{\eta}} \exp\Bigg(- \frac{\pi^2 (f_D - f_k)^2}{\eta} \\ & + j\left[2\pi(f_D - f_k)t_a + \phi_0\right] \Bigg). \end{aligned} \tag{4.33}$$

and the PSD in the spectral line k is

$$P(f_k) = A_P \exp\left[-\eta_P (f_k - f_D)^2\right], \tag{4.34a}$$

$$A_P = \frac{\pi f_s a^2}{2\eta N}, \tag{4.34b}$$

$$\eta_P = \frac{2\pi^2}{\eta}, \tag{4.34c}$$

where $k = 0, 1, ..., N/2$, $f_k = k f_s / N$, f_s is the sampling frequency, and N is the record length.

In the case of measuring the solid surface, the SMI signal is the sum of several signals, which can be written as

$$\begin{aligned} s(t_i) &= \sum_{m=1}^{M} s_m(t_i) \\ &= \sum_{m=1}^{M} a_m \exp[-\eta(t_i - t_{a_m})^2] \cos(2\pi f_{D_m} t_i + \phi_m). \end{aligned} \tag{4.35}$$

According to (4.5), the DFT of (4.35) is written as

$$X(h) = \sum_{m=1}^{M} \sum_{k=0}^{N-1} s_m(k) \exp\left(-j\frac{2\pi}{N}hk\right), \tag{4.36}$$

where $k = 0, 1, 2, \cdots, N-1$. According to (4.34a), the PSD generated by a single speckle is a Gaussian distribution centered at the Doppler frequency. The sum of several Gaussian distributed PSDs centered at the Doppler frequency is still a Gaussian distribution,

$$P(f_k) = A_{Pm} \exp\left[-\eta_{Pm}(f_k - f_D)^2\right], \tag{4.37}$$

where $k = 0, 1, ..., N/2$.

For a centered burst with a Gaussian envelope, according to (4.34a), the PSD of the SMI velocity signal is a Gaussian distribution centered at the Doppler frequency. Taking the logarithm of the PSD, a parabolic curve can be derived. Therefore, the Doppler frequency can be obtained by fitting a parabolic curve using the spectral peak and several adjacent spectral lines. The logarithm of (4.37) can be expressed as

$$\ln\left[P(f_k)\right] = \ln(A_{Pm}) - \eta_{Pm}(f_k - \hat{f}_D)^2. \tag{4.38}$$

Assuming that the spectral peak is at frequency f_{k0}. Subtracting the corresponding PSD of f_{k0+n} and f_{k0-n} by the PSD of f_{k0}, respectively, we have

$$\ln\left[\frac{P(f_{k_0+n})}{P(f_{k_0})}\right] = \eta_P(f_{k_0+n} - \hat{f}_D)^2 - \eta_P(f_{k_0} - \hat{f}_D)^2, \tag{4.39a}$$

$$\ln\left[\frac{P(f_{k_0-n})}{P(f_{k_0})}\right] = \eta_P(f_{k_0-n} - \hat{f}_D)^2 - \eta_P(f_{k_0} - \hat{f}_D)^2. \tag{4.39b}$$

Subtract (4.39b) by (4.39a)

$$\begin{aligned} &\ln\left[\frac{P(f_{k_0-n})}{P(f_{k_0})}\right] - \ln\left[\frac{P(f_{k_0+n})}{P(f_{k_0})}\right] \\ =&\eta_P(f_{k_0-n} - \hat{f}_D)^2 - \eta_P(f_{k_0+n} - \hat{f}_D)^2 \\ =&\eta_P(f_{k_0-n} + f_{k_0+n} - 2\hat{f}_D)(f_{k_0-n} - f_{k_0+n}). \end{aligned} \tag{4.40}$$

Add (4.39b) to (4.39a) is

$$\begin{aligned} &\ln\left[\frac{P(f_{k_0-n})}{P(f_{k_0})}\right] + \ln\left[\frac{P(f_{k_0+n})}{P(f_{k_0})}\right] \\ =&\eta_P\Big[(f_{k_0-n} + f_{k_0} - 2\hat{f}_D)(f_{k_0-n} - f_{k_0}) + \\ &(f_{k_0+n} + f_{k_0} - 2\hat{f}_D)(f_{k_0+n} - f_{k_0})\Big]. \end{aligned} \tag{4.41}$$

The frequencies f_{k_0-n}, f_{k_0}, and f_{k_0+n} can be expressed as $f_{k_0-n} = (k_0 - n)\Delta f$, $f_{k_0} = k_0\Delta f$, $f_{k_0+n} = (k_0 + n)\Delta f$, where $\Delta f = f_s/N$, representing the spectral lined spacing for the FFT. Thus, (4.40) and (4.41) can be written as

$$\ln\left[\frac{P(f_{k_0-n})}{P(f_{k_0})}\right] + \ln\left[\frac{P(f_{k_0+n})}{Pf_{k_0}}\right] = 2n^2\Delta f^2\eta_P. \tag{4.42}$$

$$\ln\left[\frac{P(f_{k_0-n})}{P(f_{k_0})}\right] - \ln\left[\frac{P(f_{k_0+n})}{P(f_{k_0})}\right] = -2n\Delta f(2k_0\Delta f - 2\hat{f}_D)\eta_P. \tag{4.43}$$

Divide (4.43) by (4.42)

$$\frac{\ln\left[\frac{P(f_{k_0-n})}{P(f_{k_0})}\right] - \ln\left[\frac{P(f_{k_0+n})}{P(f_{k_0})}\right]}{\ln\left[\frac{P(f_{k_0-n})}{P(f_{k_0})}\right] + \ln\left[\frac{P(f_{k_0+n})}{P(f_{k_0})}\right]} = -\frac{2(k_0\Delta f - \hat{f}_D)}{n\Delta f}. \tag{4.44}$$

The Doppler frequency estimated with parabola fit is

$$\hat{f}_D = k_0\Delta f + n\Delta f\frac{\ln\left[\frac{P(f_{k_0-n})}{P(f_{k_0})}\right] - \ln\left[\frac{P(f_{k_0+n})}{P(f_{k_0})}\right]}{2\left\{\ln\left[\frac{P(f_{k_0-n})}{P(f_{k_0})}\right] + \ln\left[\frac{P(f_{k_0+n})}{P(f_{k_0})}\right]\right\}} \tag{4.45}$$

$$= k_0\Delta f + \frac{n\Delta f}{2}\frac{\ln\left[\frac{P(f_{k_0-n})}{P(f_{k_0+n})}\right]}{\ln\left[\frac{P(f_{k_0-n})P(f_{k_0+n})}{P(f_{k_0})^2}\right]}. \tag{4.46}$$

Zero-padding is another method used to enhance the estimating accuracy of the frequency of spectral peaks. It simply adds zeros at the end of the time-domain signal to increase its length. This is useful for resolving ambiguities and reducing the quantization errors when estimating the spectral peaks.

4.4.4 Simulative evaluation

To evaluate the performance of the methods mentioned in the preceding section, simulations are carried out to estimate the frequency of sinusoids and the simulated SMI signals.

Figure 4.15 shows the estimated frequency error of sinusoids using the FFT and rectangular interpolation (FR), FFT and Hanning interpolation (FH), and FFT and parabolic

fit (FP). Since the errors of the FFT method are much larger than other methods with interpolation, they are not drawn in the figure. The sinusoids are noise-free signals with frequencies from 200 Hz to 3 kHz. The sampling frequency is 10 kHz, and the signal length is $N = 128$. The error is given by

$$\text{Error} = \frac{\hat{f} - f_0}{f_r} \times 100\%, \tag{4.47}$$

where the $\hat{f}$ is the estimated frequency, f_0 is the actual frequency, and f_r is the measurement range. It is clear to see in Figure 4.15 that the error estimated using the FH method is superior to the other two methods. The error estimated using the FR method is better than the FP method in the range of 1.7 kHz to 3 kHz, but in the range of 200 Hz to 1.7 kHz, the error of using the FR method is much larger at some points. In the whole range, the error of using the FP method is within 0.04%.

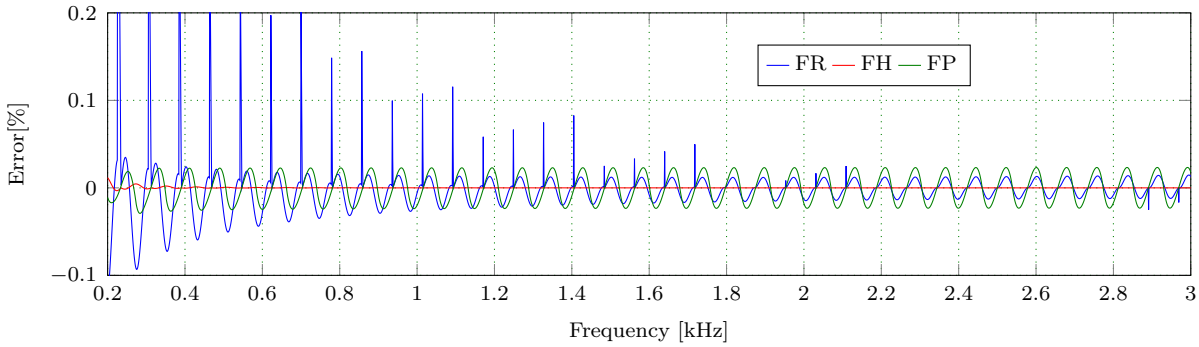

Figure 4.15: Estimated frequency error of sinusoids using the FR, FH, and FP methods.

The maximum absolute error (MAAE) and the RMSE of estimated frequency in Figure 4.15 are listed in Table 4.1. The MAAE and the RMSE of the FFT method are much larger than other methods, while the FH method is superior to the FR and FP methods.

The SMI signal working under weak feedback regime is simulated using (4.35) and an example of the simulated signal is shown in Figure 4.16. The signal frequency is 1 kHz, and the sampling frequency is 10 kHz. The modulated amplitude of signal caused by the multiplicative noise is seen in Figure 4.16. The corresponding power/frequency of the signal obtained using the FFT and the Gaussian window is shown in Figure 4.17.

Figure 4.18 shows the estimated frequency error of simulated SMI signals using the FR, FH, and FP methods. The frequencies of the SMI signals are from 200 Hz to 3 kHz. The sampling frequency is 10 kHz, and the length of the signal is $N = 128$. The MAAE and the RMSE of signals in Figure 4.18 are listed in Table 4.1. It can be seen that the frequency estimation performance of the FR method is the worst, and the MAAE and RMSE obtained by the FP method are better than the FFT and FH methods.

The time range of the signal for processing in Figure 4.15 and Figure 4.18 is $0 \sim (N-1)T_s$, where T_s is the sampling period. It should be noted that, unlike the sinusoid

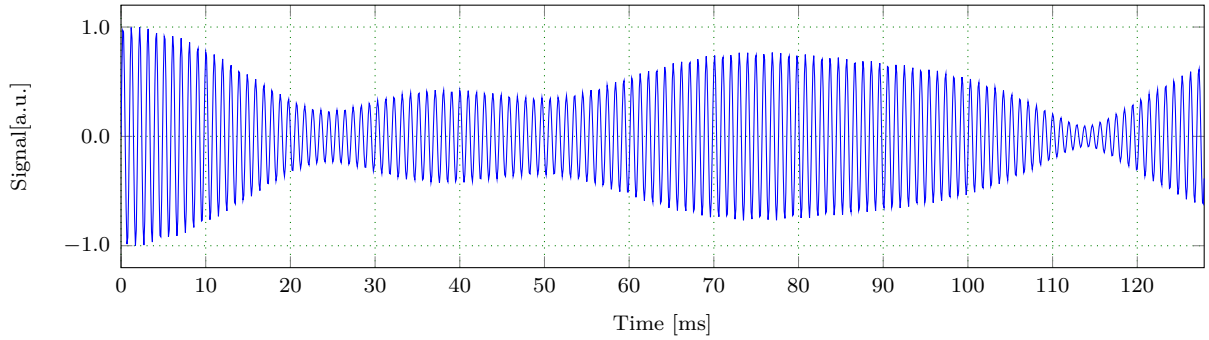

Figure 4.16: An example of the simulated SMI signal.

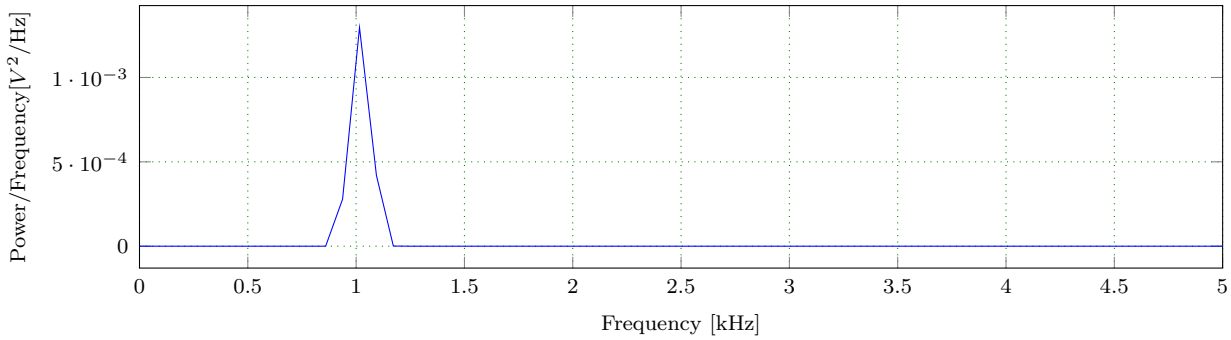

Figure 4.17: The corresponding power/frequency of the signal in Figure 4.16.

that the estimated frequencies are almost the same in any part of the time-domain signal, the estimated frequencies using different time range of the SMI signal are different because of the modulated amplitude. Therefore, the performance of the FFT method being better than the FR is obtained in Table 4.1. To compare the performance of these methods, the normalized root-mean-square error (NRMSE) of the mentioned methods in different frequencies are shown in Fig 4.19. Each NRMSE is achieved with 50 estimated frequencies that are obtained using the signal in the time range of $(n-1)T_s \sim (n-1+N)T_s, n = 1, 2, 3 \ldots 50$. Because the errors of the FFT method are much larger than other methods, they are not drawn in the figure. We can roughly notice that the bias of the NRMSE using the FR methods is larger than the other two methods. When we look closely at the figure, it can be seen that the NRMSE of the FP is slightly smaller than the FH. To clearly compare the results of different methods, the MAAE and the root mean square (RMS) value of the NRMSE, $\text{RMS}_{\text{NRMSE}}$, are listed in Table 4.2. In the case of the sinusoid, the MAAE and $\text{RMS}_{\text{NRMSE}}$ of the FH are still superior to the FR and FP methods. The MAAE is almost the same as the MAAE in Table 4.1. In the case of the SMI signal, the MAAE is totally different in Table 4.1 and Table 4.2. The MAAE and $\text{RMS}_{\text{NRMSE}}$ are the smallest when the FP method is employed. The difference between the results of the pure sinusoid signal and the simulated SMI signal is due to the broadening of the main lobe caused by the superposition of the multi-frequency signal in the SMI signal. It proves that the multiplicative noise resulting from the speckle effect has a great effect on the estimated Doppler frequency.

For frequency estimation of a signal composed of a single frequency, the frequency

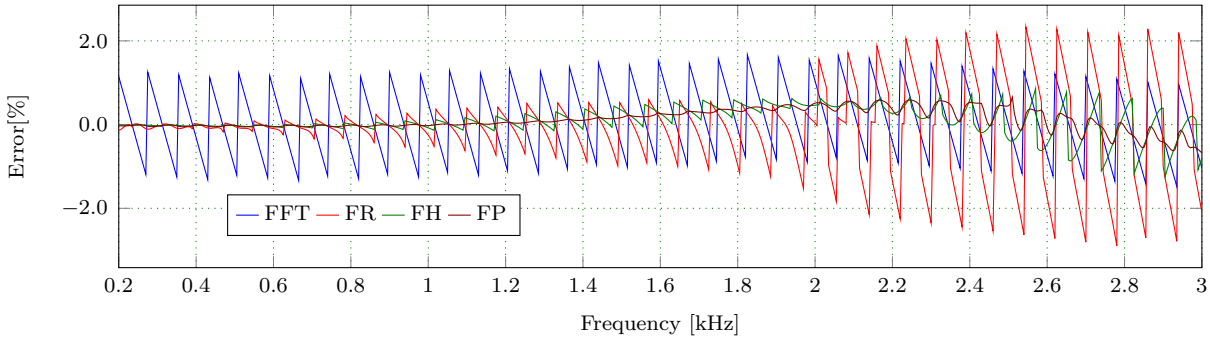

Figure 4.18: Estimated frequency error of SMI signals using the FR, FH, and FP methods.

Table 4.1: Estimated frequency errors of sinusoids and SMI signals using the FFT, FR, FH, and FP methods in noise-free condition.

	Sinusoid		SMI	
	MAAE(%)	RMSE(Hz)	MAAE(%)	RMSE(Hz)
FFT	1.32	22.5	1.68	23.5
FR	0.53	1.02	2.91	30.3
FH	0.01	0.02	1.25	10.3
FP	0.03	0.50	0.67	8.25

resolution is limited by the Cramér–Rao Lower Bound (CRLB), which applies to the variance of frequency estimation for an unbiased estimator. The CRLB is given by [145]

$$\delta_{CR}{}^2 = \frac{3{f_s}^2}{\pi^2 \rho N(N^2-1)}, \tag{4.48}$$

where ρ is the SNR, f_s is the sampling frequency, and N is the record length.

An essential factor in this comparative study is the noise sensitivity of the different methods. In practice, the measurement is always distorted by external noise sources, and the frequency estimation itself becomes a random variable that can be characterized by its mean value and its standard deviation. Some methods are biased, which means that the mean value is different from the actual value. To compare the overall quality of these methods, the NRMSE is used, which takes into account the bias as well as the uncertainty on the estimate given by its standard deviation.

Figure 4.20 shows the NRMSEs using different methods to estimate the frequency of a single sinusoid in different noise condition. The noise is white Gaussian. The actual frequency of the signal is $f = 1.1$ kHz. All the frequencies are calculated with the record length of $N = 128$. The FFT without any interpolation is still the least effective method. The increase of SNR cannot improve NRMSEs when the FFT method is used, because of the resolution of FFT is limited by the record length. It is seen that the NRMSEs of FH decrease linearly with the increase of SNR once SNR$>$ 2 dB. In the whole range (SNR$>$ 2 dB), the FH method has a good NRMSE that is close to the CRLB. When SNR$<$ 20 dB,

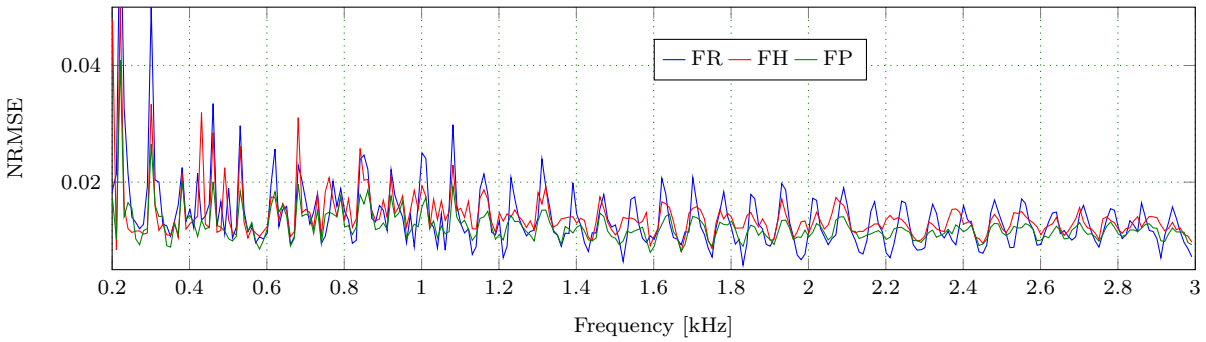

Figure 4.19: NRMSEs of estimated frequency of SMI signals using the FR, FH, and FP methods.

Table 4.2: Estimated errors and RMS values of the NRMSEs of sinusoids and SMI signals in noise-free condition using the FFT, FR, FH, and FP methods.

	Sinusoid		SMI	
	MAAE	$\text{RMS}_{\text{NRMSE}}$	MAAE	$\text{RMS}_{\text{NRMSE}}$
FFT	1.31	29.6×10^{-3}	4.62	33.0×10^{-3}
FR	0.49	3.20×10^{-3}	5.08	15.1×10^{-3}
FH	0.01	1.16×10^{-4}	4.20	14.8×10^{-3}
FP	0.03	6.9×10^{-3}	3.66	12.6×10^{-3}

the NRMSEs of FP method are equivalent to the FH method, but after SNR> 40 dB, the NRMSEs of the FP method are not able to be improved as the SNR increases. The NRMSEs of FR are worse than the other two methods as SNR<23 dB, which illustrates that the FR is not suitable for estimating the frequency of a sinusoid with low SNR.

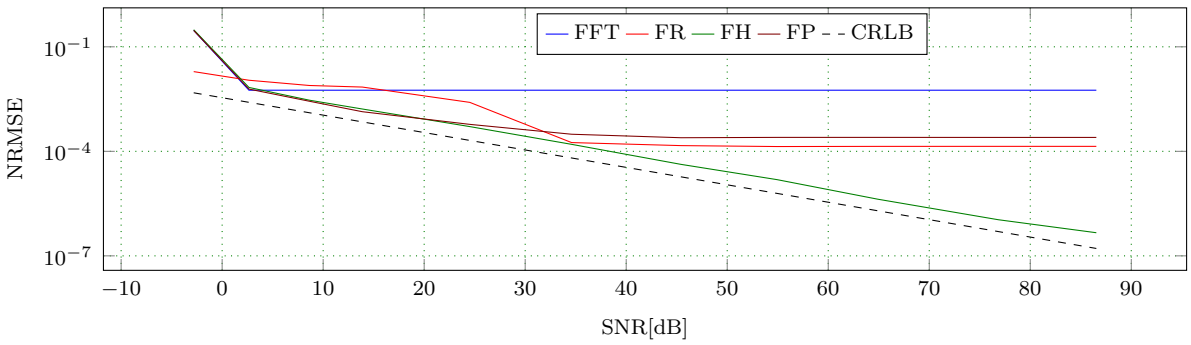

Figure 4.20: NRMSEs of estimated frequency of sinusoids using different methods in different noise condition.

Figure 4.21 presents the NRMSEs using different methods to estimate the frequency of SMI signals in different noise condition. The noise is white Gaussian. The frequency of the signal is $f_D = 1.1$ kHz. Since the purpose is to find a good solution to accurately estimate the Doppler frequency when the signal is interfered by the inevitable multiplicative noise in the experiment, the multiplicative noise is not considered as noise when calculating the SNR in Figure 4.21. As can be seen in Figure 4.17, this kind of noise cannot being

distinguished in most cases when the length of the sampling data is insufficient. In Figure 4.21, the white Gaussian noise has a small impact on NRMSE after 10 dB. When the SNR is larger than 20 dB, the NRMSEs cannot be improved with the increase of the SNR. The NRMSE of the FP method is better than the other three methods, and the NRMSE of the FH is slightly better than the FR method.

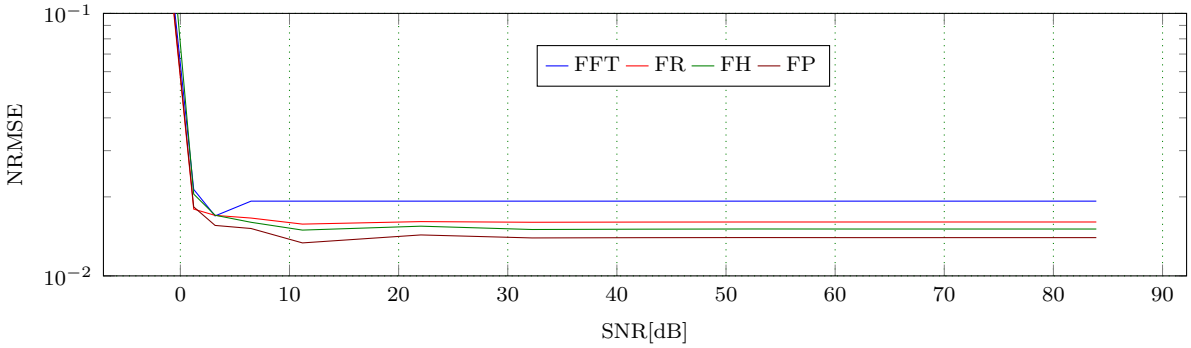

Figure 4.21: NRMSEs of estimated frequency of SMI signals using different methods in different noise condition.

In general, the FH interpolation method is more applicable for sinusoid that is not interfered by adjacent frequencies. In the case of SMI signals corrupted by the speckle effect that leads to spectral broadening, the FP method is a better solution.

4.4.5 Experimental evaluation

In this section, experiments are conducted to compare the global performance of the methods presented in the previous sections. The sensor head used to measure velocity consists of a commercial 785 nm laser diode and a collimation lens. The distance between the sensor head and the target surface is about 9.5 mm and the incident angle θ is 60°. The target is a white covered disc with the diameter of 40 mm attached on the shaft of the servo motor, of which the rotary speed is controlled by the feedback of a 21 bits optical encoder. To obtain a good velocity reference, the motor is performed to have constant rotary speed. The SMI signal modulated by the back-scattering light is acquired by time tracing the small variation of the optical power with the built-in photo-diode. The photocurrent from the photo-diode consists of a direct current bias and the SMI signal. The photocurrent is converted into voltage for further processing, and the DC bias is removed from the signal with the HPF. Since the SMI signal is extraordinarily small, the operation amplifier should have much lower offset voltage and noise. After the TIA, the filter, and the amplifier circuits, the signal is digitized for further processing. The velocity measurements are performed over the velocity range from 3 rpm (6.28 mm/s) to 400 rpm (837 mm/s).

Figure 4.22 shows an example of the time-domain SMI signal. The SMI works under weak feedback regime. The speckle phenomenon is observed as a random amplitude that

strongly modulates the SMI fringes.

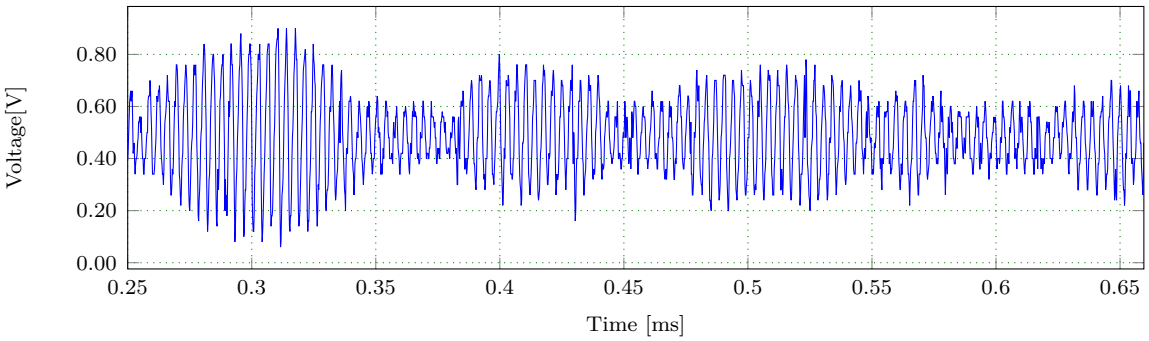

Figure 4.22: An example of the experimental SMI signal.

Figure 4.23 shows the estimated Doppler frequencies versus the rotational speed using FFT, FR, FH, and FP methods. Each frequency is the average value of 40 Doppler frequencies. Estimated Doppler frequencies using the FR, FH, and FP methods show has a quite good linear relationship with the rotational speed, while the estimated frequency using the FFT method has a very poor linearity. The errors of estimated frequencies, referring to (4.47), are shown in Figure 4.24. Since the error of the FFT method is much larger than other methods, it is not drawn in Figure 4.24. The maximum errors of FFT, FR, FH, and FP methods in Figure 4.24 are 1.61%, 0.42%, 0.35%, and 0.28%, respectively.

The NRMSEs of the estimated frequencies using different methods are listed in Table 4.3. Figure 4.25 shows the NRMSEs of frequency estimation using different methods. The FP method has a slightly better NRMEs than the FH interpolation method. This demonstrates that the FP method is also applicable to estimate the Doppler frequency of the SMI signal.

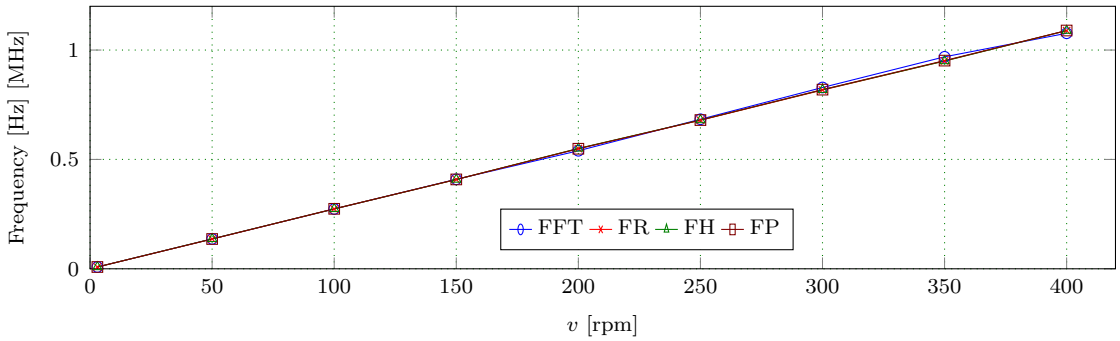

Figure 4.23: Estimated Doppler frequencies using the FFT, FR, FH, and FP methods versus the rotational speed.

4.4.6 Conclusion

This section compares the performance of different FFT interpolation methods for estimating the Doppler frequency of SMI signals. Several results of applying these methods

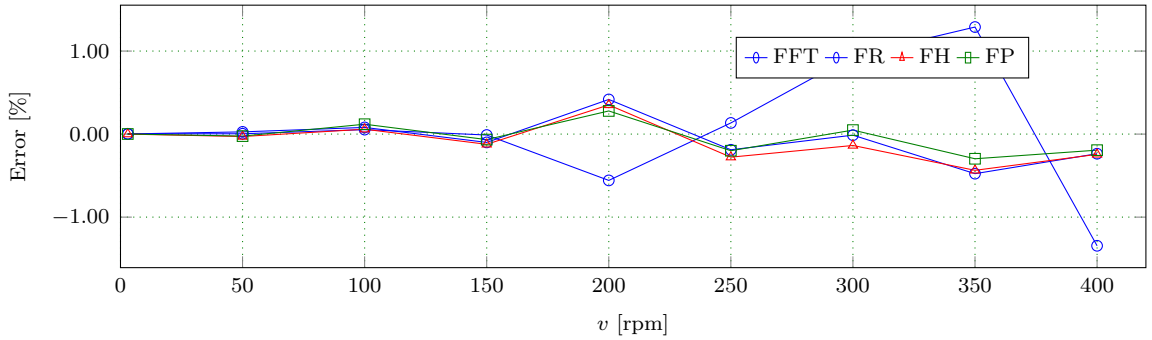

Figure 4.24: Errors of estimated Doppler frequencies using the FFT, FR, FH, and FP methods versus the rotational speed.

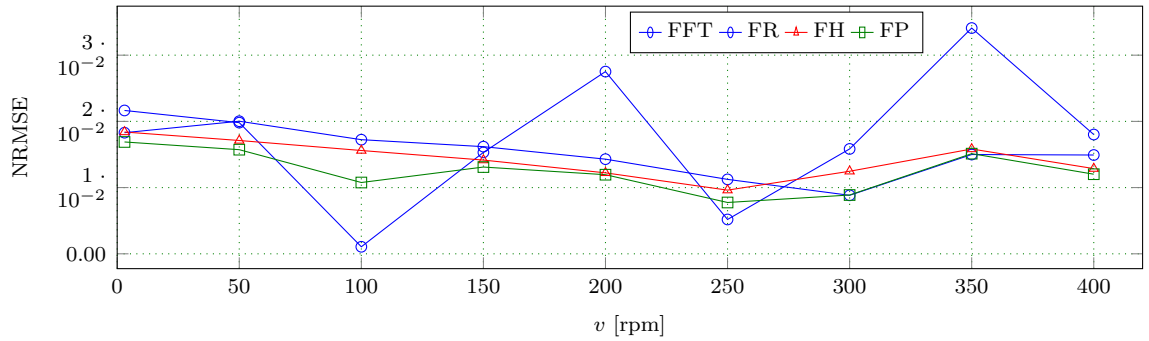

Figure 4.25: NRMSEs of estimated Doppler frequencies using the FFT, FR, FH, and FP methods versus the rotational speed.

Table 4.3: NRMSEs of estimated frequency versus rotational speed.

Speed (rpm)	FFT	FR	FH	FP
3	21.6×10^{-3}	18.3×10^{-3}	18.4×10^{-3}	16.9×10^{-3}
50	19.8×10^{-3}	20.0×10^{-3}	17.1×10^{-3}	15.7×10^{-3}
100	1.1×10^{-3}	17.2×10^{-3}	15.6×10^{-3}	10.8×10^{-3}
150	15.3×10^{-3}	16.2×10^{-3}	14.2×10^{-3}	13.1×10^{-3}
200	27.5×10^{-3}	14.3×10^{-3}	12.2×10^{-3}	11.9×10^{-3}
250	5.2×10^{-3}	11.2×10^{-3}	9.6×10^{-3}	7.8×10^{-3}
300	15.8×10^{-3}	8.8×10^{-3}	12.5×10^{-3}	8.9×10^{-3}
350	34.1×10^{-3}	15.0×10^{-3}	15.8×10^{-3}	15.1×10^{-3}
400	18.0×10^{-3}	14.9×10^{-3}	12.9×10^{-3}	12.0×10^{-3}

on a set of simulated signals have been compared to verify their performance. The experimental results proved the conclusion of the simulation and demonstrated that the parabolic fit method can estimate the frequency of SMI signals.

The SMI sensor has the advantages of small feature size and low cost. One big issue is the existence of multiplicative noise, making the estimation of Doppler frequency difficult. A suitable and efficient digital signal processing method should be developed. The parabolic fit method considers the Gaussian distribution of the time-domain signal

and the spectral broadening of the frequency-domain signal. It provides a slightly better estimation of the Doppler frequency than the FR and FH methods. Other good solutions for precisely estimating the Doppler frequency are needed for further investigation.

4.5 Maximum likelihood estimation of Doppler frequency

The main goal of this section is to study the quality of Doppler frequency estimation of the SMI signal by using the MLE. The MLE is a method to estimate parameters of a statistical model given observations. It provides the estimated parameters by finding the parameter values that maximize the likelihood. In general, the MLE has the asymptotic properties of being unbiased, achieving the CRLB, and having a Gaussian probability density function (PDF). Therefore, it can be said that it is asymptotically optimal.

The signal model regarding the SMI in the weak feedback regime, as given in (4.32), can be considered as a Trigonometric with modulated amplitude [146, 147]. The MLE method is practical when the SMI signal has a broad spectrum broadening that makes it difficult to estimate the accurate Doppler frequency. The SMI signal could be regarded as a stationary Gaussian random process, assuming that except for one or more parameters, its power spectrum is known. In this section, a parameter method based on the MLE optimizing the estimated parameters by an iterative procedure is presented.

4.5.1 Theory of maximum likelihood estimation

The first step is to mathematically model the data to determine a good estimator. Assuming a N-point data set $\{x[0], x[1], \ldots, x[N-1]\}$ that depends on an unknown parameter θ. Because the data is inherently random, it is described by its PDF, $p(x[0], x[1], \ldots, x[N-1]; \theta)$. If $N = 1$ and θ denotes the mean, the PDF is written as

$$p(x[0];\theta) = \frac{1}{(2\pi\sigma^2)^{1/2}} \exp\left[-\frac{1}{2\sigma^2}(x[0]-\theta)^2\right]. \tag{4.49}$$

According to the model of SMI signal given in (4.32), the MLE is defined with the parameters $\boldsymbol{\theta} = [A, \eta, t_a, f_D, \phi_0, h(t_i)]^T$ that maximizes the likelihood function. Generally, the MLE has the asymptotic properties of being unbiased, achieving CRLB for high SNR and having the PDF [148]:

$$p(\boldsymbol{x};\boldsymbol{\theta}) = \frac{1}{(2\pi\sigma^2)^{N/2}} \exp\left[-\frac{1}{2\sigma^2}\sum_{n=0}^{N-1}(x_n - s_n)^2\right], \tag{4.50}$$

where $\boldsymbol{x} = [x[0], x[1], \ldots, x[N-1]]^T$. It is clear that the value of $\boldsymbol{\theta}$ affects the probability, therefore, the value of $\boldsymbol{\theta}$ could be able to be inferred from the observed value $\boldsymbol{x}$. Assuming the Gaussian observations $\boldsymbol{x} \sim \mathcal{N}(\boldsymbol{\mu}(\boldsymbol{\theta}), \mathbf{C}(\boldsymbol{\theta}))$, then the PDF can be written as [148]

$$p(\boldsymbol{x};\boldsymbol{\theta}) = \frac{1}{(2\pi)^{N/2}\det^{1/2}[\mathbf{C}(\boldsymbol{\theta})]} \exp\left[-\frac{1}{2}(\boldsymbol{x}-\boldsymbol{\mu}(\boldsymbol{\theta}))^T\mathbf{C}^{-1}(\boldsymbol{\theta})(\boldsymbol{x}-\boldsymbol{\mu}(\boldsymbol{\theta}))\right], \tag{4.51}$$

where $\boldsymbol{\mu}(\boldsymbol{\theta})$ is the $N \times 1$ mean vector and $\mathbf{C}(\boldsymbol{\theta})$ is the $N \times N$ covariance matrix. The PDF is termed as a likelihood function when it is viewed as a function of $\boldsymbol{\theta}$ with $\boldsymbol{x}$ fixed. The natural logarithm of the likelihood of $\boldsymbol{\theta}$ is defined as

$$\Gamma(\boldsymbol{x};\boldsymbol{\theta}) = \ln[p(\boldsymbol{x};\boldsymbol{\theta})]. \tag{4.52}$$

The maximum likelihood estimate $\hat{\boldsymbol{\theta}}$ is the value that maximizes the logarithm $\Gamma(\boldsymbol{x};\boldsymbol{\theta})$. Generally, it can be found explicitly by solving the equation,

$$\frac{\partial\Gamma(\boldsymbol{x};\boldsymbol{\theta})}{\partial\boldsymbol{\theta}} = 0. \tag{4.53}$$

4.5.2 Asymptotic expression

It is difficult to evaluate the MLE of the Doppler frequency in the time domain since a large dimension covariance matrix in (4.51) needs to be inverted. Another approximation method can be used with the power spectrum, which is a known function of the parameter $\boldsymbol{\theta}$, when the random process is stationary, Gaussian, and zero mean. Almost any wide sense stationary Gaussian random process $x[n]$ may be modeled as the output of a causal linear shift invariant filter with a narrow band-pass frequency response $H(f)$ driven at the input by white Gaussian noise $\mu[n]$. With these assumptions, $x[n]$ can be written as [148]

$$x[n] = \sum_{k=0}^{\infty} h[k]\mu[n-k], \tag{4.54}$$

where $h[0] = 1$. The only condition is that the PSD should satisfy

$$\int_{f_1}^{f_2} \ln P(f)df > -\infty. \tag{4.55}$$

The signal PSD is contained in the $[f_1, f_2]$ interval.

The PSD of $x[n]$ is

$$P(f) = |H(f)|^2\sigma_\mu^2, \tag{4.56}$$

where σ_μ^2 is the variance of $\mu[n]$, $H(f) = \sum_{k=0}^{\infty} h[k]\exp(-j2\pi fk)$.

If N is larger, the representation is approximated by

$$x[n] = \sum_{k=0}^{n} h[k]\mu[n-k], \tag{4.57}$$

Therefore, $\boldsymbol{x}$ can be written as

$$\boldsymbol{x} = \underbrace{\begin{bmatrix} h[0] & 0 & 0 & \dots & 0 \\ h[1] & h[0] & 0 & \dots & 0 \\ \vdots & \vdots & \vdots & \ddots & \vdots \\ h[N-1] & h[N-2] & h[N-3] & h[N-3] & \dots h[0] \end{bmatrix}}_{\mathbf{H}} \boldsymbol{\mu}, \tag{4.58}$$

where $\mathbf{H}$ has a determinant of $(h[0])^N = 1$, thus it is invertible. Because $\boldsymbol{\mu} \sim \mathcal{N}(\mathbf{0}, \sigma_\mu^2 \mathbf{I})$, the PDF of $\boldsymbol{x}$ is $\mathcal{N}(\mathbf{0}, \sigma_\mu^2 \mathbf{H}\mathbf{H}^\mathbf{T})$, that is [148]

$$p(\boldsymbol{x}; \boldsymbol{\theta}) = \frac{1}{(2\pi)^{N/2} \det^{1/2}(\sigma_\mu^2 \mathbf{H}\mathbf{H}^\mathbf{T})} \exp\left[-\frac{1}{2} \boldsymbol{x}^T (\sigma_\mu^2 \mathbf{H}\mathbf{H}^\mathbf{T})^{-\mathbf{1}} \mathbf{x}\right]. \tag{4.59}$$

Because

$$\det(\sigma_\mu^2 \mathbf{H}\mathbf{H}^\mathbf{T}) = \sigma_\mu^{\mathbf{2N}} \det^{\mathbf{2}}(\mathbf{H}) = \sigma_\mu^{\mathbf{2N}}, \tag{4.60}$$

$$\boldsymbol{x}^T (\sigma_\mu^2 \mathbf{H}\mathbf{H}^\mathbf{T})^{-\mathbf{1}} \mathbf{x} = \frac{\mathbf{1}}{\sigma_\mu^{\mathbf{2}}} \boldsymbol{\mu}^\mathbf{T} \boldsymbol{\mu}, \tag{4.61}$$

then,

$$p(\boldsymbol{x}; \boldsymbol{\theta}) = \frac{1}{(2\pi\sigma_\mu^2)^{N/2}} \exp\left(-\frac{1}{2\sigma_\mu^2} \boldsymbol{\mu}^T \boldsymbol{\mu}\right). \tag{4.62}$$

By the Parseval's theorem

$$\begin{aligned} \frac{1}{\sigma_\mu^2} \boldsymbol{\mu}^T \boldsymbol{\mu} &= \frac{1}{\sigma_\mu^2} \sum_{n=0}^{N-1} \mu^2[n] \\ &= \int_{f_1}^{f_2} \frac{|X(f)|^2}{P(f)} df. \end{aligned} \tag{4.63}$$

And

$$\ln \sigma_\mu^2 = \int_{f_1}^{f_2} \ln \sigma_\mu^2 df = \int_{f_1}^{f_2} \ln P(f) df - \int_{f_1}^{f_2} \ln |H(f)|^2 df. \tag{4.64}$$

Because $\int_{f_1}^{f_2} \ln |H(f)|^2 df = 0$, we have

$$\ln \sigma_\mu^2 = \int_{f_1}^{f_2} \ln P(f) df. \tag{4.65}$$

Finally, the asymptotic log PDF is [148]

$$\ln p(\boldsymbol{x}; \boldsymbol{\theta}) = -\frac{N}{2} \ln 2\pi - \frac{N}{2} \int_{f_1}^{f_2} \ln P(f) df - \frac{1}{2} \int_{f_1}^{f_2} \frac{|X(f)|^2}{P(f)} df. \tag{4.66}$$

The approximate $\hat{\boldsymbol{\theta}}$ could be found by maximizing the approximate log likelihood function

$$\Gamma(\boldsymbol{x};\boldsymbol{\theta}) = -\frac{1}{2}\int_{f_1}^{f_2}\left[N\ln P(f) + \frac{I(f)}{P(f)}\right]df, \tag{4.67}$$

where $I(f)$ is the PSD obtained with the periodogram method,

$$I(f) = \frac{1}{N}\left|\sum_{n=0}^{N-1} x[n]\exp(-j2\pi fn)\right|^2, \tag{4.68}$$

and the dependence of $\Gamma(\boldsymbol{x};\boldsymbol{\theta})$ on $\boldsymbol{\theta}$ is through the PSD $P(f)$.

4.5.3 Doppler frequency estimation

In the case of Doppler frequency estimation, the equation has the form of

$$\Gamma(\boldsymbol{x}; f_D) = -\frac{1}{2}\left[N\int_{f_1}^{f_2}\ln P(f)df + \int_{f_1}^{f_2}\frac{I(f)}{P(f)}df\right], \tag{4.69}$$

where f_D is the Doppler frequency. Assume that for all f_D, $P(f_1) = P(f_2)$, then the first integral in (4.69) is independent of f_D. Therefore, the maximization of (4.69) could be obtained by minimizing

$$\Psi(f; f_D) = \int_{f_1}^{f_2}\frac{I(f)}{P(f)}df. \tag{4.70}$$

The minimization of (4.70) cannot be obtained directly. But it can be accomplished with the Newton-Raphson or scoring method. This leads to an iterative procedure that optimizes the estimated parameters.

The asymptotic value of the CRLB has the expression [148]

$$\begin{aligned} var(\hat{\boldsymbol{\theta}}) &\geq \left[\frac{N}{2}\int_{f_1}^{f_2}\left(\frac{\partial P(f)}{\partial\boldsymbol{\theta}}\Big/P(f)\right)^2 df\right]^{-1} \\ &= \left[\frac{N}{2}\int_{f_1}^{f_2}\left(\frac{\partial\ln P(f)}{\partial\boldsymbol{\theta}}\right)^2 df\right]^{-1}. \end{aligned} \tag{4.71}$$

And in the case of Doppler frequency estimation, the CRLB is [149]

$$\begin{aligned} var(\hat{f}_D) &\geq \left[\frac{N}{2}\int_{f_1}^{f_2}\left(\frac{dP(f)}{df_D}\Big/P(f)\right)^2 df\right]^{-1} \\ &= \left[\frac{N}{2}\int_{f_1}^{f_2}\left(\frac{d\ln P(f)}{df_D}\right)^2 df\right]^{-1}. \end{aligned} \tag{4.72}$$

According to the CRLB, the lack of knowledge of the PSD amplitude does not affect the estimation variance of the Doppler frequency when the assuming $P(f_1) = P(f_2)$ holds.

The FFT algorithm is a typical way for Doppler frequency estimation when the spectrum broadening is small. In this section, it focuses on the condition that the signal has a broad spectrum broadening, and the FFT algorithm could not accurately estimate the Doppler frequency anymore. Figure 4.26 shows the processing steps of velocity measurement with the MLE method. The initial Doppler frequency is estimated by finding the maximum peak of the spectrum from the FFT algorithm. To minimize the MLE function in equation (4.70), the derivative is taken and set equal to zero, and it attempts to solve this equation iteratively,

$$g(f; f_D) = \frac{\partial \Psi(f; f_D)}{\partial f} = 0. \tag{4.73}$$

The Doppler frequency obtained with the spectrum is considered as the initial value f_{D0}. If $g(f; f_D)$ is approximately linear near f_{D0}, we have

$$g(f_D) \approx g(f_{D0}) + \left.\frac{dg(f_D)}{df}\right|_{f_D=f_{D0}} (f_D - f_{D0}). \tag{4.74}$$

With the iterative procedure, the Doppler frequency minimizing (4.70) could be obtained. However, it may not be the global minimum, but possibly only a local minimum. To avoid this problem, it is essential to determine the initial point close to the global minimum. The optimized Doppler frequency is then used to obtain the velocity v through (2.63).

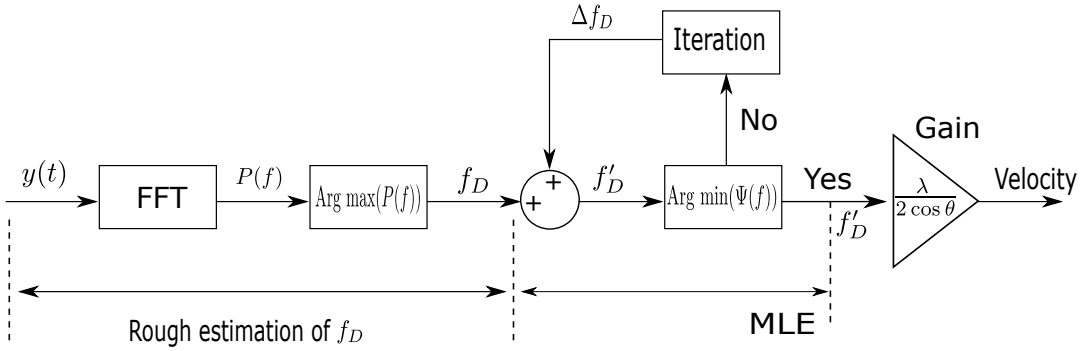

Figure 4.26: Processing steps of velocity measurement with the MLE method.

4.5.4 Performance evaluation

To illustrate the global performance of the method, Monte-Carlo simulations are carried out with SMI signals obtained from (4.32). Following, the experimental results are presented as well.

To verify the ability of the MLE method to estimate the Doppler frequency of the SMI signal, 100 Monto-Carlo runs are used. The actual Doppler frequency is 1000 Hz. For each run, the Doppler frequency is obtained by the MLE. In the simulation, the Newton-Raphson method is used to accomplish the numerical minimization. The RMSE of the Doppler frequency using different methods versus the number of samples N is displayed in Figure 4.27. The MLE method has a much smaller RMSE than the FFT and FH methods for long data record lengths. The FH method is more accurate than the FFT method for short data record lengths. As the value of N is larger than 1024, the RMSEs of the FH method and the FFT method are very similar.

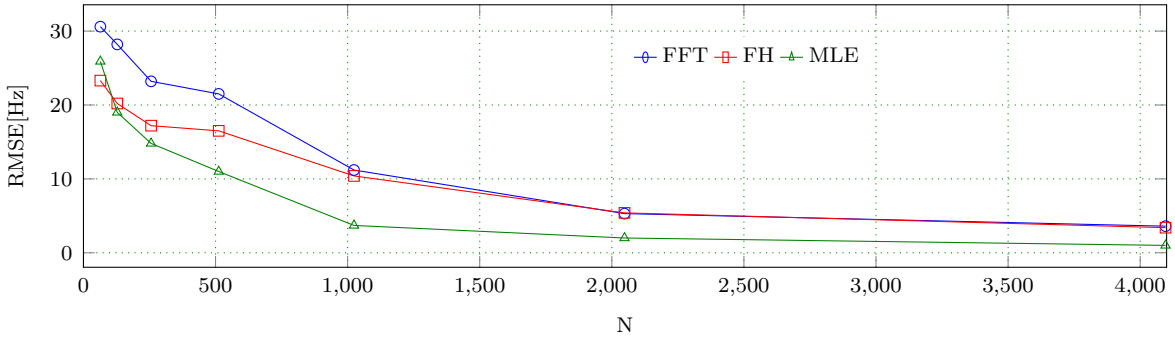

Figure 4.27: RMSEs of the estimated Doppler frequency with different methods versus number of samples.

Table 4.4, Table 4.5, and Table 4.6 show the RMSEs of estimating different frequencies using different methods. The record data lengths are $N = 256$, $N = 512$, and $N = 1024$, respectively. It can be seen that the RMSEs of the MLE method, RMSE_{MLE}, are smaller than the RMSEs of the other two methods for different data record lengths. With the increase of the record length, the difference between the RMSE_{MLE} and RMSE_{FH} is more significant. The RMSEs of the FH method, RMSE_{FH}, are smaller than RMSEs of the FFT method, RMSE_{FFT}, as $N = 256$ and $N = 512$, while the RMSEs of these two methods are quite similar in the case of $N = 1024$.

Table 4.4: RMSEs of estimated frequencies using different methods, $N = 256$.

f_0(Hz)	RMSE_{FFT}(Hz)	RMSE_{FH}(Hz)	RMSE_{MLE}(Hz)
500	34.0	11.5	11.5
1000	20.6	17.1	13.0
1500	27.0	22.6	18.0
2000	44.3	27.2	22.0
2500	25.9	28.2	19.1
3000	18.0	14.1	4.0

The sensor head applied to measure velocity consists of a commercial 785 nm laser diode and a collimation lens. The target is a white covered disc with the diameter of 40 mm attached on a servo motor, of which the rotary speed is controlled by the feedback of a 21 bits optical encoder. To obtain a good velocity reference, the motor is performed to

Table 4.5: RMSEs of estimated frequencies using different methods, $N = 512$.

f_0(Hz)	RMSE_{FFT}(Hz)	RMSE_{FH}(Hz)	RMSE_{MLE}(Hz)
500	11.9	9.5	6.8
1000	23.2	16.5	10.9
1500	20.2	16.4	10.5
2000	20.8	19.4	8.8
2500	5.5	19.1	7.9
3000	26.4	26.3	10.7

Table 4.6: RMSEs of estimated frequencies using different methods, $N = 1024$.

f_0(Hz)	RMSE_{FFT}(Hz)	RMSE_{FH}(Hz)	RMSE_{MLE}(Hz)
500	11.2	6.6	4.8
1000	11.2	10.3	3.7
1500	12.0	12.0	4.0
2000	12.1	12.1	5.1
2500	0.0	18.6	1.8
3000	18.0	14.1	4.1

have constant rotating speed. The self-mixing signal modulated by the back-scattering light was acquired by time tracing the small variation of optical power with the built-in photo-diode.

Figure 4.28 shows the Doppler frequencies of the SMI signal and their relative errors versus velocities. This relative error is calculated as the subtraction of the estimated velocity and the actual velocity divided by the measurement range of velocity. It can be seen that Doppler frequencies obtained with all three methods are roughly linear to the velocities. The errors in Figure 4.28 clearly show that the errors obtained by the MLE method are superior to the other two methods. The errors of the MLE method are within 0.5%, while the errors of FFT and FH are within 1.1% and 0.8%, respectively.

To further compare the results of the estimated velocities, the RMSEs of the estimated frequency using different methods are shown in Figure 4.29. The RMSEs of the MLE method are much smaller than the FFT and FH methods. The results of the FFT and FH are similar, and the FH method is only slightly better than the FFT method.

4.5.5 Conclusion

The FFT algorithm is a typical way for Doppler frequency estimation when the spectrum broadening is small. In this section, it focuses on the condition that the signal has a broad spectrum broadening. A parameter method based on the MLE is presented. It

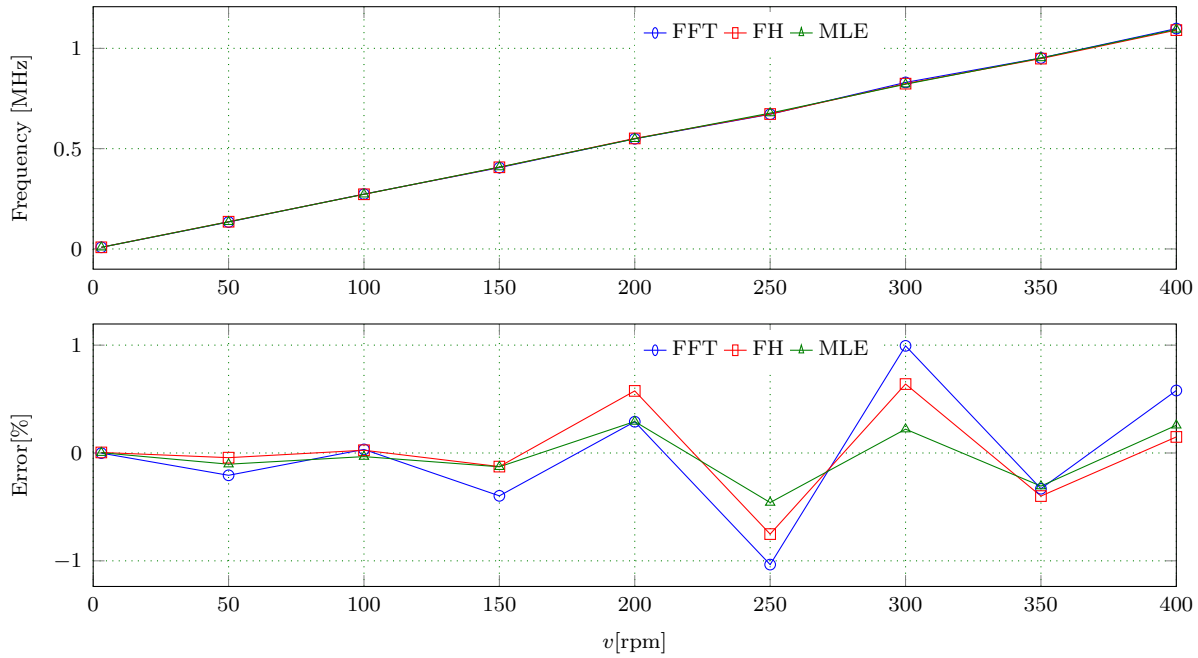

Figure 4.28: The estimated Doppler frequency and the estimated error versus velocities.

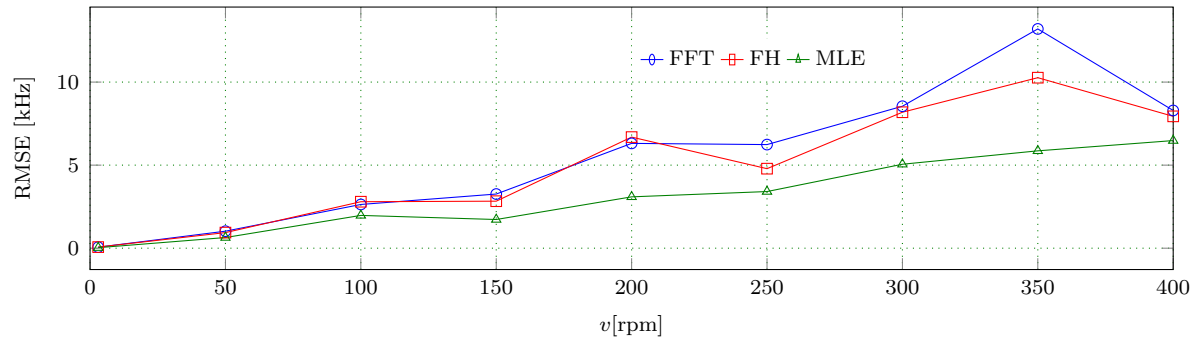

Figure 4.29: RMSEs of the estimated Doppler frequency versus velocities.

optimizes the estimated parameters by an iterative procedure, thus generates an accurate estimation. The parameter optimization is implemented in the frequency domain, and it is also possible to perform it in the correlation domain. The comparison of the FFT method, FH method, and MLE method clearly shows that the RMS frequency error and relative error of the MLE method are better than the other two methods.

Although the MLE method for Doppler frequency estimation could obtain better accuracy, the iterative procedure is time-consuming. That's why it is presently not widely applied. However, it has great potential. With the speed and flexibility of digital signal processors increase, the MLE method could be implemented efficiently for Doppler frequency estimation of SMI in the future.

4.6 Extended Kalman filter

4.6.1 Introduction

The interpolation methods and MLE method for accurate Doppler frequency estimation were introduced in previous sections. They are both the spectral analysis methods based on the use of N points FFT. The main disadvantage of the classic spectral estimation techniques is in the distorting impact of the inherent windowing of the finite data set. This remark is important because the velocimeter application requires a high-precision estimation of the Doppler frequency. Therefore, a long data sequence is required.

In this section, to reduce the record length needed in traditional FFT based methods, an algorithm based on the EKF for velocity measurement using the SMI is proposed. Based on the model of the self-mixing interference signal, the multiplicative noise caused by the speckle effect and the direction of the velocity are taken into account. The numerical simulations illustrate that this parametric method can track the velocity and discriminate the direction of the velocity without any other calculation or modulation, even when the feedback level is weak. The SMI sensor working under weak feedback is tested in comparison with a commercial velocimeter.

The Doppler frequency of the SMI signal gives only the absolute value of the velocity, but not the sign of the velocity. Based on the direction of the inclination of the power fringe, the direction of motion can be determined. The usually used method is to differentiate the SMI signal, and the sign of the differentiation discriminates the direction. However, in practice, some effects impact the signal (such as the speckle effect and weak feedback level), making it challenging to obtain the direction. Tsukuda proposed another method in 1994. The direction was successfully discriminated using the triangular current modulation of the laser diode in a velocity range of 4-30 mm/s [89]. In 2004, G. Plantier et al. proposed a second-order adaptive linear predictor filter, which enables to track the digital instantaneous Doppler frequency [150]. A model of the output signal of the laser diode was reported, which showed that the sensor and its associated algorithm have a global first-order low-pass transfer function with a cutoff frequency expressed as a function of the speckle perturbations, the SNR, and the mean Doppler frequency.

This section aims to design a velocity estimation method based on the model of the SMI that can measure the target speed with a sign using only one optical channel without any additional modulation. Accordingly, the parametric method based on the EKF is proposed to estimate the velocity and its direction based on the model of SMI signal.

This section is organized as follows: the theory of the EKF and its application for estimating velocity from the SMI signal are discussed in Section 4.6.2 and Section 4.6.3. Following, Section 4.6.4 and Section 4.6.5 show the simulative and experimental results using the developed EKF method to confirm its effectiveness. Finally, concluding remarks

are summarized in Section 4.6.6.

4.6.2 Theoretical equations

The EKF is widely used in many areas of signal processing, control, and optimization, such as estimation [151, 152], adaptive filtering, prediction, robust control, state observation, system identification, target tracking, training of neural networks [153]. The EKF is an extension of the KF, which was firstly introduced by R.E. Kalman [154] as a recursive solution to the discrete-data linear filter problem. It is characterized by fast convergence and robustness in most cases. To reduce the number and complexity of the numerical calculations, the EKF has been proposed to estimate the Doppler frequency [155, 156]. EKF targets to minimize the covariance of the state estimation error of a nonlinear system. It is an optimum filter when the system uncertainties and measurement noises exist.

For linear systems, the dynamics matrix, measurement matrix, and fundamental matrix of the systems are all linear. However, these matrices of the EKF may be nonlinear because they depend on the system state estimates. The Riccati equations required for the computation of the Kalman gain are identical to those of the linear case.

The state-space form of a non-linear system is expressed as

$$\dot{\boldsymbol{x}} = f(\boldsymbol{x}, \boldsymbol{\mu}) + \boldsymbol{w}, \tag{4.75}$$

where $\boldsymbol{x} = [x_1, \cdots, x_n]^T \in \mathbb{R}^n$ is a vector of the system states, $f(\boldsymbol{x})$ is a nonlinear function of those states, $\boldsymbol{\mu}$ is the control vector, $\boldsymbol{\mu} = [\mu_1, \cdots, \mu_n]^T \in \mathbb{R}^m$, $n, m \in \mathbb{N}$. $\mathbb{R}$ and $\mathbb{N}$ are real and natural numbers, respectively. $\boldsymbol{w} = [w_1, \cdots, w_n]^T \in \mathbb{R}^n$ is a random zero-mean process described by the process-noise matrix $\mathbf{Q}$, i.e., system modeling uncertainties, which is defined as

$$\varepsilon\left\{\boldsymbol{w}\boldsymbol{w}^T\right\} = \sigma_w^2 = \mathbf{Q}, \tag{4.76}$$

where $\varepsilon\{\}$ denotes the expected value.

The measurement equation of the EKF is considered as a nonlinear function of states,

$$\boldsymbol{y} = h(\boldsymbol{x}) + \boldsymbol{v}, \tag{4.77}$$

where $\boldsymbol{y} = [y_1, \cdots, y_m]^T \in \mathbb{R}^m$ is the measurement vector, $\boldsymbol{v} = [v_1, \cdots, v_m]^T \in \mathbb{R}^m$ is a zero-mean random process.

The measurement-noise matrix $\mathbf{R}$ describing the random noise $\boldsymbol{v}$ is given by

$$\mathbf{R} = \sigma_v^2 = \varepsilon\left\{\boldsymbol{v}\boldsymbol{v}^T\right\}. \tag{4.78}$$

$\boldsymbol{w}$ and $\boldsymbol{v}$ are assumed to be independent (i.e., $\varepsilon\{\boldsymbol{ww}\} = \mathbb{O}^{n\times m}$, while $\varepsilon\{\boldsymbol{w}\} = \mathbb{O}^n$ and $\varepsilon\{\boldsymbol{v}\} = \mathbb{O}^m$) and with normal probability distributions (i.e.,$\mathcal{P}(X_i) = \frac{1}{\delta X_i\sqrt{2\pi}} \exp\frac{-(\varepsilon\{X_i\}-X_i)^2}{2\delta_X^2}$, with $\delta_X^2 = \varepsilon\{(\varepsilon\{X_i\} - X_i)^2\}$, and $X_i \in \{\boldsymbol{w}, \boldsymbol{v}\}$), $\mathcal{P}\{\cdot\}$ represents the distribution calculation.

In the discrete system, the nonlinear measurement equation can be written as

$$\boldsymbol{y_k} = h(\boldsymbol{x}_k) + \boldsymbol{v}_k. \tag{4.79}$$

The state transition model is

$$\boldsymbol{x}_k = f(\boldsymbol{x}_{k-1}, \boldsymbol{\mu}_k) + \boldsymbol{w}_k. \tag{4.80}$$

The estimation error is defined as

$$\boldsymbol{\zeta}_k = \boldsymbol{y}_k - \hat{\boldsymbol{y}}_k, \tag{4.81}$$

where $\hat{\boldsymbol{y}}_k$ is the estimated state.

Since the system and measurement equations are nonlinear, a first-order approximation is used to define the state transition and observation matrices by the following Jacobians [157]

$$\mathbf{F}_k = \left.\frac{\partial f(\boldsymbol{x}, \boldsymbol{\mu})}{\partial \boldsymbol{x}}\right|_{x=\hat{x}_k} = \begin{bmatrix} \frac{\partial f_1}{\partial x_1} & \frac{\partial f_1}{\partial x_2} & \cdots & \frac{\partial f_1}{\partial x_n} \\ \frac{\partial f_2}{\partial x_1} & \frac{\partial f_2}{\partial x_2} & \cdots & \frac{\partial f_n}{\partial x_n} \\ \vdots & \vdots & \ddots & \vdots \\ \frac{\partial f_n}{\partial x_1} & \frac{\partial f_n}{\partial x_n} & \cdots & \frac{\partial f_n}{\partial x_n} \end{bmatrix}, \tag{4.82}$$

$$\mathbf{H}_k = \left.\frac{\partial h(\boldsymbol{x})}{\partial \boldsymbol{x}}\right|_{x=\hat{x}_k} = \begin{bmatrix} \frac{\partial l_1}{\partial x_1} & \frac{\partial l_1}{\partial x_2} & \cdots & \frac{\partial l_1}{\partial x_n} \\ \frac{\partial h_2}{\partial x_1} & \frac{\partial h_2}{\partial x_2} & \cdots & \frac{\partial h_n}{\partial x_n} \\ \vdots & \vdots & \ddots & \vdots \\ \frac{\partial h_n}{\partial x_1} & \frac{\partial h_n}{\partial x_n} & \cdots & \frac{\partial h_n}{\partial x_n} \end{bmatrix}. \tag{4.83}$$

To facilitate understanding and simplify the algorithm description, a recursive algorithm including the implementation instruction for a generalized nonlinear system is listed in Algorithm 3, where $\mathbf{P}_k$ is a covariance matrix representing errors in the state estimates after an update and $\mathbf{P}_k^-$ is the covariance matrix representing errors in the state estimates before an update. Because the functions f and h are nonlinear functions of the state estimates, the Kalman gain cannot be computed off-line. The whole process of EKF involves two sub-processes, which are prediction and correction. In the prediction step,

the current state variables are estimated along with their uncertainties. Once the next measurement that is corrupted with some amount of error is observed, these estimates are updated using a weighted average. The EKF is recursive and can run in real-time, using only the present input measurements and the previously calculated state and its uncertainty matrix, no additional past information is required.

If the dynamic model of a linear KF matches the real world, the covariance matrix $\mathbf{P}_k$ can be used not only to calculate the Kalman gain, but also to provide a prediction of the error in the state estimates. The EKF does not offer such guarantees, in fact, the EKF covariance matrix may indicate excellent performance when the filter performance is poor or even broken. A basic feature of the EKF is that the Jacobian $\mathbf{H}_k$ in the equation of the Kalman gain $\mathbf{K}_k$ serves to correctly propagate or "magnify" only the relevant components of the measurement information. For example, if there is no one-to-one mapping relationship between the measurement $\boldsymbol{y}_k$ and the state through the function h, then the Jacobian $\mathbf{H}_k$ affects the Kalman gain, so it will only magnify the portion of the residual $\boldsymbol{y}_k - h(\hat{\boldsymbol{x}}_k)$ that does affect the state.

function EKF($\boldsymbol{x}, \boldsymbol{\mu}, k$)
  if $k = 0$ **then**
    State initialization: $\hat{x}_0, P_0 = diag, k = 1$;
  end if
  if $k > 1$ **then**
    Prediction:
    Predicted state estimate, $\hat{\boldsymbol{x}}_k^- = f(\hat{\boldsymbol{x}}_{k-1}, \boldsymbol{u}_{k-1})$;
    System Jacobian matrix calculation, $\mathbf{F} = \frac{\partial \boldsymbol{f}(\boldsymbol{x},\boldsymbol{u})}{\partial \boldsymbol{x}}\Big|_{\boldsymbol{x}=\hat{\boldsymbol{x}}_k^-}$;
    Predicted state covariance, $\mathbf{P}_k^- = \mathbf{F}\mathbf{P}_{k-1}\mathbf{F}^T + \mathbf{Q}_k$;
    Measurement Jacobian matrix calculation, $\mathbf{H} = \frac{\partial \boldsymbol{h}(\boldsymbol{x},\boldsymbol{u})}{\partial \boldsymbol{x}}\Big|_{\boldsymbol{x}=\hat{\boldsymbol{x}}_k^-}$;
    Correction:
    Optimal Kalman gain, $\mathbf{K}_k = \mathbf{P}_k^-\mathbf{H}^T\left(\mathbf{H}\mathbf{P}_k^-\mathbf{H}^T + \mathbf{R}_k\right)^{-1}$;
    Corrected state estimate, $\hat{\boldsymbol{x}}_k = \hat{\boldsymbol{x}}_k^- + \mathbf{K}_k\left(\boldsymbol{y}_k - h(\hat{\boldsymbol{x}}_k^-)\right)$;
    Corrected estimate covariance, $\mathbf{P}_k = (\mathbf{I} - \mathbf{K}_k\mathbf{H})\,\mathbf{P}_k^-$;
  end if
    $k = k + 1$;
end function

Algorithm 3: The EKF for nonlinear system.

In practical implementation, the measurement noise covariance $\mathbf{R}$ is usually measured in advance. It is generally possible to measure the measurement error covariance $\mathbf{R}$ by taking some off-line sample measurements. The determination of the process noise covariance $\mathbf{Q}$ is usually tricky, because commonly it is not able to directly observe the process that is estimated. Usually, a superior filter performance can be obtained by tuning the filter parameters $\mathbf{Q}$ and $\mathbf{R}$, and the tuning is generally implemented off-line.

4.6.3 Tracking the self-mixing signal

The analysis of optical feedback in semiconductor lasers relies on the rate equation model published by Lang and Kobayashi in 1980 [64]. The back injected light interferes with the light existing in the laser cavity and changes the threshold condition of semiconductor laser. As a consequence, the emitted power of the semiconductor laser changes as the injected current remains constant while the target is being displaced [63,158]. The emitted power could be expressed as

$$P(t) = P_0 \left[1 + m \cos\left(\phi_F\left(t\right)\right)\right], \tag{4.84}$$

where P_0 is the power emitted by the semiconductor laser without optical feedback, m is the modulation index. According to the equations first derived by Lang and Kobayashi, the theory of SMI has been researched in a massive number of articles. The phase equation can be achieved by (2.55),

$$\phi_F(t) = \phi_0(t) - C \sin\left[\phi_F(t) + \arctan\alpha\right], \tag{4.85}$$

where α is the linewidth enhancement factor and C is the feedback factor.

Since the amplitude and frequency of laser field are modulated by the term $\phi = 2kL$, where $k = 2\pi/\lambda$, the phases are given by

$$\phi_F(t) = 2\pi\nu_F(t)\tau(t) = 2\pi\frac{L_0 + v(t)\Delta t}{\frac{1}{2}\lambda_F(t)}, \tag{4.86}$$

$$\phi_0(t) = 2\pi\nu_0(t)\tau(t) = 2\pi\frac{L_0 + v(t)\Delta t}{\frac{1}{2}\lambda_0(t)}, \tag{4.87}$$

where $\phi_F(t)$ and $\phi_0(t)$ are the phases with and without optical feedback, respectively. $\nu_F(t)$ and $\nu_0(t)$ represent the laser frequencies with and without optical feedback. $\tau(t)$ is the round-trip time delay. $\lambda_F(t)$ and $\lambda_0(t)$ are the laser wavelengths with and without optical feedback. L_0 is the initial distance between the laser and the target. $v(t)$ is the velocity component of the target in the direction of the light beam. These equations eqs. (4.84) to (4.87) are usually used as the signal model to retrieve displacement when SMI is used to measure displacement. Regarding the use of SMI for velocity measurement, the signal can also be considered as a special form of this model, in which the speckle effect modulates the amplitude.

The behavior of laser diodes depends significantly on factor C, whereas the SMI signal is only slightly affected by the factor α. For ordinary lasers, such as gas lasers, the value of the linewidth enhancement factor α is almost equal to zero. The α of usual semiconductor lasers is a positive value from 3 to 7 [57]. Sabina et al. performed some numerical simulations to demonstrate that the factor α does not critically affect the displacement measurement [96]. The effect of the value of α on the estimated displacement will be discussed in detail in the following chapter in Figure 5.3 and Figure 5.13. In the model parameters, α is considered as a constant with the value of 4. Applying the EKF requires

a system model. In this case, the system state to estimate is $\boldsymbol{x} = \begin{bmatrix} A & \phi_F & v & a & C \end{bmatrix}^T$. where A is the amplitude of the signal, ϕ_F is the phase of SMI signal with optical feedback, v and a are the velocity and acceleration of the moving target, and C is the feedback factor. The system transition function can be written as

$$f(\boldsymbol{x}) = \begin{bmatrix} A \\ \phi_F + \frac{1}{1+C\cos(\phi_F + \arctan\alpha)} \\ v + aT_s \\ a \\ C \end{bmatrix}, \tag{4.88}$$

where T_s is the sampling period. The observation function is

$$\mathbf{H} = \begin{bmatrix} \cos(\phi_F) & -A\sin(\phi_F) & 0 & 0 & 0 \end{bmatrix}. \tag{4.89}$$

The partial derivative in the transition matrix is easily evaluated, thereby obtaining the linearized transition matrix

$$\mathbf{F} = \begin{bmatrix} 1 & 0 & 0 & 0 & 0 \\ 0 & \frac{\partial f}{\partial \phi_F} & \frac{\partial f}{\partial v} & \frac{\partial f}{\partial a} & \frac{\partial f}{\partial C} \\ 0 & 0 & Ts & 1 & 0 \\ 0 & 0 & 0 & 1 & 0 \\ 0 & 0 & 0 & 0 & 1 \end{bmatrix}, \tag{4.90}$$

where,

$$\frac{\partial f}{\partial \phi_F} = 1, \tag{4.91}$$

$$\frac{\partial f}{\partial v} = \frac{4\pi T_s}{\lambda[1 + C\cos(\phi_F + \arctan\alpha)]}, \tag{4.92}$$

$$\frac{\partial f}{\partial a} = \frac{4\pi T_s^2}{\lambda[1 + C\cos(\phi_F + \arctan\alpha)]}, \tag{4.93}$$

$$\frac{\partial f}{\partial C} = \frac{-4\pi v T_s \cos(\phi_F + \arctan\alpha)}{\lambda[1 + C\cos(\phi_F + \arctan\alpha)]^2}. \tag{4.94}$$

The initial covariance matrix is chosen that the off-diagonal elements are zero, and the diagonal elements represent the square of the best guess in the errors of the initial estimates. It is a significant step to choose the values of matrices $\mathbf{P}_0$, $\mathbf{Q}$, and $\mathbf{R}$, because they will greatly affect the performance of the EKF and even the convergence.

$\mathbf{P}_0$ represents the covariance (i.e. mean-squared errors) from the initial condition, and it determines the initial amplitude of the transient behavior. It expresses how much the initial estimate of the state $\boldsymbol{x}_0$ is known. Since the coupling effect between the system states is usually neglected, the value of $\mathbf{P}_0$ is often selected as a diagonal matrix.

$\mathbf{Q}$ and $\mathbf{R}$ denote the model accuracy (or model confidence) and measurement noise characters, respectively. A large value of $\mathbf{Q}$ represents that there is considerable uncertainty in the model parameters and will result in a larger Kalman gain (i.e. a faster filter dynamics). On the other hand, a small value of $\mathbf{Q}$ indicates a high degree of confidence in the system model, and may lead to slow measurement update (i.e. slow but smooth filter dynamics). Similarly, the value of $\mathbf{R}$ is enlarged only when the measurement is greatly affected by noise.

In this work, these parameters are selected partially following the guiding principles of the proper parameter selection given in previous articles, and partially through trial and error manner.

4.6.4 Simulation

To illustrate the global performance of the proposed method, numerical simulations are carried out. The initial point of the EKF is important for estimation, therefore, in the simulation, the EKF starts to estimate the velocity only when the signal amplitude is greater than 0.5. Usually, the feedback level is weak in the self-mixing velocimeter, especially when the signal is severely corrupted by multiplicative noise caused by the speckle effect. Therefore, in the simulation, the feedback factor C of the simulated signal is set to 0.3.

Figure 4.30 shows an estimate of a positive square wave velocity under noise-free condition. The signal amplitude is not modulated by the speckle effect , therefore the amplitude is a constant. The results show that the EKF has a very good behavior for tracking the signal, the displacement, and the velocity, even when the inclinations of the fringes are not obvious. After approximate five fringes the estimated velocity is close to the real one. The estimated displacement $\hat{L}$ has a linear relationship with time and is very close to the actual displacement L.

Errors of the estimated displacement δ_L and velocity δ_v are shown in Figure 4.31. It can be seen that the error ΔL of estimated displacement is less than 20 nm. The error δv of estimated velocity is 0.06% after 0.02 ms. This error δv can be further reduced by changing the parameter of EKF but this leads to lower response speed.

To further test the robustness of the proposed method, another case where the actual velocity is negative. We can see from Figure 4.32 that the filter can track the negative displacement $\hat{L}$ and the negative velocity $\hat{v}$. Besides, the directions of the displacement

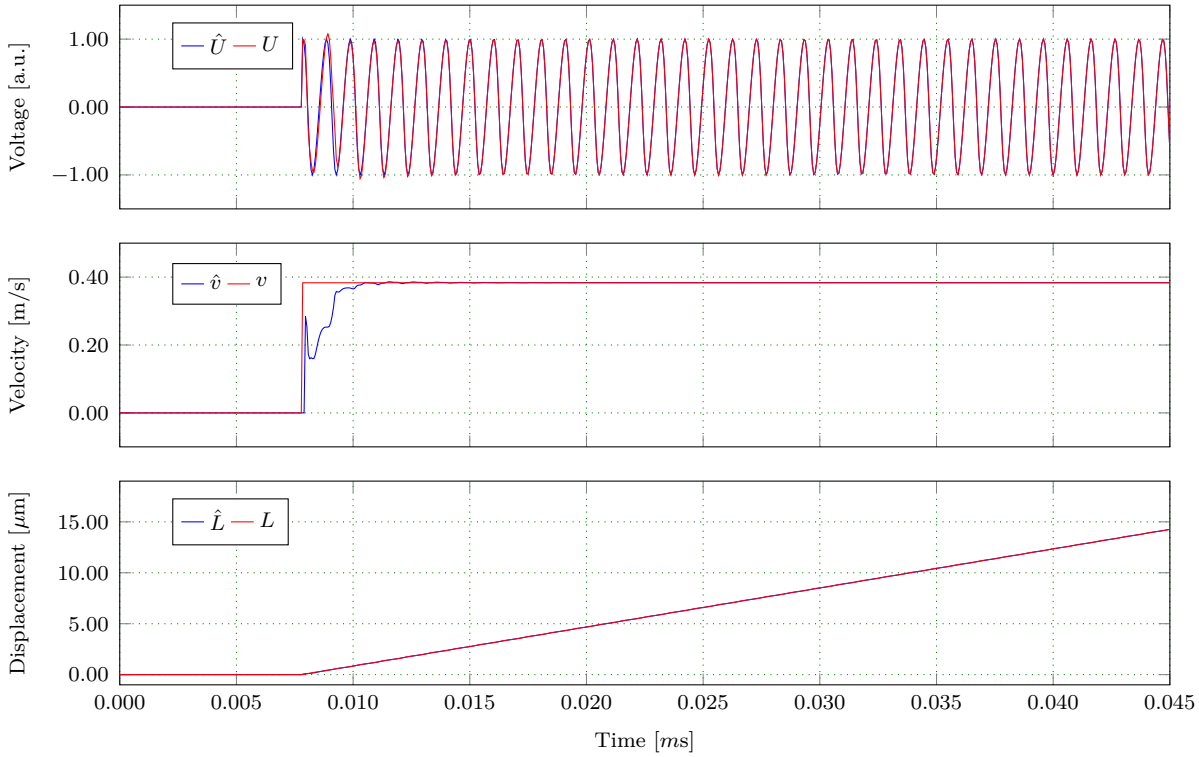

Figure 4.30: Estimation of positive step velocity with a simulated noise-free and unmodulated SMI signal. The $\hat{U}$ and U are tracked signal and ideal signal. $\hat{L}$, L, $\hat{v}$, and v are estimated displacement, ideal displacement, estimated velocity, and ideal velocity, respectively.

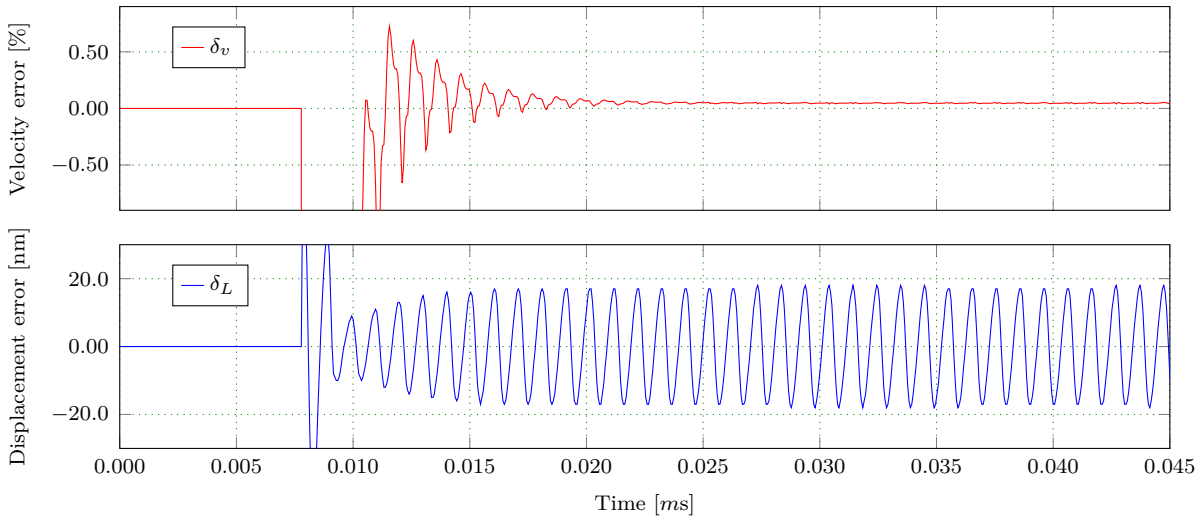

Figure 4.31: Errors of estimated positive velocity in Figure 4.30. δ_L and δ_v are the estimated errors of $\hat{L}$ and $\hat{v}$.

and velocity are correctly discriminated. Estimated errors are shown in Figure 4.33, which indicates that under these circumstances the EKF tracks the negative displacement and the negative velocity fairly rapid and they are approximate to the actual displacement and velocity after around 0.01 ms. The error δ_L of the estimated displacement is less than

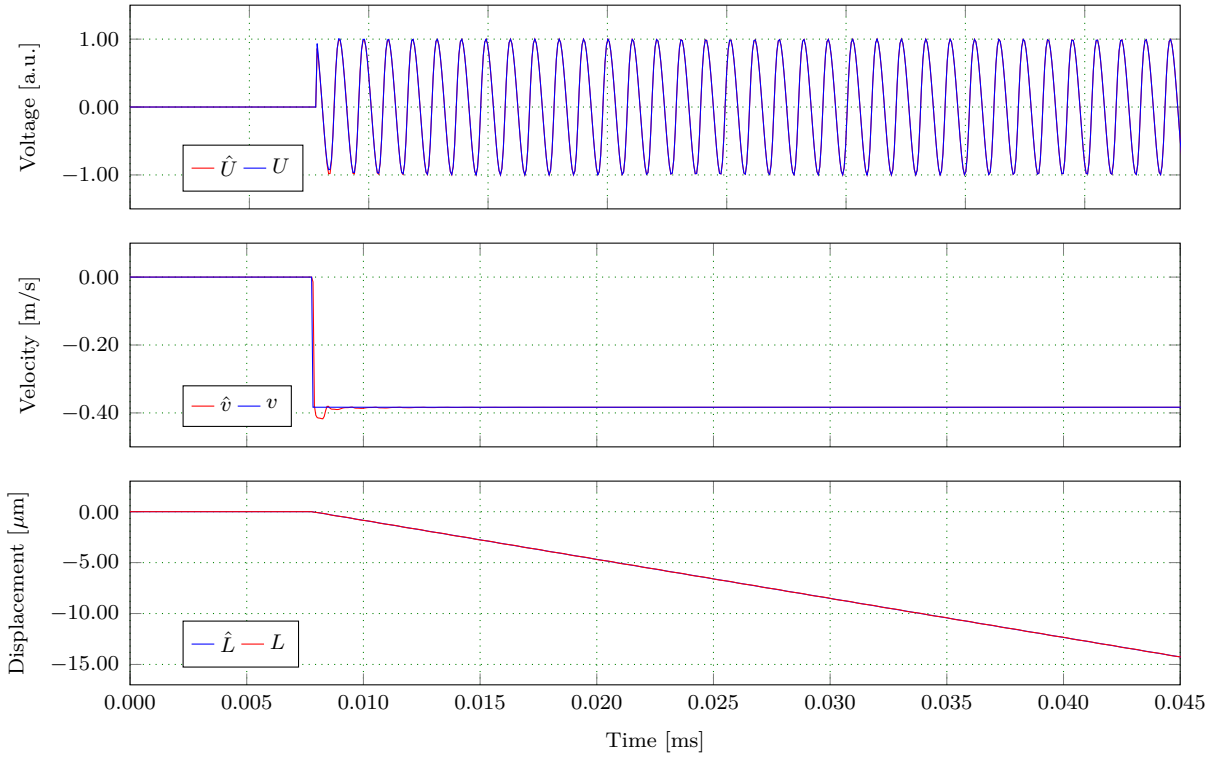

Figure 4.32: Estimation of negative step velocity with a simulated noise-free and unmodulated SMI signal.

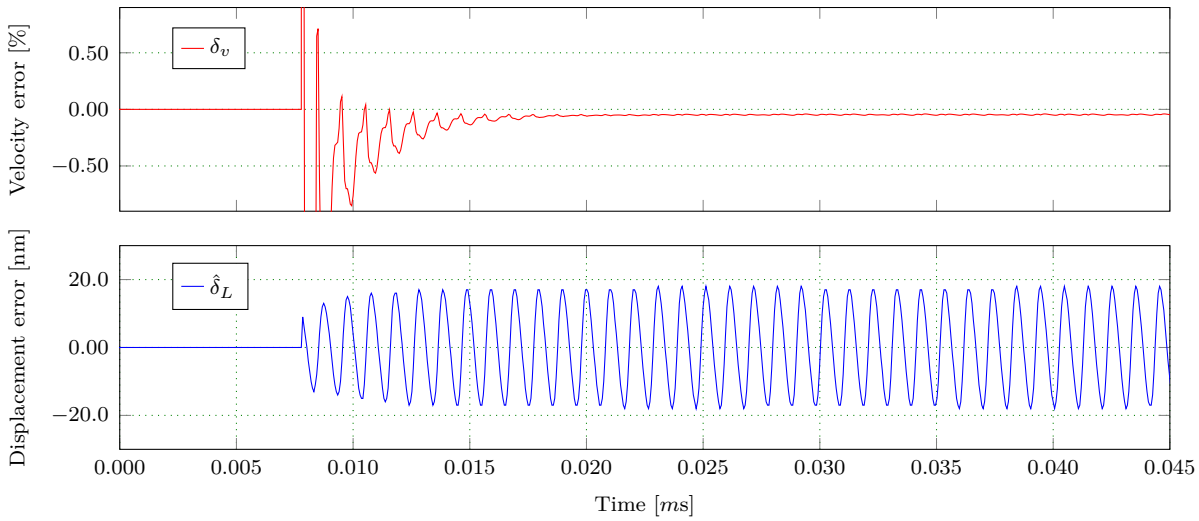

Figure 4.33: Errors of estimated negative velocity in Figure 4.32.

20 nm and the error δ_v of the estimated velocity is about 0.06%. These results are very similar to the positive velocity in Figure 4.30 and Figure 4.31.

In practice, when a rough target back-scatters the coherent light from the laser diode, the SMI signal will be corrupted by the multiplicative noise resulting from the speckle effect. It causes random modulation of the signal amplitude and leads to the loss of the ideal waveform of the signal. Therefore, to further test the characteristics of the EKF,

another case is run in which the noise is added to the signal and the signal amplitude is modulated.

Figure 4.34 shows the estimate results of the positive velocity with noise and amplitude-modulated signal. The multiplicative noise that modulates the amplitude is taken into consideration in the signal model. At first glance, the EKF seems to be working properly and can appropriately track the signal as well as the velocity and the displacement. Errors of estimated displacement and velocity are shown in Figure 4.35. It can be seen that the EKF correctly estimates the positive velocity and displacement. The estimated displacement and velocity are close to the actual values after about 0.01 ms. It is similar to the results of the noise-free condition in Figure 4.31. The error of the estimated displacement is 20 nm, which is the same as the noise-free condition. The error of the estimated velocity is 0.2%, which is worse than the error under ideal condition.

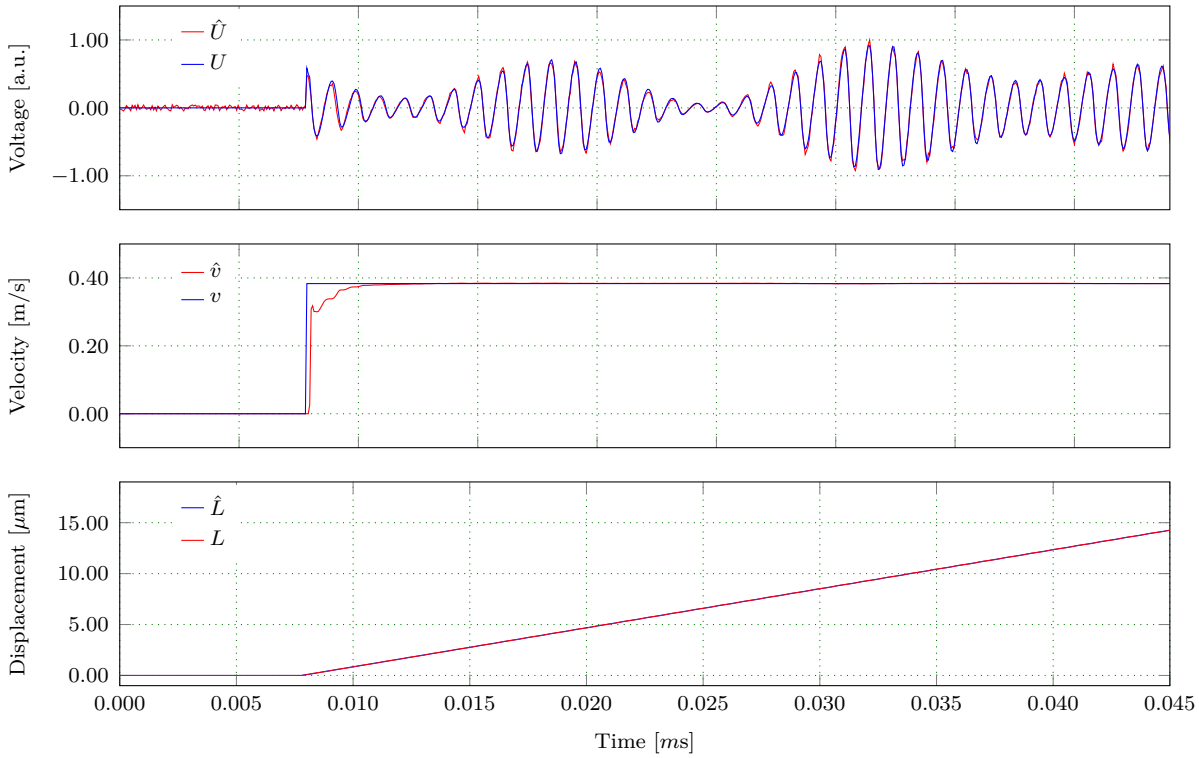

Figure 4.34: Estimation of positive velocity with a simulated noisy signal, of which the amplitude is modulated.

Another case is run where the actual velocity is negative, as can be seen in Figure 4.36. It is observed that the signal amplitude is modulated, and the actual quantities and their estimates are quite close. The direction of the displacement and velocity is determined correctly. The rising time of the estimated step velocity is similar to other cases aforementioned. Errors of estimated displacement and velocity are shown in Figure 4.37. The error δ_L of estimated displacement is 20 nm that is the same as other cases. The error δ_v of the estimated velocity is 0.3%, which is similar to the estimated error in Figure 4.35.

In general, the simulation results demonstrate that the EKF can estimate velocity

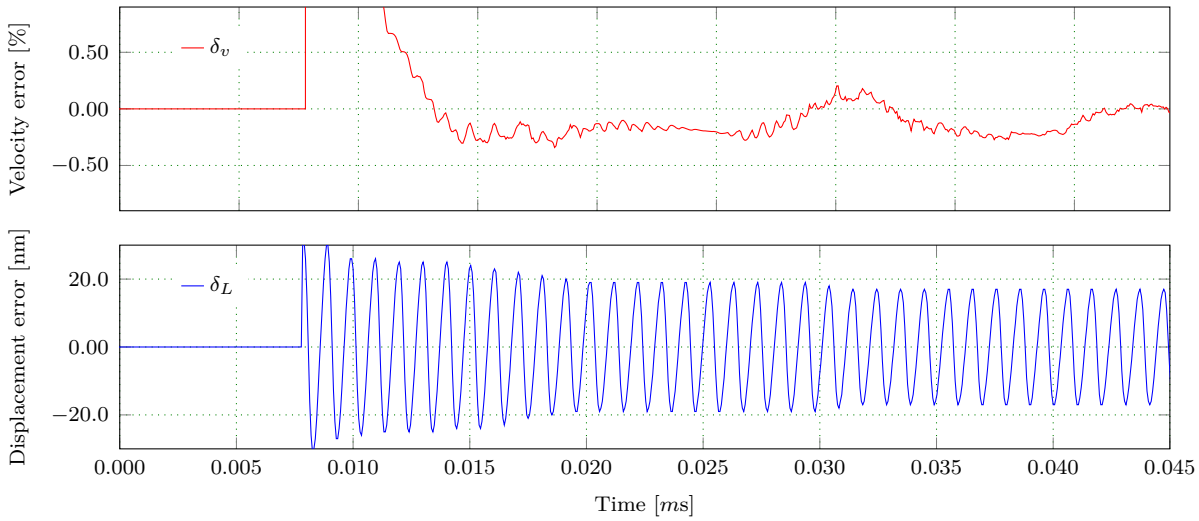

Figure 4.35: Errors of estimated positive velocity in Figure 4.34.

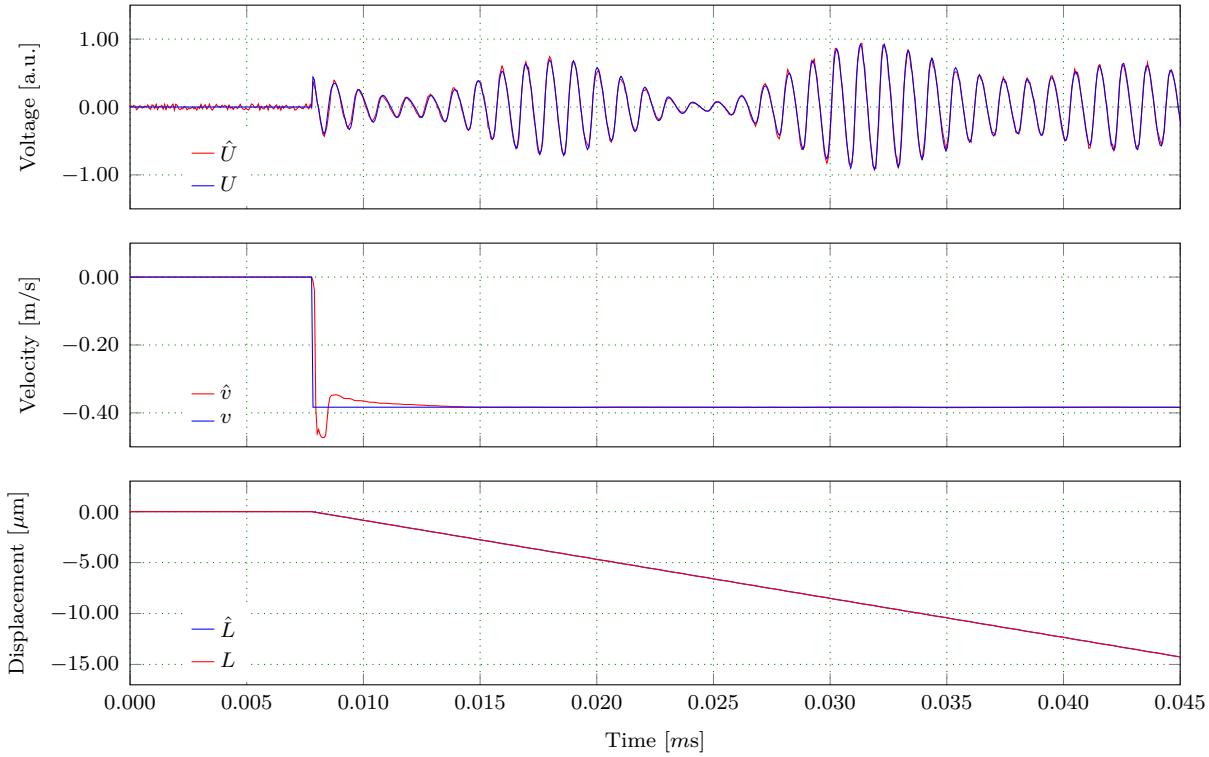

Figure 4.36: Estimation of negative velocity with a simulated noisy signal that the amplitude is modulated.

and displacement from the SMI signal in both noise-free conditions and noise conditions, even when the signal amplitude is modulated. Meanwhile, it can correctly discriminate the directions of displacement and velocity. The simulation also shows that noise and modulated amplitude will increase the velocity estimation error.

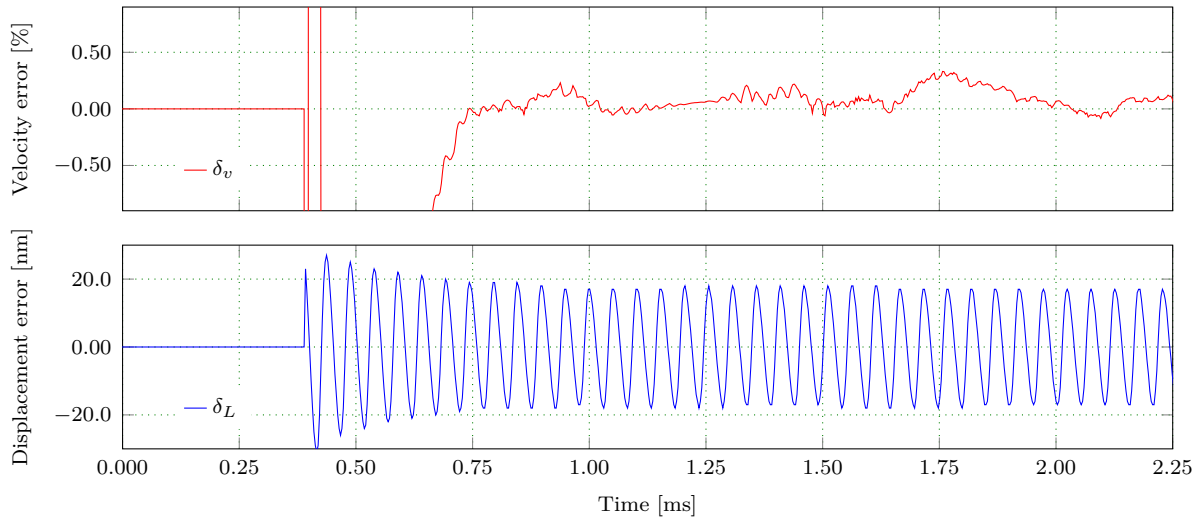

Figure 4.37: Errors of estimated negative velocity in Figure 4.36.

4.6.5 Experiment

In this section, the implementation of the proposed algorithm to obtain velocity in the experiment is described and explained in detail. The initial values of $\boldsymbol{x}$, $\mathbf{P}$, $\mathbf{Q}$, and $\mathbf{R}$ for the experiment are chosen as,

$$\boldsymbol{x_0} = \begin{bmatrix} 0.4 & 0.01 & 0.01 & 10 & 0.5 \end{bmatrix}^T, \tag{4.95}$$

$$\mathbf{P_0} = \begin{bmatrix} 1 & 0 & 0 & 0 & 0 \\ 0 & 1 & 0 & 0 & 0 \\ 0 & 0 & 10 & 0 & 0 \\ 0 & 0 & 0 & 1 & 0 \\ 0 & 0 & 0 & 0 & 1 \end{bmatrix}, \tag{4.96}$$

$$\mathbf{Q_0} = \begin{bmatrix} 0.005 & 0 & 0 & 0 & 0 \\ 0 & 0.005 & 0 & 0 & 0 \\ 0 & 0 & 10^{-5} & 0 & 0 \\ 0 & 0 & 0 & 40 & 0 \\ 0 & 0 & 0 & 0 & 10^{-8} \end{bmatrix}, \tag{4.97}$$

$$\mathbf{R_0} = 1. \tag{4.98}$$

The experiment setup of the self-mixing sensor is presented in Figure 4.2. The reference velocity v is obtained from the average of the velocity measured with LDV.

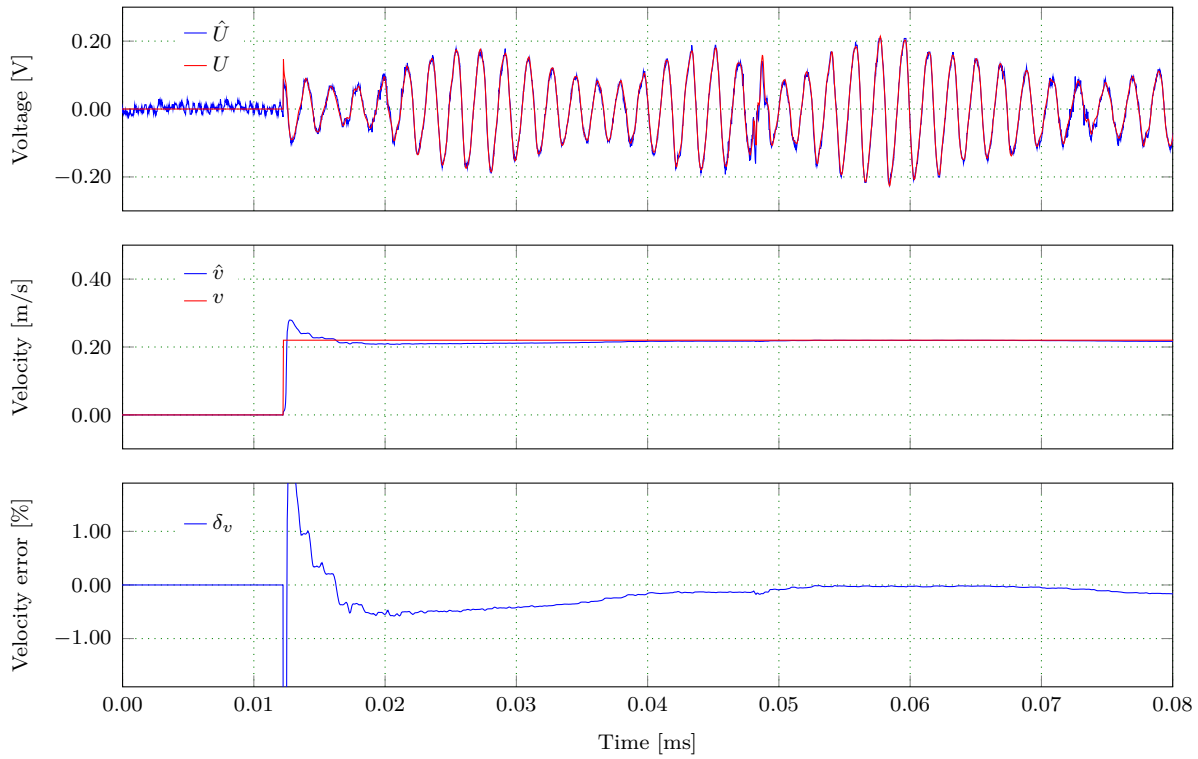

Figure 4.38: Positive velocity estimation with experimental signal.

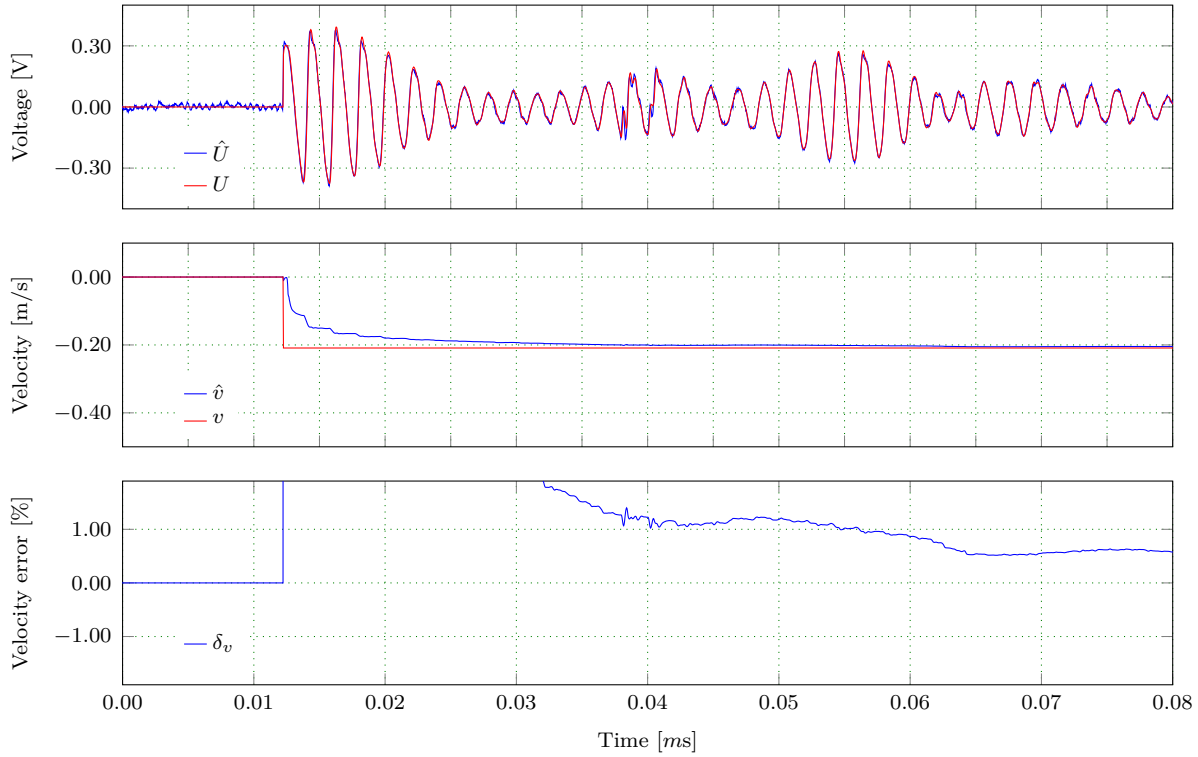

Figure 4.39: Negative velocity estimation with experimental signal.

Figure 4.38 and Figure 4.39 show estimation of the positive and negative velocity from the experimental signals. It is seen that the amplitude of the SMI signal is strongly

altered by speckle effect. In Figure 4.38, the EKF successfully tracks the experimental SMI signal and velocity. After around 7 fringes, the EKF can estimate the velocity quite good. This time largely depends on the initial point. The error of velocity is about 0.2%. In Figure 4.39, the EKF correctly tracks the negative velocity and discriminates the direction of the velocity. The estimated velocity is close to the reference velocity after 0.03 ms, and after around 0.065 ms the error is 0.6%.

The application of this algorithm is not limited to a unidirectional movement, but is developed for measuring arbitrary movement. Figure 4.40 shows the estimation of an experimental variable velocity from positive to negative. The results are very encouraging that the SMI signal is correctly tracked, and the velocity, the displacement, and the direction of movement are properly retrieved.

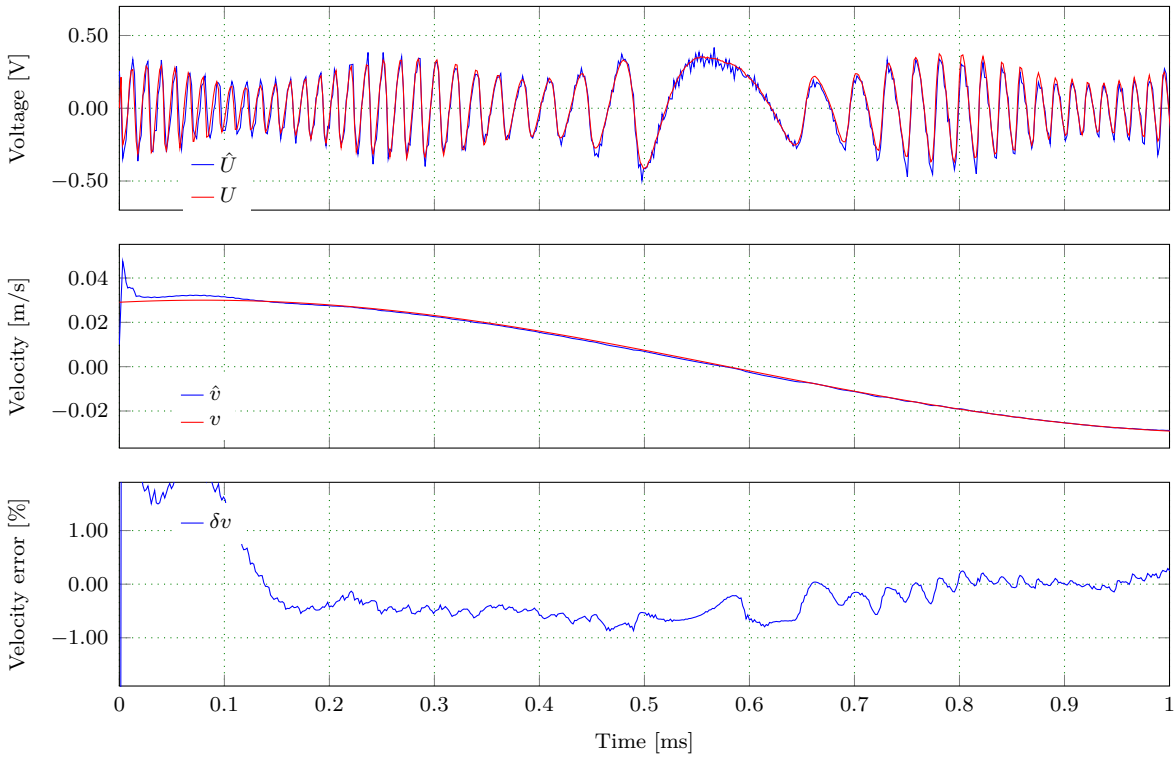

Figure 4.40: Estimation of a variable velocity from positive to negative in the experiment.

Taking the rotational speed of the motor as the abscissa, the measured velocity, and the errors as the ordinate, draw Figure 4.41. The range of the measured velocity is from 0.1 m/s to 2 m/s. The measured velocities in Figure 4.41 are the average value of the measured velocities, and the error bars represent the maximum error and minimum error of the measured velocity. It can be seen that the velocities measured by the LDV have superior linearity compared with the SMI sensor. Nevertheless, we can see from the velocity errors that even the errors of the SMI sensor is inferior to the LDV, the average error is still within 1%. And the maximum and minimum errors are within 1.5%.

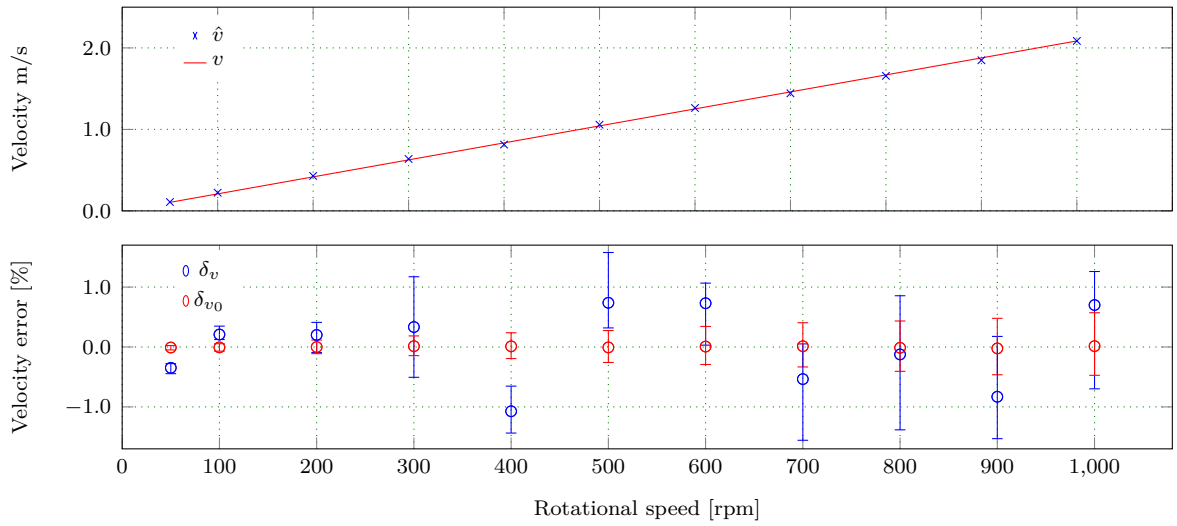

Figure 4.41: The measured velocities and errors versus the rotational speed of the motor. v and $\hat{v}$ are the measured velocities with the LDV and the SMI, respectively. δv_0 and δv are the measured errors with the LDV and the SMI.

4.6.6 Conclusion

In this section, an algorithm based on the EKF to measure velocity from the SMI signal is proposed. Based on the model of the SMI signal, the multiplicative noise caused by the speckle effect is taken into account. Thus, this parametric method can track a time-varying velocity and discriminate the direction of velocity without any other calculation or modulation when the feedback level is weak. The model of the SMI signal in this section is based on the model of signal for displacement measurement. Therefore, it can also be applied to the displacement measurement. In the next chapter, the displacement measurement using SMI sensor based on the EKF will be discussed in detail.

4.7 Summary

In this chapter, the application of SMI in velocity measurement has been revisited and summarized. Different signal processing algorithms have been presented to improve the estimation results. These include interpolation of the spectrum, MLE, and EKF. The derivation process and detailed theoretical principles were introduced, and their performance was evaluated using the experiment setup.

The experiment results confirm that the FH method and the FP method are satisfactorily applied to the SMI signal affected by the speckle effect when the data record length is limited. The performance of the FP method is slightly better than the FH method. To further improve the estimate accuracy, the parameters optimization based on the MLE was performed in the frequency domain. The comparison of the MLE with the FFT

and FH methods indicates that the RMSE and relative error of the MLE method are smaller than the other two methods. However, the iterative procedure of MLE is very time-consuming. Finally, the EKF method based on the SMI signal model was proposed. The experimental results verify that the EKF can track the time-varying velocity and discriminate the direction of velocity.

Chapter 5

Displacement measurement with self-mixing interferometry

This chapter introduces the application of SMI in measuring displacement. The methods for improving the displacement resolution of SMI are closely investigated. Their performance improvements in comparison with the traditional methods are evaluated. In Section 5.2, a simple factor C estimation method is used under both the weak and moderate feedback regimes. Without the complicated and tedious calculation process of the general C estimation method, a final equation is obtained through analysis. Thus, the estimation of C only involves a few simple calculations. Section 5.3 develops an algorithm based on the EKF for displacement retrieval without any beforehand knowledge of the displacement. It can unambiguously measure the displacement using a single interference signal under the weak feedback regime. Comparing to the traditional PUM, it does not require cumbersome normalization, transition detection, C estimation, etc.

5.1 Background

Displacement retrieval by the SMI is a promising technique due to its compact, self-aligned, and cost-effective nature. A basic SMI sensor can reach the resolution of $\lambda_0/2$ by easily counting the number of interference fringes, where λ_0 represents the laser wavelength under free-running condition. In the last few decades, different methods have been proposed to improve the resolution of displacement reconstruction. An SMI with an electro-optic modulator was demonstrated by N. Servagent et al. in 2000 [94]. The resolution of the reconstructed displacement is $\lambda_0/2N$ with the separated phase of $2\pi/N$. A differential optical feedback interferometry was proposed by F. J. Azcona et al. in 2013. It can measure the displacement of nanometer-size amplitude by comparing the optical power of two lasers via optical feedback [159]. However, these two methods increase the

complexity of sensors and raise the cost. Efforts have been made to improve the resolution by different processing algorithms. These methods do not need to add external optical, mechanical or electronic components. In 1997, S. Merlo and S. Donati using the analytical expressions to exploited a method, whose reconstruction accuracy is on the order of tens of nanometers for displacements of a few micrometers. The factor C was obtained by measuring the time duration of increasing and decreasing semi-periods of the signal. The experiment results showed that waveform retrieval can be achieved under the weak-feedback regime [96]. The linear interpolation method under the moderate regime ($1 < C < 4.6$) was proposed by N. Servagent et al. in 1998 [95] to improve the resolution to $\lambda_0/12$. In 2001, M.Wang et al. proposed a method using the Fourier transform to demodulate the self-mixing signal. The temporal signal phase is extracted by using the first component of the Fourier spectrum [160]. The Hilbert transform was applied to obtain the phase for speckle-insensitive fringe detection in 2014. An accurate instantaneous phase can be extracted without being affected by amplitude variations induced by speckle phenomenon [161]. All of these techniques require approximate and local output signal linearization and/or external optical components, which are either very expensive or not fully compatible with real-time displacement measurement. Hence, they drastically reduce the interest of using SMI sensors in industrial applications.

In 2007, the method based on the EKF and using the behavioral model of the SMI signal was proposed to improve the resolution of SMI displacement sensor. It should be noted that the displacement of the moving target was sinusoidal with a known frequency [162]. Thus, the displacement, velocity, and an unknown constant position were taken as the state vector. In 2008, the possibility of using a GaN laser to increase the resolution was proved, since it has a shorter wavelength (405 nm) than other laser diodes (generally around 800 nm for SMI) [163]. However, the SNR of the GaN laser was noticeably lower than either of the investigated infrared lasers or red lasers. A real-time fully analog laser self-mixing vibrometer was developed by M. Norgia and A. Pesatori in 2011. When the signal was unwrapped and the jumps of the signal are compensated by analog elaborations, the resolution was 35 nm with a displacement range of 1 mm [164]. G. Plantier and C. Bes et al. applied an auto-adaptive signal processing method to retrieve displacement, in which the PUM was used for harmonic displacement and aleatory displacement of a remote piezoelectric actuator. This method realizes a joint, online, and adaptive estimation of the target displacement and the two self-mixing fundamental parameters C and α. It can measure 10 μm displacement within an accuracy of ± 80 nm [35, 36]. To improve the PUM, an analysis of its inherent error and robustness was carried out in a detailed manner in 2013 [41], where an improved phase unwrapping method (IPUM) was deduced from the PUM to theoretically remove the errors of the PUM while keeping its inherent robustness. However, errors of the peaks or valleys are still larger than other points because of the noise.

5.2 Phase unwrapping method and feedback factor

The PUM with the estimation of factors C and α is a promising method to realize real-time measurement with improved resolution. This section aims to present a novel method to estimate the factor C under both weak and moderate feedback regimes with less calculation. With this simple estimation method (SEM), the resolution is improved well beyond the basic resolutions. Considering the errors resulting from the noise and the estimation bias of C, the KF is used to further improve the accuracy of retrieval displacement. Namely, the general PUM is used to obtain an initial displacement, and then the KF is employed for further improvement.

5.2.1 Theory

The analysis of optical feedback in semiconductor lasers relies on the rate equation model published by Lang and Kobayashi in 1980 [64]. It is worth noting that the theoretical model of Lang and Kobayashi was derived under the assumption of a single-mode laser [96]. The back injected light interferes with the light existing in the laser cavity and changes the threshold condition of the semiconductor laser. As a result, when the target moves, the emitted power changes as the injected current remains constant. Enormous publications have dealt with the theory of SMI based on the Lang and Kobayashi equation. The emitted power of the semiconductor laser can be expressed by (4.84). The phase equation is given by (4.85). The relationships between the phase and the distance between the laser and the target are given by

$$\phi_F(t) = 2\pi\nu_F(t)\tau(t) = 2\pi\frac{L(t)}{\frac{1}{2}\lambda_F(t)}, \tag{5.1}$$

$$\phi_0(t) = 2\pi\nu_0(t)\tau(t) = 2\pi\frac{L(t)}{\frac{1}{2}\lambda_0(t)}, \tag{5.2}$$

where $\phi_F(t)$ and $\phi_0(t)$ are the phases with and without optical feedback, respectively. $\nu_F(t)$ and $\nu_0(t)$ represent the laser frequencies with and without optical feedback. $\tau(t)$ is the round-trip time delay. $\lambda_F(t)$ and $\lambda_0(t)$ are the laser wavelengths with and without optical feedback. $L(t)$ is the distance from the laser to the target.

Generally, the output power P of the laser in SMI sensors is converted to voltage signal by a monitor photo-diode. The wrapped phase $\hat{\phi}_F(t)$ could be easily retrieved by the arccos function on the normalized signal,

$$\hat{\phi}_F(t) = \arccos\left[(U(t) - U_0)/U_m\right], \tag{5.3}$$

where $U(t)$ is the SMI signal, U_0 is a non-zero voltage offset that is usually removed by the electric circuit, and U_m is the maximum voltage.

Figure 5.1 shows a typical SMI signal $U(t)$ with a sawtooth shape under the moderate feedback regime. The wrapped phase $\hat{\phi}_F$ is acquired by (5.3) and the unwrapped phase $\hat{\phi}_F^U$ is obtained by adding or subtracting 2π (depending on the sign of the discontinuity) at the instant of phase discontinuities, which is achieved by a transition detector. According to (5.1), the factors C and α should be estimated for retrieving the displacement. Thus, the displacement retrieval using the PUM involves four basic steps [35]:

1) normalization of the SMI signal;

2) a rough estimation and unwrapping of phase $\hat{\phi}_F$ by adding or subtracting 2π;

3) estimation of C and α;

4) retrieving the displacement with $\hat{\phi}_F^U$, C, and α.

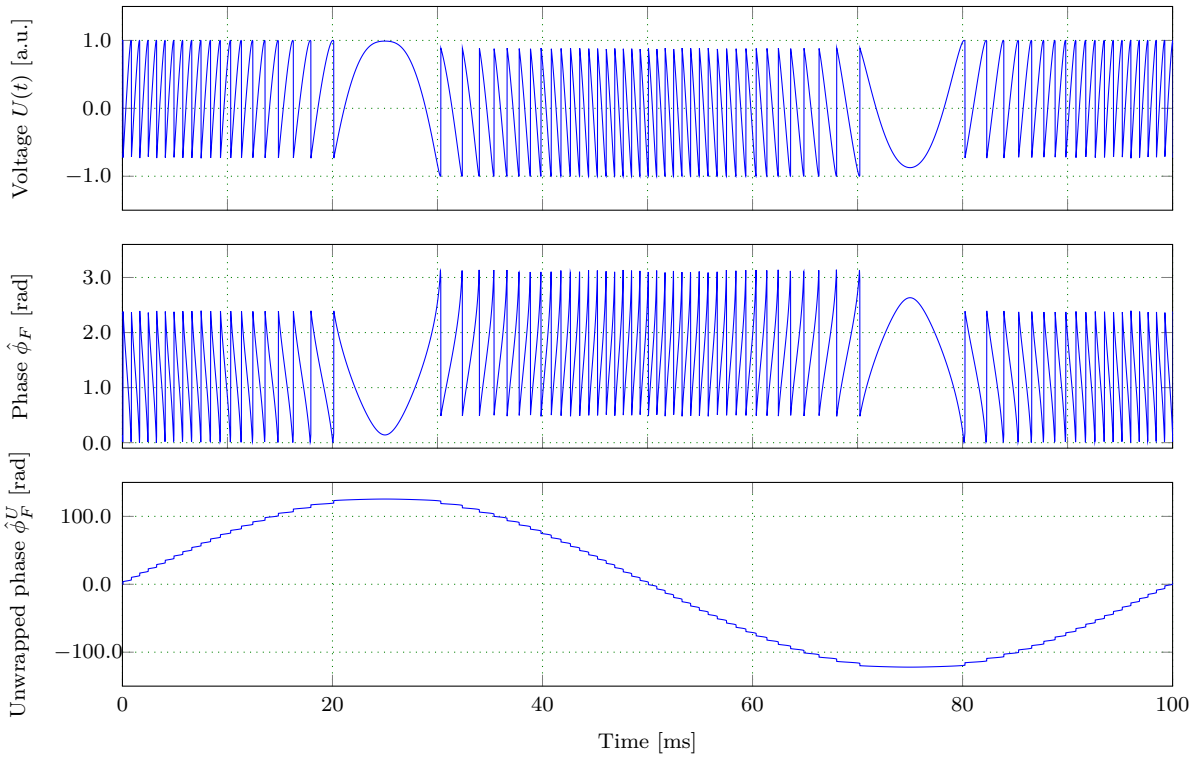

Figure 5.1: An example of SMI signal with $C = 2.0$ and $\alpha = 3.0$ and its corresponding retrieved phase $\hat{\phi}_F$ and unwrapped phase $\hat{\phi}_F^U$.

For ordinary lasers such as gas lasers, the value of the linewidth enhancement factor α is almost equal to zero, while the value of usual semiconductor lasers is a positive value from 3 to 7 [57]. Sabina et al. performed some numerical simulations to demonstrate that the factor α does not critically affect the displacement measurement [96]. In this work, a semiconductor laser is used, and the factor α is therefore assumed to be 4. Consequently, only the factor C should be estimated. The effect of α on the estimated displacement will be discussed in the simulation.

5.2.2 Feedback factor estimation

The time duration of increasing and decreasing semi-periods of the SMI signal has been used to estimate the factor C by S. Merlo and S. Donati [96]. In this work, a similar method using the increasing and decreasing semi-periods with the values of the peak and the valley is applied to estimate C under weak feedback regime and moderate feedback regime.

After the normalization of the SMI signal, the phase $\hat{\phi}_F$ is obtained by (5.3). According to (4.85), the phases $\hat{\phi}_F$ at point A and point B in Figure 5.2(a) are expressed as

$$\begin{aligned} \phi_{\mathrm{FA}} - \phi_{0\mathrm{A}} &= -C \sin\left(\phi_{\mathrm{FA}} + \arctan\alpha\right), \\ \phi_{\mathrm{FB}} - \phi_{0\mathrm{B}} &= -C \sin\left(\phi_{\mathrm{FB}} + \arctan\alpha\right), \end{aligned} \tag{5.4}$$

where the signal amplitude at point B is the maximum and the amplitude at point A is the minimum. In the case of $0 < C \leq 1$, as the signal U_1 shown in Figure 5.2(a), we have $\phi_{\mathrm{FA}} = (2k-1)\,\pi$, $\phi_{\mathrm{FB}} = 2k\pi$, $k = 0, 1, 2, 3, 4 \ldots$.

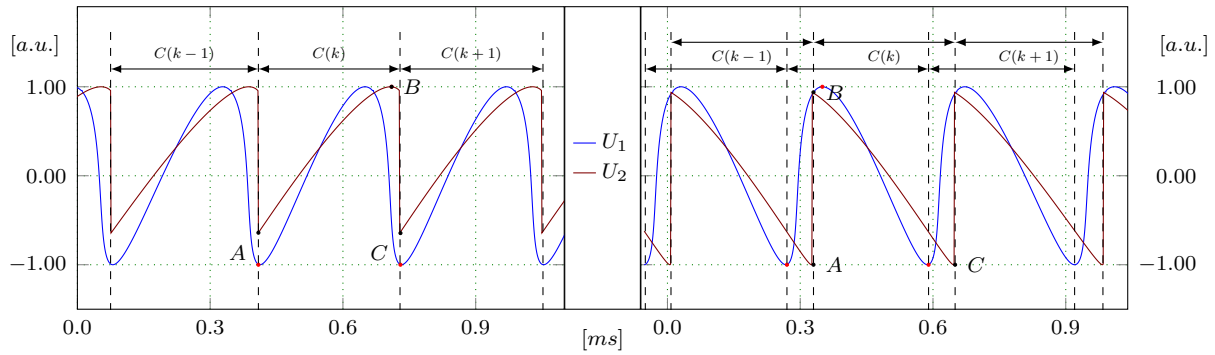

(a) Target moving away (b) Target moving toward

Figure 5.2: Analysis of SMI signal for C estimation. The feedback factor C of signal U_1 and signal U_2 are $C_1 = 0.8$ and $C_2 = 2$, respectively. Each fringe can be used to estimate one factor C.

The phase without optical feedback is written as

$$\phi_{0\mathrm{B}} = \frac{4\pi L_{\mathrm{B}}}{\lambda_0} = \frac{4\pi}{\lambda_0}\left[L_A + \int_{t_{\mathrm{A}}}^{t_{\mathrm{B}}} v(t)dt\right], \tag{5.5}$$

where t_{A} and t_{B} are the sampling time at point A and point B. Since the discontinuity of the target displacement is far less frequent than discontinuity of the SMI signal, to simplify the estimation process of C, the algorithm assumes that the velocity change during a period of the discontinuity of the SMI signal can be ignored, namely, $v(t) = v_x = \lambda_0[2(t_{\mathrm{C}} - t_{\mathrm{A}})]^{-1}$ on $[t_{\mathrm{A}}, t_{\mathrm{B}})$, where v_x is constant. Thus, the equation (5.5) is written as

$$\begin{aligned} \phi_{0\mathrm{B}} &= \frac{4\pi}{\lambda_0}\left[L_{\mathrm{A}} + v_x(t_{\mathrm{B}} - t_{\mathrm{A}})\right] \\ &= \phi_{0\mathrm{A}} + 2\pi\frac{t_{\mathrm{B}} - t_{\mathrm{A}}}{t_C - t_{\mathrm{A}}}. \end{aligned} \tag{5.6}$$

The factor C within $0 < C \leq 1$ is

$$C = \frac{-\pi + 2\pi \frac{t_{\mathrm{B}} - t_{\mathrm{A}}}{t_{\mathrm{C}} - t_{\mathrm{A}}}}{2 \sin\left(\arctan \alpha\right)}. \tag{5.7}$$

If the factor $C > 1$, as the signal U_2 shown in Figure 5.2(a), $\phi_{\mathrm{FA}} \neq (2k-1)\,\pi$ and $\phi_{\mathrm{FB}} \neq 2k\pi$. The phases are

$$\begin{aligned} &\phi_{\mathrm{FA}} - \phi_{0\mathrm{A}} - (\phi_{\mathrm{FB}} - \phi_{0\mathrm{B}}) \\ &= \phi_{\mathrm{FA}} - 2k\pi + 2\pi \frac{t_{\mathrm{B}} - t_{\mathrm{A}}}{t_{\mathrm{C}} - t_{\mathrm{A}}}. \end{aligned} \tag{5.8}$$

The factor C is

$$C = \frac{\phi_{\mathrm{FA}} - \phi_{\mathrm{FB}} + 2\pi \frac{t_{\mathrm{B}} - t_{\mathrm{A}}}{t_{\mathrm{C}} - t_{\mathrm{A}}}}{\sin\left(\phi_{\mathrm{FB}} + \arctan \alpha\right) - \sin\left(\phi_{\mathrm{FA}} + \arctan \alpha\right)}, \tag{5.9}$$

where $\phi_{\mathrm{FB}} = 2k\pi$.

Thus, when the target is moving away from the laser, the factor C of both the weak and moderate feedback regimes could be written as (5.9).

As for the reverse direction that the target is moving toward the laser, as shown in Figure 5.2(b), the factor C for both weak and moderate feedback regimes is

$$C = \frac{\phi_{\mathrm{FB}} - \phi_{\mathrm{FC}} - 2\pi \frac{t_{\mathrm{C}} - t_{\mathrm{B}}}{t_{\mathrm{C}} - t_{\mathrm{A}}}}{\sin\left(\phi_{\mathrm{FC}} + \arctan \alpha\right) - \sin\left(\phi_{\mathrm{FB}} + \arctan \alpha\right)}. \tag{5.10}$$

This method is very easy to implement, and each fringe is used to obtain a factor C, as shown in Figure 5.2. The estimated accuracy of factor C mainly depends on the reconstructed phases of the peak and valley values of the signal and the factor α. This requires a good normalization of the signal, which is also a significant factor that influences the final retrieval displacement. Note that the position where the displacement changes its direction cannot be applied to estimate C.

One limitation of the feedback factor C estimation method is that the signal amplitude changes continuously in practice, which causes the difficulty of the normalization procedure and increases the estimation error of the factor C. Besides, due to the noise, the maximum and minimum values of the signal may not be determined correctly. Thus, the errors of retrieved displacement increase. The error caused by noise was introduced in detail in [41]. The authors proposed that reducing the noise level of the experimental SMI signal would further improve the accuracy of displacement measurement.

To solve these issues, the KF is proposed to process the retrieved displacement. The KF was firstly introduced by R.E. Kalman [154] as a recursive solution to the discrete-data linear filter problem. It is well suited to online digital processing. Its recursive

structure allows its real-time execution without storing observations or past estimates. The dynamic model of the KF assumes the true state at time $k+1$ is evolved from the state at k according to (2.3).

At time k the measurement $\boldsymbol{y}_k$ of the true state x_k is made according to (2.4).

The relation regarding the displacement L and velocity v can be described by $\dot{\boldsymbol{x}} = \mathbf{A}(\mathbf{t})\boldsymbol{x}$, where the state vector $\boldsymbol{x}$ contains displacement and speed $\boldsymbol{x} = \begin{bmatrix} L & v \end{bmatrix}^T$,

The state matrix $\mathbf{A}(t)$ is

$$\mathbf{A}(t) = \begin{bmatrix} 0 & 1 \\ 0 & 0 \end{bmatrix}. \tag{5.11}$$

In a digital control system, the measurements are usually obtained at time $t_k = kT_s$. When the state at time t_k is taken as the initial state, $\boldsymbol{x}_0 = \boldsymbol{x}(t_k)$. The system matrix described in (2.3) is

$$\mathbf{F} = e^{\int_{t_k}^{t_{k+1}} \mathbf{A}(\tau)d\tau} = \begin{bmatrix} 1 & T_s \\ 0 & 1 \end{bmatrix} \tag{5.12}$$

where T_s is the sample interval.

If the initial state $\boldsymbol{x_0}$ is known, the matrix $\mathbf{P}$ is initialized with zero. Otherwise, the matrix $\mathbf{P}$ should be initialized with suitable values on its diagonal. According to (5.12), the state transition matrix $\mathbf{F}$ only depends on the time interval T_s.

Since the displacement is the only input, the observation matrix is expressed as

$$\mathbf{H} = \begin{bmatrix} 1 & 0 \end{bmatrix}. \tag{5.13}$$

Based on the preceding analysis, the proposed signal processing method is tested by simulations and experiments. To evaluate the performance of the proposed SEM, the simulations and experiments compare the retrieved displacements obtained using the general joint estimation method (JEM) and the proposed SEM with the KF.

5.2.3 Simulative evaluation

Figure 5.3 presents errors of the retrieved displacement varying with different linewidth factors α. The results are obtained under the noise-free condition with a constant feedback factor $C = 2.0$. Since the α of usual semiconductor lasers is $\alpha = 3.0 \sim 7.0$, the range of α

used for simulation is chosen from 2.0 to 8.0. In Figure 5.3, α is the actual linewidth factor. Considering the range of α, in this section, the value of $\hat{\alpha}$, which is the linewidth factor used to reconstruct the displacement, is set to a constant $\hat{\alpha}$ =4.0. The reconstructed results are evaluated with the maximum error $\delta_{\max}$, the minimum error $\delta_{\min}$, and the RMSE of the displacement. The error δ is given by the difference between the measured displacement and its actual value. The RMSE is defined as

$$\mathrm{RMSE} = \sqrt{\frac{\sum_{k=1}^{n} \left(\hat{L}_k - L_k\right)^2}{n}}, \tag{5.14}$$

where n is the number of simulated sampling points, $\hat{L}_k$ is the estimated displacement, and L_k is the true value at the kth sampling instant. The maximum $\delta_{\max}$ ($\delta_{\max} = 29.0$nm) and maximum RMSE (RMSE = 22.4nm) in Figure 5.3 occur at $\alpha = 2.0$, while the minimum $\delta_{\min}$ ($\delta_{\min} = -17.8$nm) appears at $\alpha = 8.0$. When α is in the range of 3.0 to 7.0, the maximum $\delta_{\max}$ is 10.6nm, the minimum $\delta_{\min}$ is -15.1nm, and the maximum RMSE is 11.2nm.

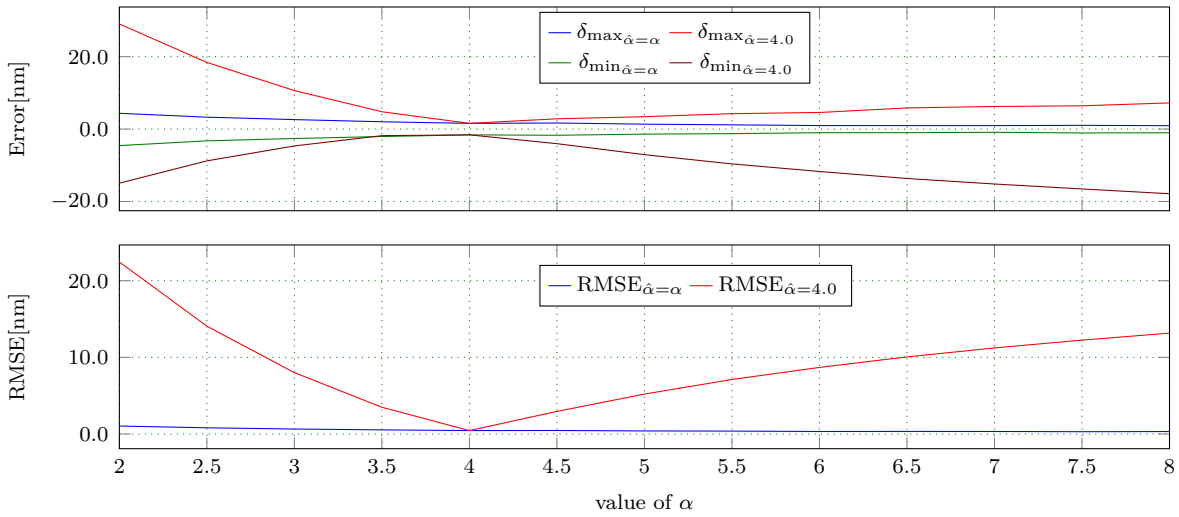

Figure 5.3: The dependence of errors and RMSEs of reconstructed displacement on the linewidth enhancement factor α. The range of α is from 2.0 to 8.0, $C = 2.0$, and $\hat{\alpha} = 4.0$. $\delta_{\max}$ is the maximum displacement error, $\delta_{\min}$ is the minimum displacement error.

Figure 5.4 shows an example of the reconstructed displacement using the SEM and KF with $C = 2.0$, $\alpha = 3.0$, and $\hat{\alpha} = 4.0$ in noise-free condition. The KF in figures represents that the KF is used following the SEM. It can be seen that the inaccurate linewidth factor $\hat{\alpha}$ results in a bias of the estimated displacement. The KF is not able to improve the estimation accuracy in this case.

To evaluate these methods under noisy conditions, simulations are implemented by adding Gaussian random noise and varying amplitude to the SMI signal. The presence of noise in the SMI signal will not only lead to noise in the recovered phase $\hat{\phi}_F$, but also cause jitter when locating actual peak and valley points, which directly reduces the accuray of displacement retrieval. Figure 5.5 shows the retrieval of a sinusoidal displacement with

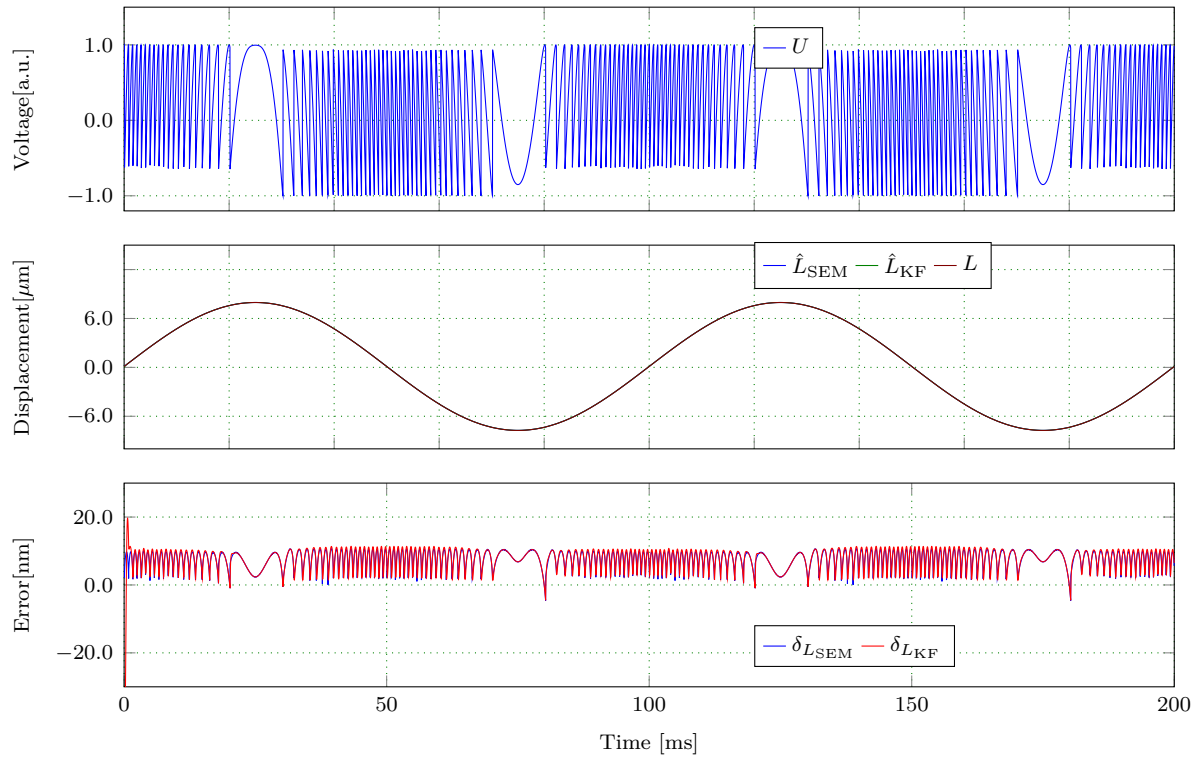

Figure 5.4: Reconstruction of a sinusoidal displacement with an ideal SMI signal. $C = 2.0$, $\alpha = 3.0$, and $\hat{\alpha} = 4.0$. U is the SMI signal, $\hat{L}_{\mathrm{SEM}}$, $\hat{L}_{\mathrm{KF}}$, and L are the reconstructed displacements with the SEM and KF, and the true displacement, respectively. $\delta_{L_{\mathrm{SEM}}}$ and $\delta_{L_{\mathrm{KF}}}$are the errors of reconstructed displacement.

a noisy SMI signal for $C = 2.0$ and $\alpha = 3.0$. The sampling frequency is 409.6 kHz and the SNR of the signal is 35 dB. The corresponding estimated $\hat{C}$ of the signal in the red frame in Figure 5.5 are shown in Table 5.1. The displacement is reconstructed using the $\hat{C}$ estimated at each fringe.

It can be noticed that the noise causes significant retrieval errors, especially in certain positions where the peaks or valleys are incorrectly determined. In article [41], an IPUM was proposed to remove this inherent error while maintaining the robustness of the PUM. In this paper, the KF is used to reduce this kind of errors. The KF needs time to track the displacement at the very beginning, which causes a large error. In comparison with the δ_{JEM} and δ_{SEM}, the error δ_{KF} is greatly reduced by the KF. Ultimately, at the points where the displacement changes its direction, the error is around 35 nm, and at other points, the error is only around 20 nm.

The retrieval of displacement with $C = 0.8$ and $\alpha = 3.0$ under noisy conditions is exhibited in Figure 5.6. The sampling frequency is 51.2 kHz and the SNR of the signal is 35 dB. The corresponding estimated $\hat{C}$ of the signal in the red frame in Figure 5.6 are shown in Table 5.2. The displacement is correctly reconstructed with the SEM method in the case of weak feedback. In comparison with the results in Figure 5.5, the large errors caused by incorrectly determining peaks or valley are not visible.

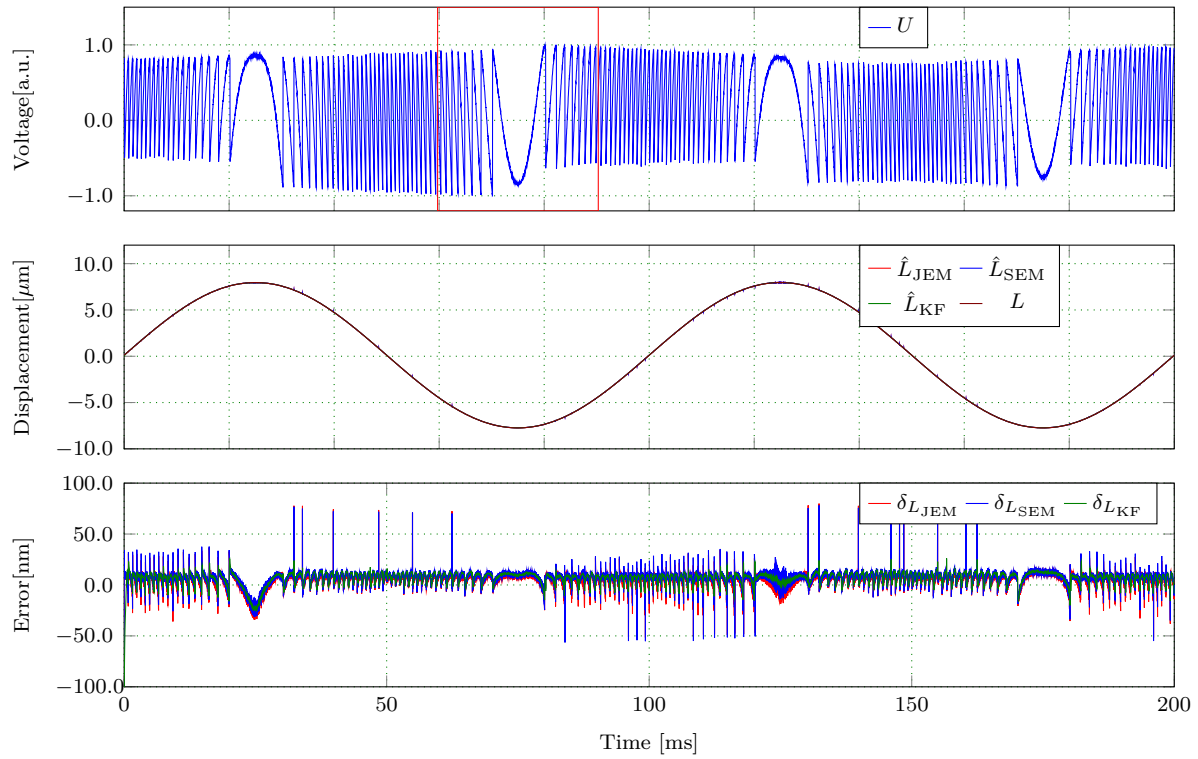

Figure 5.5: Reconstruction of a sinusoidal displacement with a noisy SMI signal for $C = 2.0$ and $\alpha = 3.0$. U is the SMI signal. $\hat{L}_{\text{JEM}}$, $\hat{L}_{\text{SEM}}$, and $\hat{L}_{\text{KF}}$ are the reconstructed displacement using JEM, SEM, and KF, respectively. L is the true displacement. $\delta_{L_{\text{JEM}}}$, $\delta_{L_{\text{SEM}}}$, and $\delta_{L_{\text{KF}}}$ are the errors of the reconstructed displacement using the JEM, SEM, and KF, respectively.

Table 5.1: Estimated C values of a sinusoidal displacement with noise under moderate regime using the SEM.

C_1	C_2	C_3	C_4	C_5	C_6	C_7
1.93	1.92	1.92	1.93	1.90	1.93	1.91
C_8	C_9	C_{10}	C_{11}	C_{12}	C_{13}	C_{14}
1.91	2.05	2.08	2.03	2.02	1.97	2.01

Table 5.3 shows the estimated errors in Figure 5.5 and Figure 5.6, where the sinusoidal displacements under weak and moderate feedback regimes are retrieved. The mean absolute error (MAE) is defined as the average absolute difference between the reconstructed displacement and the actual displacement. It is clear that the usage of the KF significantly reduces the maximum absolute error AE_{max}, which is caused by incorrectly determining the peaks and valleys. When $C = 2.0$, the MAE and RMSE of the three methods are similar, but in the case of $C = 0.8$, the MAE and RMSE of the JEM is slightly better than the other two.

Figure 5.7 shows the retrieval of an aleatory displacement. The SMI signal is noisy with $C = 2.0$ and $\alpha = 3.0$. The sampling frequency is 409.6 kHz and the SNR of the signal is

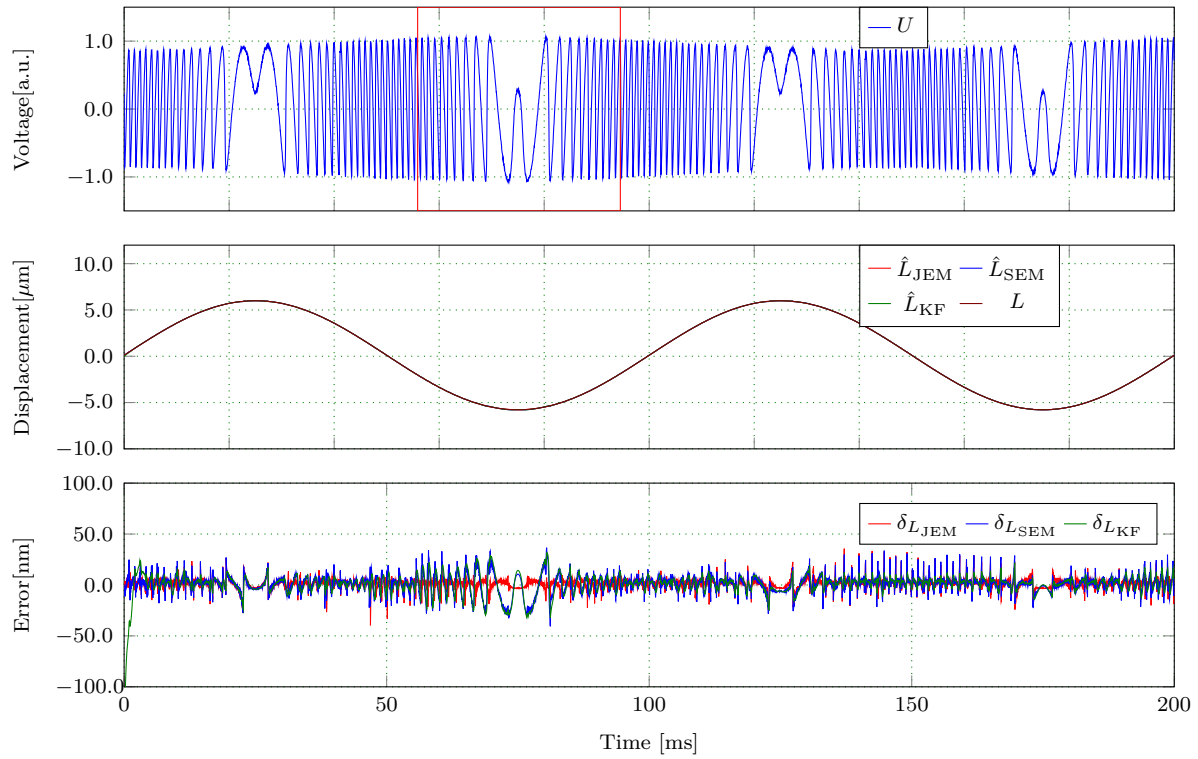

Figure 5.6: Reconstruction of a sinusoidal displacement with a noisy SMI signal. $C = 0.8$ and $\alpha = 3.0$. U is the SMI signal. $\hat{L}_{\text{JEM}}$, $\hat{L}_{\text{SEM}}$, and $\hat{L}_{\text{KF}}$ are the reconstructed displacement using JEM, SEM, and KF, respectively. L is the true displacement. $\delta_{L_{\text{JEM}}}$, $\delta_{L_{\text{SEM}}}$, and $\delta_{L_{\text{KF}}}$ are the errors of the reconstructed displacement using the JEM, SEM, and KF, respectively.

Table 5.2: Estimated $C = 0.8$ values of a sinusoidal displacement with noise under weak regime using the SEM.

C_1	C_2	C_3	C_4	C_5	C_6	C_7
0.96	0.89	0.83	0.80	0.84	0.95	0.81
C_8	C_9	C_{10}	C_{11}	C_{12}	C_{13}	C_{14}
0.90	0.84	0.83	0.75	0.91	0.90	0.92

35 dB. The similar results as in Figure 5.5 are obtained. The proposed SEM successfully retrieves the displacement. The errors caused by the wrongly identified peaks and valleys are effectively reduced with the usage of KF. The maximum absolute errors of the JEM, SEM, and KF are 79.5nm, 81.2nm, and 39.8nm, and the RMSEs of them are 15.1nm, 10.3nm, and 9.3nm, respectively.

The simulated signal with $\alpha = 2.0$ is used to analyze the dependence of the errors on the SNR, because the errors and RMSEs are maximum when $\alpha = 2.0$, as can be seen in Figure 5.3. In Figure 5.8, the AE_{max} of the JEM is larger than the SEM when the SNR is lower than 80 dB, and the KF has the ability to reduce the AE_{max}. The SEM has a superior RMSE compared to the JEM when the SNR is lower than 30 dB, but it reaches

Table 5.3: Estimated errors of a sinusoidal displacement with noise under weak and moderate feedback regimes.

	$C = 2.0$			$C = 0.8$		
	JEM	SEM	KF	JEM	SEM	KF
AE_{max}(nm)	83.8	82.3	33.2	39.5	40.3	34.5
MAE(nm)	7.6	8.5	7.9	4.0	6.3	5.7
RMSE(nm)	9.5	10.4	8.9	5.6	8.7	8.2

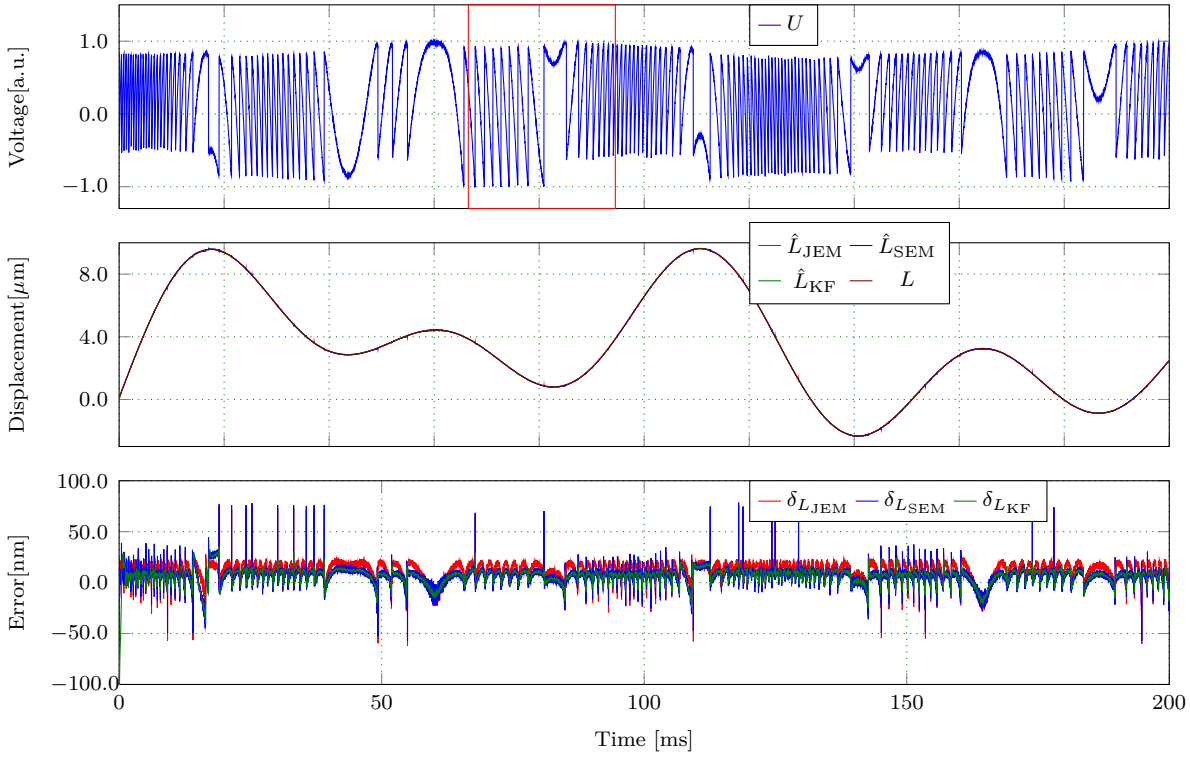

Figure 5.7: Reconstruction of an aleatory displacement with a noisy SMI signal. $C = 2.0$ and $\alpha = 3.0$. U is the SMI signal. $\hat{L}_{JEM}$, $\hat{L}_{SEM}$, and $\hat{L}_{KF}$ are the reconstructed displacement using JEM, SEM, and KF, respectively. L is the true displacement. $\delta_{L_{JEM}}$, $\delta_{L_{SEM}}$, and $\delta_{L_{KF}}$ are the errors of the reconstructed displacement using the JEM, SEM, and KF, respectively.

its error limitation (RMSE = 22.5nm) after 30 dB, while the errors of the JEM are much smaller than that of the SEM after 30 dB. This is proven in Figure 5.3 that the RMSE of the noisy-free signal using the SEM method is 22.4 nm. All the other α within the range of 2.0 to 8.0 leads to a smaller error and RMSE than that in Figure 5.8.

In general, the proposed SEM can adequately estimate the factor C under both weak and moderate regimes, even when the displacement is aleatory. The errors of retrieved displacements using the SEM are comparable to the JEM. The SEM is more effective for low SNR (SNR$<$ 30dB), and the JEM might be superior for high SNR. The use of KF effectively reduces the error of displacement retrieval under the noisy condition, especially at the discontinues points that the peaks and valleys are incorrectly determined.

Table 5.4: Estimated C value of an aleatory displacement with noise under moderate regime using the SEM.

C_1	C_2	C_3	C_4	C_5	C_6	C_7
1.93	1.92	1.91	1.94	1.94	1.94	1.94
C_8	C_9	C_{10}	C_{11}	C_{12}	C_{13}	C_{14}
2.05	2.10	2.02	1.97	2.06	2.08	2.02

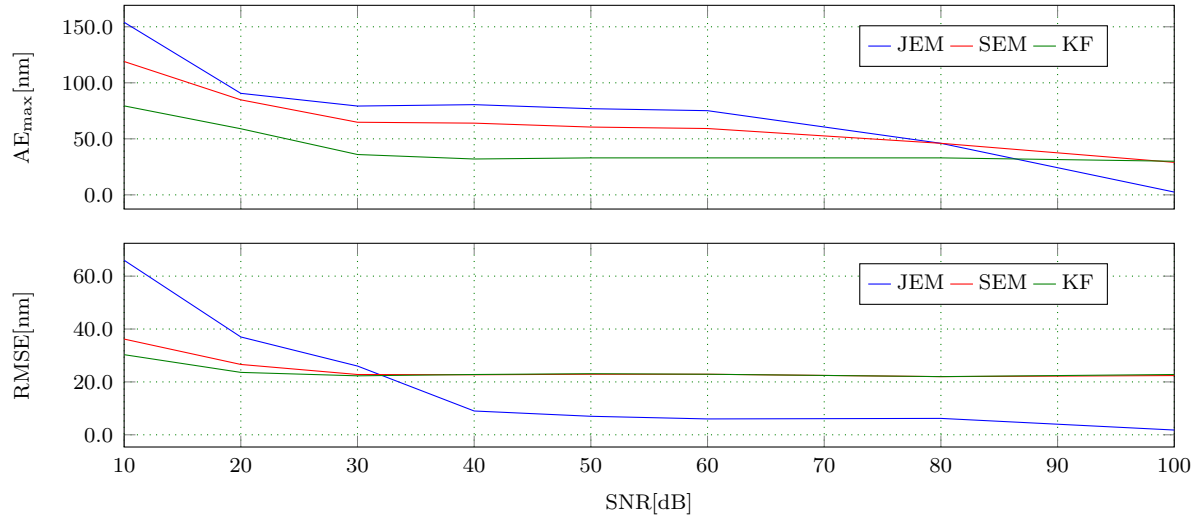

Figure 5.8: The AE_{max} and RMSE versus SNR curves. $\alpha = 2.0$, $\hat{\alpha} = 4.0$, and $C = 2.0$.

5.2.4 Experimental evaluation

These methods are tested experimentally. In the experiment, the SMI sensor used to measure displacement consists of a commercial 785 nm laser diode (L785P5) with a power of 5 mW, a lens, a laser driver, and a preprocessing circuit. The typical threshold current of the laser diode is 20 mA. Figure 5.9 shows the experimental setup for displacement measurement using the SMI sensor. The distance between the sensor head and the target surface is 9.5 cm. The drive current of the laser diode is 30 mA, which is provided by a self-designed current source. The light beam is focused by a lens on a loudspeaker, which is excited by a 500 Hz sine wave. This generates a sinusoidal displacement signal with an amplitude of approximately 5 μm. The SMI signal is directly detected by the monitoring photo-diode enclosed in the laser package, and processed by a personal computer after a data-acquisition card.

The collected signals are exhibited in Figure 5.10 and Figure 5.11, of which the sampling frequencies are 500 kHz and 2.5 MHz. The signals are processed as described earlier. Firstly, the signal U is normalized to U_n. Then $\hat{\phi}_F$ is reconstructed, and $\hat{C}$ is estimated by locating the maximum and minimum values within a fringe of the signal. Next, the displacement $\hat{L}$ is reconstructed with $\hat{\phi}_F$ and $\hat{C}$. Finally, a more accurate displacement $\hat{L}_{\mathrm{KF}}$ is obtained using KF.

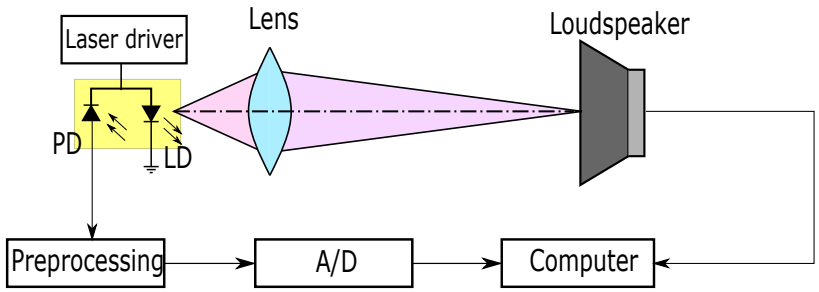

Figure 5.9: Experiment setup of the SMI sensor for displacement measurement.

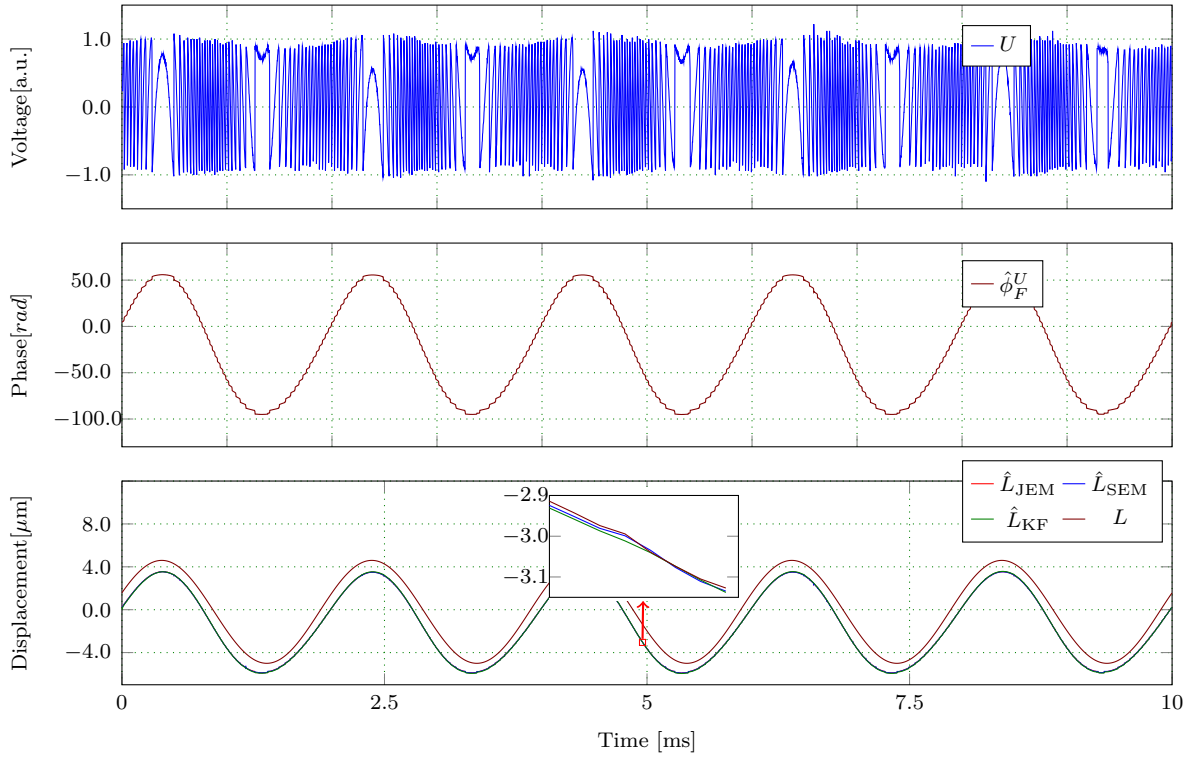

Figure 5.10: Experimental reconstruction of a sinusoid displacement with different methods. U is the original SMI signal and $\hat{\phi}_F^U$ is the unwrapped phase. $\hat{L}_{\mathrm{JEM}}$, $\hat{L}_{\mathrm{SEM}}$, and $\hat{L}_{\mathrm{KF}}$ are the reconstructed displacement using JEM, SEM, and KF, respectively. L is the referenced displacement. $\delta_{L_{\mathrm{JEM}}}$, $\delta_{L_{\mathrm{SEM}}}$, and $\delta_{L_{\mathrm{KF}}}$ are the errors of reconstructed displacement using JEM, SEM, and KF, respectively.

In Figure 5.10, the retrieved displacement $\hat{L}_{\mathrm{SEM}}$ is similar as the displacement $\hat{L}_{\mathrm{JEM}}$. The KF slightly decreases the error caused by noise and the bias estimate of the factor C. The error resulting from the incorrectly determined maximum or minimum values is not obvious in Figure 5.10 because the sampling frequency is not very high compared to the frequency of the signal. The noise has less impact on the signal, and it is easy to determine the correct peak and valley positions of the signal.

The error resulting from noise is prominent in Figure 5.11. It can be seen clearly in Figure 5.12, which is zoomed in from the red frame in Figure 5.11, that small gaps

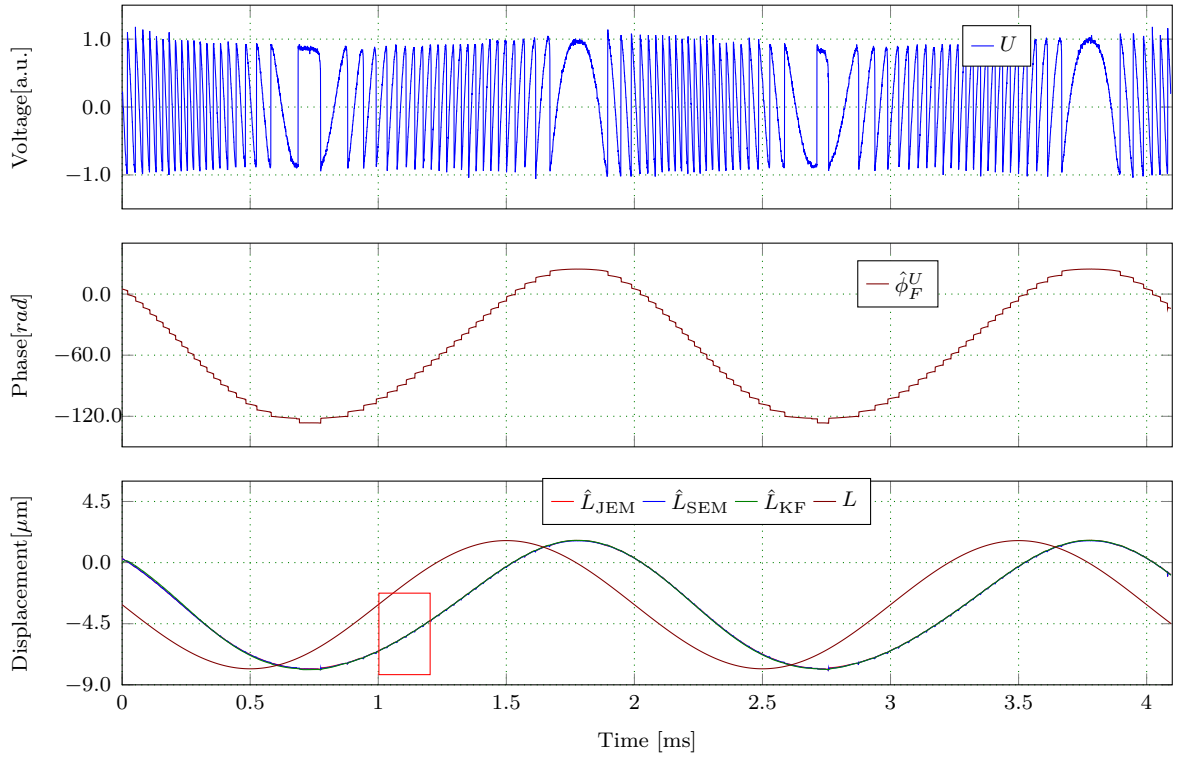

Figure 5.11: Experimental reconstruction of a sinusoid displacement with different methods. U is the original SMI signal and $\hat{\phi}_F^U$ is the unwrapped phase. $\hat{L}_{\text{JEM}}$, $\hat{L}_{\text{SEM}}$, and $\hat{L}_{\text{KF}}$ are the reconstructed displacement using the JEM, SEM, and KF, respectively. L is the referenced displacement. $\delta_{L_{\text{JEM}}}$, $\delta_{L_{\text{SEM}}}$, and $\delta_{L_{\text{KF}}}$ are the errors of the reconstructed displacement using the JEM, SEM, and KF, respectively.

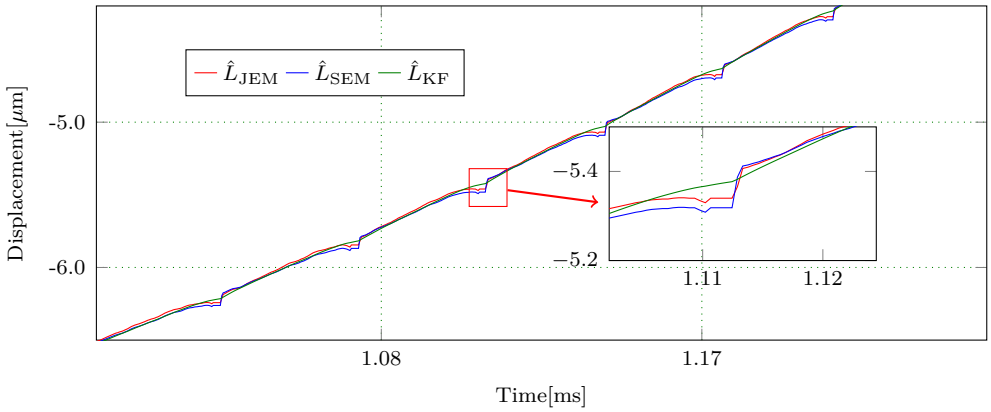

Figure 5.12: The partial enlarged drawing of retrieved displacement in Figure 5.11.

occur in the retrieved displacement $\hat{L}_{\text{SEM}}$ and $\hat{L}_{\text{JEM}}$. It means that the peak and valley locations of the signal are not correctly determined due to the noise. When the KF is employed, this issue can be significantly eased and the gaps in the retrieved displacement are effectively decreased.

5.2.5 Conclusion

The presented work is inspired by the idea that a simple and effective algorithm, which is suitable for the online application, should be developed for displacement retrieval and vibration measurement using SMI sensors. Therefore, an SMI sensor using a simple factor C estimation method along with the KF is used under both weak and moderate feedback regimes. Without the complicated and tedious calculation process of the general C estimation method, a final equation is obtained with the proposed SEM. Thus, the estimation of C only involves a few simple calculations. To deal with the errors caused by noise and estimation deviation of C, and to achieve a more accurate displacement, the KF is used to improve the results obtained by the general PUM. The simulation and experiment results show that the error of the retrieved displacement using the SEM is equivalent to the JEM. And the KF can significantly reduce the measurement errors, especially the error caused by wrongly locating the peak and valley position in signals.

5.3 Extended Kalman filter for displacement measurement

5.3.1 Background

PUM is proposed initially to work for moderate feedback due to the simplicity of fringe detection and the unambiguity retrieval of direction. It requires a tedious process of normalization, transition detection, and estimation of C and calibration. It is foreseeable that the implementation of a complete detection-reconstruction algorithm for real-time calculation should be compromised by adding more elaborated steps to the derivative-based fringe detection step of PUM [165]. The wavelet transform was proposed when the signal is disturbed by electromagnetic fields, mechanical coupling, or speckle effect [166]. This method is dedicated to moderate feedback at present. An algorithm based on the EKF by using a behavioral model of the SMI signal was proposed to improve the resolution of SMI displacement sensor. It requires that the displacement of the moving target is sinusoidal with a known frequency [162].

The main objective of this section is to develop an algorithm based on the EKF to estimate displacement without any beforehand knowledge of the displacement. It can unambiguously measure the displacement under the weak feedback regime by using a single interference signal. The proposed adaptive signal processing algorithm increases the resolution well beyond the half-wavelength, without any external optical components, preliminary separate measurements, or target surface preparation. Comparing to the traditional PUM, it does not need cumbersome normalization, transition detection, C estimation, etc. Besides, the error of estimated displacement caused by the noise in PUM

will be greatly reduced when the EKF is used.

This section is organized as follows. The theories and analysis of the proposed algorithm based on the EKF are introduced in Section 5.3.2. Following, Section 5.3.3 and Section 5.3.4 present the simulation and experiment results of displacement retrieval. Finally, conclusions are drawn in Section 5.3.5.

5.3.2 Theory

According to the equations firstly derived by Lang and Kobayashi, the wavelength of laser is changed with optical feedback and could be achieved by solving the phase equations eqs. (4.85) to (4.87). According to (4.85) and (4.87), the displacement can be written as

$$L(t) = \frac{\phi_F(t) + C\sin[\phi_F(t) + \arctan\alpha]}{4\pi}\lambda_0(t). \tag{5.15}$$

where $\phi_F(t)$ is the phase with optical feedback, $\lambda_0(t)$ is the laser wavelength without optical feedback, α is the line-width enhancement factor, and C is the feedback factor. The equation shows that for a constant current injection diode, the displacement measurement using the SMI can be achieved by correctly estimating ϕ_F, C, and α.

The state transition model of EKF is

$$\boldsymbol{x}_k = f(\boldsymbol{x}_{k-1}, \boldsymbol{\mu}_k) + \boldsymbol{w_k}. \tag{5.16}$$

The measurement equation is

$$\boldsymbol{y_k} = h(\boldsymbol{x}_k) + \boldsymbol{v}_k. \tag{5.17}$$

Because the system and measurement equations are nonlinear, a first-order approximation is used in the Riccati equations for the systems dynamics matrix $\mathbf{\Phi}$ and the measurement matrix $\mathbf{H}$. The matrices are calculated by

$$\mathbf{\Phi} = \left.\frac{\partial f(\boldsymbol{x})}{\partial \boldsymbol{x}}\right|_{x=\hat{x}}, \tag{5.18}$$

$$\mathbf{H} = \left.\frac{\partial h(\boldsymbol{x})}{\partial \boldsymbol{x}}\right|_{x=\hat{x}}. \tag{5.19}$$

In the case of displacement measurement, the measurement state is the voltage of the signal. Based on the model of the SMI signal, the system transition function can be

written as

$$\begin{bmatrix} A_k \\ \phi_{F_k} \\ v_k \\ a_k \\ C_k \end{bmatrix} = \begin{bmatrix} A_{k-1} \\ \phi_{F_{k-1}} + \frac{1}{1+C_{k-1}\cos(\phi_{F_{k-1}}+\arctan\alpha)} \\ v_{k-1} + a_{k-1}Ts \\ a_{k-1} \\ C_{k-1} \end{bmatrix} + \mathbf{Q}. \tag{5.20}$$

The system state to be estimated in this case is $\boldsymbol{x} = \begin{bmatrix} A & \phi_F & v & a & C \end{bmatrix}^T$, where A is the amplitude of the signal, v and a are the velocity and acceleration of the target.

Then we can recursively calculate the estimate of the current state vector

$$\hat{\boldsymbol{x}}(k|k-1) = f(\hat{\boldsymbol{x}}(k-1|k-1)). \tag{5.21}$$

The predicted state covariance is calculated with its predicted value at $k-1$,

$$\mathbf{P}(k|k-1) = \mathbf{\Phi}(k)\mathbf{P}(k-1|k-1)\mathbf{\Phi}^T(k) + \mathbf{Q}(k). \tag{5.22}$$

The Kalman gain $\mathbf{K}(k)$ is calculated using the predicted state covariance,

$$\mathbf{K}(k) = \mathbf{P}(k|k-1)\mathbf{H}^T(k)[\mathbf{H}(k)\mathbf{P}(k|k-1)\mathbf{H}^T(k) + \mathbf{R}(k)]^{-1}. \tag{5.23}$$

The current estimate state is corrected with the Kalman gain,

$$\hat{\boldsymbol{x}}(k|k) = \hat{\boldsymbol{x}}(k|k-1) + \mathbf{K}(k)[\boldsymbol{y}(k) - h(\hat{\boldsymbol{x}}(k|k-1))]. \tag{5.24}$$

The current estimate covariance is corrected by the Kalman gain,

$$\mathbf{P}(k|k) = [\mathbf{I} - \mathbf{K}(k)\mathbf{H}(k)]\mathbf{P}(k|k-1). \tag{5.25}$$

With the EKF, the state vectors in (5.20) can be estimated. Therefore, two solutions are able to be applied to obtain the displacement: 1) using estimated phase ϕ_F with (5.15); 2) using the estimated velocity v, and the displacement is $L_k = L_{k-1} + v_k T_s$. The signs of the phase ϕ_F and velocity v are inherently obtained during the estimate process, and no extra efforts are needed for the direction discrimination. However, the displacement obtained from velocity is inherently inaccurate, since the integration typically provides advantageous noise attenuation. Hence, in the following parts, the displacement is acquired by the estimated phase.

5.3.3 Simulative verification

To verify the effect of the value of linewidth enhancement factor α on the estimated displacement. Figure 5.13 shows errors of the retrieved displacement varying with different linewidth factors α. The results are obtained using the EKF under noise-free conditions with a constant feedback factor $C = 0.5$. The displacement is sinusoidal. Since the value of α of usual semiconductor lasers is $\alpha = 3.0 \sim 7.0$, the range of α in Figure 5.13 is chosen from 2.0 to 8.0. α is the actual linewidth factor and $\hat{\alpha}$ is the linewidth factor used to reconstruct the displacement. Considering the range of α, the value of $\hat{\alpha}$ is set to be constant $\hat{\alpha}$ =4.0, which is the same as the $\hat{\alpha}$ in Section 5.2. The reconstructed results are evaluated with the RMSE of estimated displacement.

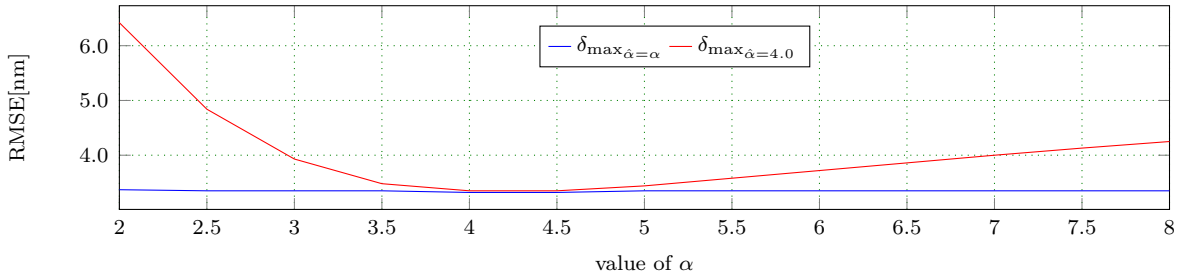

Figure 5.13: The effect of α on RMSEs of the reconstructed displacement. The range of α is 2.0 to 8.0, $C = 0.5$, and $\hat{\alpha} = 4.0$.

It can be seen that when $\hat{\alpha}$ is equal to the actual value of α, the RMSE of the displacement is 3.3 nm, while the RMSE of the displacement is within 6.7 nm when $\hat{\alpha} = 4$. In the range of $\alpha = 3.0 \sim 7.0$, the RMSE is within 4 nm. It can be concluded that the value of α has a negligible effect on the measured displacement when the proposed EKF method is used. Therefore, the value of the $\hat{\alpha}$ is chosen to be 4.0 in the following simulations and experiments. Sabina et al. suggested that the linewidth enhancement factor α could be actually evaluated by a preliminary, separate measurement on a well-known ramp-like displacement signal or current modulation. By applying the reconstruction routine with several trial values for α, the best estimate of the linewidth enhancement factor was clearly identified as the one yielding the reconstructed waveform closest to an ideal ramp [96].

To theoretically test the validity of the solution, it is evaluated under ideal conditions that do not contain any noise. For a given simulated displacement, the corresponding optical output power is calculated according to the previous analysis. In Figure 5.14, the retrieval of a sinusoidal displacement of peak-to-peak amplitude 16 μm using the EKF is shown, where the feedback factor and linewidth factor of the SMI signal are $C = 0.5$ and $\alpha = 5$. It is observed that the SMI signal and the phase are correctly tracked. The estimated displacement $\hat{L}_K$ obtained with the phase $\hat{\phi}_F$ is very close to the ideal displacement L.

The errors of estimated phase and displacement are shown in Figure 5.15. The error is calculated as the difference between the reconstructed displacement and the actual displacement. As can be seen that the maximum phase error $\hat{\delta}_{\phi_F}$ is about 0.18 rad, and

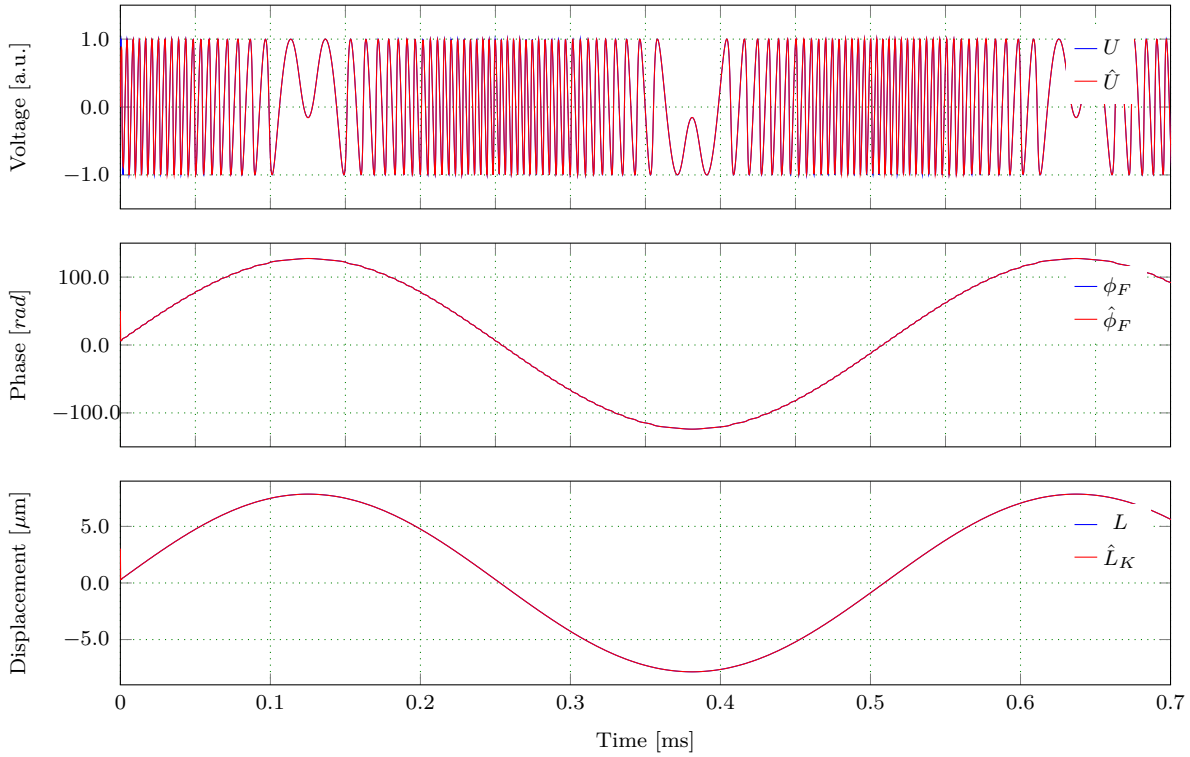

Figure 5.14: Reconstruction of a sinusoidal displacement using the EKF method under noise-free condition. $\hat{U}$ and U are the retrieved and the ideal SMI signals, $\hat{\phi}_F$ and ϕ_F represent the reconstructed phase with the EKF and the ideal phase, $\hat{L}_K$ is the estimated displacement with the EKF, the L is the ideal displacement.

the maximum error of displacement $\hat{\delta}_{L_K}$ is only about 10 nm.

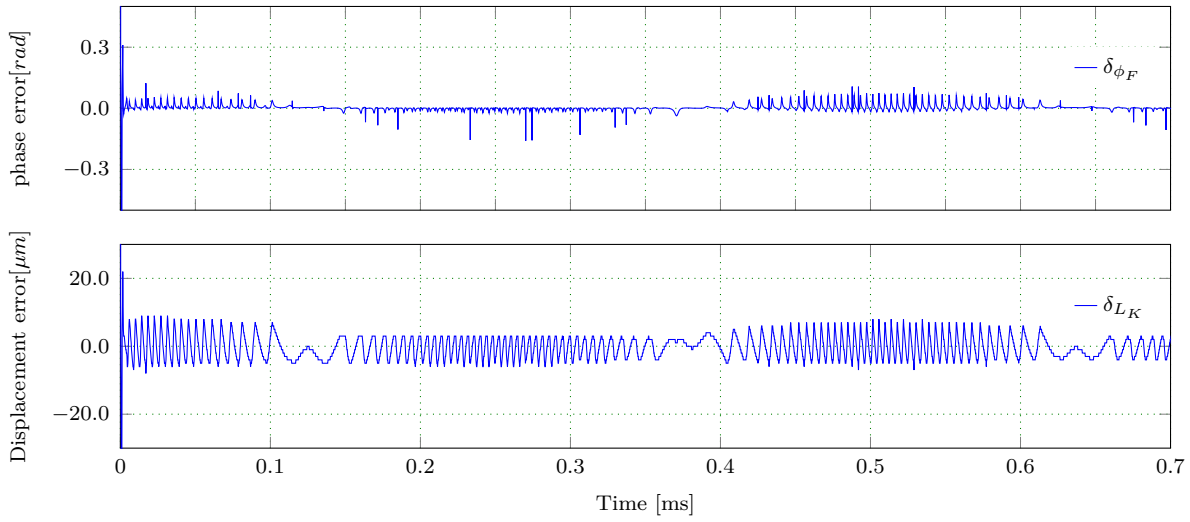

Figure 5.15: Errors of the retrieved sinusoidal displacement using the EKF method in Figure 5.14. $\delta\phi_F$ is the error of the estimated phase $\hat{\phi}_F$ with the EKF. δ_{L_K} is the error of the estimated displacement with the EKF.

Figure 5.16 shows the reconstruction of an aleatory displacement based on the EKF method, where the signal is noise-free. It can be noticed that the SMI signal U and the phase ϕ_F are successfully tracked. The estimated displacement $\hat{L}_K$ is close to the ideal displacement L. The estimated errors are illustrated in Figure 5.17. It can be seen clearly that the maximum error of the estimated phase is about 0.3 rad, which is slightly worse than that in the sinusoidal displacement reconstruction. The estimated error of displacement $\hat{L}_K$ has a similar value (about 10 nm) as that of the sinusoidal case.

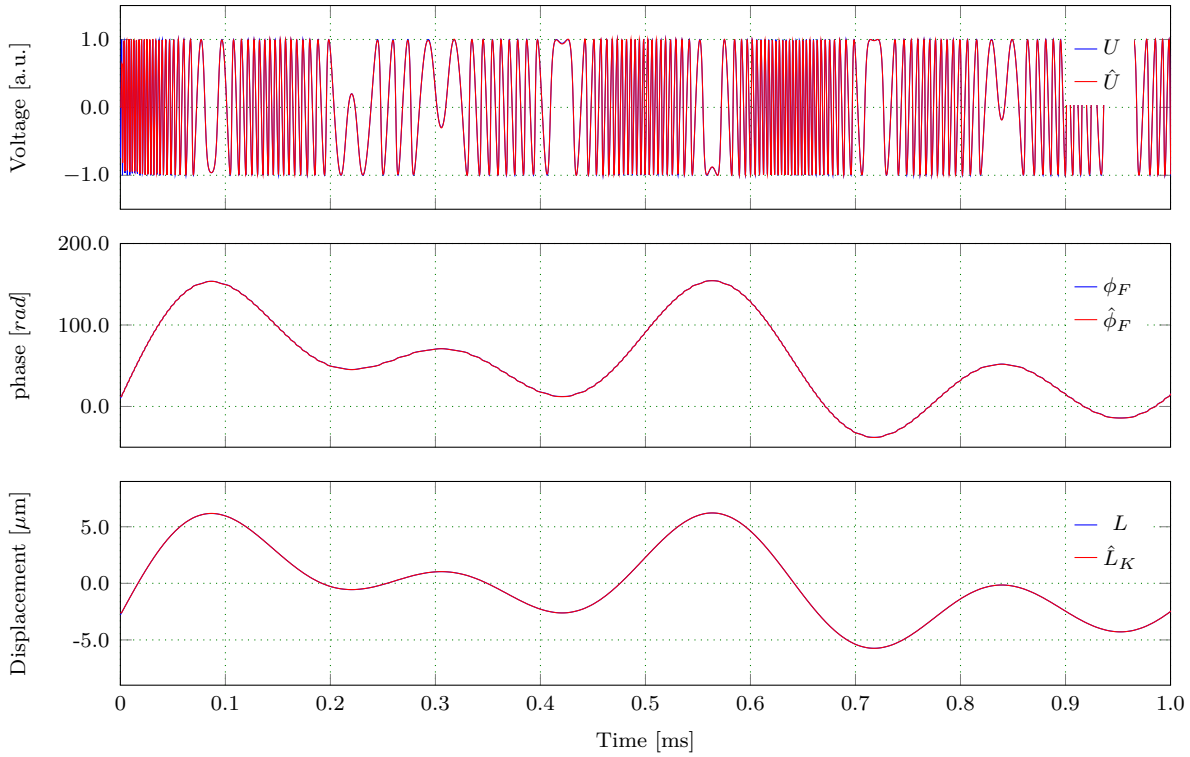

Figure 5.16: Reconstruction of an aleatory displacement using the EKF method in noise-free condition.

In practice, the SMI signal is corrupted by noise and amplitude modulation caused by the variation of the back-reflected or back-scattered optical power. When the target is at the focus of the optical system, the intensity of the back-reflected or scattered light is maximum, which leads to the maximum amplitude of the SMI signal. And the amplitude gets smaller when the target moves away from the focus. The simulated noisy SMI signal is shown in Figure 5.18, where the signal amplitude is variable. It can be seen that the EKF is also able to track the signal U and the phase ϕ_F under this condition. The estimated sinusoidal displacement $\hat{L}_K$ is very close to the ideal displacement L. In Figure 5.19, the estimated error of Figure 5.18 is displayed. The estimation error of the phase is within 0.2 rad, and the error of the displacement is within 20 nm.

Figure 5.20 shows the reconstruction of simulated noisy aleatory displacement. The aleatory displacement reconstruction is successful, but the errors in Figure 5.21 show that the results are not as good as the sinusoidal displacement tracking. The errors of the phase and displacement are within 0.5 rad and 30 nm, except at around 0.72 ms, the

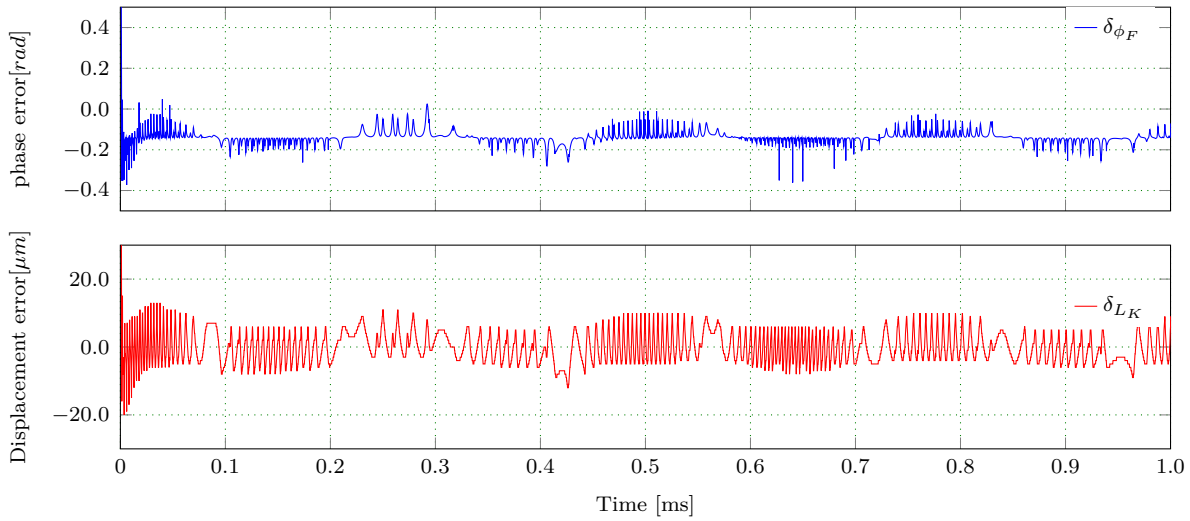

Figure 5.17: Errors of the retrieved aleatory displacement in Figure 5.16.

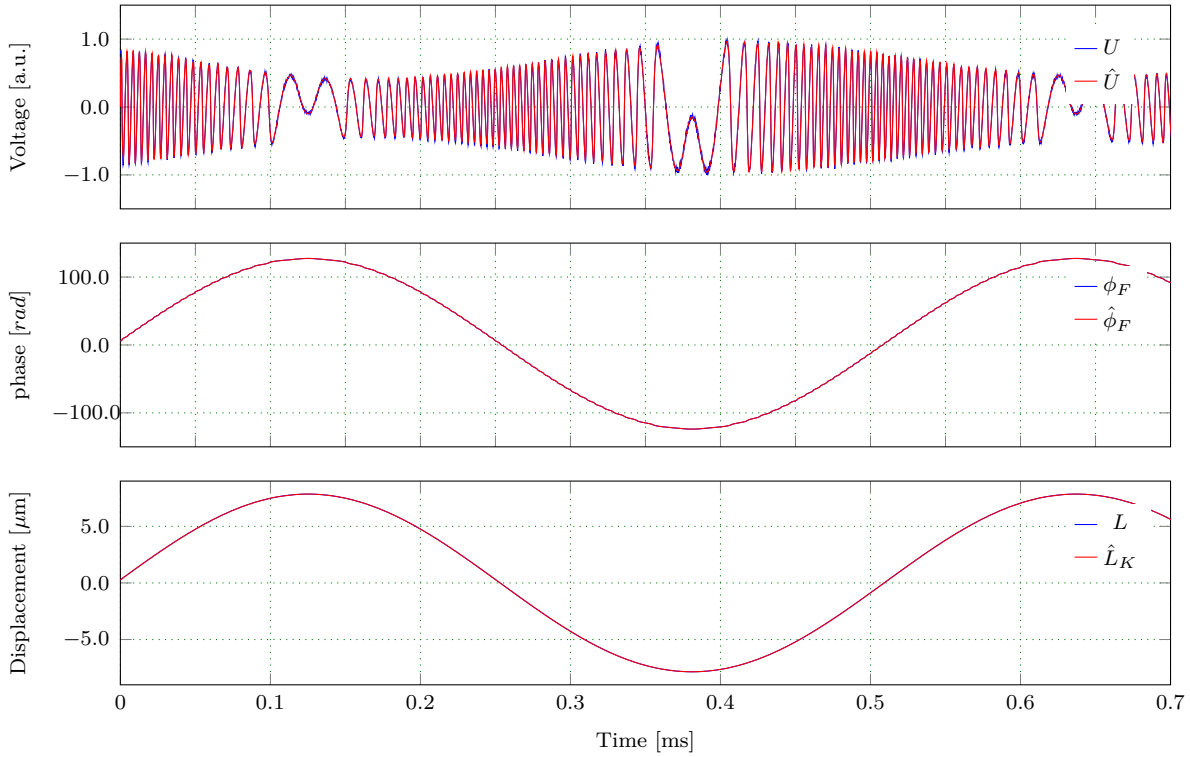

Figure 5.18: Reconstruction of a simulated sinusoidal displacement using the EKF method under noisy condition.

displacement error is as high as 40 nm. In general, the simulation illustrates that EKF can estimate the sinusoidal and the aleatory displacement. All these test results show reliability and robustness under various optical conditions.

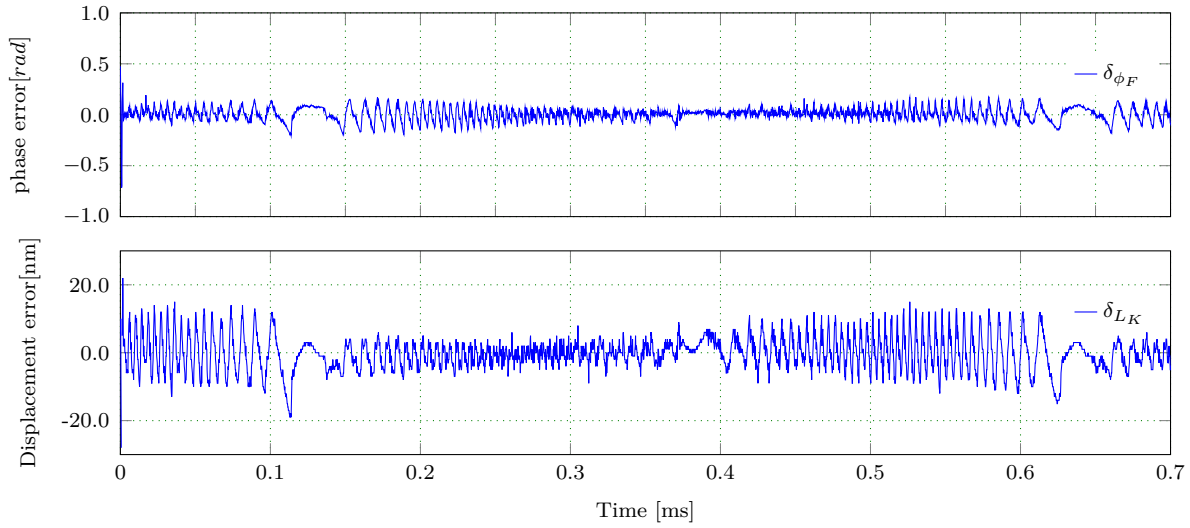

Figure 5.19: Errors of the retrieved sinusoidal displacement using the EKF method in Figure 5.18.

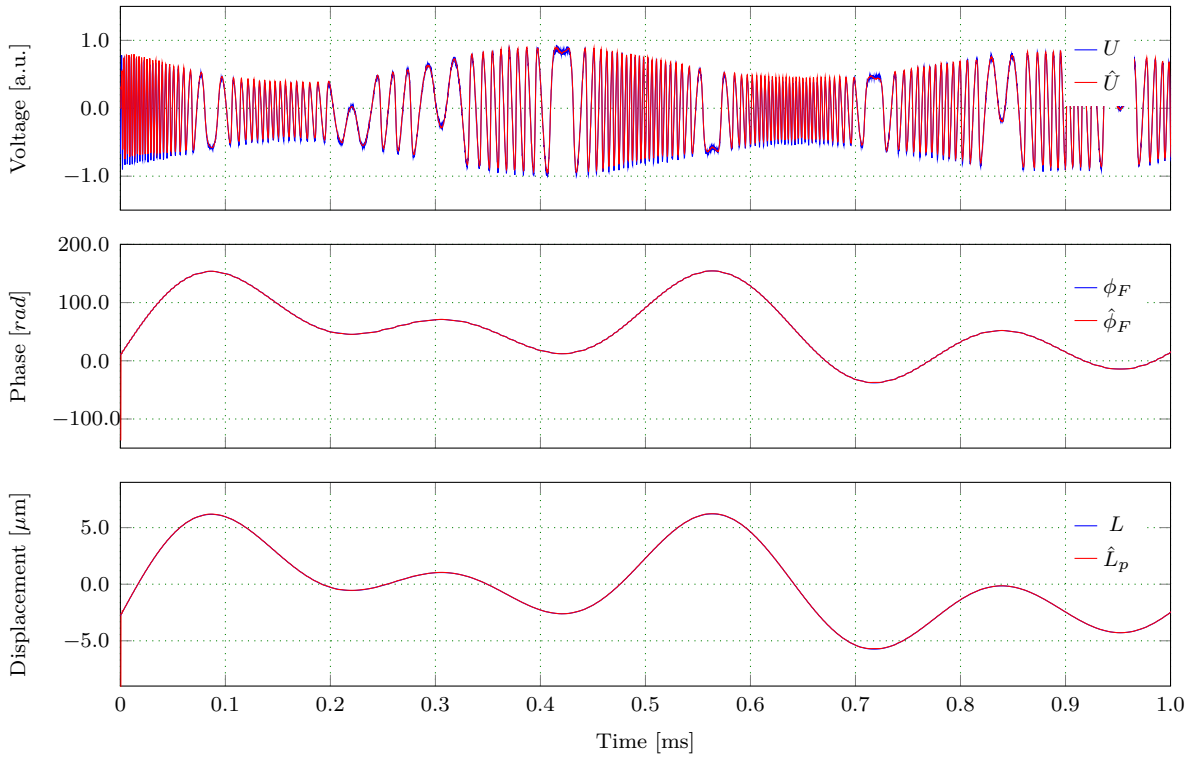

Figure 5.20: Reconstruction of simulated noisy aleatory displacement using the EKF method, where $\hat{U}$ and U are the retrieved and the ideal SMI signal, $\hat{\phi}_F$ and ϕ_F represent the reconstructed phase and the ideal phase, $\hat{L}_K$ is the estimated displacements with the EKF, the L is the ideal displacement.

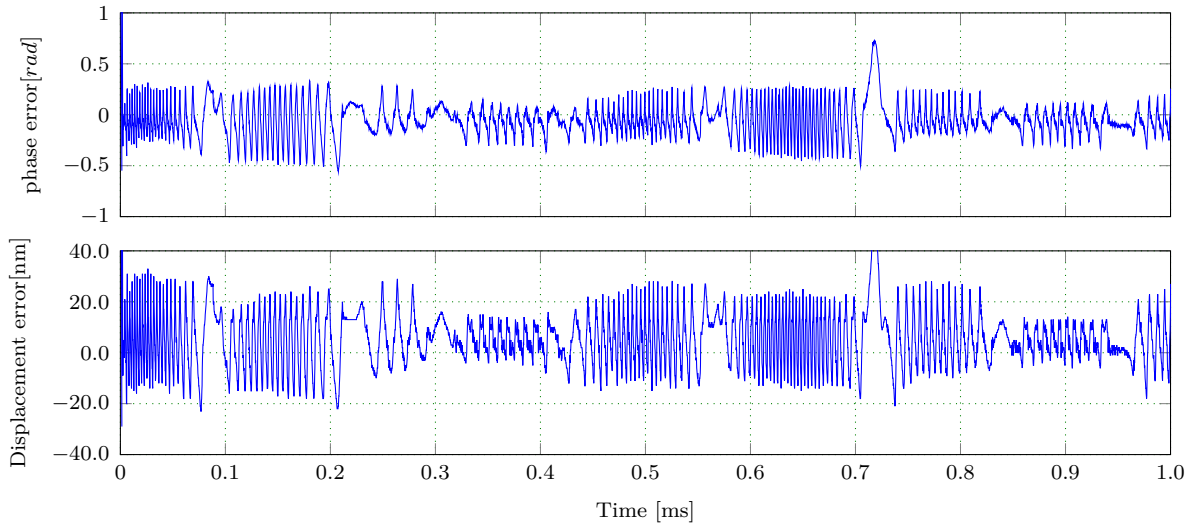

Figure 5.21: Errors of the retrieved aleatory displacement using the EKF method under noisy condition. $\delta\phi_F$ is the error of the estimated phase $\hat{\phi}_F$. δ_{L_K} is the error of the estimated displacement.

5.3.4 Experimental verification

In the real experimental setup, some parameters appear to add noise to the measurement and further affect the accuracy. To verify the performance of the EKF to estimate displacement, this method has been tested on actual signal after the tests performed on simulated signal. The results are compared with the displacement obtained using the IPUM.

The proposed strategy is also incorporated into the experiment setup mentioned above in Section 5.2, shown in Figure 5.9. The laser is driven by a self-designed current source and the light beam is focused by a lens to the loudspeaker, which generates displacement needed to be measured. The laser yields a single longitudinal mode when biased well above threshold current. It should be noted that good SMI waveforms can be obtained by commercially laser diodes as long as the residual side-modes are down concerning the main mode by 20/30 dB [96]. As a target, the loudspeaker is placed about 9.5 mm away from the laser and driven by a function generator. Many tests are performed by subjecting the speaker to sinusoidal and aleatory signals with different frequencies and amplitude of vibration. The variations in optical output power of the laser are directly detected by the monitoring photo-diode enclosed in the laser package, and processed by a personal computer after an electrical circuit and a data-acquisition card.

Figures 5.22 shows the acquired signal and the corresponding reconstruction of the phase and sinusoidal displacement using the IPUM and EKF. The peak-to-peak value of the sinusoidal displacement is 9 μm, and the frequency is 200 Hz. The upper part of the figure shows a typical SMI signal, which is characterized by a fringe in correspondence to a target displacement equal to half the wavelength. The variation of signal amplitude

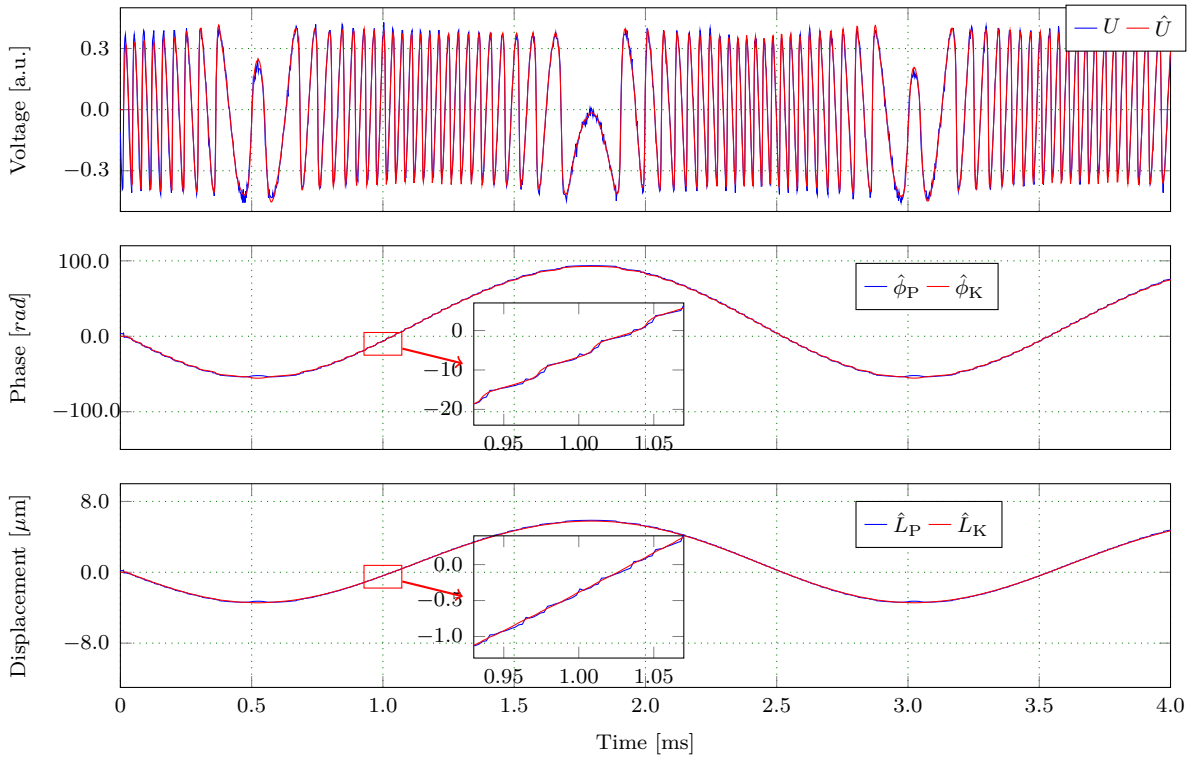

Figure 5.22: Experimental reconstruction of a sinusoid displacement using the IPUM and EKF method. U is the original obtained SMI signal and $\hat{U}$ is the tracked signal by EKF. $\hat{\phi}_P$ and $\hat{\phi}_K$ are the reconstructed phases by using the IPUM and EKF, respectively. $\hat{L}_P$ and $\hat{L}_K$ are the reconstructed displacements by using the IPUM and EKF, respectively.

is very small. It can be observed that the EKF successfully tracks the SMI signal. The reconstructed phases and displacements using these two methods are very close. A deeper view of the partial enlarged drawing of the retrieved phase and displacement shows that these two methods achieve similar phase and displacement. Because of the noise, the ripple of the displacement $\hat{L}_P$ is more significant than the ripple of the displacement $\hat{L}_K$.

Figure 5.23 shows an example of displacement reconstruction using the IPUM and EKF with a peak-to-peak value 19 μm and frequency 200 Hz. The signal amplitude slightly changes with the movement of the target. The upper part of the figure presents that in this condition, the EKF can also track the SMI signal. The comparison with the IPUM shows that the EKF correctly retrieves the phase and displacement. In the red circle in Figure 5.23, when the direction of displacement changes, the IPUM cannot detect it correctly, because such small change in the SMI signal is difficult to measure according to the detecting principle of the IPUM. A close look into the phase and displacement of the zoomed-in part, it is found that the EKF can smooth out the noise of the retrieved phase and displacement compared with the IPUM.

In Figure 5.24, the reconstruction of an aleatory displacement using the IPUM and EKF is shown, indicating that the EKF can effectively track the SMI signal. The displacement is well retrieved by comparing with the IPUM. The partial enlarged drawing shows that

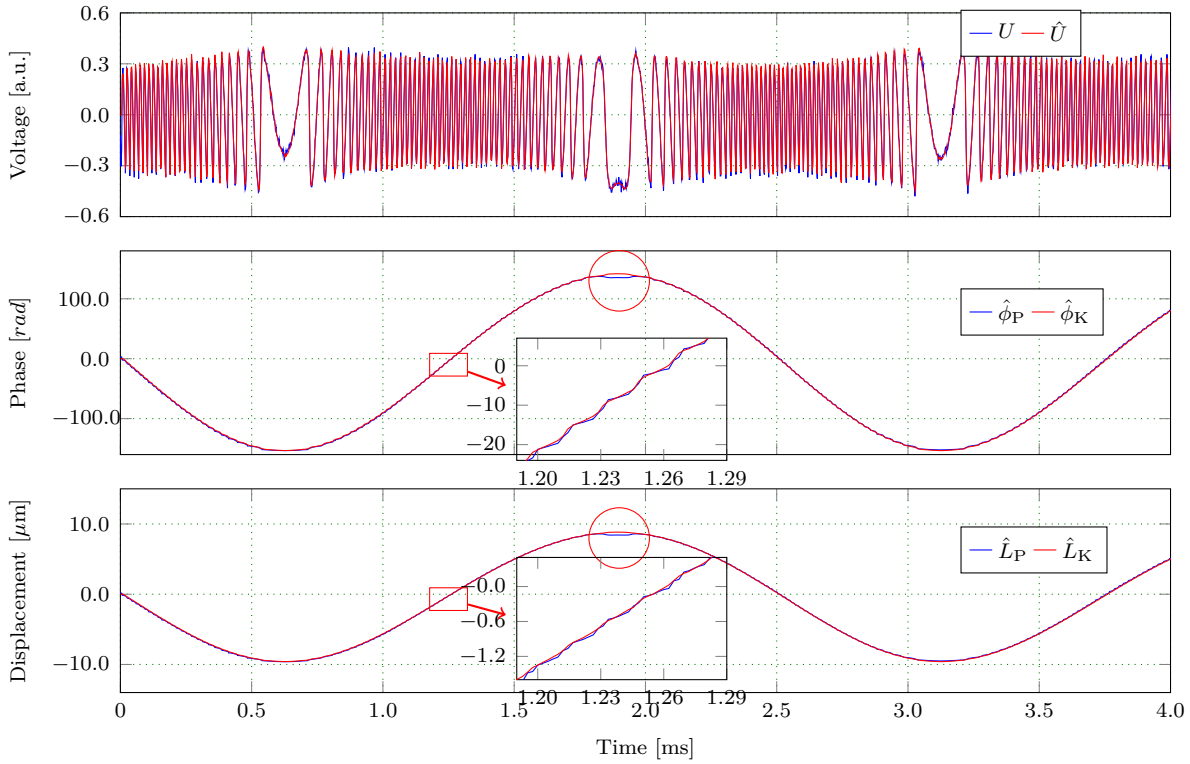

Figure 5.23: Experimental reconstruction of a sinusoid displacement using the IPUM and EKF.

the retrieved phase and displacement have ripples caused by the noise of the SMI signal, and the EKF can effectively smooth them.

In conclusion, under the weak feedback regime, the displacement retrieval method based on the EKF has good tracking behavior for both the sinusoid displacement and the aleatory displacement. The comparison between the IPUM and EKF illustrates that the EKF can correctly reconstruct the displacement and reduce the effect of the noise. The results of the proposed method are very encouraging, especially when compared with the results obtained from the derivative processing. As demonstrated in theory, the displacement of the target is retrieved without any problem in the case of weak feedback regime ($C < 1$).

5.3.5 Conclusion

An algorithm based on the theory of EKF is proposed in this section for retrieving displacement using the SMI sensor under weak feedback regime. According to the behavior model of the SMI signal, the phase of the signal and the displacement of the target are obtained by the tracking algorithm. The main novelty of the algorithm is the ability to discriminate the direction of the displacement inherently without extra effort. It discards the process of normalization, transition detection, and feedback factor C estimation of the

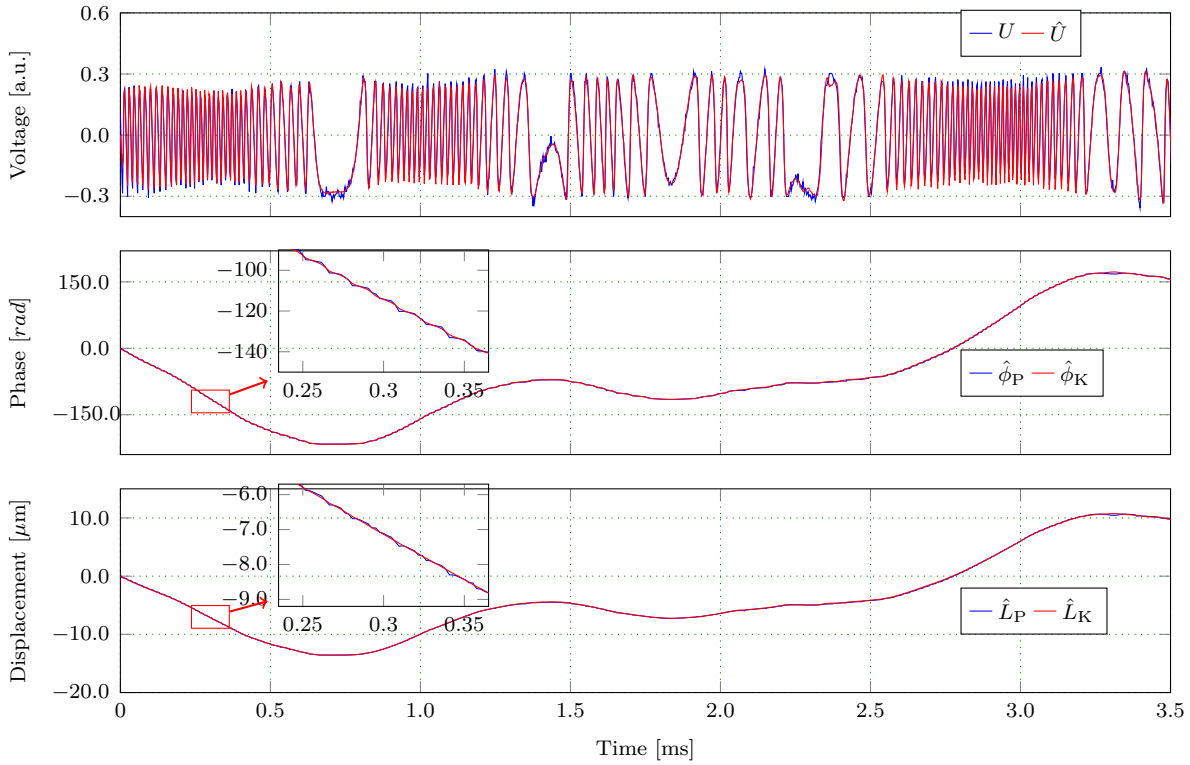

Figure 5.24: Experimental reconstruction of an aleatory displacement using the EKF method.

general PUM. The simulation is conducted with both sinusoid and aleatory displacement under ideal and noisy conditions. It has been tested for estimating random and sinusoidal displacements at different target vibration frequencies. The experimental results confirm that comparing to the IPUM, the EKF can retrieve sinusoidal displacement and aleatory displacement under the weak feedback regime.

5.4 Summary

This chapter closely studied the use of SMI for displacement measurement. A novel method was proposed to estimate the factor C under weak and moderate feedback regimes with less calculation. Without the complicated and tedious calculation process of the general C estimation method, a final equation is obtained with the proposed method. On this basis, the KF was used to improve the results obtained by the general IPUM and this simple C estimation method. Besides, an EKF based method was investigated to estimate displacement under the weak feedback regime. In comparison with the traditional PUM, the EKF does not require the tedious process of normalization, transition detection, C estimation, etc. The experimental verification confirmed that the EKF could estimate the displacement from the SMI signal.

Chapter 6

Conclusions and future prospects

6.1 Conclusions

This dissertation was started with the purpose to optimize the velocity measurement in electric drives. Another solution for velocity measurement was then investigated by using the laser SMI, which provides good flexibility and a compact system. Accordingly, the application and improvement of the SMI in displacement measurement have also been discussed in detail.

In Chapter 2, traditional methods estimating position, velocity, and acceleration from the position signal in the optical encoder were introduced. Then the theory of laser SMI was fully detailed, including the resonator model and rate equation mode, as well as the applications of SMI.

In Chapter 3, an efficient and tuning-easy solution called FGF was proposed to estimate position, velocity, and acceleration from the shaft encoder position. The novelty is that, unlike the conventional KF that requires an online tuning process of the feedback gain matrix, the proposed FGF uses an optimal fixed feedback gain matrix obtained through a straight-forward calculation process. The experimental results and implementation steps show that the FGF significantly reduces the computational burden and executive time. Additionally, the proposed filter has a single tunable parameter, which greatly eases the required tuning work. The property of a fixed gain and a narrow tunable range would considerably simplify the application of the proposed FGF strategy in industry.

In Chapter 4, an in-depth study of the system using the SMI to measure velocity was conducted. The self-designed test bench for experiments has been presented. Error analysis and different algorithms for accurately measuring velocity were discussed.

The parabolic fit algorithm considering the Gaussian distribution of the time-domain

signal and the spectral broadening of the frequency-domain signal was compared with the traditional interpolation methods. Their performance has been evaluated on the test-bench, and the experimental results showed that this method could be applied when the signal is interfered by the speckle effect.

Then a parameter method based on the MLE was presented in the case of the signal with a wider spectrum broadening. It optimizes the estimated parameters through an iterative process and generates accurate estimates. This parameter optimization was implemented in the frequency domain, and it may also be realized in the correlation domain. Its performance has been verified in both simulation and experimental data. In comparison with the FFT method and the FH method, the RMS frequency error and relative error of MLE method were slightly reduced.

To reduce the data record length required by traditional FFT based methods, according to the model of SMI signal, a new algorithm based on the EKF for velocity estimation in the SMI was proposed. The multiplicative noise caused by the speckle effect and the direction of the velocity were taken into account. The numerical simulations and experimental verification illustrated that this parametric method can track the velocity and displacement and discriminate the direction of movement without any other calculation or modulation, even when the feedback level is weak.

In Chapter 5, the SMI measuring displacement was deeply studied. A simple and effective method for estimating the feedback factor C in the SMI sensor was presented to retrieve displacement. Discarding the complicated and tedious calculation process of the general C estimation method, a final equation was obtained. Hence, the estimation of C only involved several simple calculations. It successfully retrieved the sinusoidal and aleatory displacement with simulated SMI signals and experimental data in both weak and moderate feedback regimes. To deal with the errors resulting from the noise and to further improve the retrieval precision, the KF was adopted.

Finally, the method based on the theory of EKF applied to retrieve displacement from the SMI sensor under weak feedback has been theoretically interpreted and experimentally assessed. It does not need the tedious process of normalization, transition detection, C estimation, etc. Another advantage of this algorithm is the ability to inherently discriminate the direction of the displacement, and no extra effort is required. The experiment results confirmed that the phase of SMI signal and the optical feedback factor C were properly obtained and the displacement was correctly calculated from them. The experimental comparison with the IPUM showed that the EKF can smooth out the noise in the retrieved displacement.

6.2 Future prospects

The FGF was used to estimate position, velocity, and acceleration from the optical encoder signal in electrical drives. It can also be used in other position feedback fields in industry, such as sensor-less control, grid synchronous, and motion control, etc. Further study using the FGF in these fields could be conducted in future work.

Many challenges need to be overcome to realize the practical application of the SMI for velocity and displacement measurement. Many new areas can yet be explored, and some points from this work can be further extended. Some ideas along these lines are presented below.

- At present, a DSP based electronic board is being designed so that various algorithms can be deployed onto it. To realize a robust, reliable, and compact sensor, the algorithms and the hardware should be further optimized.
- In this work, the bandwidth of the preprocessing system is 1.8 MHz. Future contributions in this area would be increasing the bandwidth of the circuit to extend the measuring range of velocity.

Abbreviations

AC	alternating current
ARM	advanced reduced instruction set computing machine
CRLB	Cramér–Rao Lower Bound
DC	direct current
DFB	distributed feedback
DFT	discrete Fourier transform
DSP	digital signal processor
EKF	extended Kalman filter
ETKF	edge-time Kalman filter
FDM	finite-difference method
FFT	fast Fourier transform
FGF	fixed gain filter
FH	FFT and Hanning interpolation
FLP	floating point
FP	FFT and parabolic fit
FPU	floating point unit
FPUE	floating point unit emulator
FR	FFT and rectangular interpolation
FWHM	full-width half-maximum
FXP	fixed point
HPF	high-pass filter
IFFT	interpolated fast Fourier transform
IPUM	improved phase unwrapping method
ITM	inverse-time method
JEM	joint estimation method
KF	Kalman filter
LDA	laser Doppler anemometer
LDV	laser Doppler velocimeter
LPF	low-pass filter
LUT	look-up table
MAAE	maximum absolute error
MAE	mean absolute error
MATLAB	matrix laboratory

MCU	micro-controller unit
MEMS	micro-electro-mechanical-systems
MLE	maximum likelihood estimation
MQW	multi-quantum well
MUSIC	multiple signal classification
NRMSE	normalized root-mean-square error
PCB	printed circuit board
PDF	probability density function
PLL	phase-locked loop
PPR	pulses per revolution
PSD	power spectral density
PUM	phase unwrapping method
RMS	root mean square
RMSE	root mean square error
RPM	revolutions per minute
SEM	simple estimation method
SMI	self-mixing interferometry
SNR	signal to noise ratio
TIA	trans-impedance amplifier
TNI	total number of iterations

List of Publications

1. Hui Sun, Ji-Gou Liu, Quan Zhang, and Ralph Kennel, "Self-mixing interferometry for rotational speed measurement of servo drives," Applied Optics 55, 236-241 (2016).

2. Hui Sun, Ji-Gou Liu, and Ralph Kennel, "Effect of injection current on laser self-mixing interferometry for velocity measurement," in Imaging and Applied Optics 2016, OSA Technical Digest (online) (Optical Society of America, 2016), paper JT3A.4.

3. Hui Sun, Ji-Gou Liu, and Ralph Kennel, "Improving the accuracy of laser self-mixing interferometry for velocity measurement," 2017 IEEE International Instrumentation and Measurement Technology Conference (I2MTC), Turin, 2017, pp. 1-5.

4. Hui Sun, Ji-Gou Liu, "A novel algorithm for laser self-mixing sensors used with the Kalman filter to measure displacement" Measurement Science and Technology, Measurement Science and Technology 29, 075204 (2018)

5. Cheng Liu, Yanan Xu, Ji-Gou Liu, Hui Sun, Ralph Kennel, "Rotational Speed Measurement Based on Avago ADNS-9800 Laser Mouse Sensor," PCIM Europe 2016; International Exhibition and Conference for Power Electronics, Intelligent Motion, Renewable Energy and Energy Management, Nuremberg, Germany, 2016, pp. 1-5.

6. Cheng Liu, Yanan Xu, Ji-Gou Liu, Hui Sun, Ralph Kennel, "Rotational Speed Measurement Based on Laser Mouse Sensors," in 18. GMA/ITG-Fachtagung Sensoren und Messsysteme 2016, 2016, pp. 540–545.

Bibliography

[1] M. Faccio, P. Grande, F. Parasiliti, R. Petrella, and M. Tursini, "An embedded system for position and speed measurement adopting incremental encoders," in *Conference Record of the 2004 IEEE Industry Applications Conference, 2004. 39th IAS Annual Meeting.*, vol. 2, Oct 2004, pp. 1192–1199 vol.2.

[2] Y. X. Su, C. H. Zheng, P. C. Mueller, and B. Y. Duan, "A simple improved velocity estimation for low-speed regions based on position measurements only," *IEEE Transactions on Control Systems Technology*, vol. 14, no. 5, pp. 937–942, Sep. 2006.

[3] N. Peterfreund, "Robust tracking of position and velocity with kalman snakes," *IEEE Transactions on Pattern Analysis and Machine Intelligence*, vol. 21, no. 6, pp. 564–569, Jun 1999.

[4] P. R. Belanger, "Estimation of angular velocity and acceleration from shaft encoder measurements," in *Proceedings 1992 IEEE International Conference on Robotics and Automation*, May 1992, pp. 585–592 vol.1.

[5] H.-W. Kim and S.-K. Sul, "A new motor speed estimator using kalman filter in low speed range," in *Industrial Electronics, Control and Instrumentation, 1994. IECON '94., 20th International Conference on*, vol. 1, Sep 1994, pp. 503–508 vol.1.

[6] T. Shi, Z. Wang, and C. Xia, "Speed measurement error suppression for pmsm control system using self-adaption kalman observer," *IEEE Transactions on Industrial Electronics*, vol. 62, no. 5, pp. 2753–2763, May 2015.

[7] S.-M. Yang and S.-J. Ke, "Performance evaluation of a velocity observer for accurate velocity estimation of servo motor drives," *IEEE Transactions on Industry Applications*, vol. 36, no. 1, pp. 98–104, Jan 2000.

[8] P. Drabarek and R. M. Kennel, "Are interferometric encoders a reasonable alternative in servo drive applications?" in *2008 4th IET Conference on Power Electronics, Machines and Drives*, April 2008, pp. 149–153.

[9] W.-J. Wu, C.-K. Lee, and C.-T. Hsieh, "Signal processing algorithms for doppler effect based nanometer positioning systems," *Japanese Journal of Applied Physics*, vol. 38, no. Part 1, No. 3B, pp. 1725–1729, mar 1999. [Online]. Available: https://doi.org/10.1143%2Fjjap.38.1725

[10] P. Suni and C. Grund, "Self-mixing sensor apparatus and method," U.S. Patent 6 233 045, May 15, 2001.

[11] M. Liess and G. Mimnagh-Kelleher, "Method of measuring the movement of a material sheet and optical sensor for performing the method," U.S. Patent 6 759 671, July 6, 2004.

[12] M. Liess, A. Weijers, and O. Vermeulen, "Method of measuring the movement of an input device," U.S. Patent 6 707 027, March 16, 2004.

[13] M. Liess, C. Dobrusskin, and A. Weijers, "Optical input device for measuring finger movement," U.S. Patent 6 872 931, March 29, 2005.

[14] M. Liess and A. Weijers, "Laser measurement apparatus using self-mixing effect," U.S. Patent 7 439 484, October 21, 2008.

[15] M. Liess, "Movement sensor," U.S. Patent 7 619 744, November 17, 2009.

[16] M. Liess, C. Heinks, A. Weijers, and M. V. Os, "Method of measuring the movement of an input device," U.S. Patent 7 589 709, September 15, 2009.

[17] A. H. M. Akkermans and C. Heinks, "Apparatus and method for detecting blood flow," U.S. Patent 7 708 695, May 4, 2010.

[18] C. Heinks and M. Schemmann, "Device and method for measuring relative movement," U.S. Patent 7 920 249, April 5, 2012.

[19] J. Xie, H. Ming, T. Zhao, L. Lv, H. Gui, Y. Kong, and C. Ranta, "Data input devices and methods for detecting movement of a tracking surface by detecting laser doppler self-mixing effects of a frequency modulated laser light beam," U.S. Patent 7 126 586, October 24, 2006.

[20] Y. Kong, "Laser velocimetric image scanning," U.S. Patent 7 543 750, June 9, 2009.

[21] Y. Kong, C. Ranta, T. Zhao, H. Ming, J. Xie, J. Xu, and D. He, "Laser velocimetric image scanning," U.S. Patent 7 557 795, July 7, 2009.

[22] K. Werner, C. Heinks, and M. Schemmann, "Laser self-mixing measuring device," U.S. Patent 8 416 424, April 9, 2013.

[23] E. McKenna, "Laser self-mixing sensors for biological sensing," U.S. Patent 8 532 751, September 10, 2013.

[24] H. Moench, M. Carpaij, A. V. D. Lee, S. Schwan, M. Han, and M. Schemmann, "Laser sensor system based on self-mixing interference," U.S. Patent 8 692 979, April 8, 2014.

[25] M. Han, A. Kraus, and H. Moench, "Security system comprising a self-mixing laser sensor and method of driving such a security system," U.S. Patent 8 781 687, July 15, 2014.

[26] H. Moench, M. Carpaij, and A. Comberg, "Sensor system, vehicle control system and driver information system for vehicle safety," U.S. Patent 8 751 091, June 10, 2014.

[27] M. Han, "Laser diode based self-mixing sensor for a vehicle electronic stability program," U.S. Patent 8 725 310, May 13, 2014.

[28] *VCSEL-based miniature laser-Doppler interferometer*, vol. 6908, 2008. [Online]. Available: https://doi.org/10.1117/12.775131

[29] *A VCSEL-based miniature laser-self-mixing interferometer with integrated optical and electronic components*, vol. 7221, 2009. [Online]. Available: https://doi.org/10.1117/12.808810

[30] M. Norgia and S. Donati, "A displacement-measuring instrument utilizing self-mixing interferometry," *IEEE Transactions on Instrumentation and Measurement*, vol. 52, no. 6, pp. 1765–1770, Dec 2003.

[31] F. F. M. de Mul, M. H. Koelink, A. L. Weijers, J. Greve, J. G. Aarnoudse, R. Graaff, and A. C. M. Dassel, "Self-mixing laser-doppler velocimetry of liquid flow and of blood perfusion in tissue," *Appl. Opt.*, vol. 31, no. 27, pp. 5844–5851, Sep 1992. [Online]. Available: http://ao.osa.org/abstract.cfm?URI=ao-31-27-5844

[32] M. Nikolić, E. Hicks, Y. L. Lim, K. Bertling, and A. D. Rakić, "Self-mixing laser doppler flow sensor: an optofluidic implementation," *Appl. Opt.*, vol. 52, no. 33, pp. 8128–8133, Nov 2013. [Online]. Available: http://ao.osa.org/abstract.cfm?URI=ao-52-33-8128

[33] M. Norgia, A. Pesatori, and S. Donati, "Laser diode for flow-measurement," in *2015 IEEE International Instrumentation and Measurement Technology Conference (I2MTC) Proceedings*, May 2015, pp. 1391–1394.

[34] S. Donati and M. Norgia, "Self-mixing interferometry for biomedical signals sensing," *IEEE Journal of Selected Topics in Quantum Electronics*, vol. 20, no. 2, pp. 104–111, March 2014.

[35] C. Bes, G. Plantier, and T. Bosch, "Displacement measurements using a self-mixing laser diode under moderate feedback," *IEEE Transactions on Instrumentation and Measurement*, vol. 55, no. 4, pp. 1101–1105, Aug 2006.

[36] G. Plantier, C. Bes, T. Bosch, and F. Bony, "Auto adaptive signal processing of a laser diode self-mixing displacement sensor," in *2005 IEEE Instrumentationand Measurement Technology Conference Proceedings*, vol. 2, May 2005, pp. 1013–1017.

[37] F. P. Mezzapesa, L. Columbo, M. Brambilla, M. Dabbicco, A. Ancona, T. Sibillano, F. D. Lucia, P. M. Lugarà, and G. Scamarcio, "Simultaneous measurement of multiple target displacements by self-mixing interferometry in a single laser diode," *Opt. Express*, vol. 19, no. 17, pp. 16 160–16 173, Aug 2011. [Online]. Available: http://www.opticsexpress.org/abstract.cfm?URI=oe-19-17-16160

[38] F. Gouaux, N. Servagent, and T. Bosch, "Absolute distance measurement with an optical feedback interferometer," *Appl. Opt.*, vol. 37, no. 28, pp. 6684–6689, Oct 1998. [Online]. Available: http://ao.osa.org/abstract.cfm?URI=ao-37-28-6684

[39] T. Bosch, N. Servagent, and F. Boyer, "Vibrations measurements with a self-mixing type laser displacement sensor for modal analysis," in *Quality Measurement: The Indispensable Bridge between Theory and Reality (No Measurements? No Science! Joint Conference - 1996: IEEE Instrumentation and Measurement Technology Conference and IMEKO Tec*, vol. 1, 1996, pp. 648–653 vol.1.

[40] M. Norgia, G. Giuliani, and S. Donati, "Absolute distance measurement with improved accuracy using laser diode self-mixing interferometry in a closed loop," *IEEE Transactions on Instrumentation and Measurement*, vol. 56, no. 5, pp. 1894–1900, Oct 2007.

[41] O. D. Bernal, U. Zabit, and T. Bosch, "Study of laser feedback phase under self-mixing leading to improved phase unwrapping for vibration sensing," *IEEE Sensors Journal*, vol. 13, no. 12, pp. 4962–4971, Dec 2013.

[42] G. Martini, E. Randone, and S. Donati, "Very low frequency self-mixing laser diode vibrometer," in *2012 IEEE Sensors*, Oct 2012, pp. 1–4.

[43] S. Donati, *Electro-Optical Instrumentation: Sensing and Measuring with Lasers.* Prentice Hall, 2004.

[44] L. Scalise, Y. Yu, G. Giuliani, G. Plantier, and T. Bosch, "Self-mixing laser diode velocimetry: application to vibration and velocity measurement," *IEEE Transactions on Instrumentation and Measurement*, vol. 53, no. 1, pp. 223–232, Feb 2004.

[45] *Encoders for Servo Drives*, Heidenhain, November 2016.

[46] R. E. Kalman, "A new approach to linear filtering and prediction problems," *Transactions of the ASME–Journal of Basic Engineering*, vol. 82, no. Series D, pp. 35–45, 1960.

[47] G. Welch and G. Bishop, "An introduction to the kalman filter," Department of Computer Science, University of North Carolina, Tech. Rep. TR 95-041, 2001.

[48] C. Risch and C. Voumard, "Self-pulsation in the output intensity and spectrum of gaas-algaas cw diode lasers coupled to a frequency-selective external optical cavity," *Journal of Applied Physics*, vol. 48, no. 5, pp. 2083–2085, 1977. [Online]. Available: https://doi.org/10.1063/1.323922

[49] C. Voumard, "External-cavity-controlled 32-mhz narrow-band cw gaalas-diode lasers," *Opt. Lett.*, vol. 1, no. 2, pp. 61–63, Aug 1977. [Online]. Available: http://ol.osa.org/abstract.cfm?URI=ol-1-2-61

[50] J. Ohtsubo, *Semiconductor Lasers*, 4th ed. Springer, 2017.

[51] K. Petermann, *Semiconductor Lasers with Optical Feedback*. Dordrecht: Springer Netherlands, 1988, pp. 250–290.

[52] W. M. Wang, K. T. V. Grattan, A. W. Palmer, and W. J. O. Boyle, "Self-mixing interference inside a single-mode diode laser for optical sensing applications," *Journal of Lightwave Technology*, vol. 12, no. 9, pp. 1577–1587, Sep 1994.

[53] J. Y. Law and G. P. Agrawal, "Effects of optical feedback on static and dynamic characteristics of vertical-cavity surface-emitting lasers," *IEEE Journal of Selected Topics in Quantum Electronics*, vol. 3, no. 2, pp. 353–358, Apr 1997.

[54] ——, "Feedback-induced chaos and intensity-noise enhancement in vertical-cavity surface-emitting lasers," *J. Opt. Soc. Am. B*, vol. 15, no. 2, pp. 562–569, Feb 1998. [Online]. Available: http://josab.osa.org/abstract.cfm?URI=josab-15-2-562

[55] K. I. Kallimani and M. J. O'Mahony, "Relative intensity noise for laser diodes with arbitrary amounts of optical feedback," *IEEE Journal of Quantum Electronics*, vol. 34, no. 8, pp. 1438–1446, Aug 1998.

[56] Y. Yu, H. Ye, and J. Yao, "Analysis for the self-mixing interference effects in a laser diode at high optical feedback levels," *Journal of Optics A: Pure and Applied Optics*, vol. 5, no. 2, p. 117, 2003. [Online]. Available: http://stacks.iop.org/1464-4258/5/i=2/a=307

[57] J. Ohtsubo, *Semiconductor Lasers Stability, Instability and Chaos*. Springer, 2013.

[58] D. D. Cook and F. R. Nash, "Gain-induced guiding and astigmatic output beam of gaas lasers," *Journal of Applied Physics*, vol. 46, no. 4, pp. 1660–1672, 1975. [Online]. Available: https://doi.org/10.1063/1.321769

[59] M. Osinski and J. Buus, "Linewidth broadening factor in semiconductor lasers–an overview," *IEEE Journal of Quantum Electronics*, vol. 23, no. 1, pp. 9–29, January 1987.

[60] N. Schunk and K. Petermann, "Numerical analysis of the feedback regimes for a single-mode semiconductor laser with external feedback," *IEEE Journal of Quantum Electronics*, vol. 24, no. 7, pp. 1242–1247, Jul 1988.

[61] G. Giuliani, M. Norgia, S. Donati, and T. Bosch, "Laser diode self-mixing technique for sensing applications," *Journal of Optics A: Pure and Applied Optics*, vol. 4, no. 6, p. S283, 2002. [Online]. Available: http://stacks.iop.org/1464-4258/4/i=6/a=371

[62] M. H. Koelink, M. Slot, F. F. M. de Mul, J. Greve, R. Graaff, A. C. M. Dassel, and J. G. Aarnoudse, "Laser doppler velocimeter based on the self-mixing effect in a fiber-coupled semiconductor laser: theory," *Appl. Opt.*, vol. 31, no. 18, pp. 3401–3408, Jun 1992. [Online]. Available: http://ao.osa.org/abstract.cfm?URI=ao-31-18-3401

[63] D. M. Kane and K. A. Shore, *Unlocking Dynamical Diversity: Optical Feedback Effects on Semiconductor Lasers*. Wiley, 2005.

[64] R. Lang and K. Kobayashi, "External optical feedback effects on semiconductor injection laser properties," *IEEE Journal of Quantum Electronics*, vol. 16, no. 3, pp. 347–355, Mar 1980.

[65] M. J. Rudd, "A laser doppler velocimeter employing the laser as a mixer-oscillator," *Journal of Physics E: Scientific Instruments*, vol. 1, no. 7, p. 723, 1968.

[66] S. Donati, "Laser interferometry by induced modulation of cavity field," *Journal of Applied Physics*, vol. 49, no. 2, pp. 495–497, 1978. [Online]. Available: https://doi.org/10.1063/1.324672

[67] D. S., "Developing self-mixing interferometry for instrumentation and measurements," *Laser and Photonics Reviews*, vol. 6, no. 3, pp. 393–417, 2012. [Online]. Available: http://dx.doi.org/10.1002/lpor.201100002

[68] S. Donati and G. Martini, "Self-mixing interferometry: A universal yardstick for optical measurements," in *2011 10th Euro-American Workshop on Information Optics*, June 2011, pp. 1–3.

[69] M. Nikolic, D. P. Jovanovi, Y. L. Lim, K. Bertling, T. Taimre, and A. D. Rakic, "Approach to frequency estimation in self-mixing interferometry: multiple signal classification," *Appl. Opt.*, vol. 52, no. 14, pp. 3345–3350, May 2013.

[70] S. Donati and M. Sorel, "A phase-modulated feedback method for testing optical isolators assembled into the laser diode package," *IEEE Photonics Technology Letters*, vol. 8, no. 3, pp. 405–407, March 1996.

[71] G. Giuliani, M. Norgia, and S. Donati, "Laser diode linewidth measurement by means of self-mixing interferometry," in *LEOS '99. IEEE Lasers and Electro-Optics Society 1999 12th Annual Meeting*, vol. 2, 1999, pp. 726–727 vol.2.

[72] Yanguang Yu, G. Giuliani, and S. Donati, "Measurement of the linewidth enhancement factor of semiconductor lasers based on the optical feedback self-mixing effect," *IEEE Photonics Technology Letters*, vol. 16, no. 4, pp. 990–992, April 2004.

[73] Jiangtao Xi, Yanguang Yu, J. F. Chicharo, and T. Bosch, "Estimating the parameters of semiconductor lasers based on weak optical feedback self-mixing interferometry," *IEEE Journal of Quantum Electronics*, vol. 41, no. 8, pp. 1058–1064, Aug 2005.

[74] M. Norgia, A. Pesatori, and C. Svelto, "Novel interferometric method for the measurement of laser wavelength/frequency-modulation sensitivity," *IEEE Transactions on Instrumentation and Measurement*, vol. 56, no. 4, pp. 1373–1376, Aug 2007.

[75] M. T. Fathi and S. Donati, "Thickness measurement of transparent plates by a self-mixing interferometer," *Opt. Lett.*, vol. 35, no. 11, pp. 1844–1846, Jun 2010. [Online]. Available: http://ol.osa.org/abstract.cfm?URI=ol-35-11-1844

[76] T. Dresel, G. Häusler, and H. Venzke, "Three-dimensional sensing of rough surfaces by coherence radar," *Appl. Opt.*, vol. 31, no. 7, pp. 919–925, Mar 1992. [Online]. Available: http://ao.osa.org/abstract.cfm?URI=ao-31-7-919

[77] P. J. Caber, "Interferometric profiler for rough surfaces," *Appl. Opt.*, vol. 32, no. 19, pp. 3438–3441, Jul 1993. [Online]. Available: http://ao.osa.org/abstract.cfm?URI=ao-32-19-3438

[78] S. Donati, M. Nogia, V. A. Lodi, and S. Merlo, "Measurement of mems mechanical parameters by injection interferometry," in *2000 IEEE/LEOS International Conference on Optical MEMS (Cat. No.00EX399)*, Aug 2000, pp. 89–90.

[79] V. Annovazzi-Lodi, S. Merlo, and M. Norgia, "Measurements on a micromachined silicon gyroscope by feedback interferometry," *IEEE/ASME Transactions on Mechatronics*, vol. 6, no. 1, pp. 1–6, Mar 2001.

[80] V. Annovazzi-Lodi, M. Benedetti, S. Merlo, and M. Norgia, "Spot optical measurements on micromachined mirrors for photonic switching," *IEEE Journal of Selected Topics in Quantum Electronics*, vol. 10, no. 3, pp. 536–544, May 2004.

[81] G. Beheim and K. Fritsch, "Range finding using frequency-modulated laser diode," *Appl. Opt.*, vol. 25, no. 9, pp. 1439–1442, May 1986. [Online]. Available: http://ao.osa.org/abstract.cfm?URI=ao-25-9-1439

[82] S. Shinohara, A. Mochizuki, H. Yoshida, and M. Sumi, "Laser doppler velocimeter using the self-mixing effect of a semiconductor laser diode," *Appl. Opt.*, vol. 25, no. 9, pp. 1417–1419, May 1986. [Online]. Available: http://ao.osa.org/abstract.cfm?URI=ao-25-9-1417

[83] *In-vivo blood flow velocity measurements using the self-mixing effect in a fiber-coupled semiconductor laser*, vol. 1511, 1991. [Online]. Available: https://doi.org/10.1117/12.45984

[84] S. K. Ozdemir, S. Shinohara, S. Takamiya, and H. Yoshida, "Noninvasive blood flow measurement using speckle signals from a self-mixing laser diode: in vitro and in vivo experiments," *Optical Engineering*, vol. 39, pp. 39 – 39 – 7, 2000. [Online]. Available: https://doi.org/10.1117/1.1287262

[85] E. T. Shimizu, "Directional discrimination in the self-mixing type laser doppler velocimeter," *Appl. Opt.*, vol. 26, no. 21, pp. 4541–4544, Nov 1987. [Online]. Available: http://ao.osa.org/abstract.cfm?URI=ao-26-21-4541

[86] S. Shinohara, H. Naito, H. Yoshida, H. Ikeda, and M. Sumi, "Compact and versatile self-mixing type semiconductor laser doppler velocimeters with direction-discrimination circuit," *IEEE Transactions on Instrumentation and Measurement*, vol. 38, no. 2, pp. 574–577, Apr 1989.

[87] S. Donati, L. Falzoni, and S. Merlo, "A pc-interfaced, compact laser-diode feedback interferometer for displacement measurements," *IEEE Transactions on Instrumentation and Measurement*, vol. 45, no. 6, pp. 942–947, Dec 1996.

[88] A. Magnani, A. Pesatori, and M. Norgia, "Self-mixing vibrometer with real-time digital signal elaboration," *Appl. Opt.*, vol. 51, no. 21, pp. 5318–5325, Jul 2012. [Online]. Available: http://ao.osa.org/abstract.cfm?URI=ao-51-21-5318

[89] N. Tsukuda, S. Shinohara, T. Shibata, H. Yoshida, H. Ikeda, and M. Sumi, "New range-finding speedometer using a self-mixing laser diode modulated by triangular wave pulse current," in *Conference Proceedings. 10th Anniversary. IMTC/94. Advanced Technologies in I M. 1994 IEEE Instrumentation and Measurement Technolgy Conference (Cat. No.94CH3424-9)*, May 1994, pp. 332–335 vol.1.

[90] M. Liess, G. Weijers, C. Heinks, A. van der Horst, A. Rommers, R. Duijve, and G. Mimnagh, "A miniaturized multidirectional optical motion sensor and input device based on laser self-mixing," *Measurement Science and Technology*, vol. 13, no. 12, p. 2001, 2002. [Online]. Available: http://stacks.iop.org/0957-0233/13/i=12/a=327

[91] A. Magnani, A. Pesatori, and M. Norgia, "Real-time self-mixing interferometer for long distances," *IEEE Transactions on Instrumentation and Measurement*, vol. 63, no. 7, pp. 1804–1809, July 2014.

[92] A. Magnani and M. Norgia, "Spectral analysis for velocity measurement through self-mixing interferometry," *IEEE Journal of Quantum Electronics*, vol. 49, no. 9, pp. 765–769, Sept 2013.

[93] S. Donati, G. Giuliani, and S. Merlo, "Laser diode feedback interferometer for measurement of displacements without ambiguity," *IEEE Journal of Quantum Electronics*, vol. 31, no. 1, pp. 113–119, Jan 1995.

[94] N. Servagent, T. Bosch, and M. Lescure, "Design of a phase-shifting optical feedback interferometer using an electrooptic modulator," *IEEE Journal of Selected Topics in Quantum Electronics*, vol. 6, no. 5, pp. 798–802, Sept 2000.

[95] N. Servagent, F. Gouaux, and T. Bosch, "Measurements of displacement using the self-mixing interference in a laser diode," *Journal of Optics*, vol. 29, no. 3, p. 168, 1998.

[96] S. Merlo and S. Donati, "Reconstruction of displacement waveforms with a single-channel laser-diode feedback interferometer," *IEEE Journal of Quantum Electronics*, vol. 33, no. 4, pp. 527–531, Apr 1997.

[97] *Self-mixing laser diode vibrometer with wide dynamic range*, vol. 4827, 2002. [Online]. Available: https://doi.org/10.1117/12.468177

[98] G. Giuliani, S. Bozzi-Pietra, and S. Donati, "Self-mixing laser diode vibrometer," *Measurement Science and Technology*, vol. 14, no. 1, p. 24, 2003. [Online]. Available: http://stacks.iop.org/0957-0233/14/i=1/a=304

[99] M.-C. Amann, T. M. Bosch, R. A. M. Marc Lescure, and M. Rioux, "Laser ranging: a critical review of unusual techniques for distance measurement," *Optical Engineering*, vol. 40, pp. 40 – 40 – 10, 2001. [Online]. Available: https://doi.org/10.1117/1.1330700

[100] S. Ottonelli, F. D. Lucia, M. di Vietro, M. Dabbicco, G. Scamarcio, and F. P. Mezzapesa, "A compact three degrees-of-freedom motion sensor based on the laser-self-mixing effect," *IEEE Photonics Technology Letters*, vol. 20, no. 16, pp. 1360–1362, Aug 2008.

[101] M. Dabbicco, A. Intermite, and G. Scamarcio, "Laser-self-mixing fiber sensor for integral strain measurement," *J. Lightwave Technol.*, vol. 29, no. 3, pp. 335–340, Feb 2011. [Online]. Available: http://jlt.osa.org/abstract.cfm?URI=jlt-29-3-335

[102] Y. Yu, J. Xi, J. F. Chicharo, and T. Bosch, "Toward automatic measurement of the linewidth-enhancement factor using optical feedback self-mixing interferometry with weak optical feedback," *IEEE Journal of Quantum Electronics*, vol. 43, no. 7, pp. 527–534, July 2007.

[103] J. Hast, R. Myllylä, H. Sorvoja, and J. Miettinen, "Arterial pulse shape measurement using self-mixing effect in a diode laser," *Quantum Electronics*, vol. 32, no. 11, p. 975, 2002. [Online]. Available: http://stacks.iop.org/1063-7818/32/i=11/a=A07

[104] L. Campagnolo, S. Roman, J. Perchoux, and S. Lorthois, "A new optical feedback interferometer for measuring red blood cell velocity distributions in individual capillaries: a feasibility study in microchannels," *Computer Methods in Biomechanics and Biomedical Engineering*, vol. 15, no. sup1, pp. 104–105, 2012. [Online]. Available: https://doi.org/10.1080/10255842.2012.713651

[105] J. C. A. Courteville, Tijani Gharbi, "Noncontact mmg sensor based on the optical feedback effect in a laser diode," *Journal of Biomedical Optics*, vol. 3, no. 3, pp. 281 – 285 – 5, 1998. [Online]. Available: https://doi.org/10.1117/1.429891

[106] V. Annovazzi-Lodi, S. Merlo, and M. Norgia, "Comparison of capacitive and feedback-interferometric measurements on mems," *Journal of Microelectromechanical Systems*, vol. 10, no. 3, pp. 327–335, Sep 2001.

[107] ——, "Characterization of silicon microstructures by feedback interferometry," *Journal of Optics A: Pure and Applied Optics*, vol. 4, no. 6, p. S311, 2002. [Online]. Available: http://stacks.iop.org/1464-4258/4/i=6/a=374

[108] E. Sadıkoğlu, E. Bilgiç, and B. Karaböce, "A laser pistonphone based on self-mixing interferometry for the absolute calibration of measurement microphones,"

Applied Acoustics, vol. 65, no. 9, pp. 833 – 840, 2004. [Online]. Available: http://www.sciencedirect.com/science/article/pii/S0003682X04000507

[109] O. Wallmark, L. Harnefors, and O. Carlson, "An improved speed and position estimator for salient permanent-magnet synchronous motors," *IEEE Transactions on Industrial Electronics*, vol. 52, no. 1, pp. 255–262, Feb 2005.

[110] C. K. Lai and K.-K. Shyu, "A novel motor drive design for incremental motion system via sliding-mode control method," *IEEE Transactions on Industrial Electronics*, vol. 52, no. 2, pp. 499–507, April 2005.

[111] Z. Z. Liu, F. L. Luo, and M. A. Rahman, "Robust and precision motion control system of linear-motor direct drive for high-speed x-y table positioning mechanism," *IEEE Transactions on Industrial Electronics*, vol. 52, no. 5, pp. 1357–1363, Oct 2005.

[112] R. D. Lorenz and K. W. V. Patten, "High-resolution velocity estimation for all-digital, ac servo drives," *IEEE Transactions on Industry Applications*, vol. 27, no. 4, pp. 701–705, Jul 1991.

[113] R. Petrella, M. Tursini, L. Peretti, and M. Zigliotto, "Speed measurement algorithms for low-resolution incremental encoder equipped drives: a comparative analysis," in *2007 International Aegean Conference on Electrical Machines and Power Electronics*, Sept 2007, pp. 780–787.

[114] J. Lara, J. Xu, and A. Chandra, "A novel algorithm based on polynomial approximations for an efficient error compensation of magnetic analog encoders in pmsms for evs," *IEEE Transactions on Industrial Electronics*, vol. 63, no. 6, pp. 3377–3388, June 2016.

[115] J. Kim and B. K. Kim, "Development of precise encoder edge-based state estimation for motors," *IEEE Transactions on Industrial Electronics*, vol. 63, no. 6, pp. 3648–3655, June 2016.

[116] M. Saha, R. Ghosh, and B. Goswami, "Robustness and sensitivity metrics for tuning the extended kalman filter," *IEEE Transactions on Instrumentation and Measurement*, vol. 63, no. 4, pp. 964–971, April 2014.

[117] H. Shu, E. P. Simon, and L. Ros, "Third-order kalman filter: Tuning and steady-state performance," *IEEE Signal Processing Letters*, vol. 20, no. 11, pp. 1082–1085, Nov 2013.

[118] T. Benedict and G. Bordner, "Synthesis of an optimal set of radar track-while-scan smoothing equations," *IRE Transactions on Automatic Control*, vol. 7, no. 4, pp. 27–32, Jul 1962.

[119] D. F. Crouse, "A general solution to optimal fixed-gain (α - β - γ etc.) filters," *IEEE Signal Processing Letters*, vol. 22, no. 7, pp. 901–904, July 2015.

[120] B. Friedland, "Optimum steady-state position and velocity estimation using noisy sampled position data," *IEEE Transactions on Aerospace and Electronic Systems*, vol. AES-9, no. 6, pp. 906–911, Nov 1973.

[121] J. Perchoux, L. Campagnolo, Y. L. Lim, and A. D. Rakic, "'lens-free' self-mixing sensor for velocity and vibrations measurements," in *2010 Conference on Optoelectronic and Microelectronic Materials and Devices*, Dec 2010, pp. 43–44.

[122] T. Shibata, S. Shinohara, H. Ikeda, H. Yoshida, T. Sawaki, and H. Sumi, "Laser speckle velocimeter using self-mixing laser diode," *IEEE Transactions on Instrumentation and Measurement*, vol. 45, no. 2, pp. 499–503, Apr 1996.

[123] Şahin Kaya Özdemir, S. Ito, S. Shinohara, H. Yoshida, and M. Sumi, "Correlation-based speckle velocimeter with self-mixing interference in a semiconductor laser diode," *Appl. Opt.*, vol. 38, no. 33, pp. 6859–6865, Nov 1999. [Online]. Available: http://ao.osa.org/abstract.cfm?URI=ao-38-33-6859

[124] R. W. S. Alan V. Oppenheim, *Discrete-Time Signal Processing*, 3rd ed. Pearson, 2010.

[125] J. Schoukens, R. Pintelon, and H. V. Hamme, "The interpolated fast fourier transform: a comparative study," *IEEE Transactions on Instrumentation and Measurement*, vol. 41, no. 2, pp. 226–232, Apr 1992.

[126] V. K. Jain, W. L. Collins, and D. C. Davis, "High-accuracy analog measurements via interpolated fft," *IEEE Transactions on Instrumentation and Measurement*, vol. 28, no. 2, pp. 113–122, June 1979.

[127] F. J. Harris, "On the use of windows for harmonic analysis with the discrete fourier transform," *Proceedings of the IEEE*, vol. 66, no. 1, pp. 51–83, Jan 1978.

[128] T. Grandke, "Interpolation algorithms for discrete fourier transforms of weighted signals," *IEEE Transactions on Instrumentation and Measurement*, vol. 32, no. 2, pp. 350–355, June 1983.

[129] D. C. Rife and G. A. Vincent, "Use of the discrete fourier transform in the measurement of frequencies and levels of tones," *The Bell System Technical Journal*, vol. 49, no. 2, pp. 197–228, Feb 1970.

[130] L. Campagnolo, M. Nikolić, J. Perchoux, Y. L. Lim, K. Bertling, K. Loubière, L. Prat, A. D. Rakić, and T. Bosch, "Flow profile measurement in microchannel using the optical feedback interferometry sensing technique," *Microfluidics and Nanofluidics*, vol. 14, no. 1, pp. 113–119, Jan 2013.

[131] G. Plantier, N. Servagent, A. Sourice, and T. Bosch, "Real-time parametric estimation of velocity using optical feedback interferometry," *IEEE Transactions on Instrumentation and Measurement*, vol. 50, no. 4, pp. 915–919, Aug 2001.

[132] R. Kliese and A. D. Rakić, "Spectral broadening caused by dynamic speckle in self-mixing velocimetry sensors," *Opt. Express*, vol. 20, no. 17, pp. 18 757–18 771, Aug 2012.

[133] S. Donati and G. Martini, "Systematic and random errors in self-mixing measurements: effect of the developing speckle statistics," *Appl. Opt.*, vol. 53, no. 22, pp. 4873–4880, Aug 2014. [Online]. Available: http://ao.osa.org/abstract.cfm?URI=ao-53-22-4873

[134] R. H. Hage, T. Bosch, G. Plantier, and A. Source, "Modeling and analysis of speckle effects for velocity measurements with self-mixing laser diode sensors," in *2008 IEEE Sensors*, Oct 2008, pp. 953–956.

[135] R. Atashkhooei, S. Royo, and F. J. Azcona, "Dealing with speckle effects in self-mixing interferometry measurements," *IEEE Sensors Journal*, vol. 13, no. 5, pp. 1641–1647, May 2013.

[136] A. Mowla, M. Nikolić, T. Taimre, J. R. Tucker, Y. L. Lim, K. Bertling, and A. D. Rakić, "Effect of the optical system on the doppler spectrum in laser-feedback interferometry," *Appl. Opt.*, vol. 54, no. 1, pp. 18–26, Jan 2015. [Online]. Available: http://ao.osa.org/abstract.cfm?URI=ao-54-1-18

[137] S. G. Rabinovich, *Measurement Errors and Uncertainties*. Springer, 2004.

[138] L. Scalise and N. Paone, "Laser doppler vibrometry based on self-mixing effect," *Optics and Lasers in Engineering*, vol. 38, no. 3, pp. 173 – 184, 2002, vibration Measurements by Laser Techniques - Advances and Applica tions. [Online]. Available: http://www.sciencedirect.com/science/article/pii/S014381660200009X

[139] W. Huang, H. Gui, L. Lu, J. Xie, H. Ming, D. He, H. Wang, and T. Zhao, "Effect of angle of incidence on self-mixing laser doppler velocimeter and optimization of the system," *Optics Communications*, vol. 281, no. 6, pp. 1662 – 1667, 2008. [Online]. Available: http://www.sciencedirect.com/science/article/pii/S0030401807012230

[140] G. Andria, M. Savino, and A. Trotta, "Windows and interpolation algorithms to improve electrical measurement accuracy," *IEEE Transactions on Instrumentation and Measurement*, vol. 38, no. 4, pp. 856–863, Aug 1989.

[141] C. Offelli and D. Petri, "Interpolation techniques for real-time multifrequency waveform analysis," *IEEE Transactions on Instrumentation and Measurement*, vol. 39, no. 1, pp. 106–111, Feb 1990.

[142] H. Renders, J. Schoukens, and G. Vilain, "High-accuracy spectrum analysis of sampled discrete frequency signals by analytical leakage compensation," *IEEE Transactions on Instrumentation and Measurement*, vol. 33, no. 4, pp. 287–292, Dec 1984.

[143] R. H. Park, "Energy centrobaric correction method for discrete spectrum," *Journal of Vibration Engineering*, vol. 14, no. 3, pp. 354–358, September 2001.

[144] Albrecht, H.-E., Damaschke, N., M. Borys, and C. Tropea, *Laser Doppler and Phase Doppler Measurement Techniques*. Springer, 2003.

[145] D. Rife and R. Boorstyn, "Single tone parameter estimation from discrete-time observations," *IEEE Transactions on Information Theory*, vol. 20, no. 5, pp. 591–598, Sep 1974.

[146] S. Yazdanfar, C. Yang, M. V. Sarunic, and J. A. Izatt, "Frequency estimation precision in doppler optical coherence tomography using the cramer-rao lower bound," *Opt. Express*, vol. 13, no. 2, pp. 410–416, Jan 2005. [Online]. Available: http://www.opticsexpress.org/abstract.cfm?URI=oe-13-2-410

[147] C. Mellet and J. C. Valiere, "Maximum likelihood approaches for sound field measurement using ldv," in *Laser Techniques for Fluid Mechanics*. Berlin, Heidelberg: Springer Berlin Heidelberg, 2002, pp. 95–109.

[148] S. M. Kay, *Fundamentals of Statistical Signal Processing: Estimation Theory*. Upper Saddle River, NJ, USA: Prentice-Hall, Inc., 1993.

[149] M. Levin, "Power spectrum parameter estimation," *IEEE Transactions on Information Theory*, vol. 11, no. 1, pp. 100–107, Jan 1965.

[150] G. Plantier, N. Servagent, T. Bosch, and A. Sourice, "Real-time tracking of time-varying velocity using a self-mixing laser diode," *IEEE Transactions on Instrumentation and Measurement*, vol. 53, no. 1, pp. 109–115, Feb 2004.

[151] P. K. Dash, G. Panda, A. K. Pradhan, A. Routray, and B. Duttagupta, "An extended complex kalman filter for frequency measurement of distorted signals," in *2000 IEEE Power Engineering Society Winter Meeting. Conference Proceedings (Cat. No.00CH37077)*, vol. 3, Jan 2000, pp. 1569–1574 vol.3.

[152] A. Routray, A. K. Pradhan, and K. P. Rao, "A novel kalman filter for frequency estimation of distorted signals in power systems," *IEEE Transactions on Instrumentation and Measurement*, vol. 51, no. 3, pp. 469–479, Jun 2002.

[153] K. Reif, S. Gunther, E. Yaz, and R. Unbehauen, "Stochastic stability of the discrete-time extended kalman filter," *IEEE Transactions on Automatic Control*, vol. 44, no. 4, pp. 714–728, Apr 1999.

[154] R. E. Kalman, "A new approach to linear filtering and prediction problems," *ASME Journal of Basic Engineering*, 1960.

[155] A. L. Duff, G. Plantier, and A. Sourice, "Particle detection and velocity measurement in laser doppler velocimetry using kalman filters," in *2004 IEEE International Conference on Acoustics, Speech, and Signal Processing*, vol. 2, May 2004, pp. ii–365–8 vol.2.

[156] A. L. Duff, G. Plantier, and B. Gazengel, "Real-time particle detection and velocity measurement by means of laser doppler velocimetry," in *2005 IEEE Instrumentationand Measurement Technology Conference Proceedings*, vol. 3, May 2005, pp. 2222–2225.

[157] H. M. Paul Zarchan, *Fundamentals of Kalman Filtering: A Practical Approach.* American Institute of Aeronautics and Astronautics, 2008.

[158] G. Acket, D. Lenstra, A. D. Boef, and B. Verbeek, "The influence of feedback intensity on longitudinal mode properties and optical noise in index-guided semiconductor lasers," *IEEE Journal of Quantum Electronics*, vol. 20, no. 10, pp. 1163–1169, October 1984.

[159] F. J. Azcona, R. Atashkhooei, S. Royo, J. M. Astudillo, and A. Jha, "A nanometric displacement measurement system using differential optical feedback interferometry," *IEEE Photonics Technology Letters*, vol. 25, no. 21, pp. 2074–2077, Nov 2013.

[160] M.Wang and G. M. Lai, "Displacement measurement based on fourier transform method with external laser cavity modulation," *Review of Scientific Instruments*, vol. 72, pp. 3440–3445, 2001.

[161] A. L. Arriaga, F. Bony, and T. Bosch, "Speckle-insensitive fringe detection method based on hilbert transform for self-mixing interferometry," *Appl. Opt.*, vol. 53, no. 30, pp. 6954–6962, Oct 2014. [Online]. Available: http://ao.osa.org/abstract.cfm?URI=ao-53-30-6954

[162] C. Bes, V. Belloeil, G. Plantier, Y. Gourinat, and T. Bosch, "A self-mixing laser sensor design with an extended kalman filter for optimal online structural analysis and damping evaluation," *IEEE/ASME Transactions on Mechatronics*, vol. 12, no. 3, pp. 387–394, June 2007.

[163] R. Kliese, Y. L. Lim, K. Bertling, A. A. A. Bakar, T. Bosch, and A. D. Rakic, "Self-mixing displacement sensing using the junction voltage variation in a gan laser," in *2008 Conference on Optoelectronic and Microelectronic Materials and Devices*, July 2008, pp. 23–25.

[164] M. Norgia and A. Pesatori, "Fully analog self-mixing laser vibrometer," in *2011 IEEE International Instrumentation and Measurement Technology Conference*, May 2011, pp. 1–4.

[165] A. L. Arriaga, F. Bony, and T. Bosch, "Real-time algorithm for versatile displacement sensors based on self-mixing interferometry," *IEEE Sensors Journal*, vol. 16, no. 1, pp. 195–202, Jan 2016.

[166] C. Bes, T. M. Bosch, G. Plantier, and F. Bony, "Characterization of a self-mixing displacement sensor under moderate feedback," *Optical Engineering*, vol. 45, pp. 45 – 45 – 6, 2006. [Online]. Available: https://doi.org/10.1117/1.2337575